

**Modelling, Measurement and Interpretation of Space Charge
Accumulation in Polyethylene Insulation for High Voltage
DC Applications**

**Thesis submitted for the degree of
Doctor of Philosophy
at the University of Leicester**

by

**Awat Abdullah Mulla
Department of Engineering
University of Leicester**

2019

Modelling, Measurement and Interpretation of Space Charge Accumulation in Polyethylene Insulation for High Voltage DC Applications

by

Awat Abdullah Mulla

Abstract

The formation of space charge inside insulating materials causes non-uniformity of the internal electric field leading to overstress of the insulation material and reduced lifetime. The pulsed electro-acoustic (PEA) method is an important tool to determine space charge distributions in insulating materials. This work proposes a novel approach for the interpretation of raw PEA data that offers a more robust and objective method for the determination of space charge and electric field profiles than traditional space charge recovery techniques proposed in the literature.

This work integrates an electro-thermal charge transport model incorporating electric field, temperature and impurity dependent electrical conductivity with a PEA simulation model to provide simulated raw PEA output data. The electro-thermal charge transport model calculates the time dependent space charge accumulation in insulating materials whilst the PEA simulation takes the space charge profile at a given time and calculates the raw PEA output waveform. The dynamics of space charge accumulation and decay under DC and DC containing an AC ripple voltage were then studied using single and double layer samples and under isothermal and temperature gradient conditions.

In the case of low density polyethylene (LDPE), the electrical conductivity and the resultant space charge accumulation was controlled by impurities. Impurities could be removed by thermal conditioning under vacuum at elevated temperatures but a temperature in excess of 50°C runs the risk of thermal ageing and increased electrical conductivity. The rate of decay of space charge following voltage removal was found to be much lower than during charging owing to the field dependent electrical conductivity. Under thermal gradient conditions the combined model gave superior fits to the raw PEA data than were obtained using a bipolar transport model. The effect of the ripple voltage on the DC voltage was to enhance space charge accumulation and therefore enhance electro-thermal ageing.

Acknowledgements

First and foremost, I am greatly thankful to my supervisor, Dr Stephen Dodd, his excellent guidance and continues support made this work possible. Despite his workload, he has been always patient in helping me get through my difficulties and problems. His broad knowledge, optimistic character, generous mind and kind heart have impressed and moved me. I feel lucky to be a student of such a great person.

I also sincerely thank Professor Dissado for his encouragement in this study and my life in general. He was always patient and kind with me.

My special thanks to Dr Nikola Chalashkanov, for his support on my study and life. He always treated me as a friend.

I would like to thank Mr Andy Willby, for his assistance in my experimental and practical work.

My gratitude also goes to Dr Paul Lefley for his precious advice on my first year and second year report which formed a good basis for my PhD thesis.

I would like to thank High committee of Educational development of Iraq (HCED) for the sponsorship and giving me the chance to study abroad.

I would sincerely like to dedicate this thesis to my wife, Naska and to my lovely children Arina and Arios. Naska constantly encouraged and she always showed her patience to me despite my long hours at work.

I must thank my parents, my brothers and my sisters, who always gave me unconditional support.

Last but not least, I would like to thank all those people who have not mentioned but have contributed in some way to my research work, I hope the lack of acknowledgment will not be taken to imply lack of gratitude.

Contents

List of tablest	v
List of figures.....	vi
Definition and Abbreviations.....	x
2 Introduction.....	1
2.1 HVDC transmission system.....	1
2.2 HVDC insulators	3
2.2.1 Paper based insulation	4
2.2.2 Polyethylene based cable.....	4
2.3 Space charge accumulation in DC voltage system	6
2.4 Space charge measurements.....	7
2.5 Justification for the proposed work.....	8
2.6 Outline of the thesis.....	13
3 Background	14
3.1 Overview	14
3.2 Theory and fundamental concepts	14
3.2.1 Electrical materials.....	14
3.2.2 Origin of charge carriers in insulating materials	15
3.3 Charge transport mechanism in dielectric materials	16
3.4 Fundamental equations that represent space charge accumulation in DC system.	18
3.4.1 Electrostatic model	18
3.4.2 Thermal model.....	21
3.5 Conductivity model in DC system	22
3.6 PEA measurement technique	25
3.6.1 Basic theory behind PEA	25
3.6.2 Typical setup of PEA for thin film sample	27
3.6.3 PEA system responses	29
3.7 Space charge observations.....	31
3.7.1 Electrode-dielectric interface	31
3.7.2 Dielectric – Dielectric interface	33
3.8 Finite Difference Method (FDM).....	36
4 Space charge measurements using traditional PEA methodologies	39
4.1 Overview	39

4.2	Traditional signal processing approach for recovery of space charge distribution measured by PEA	39
4.2.1	Base line correction:	41
4.2.2	De-noising:	42
4.2.3	Deconvolution:	43
4.2.4	Attenuation and Dispersion Correction	45
4.2.5	Calibration	48
4.3	Space charge measurement under voltage-on and voltage- off conditions	50
4.3.1	Experiment protocol	51
4.3.2	Space charge measurement inside one layer thin film samples	51
4.3.3	Space charge measurement inside double layer thin film samples	57
4.4	Conductivity measurement	63
4.5	Summary	64
5	Electro-Thermal Charge Transport Model for Space Charge Formation inside a Dielectric	67
5.1	Electro-thermal charge transport model	68
5.2	Electro-thermal conductivity model	69
5.2.1	Electrostatic part	69
5.2.2	Thermal part	70
5.2.3	Inclusion of homocharge or heterocharge accumulation	71
5.3	Model implementation	72
5.3.1	FDM formula for 1-D thin film sample	72
5.3.2	FDM formula for 2-D thin film samples	74
5.4	Space charge accumulation in 1-D thin film samples	77
5.4.1	Single layer samples	77
5.4.2	Two layer thin film samples	93
5.5	Extension of the charge transport model in single layer from 1-D to 2-D	95
5.5.1	Simulation of space charge accumulation in 2-D thin film sample when the conductivity is just field dependent, $\sigma(E)$	96
5.5.2	Simulation of space charge accumulation in 2-D thin film sample when the conductivity is field and temperature dependent	102
5.6	Summary	105
6	Simulation of the PEA Space Charge Measurement System	107
6.1	Overview	107
6.2	Forces on space charge in solid dielectrics	108
6.3	Origin of the acoustic pressure waves	109

6.4	Propagation of pressure wave in plane-plane geometry	111
6.4.1	Perfectly-matched layer (PML)	114
6.5	PEA Model Implementation - FDTD equations in MATLAB	115
6.6	Initial simulations in the absence of space charge	118
6.7	Corrections for acoustic attenuation and dispersion of the pressure waves	130
6.8	Acoustic attenuation and dispersion to PEA simulation output data	131
6.9	Correction for the PVDF/Buffer amplifier and oscilloscope frequency response	133
6.10	Comparing the simulation result with experimental PEA raw data when there is no space charge	133
6.11	Simulation and experiment to show the effect of the top electrode material on the PEA response in free charge sample	137
6.12	Effect of temperature gradient on PEA acoustic wave	138
6.13	Summary	144
7	Combining the Simulation Models and Comparing Their Results with the PEA Measuring Result	146
7.1	Overview	146
7.2	Combining the two simulation models	146
7.3	Simulation of charge accumulation and PEA raw data in single layer LDPE sample under isothermal conditions	148
7.3.1	Space charge accumulation under positive voltage application	148
7.3.2	Space charge decay following positive voltage application	152
7.3.3	Space charge accumulation under negative voltage application	155
7.4	Simulation of charge accumulation and PEA raw data in single layer LDPE sample under temperature gradient	161
7.4.1	Experimental data	162
7.4.2	Simulation of experimental data using the combined model	164
7.5	Simulation of charge accumulation and PEA raw data in double layer LDPE samples	167
7.5.1	Polarisation experiments and simulation	168
7.5.2	Depolarisation experiments and simulation	172
7.6	Summary	175
8	Assessment of the Impact of AC Ripple Voltage on the Space Charge Accumulation Inside Solid Thin Film Samples	177
8.1	Overview	177
8.2	AC ripple voltage in DC system	177
8.3	Space charge measurements	178

8.3.1	Experimental setup for raw PEA space charge measurement under pure DC voltage with superimposed AC ripple voltage	178
8.3.2	Experimental PEA measurement results – single layer LDPE	181
8.3.3	Experimental PEA measurement results – double layer LDPE	182
8.4	Combined charge transport and PEA simulations	184
8.4.1	Simulation of raw PEA space charge measurement under pure DC voltage with superimposed AC ripple voltage.....	184
8.4.2	Simulation results of single layer LDPE sample.....	185
8.4.3	Simulation results of double layer LDPE samples	190
8.5	Effect of dielectric heating+ Joule heating (result in the rippled DC voltage) on space charge accumulation inside single layer insulation sample.	193
8.6	Summary	196
9	Discussion	198
9.1	Overview	198
9.2	Space charge accumulation in single layer samples.....	201
9.3	Effect of thermal gradient on charge accumulation	203
9.4	Space charge accumulation in double layer samples	204
9.5	Effect of ripple voltage on space charge accumulation.....	205
9.6	Samples containing conducting defects.....	206
9.7	Charge transport in LDPE.....	207
9.8	Impact on electro-thermal ageing.....	208
10	Conclusions and Future Work.....	210
10.1	Conclusions	210
10.2	Main contribution of this work to the research field	213
10.3	Suggestion for future work.....	216
Appendix A: Publications		218
Appendix B: High pass and low pass filter circuits		219
Appendix C: FDM Formula to Derive Poisson’s Equation and Heat conduction Equation in 1-D thin film sample:.....		219
Appendix D: FDM Formula to Derive Poisson’s and Heat Conduction Equation in 2-D thin film sample:		220
Appendix E: Maxwell’s Tensor for PEA		221
References		224

List of tables

Table 4.1: Model parameters for field dependent conductivity.....	79
Table 4.2: Model parameters for temperature dependent conductivity.	83
Table 4.3: Model parameters for field dependent conductivity.....	90
Table 4.4: Double layer model constants in case of field dependent conductivity.	93
Table 4.5: 2-D Model constants in case of field dependent conductivity.....	97
Table 4.6: 2-D Model constants in case of field and temperature dependent conductivity.	103
Table 5.1: Model constants.....	117
Table 5.2: Material properties used in PEA simulation.....	120
Table 5.3: Material properties used in PEA simulation in case of mismatch between PVDF/PMMA.	126
Table 5.4: Material properties used in PEA simulation.....	135
Table 5.5: Material properties of LDPE sample at different temperature gradient.	140
Table 5.6: Material properties used in PEA simulation in case of temperature gradient $\Delta T=0$ °C.....	142
Table 6.1: Charge transport model constants.....	150
Table 6.2: Charge transport model constants.....	156
Table 6.3: Charge transport model constants in case of temperature gradient between the electrodes.....	165
Table 6.4: Material properties of PEA layers in case of temperature $T= 20$ °C	165
Table 6.5: Charge transport model constants in case of double layer LDPE sample...	170
Table 7.1: Charge transport model parameters of single layer LDPE sample under pure DC voltage.....	187
Table 7.2: Electrical conductivity parameters in case of 10% AC ripple that superimposed on DC voltage.	188
Table 7.3: Electrical conductivity parameters in case of 20% AC ripple that superimposed on DC voltage.	188
Table 7.4: Charge transport model parameters of double layer LDPE samples under pure DC voltage.	191
Table 7.5: Electrical conductivity enhancement parameters of double layer LDPE samples in case of 10% AC ripple that superimposed on DC voltage.	192
Table 7.6: Charge transport model parameters for calculating the joule heating and dielectric heating inside the insulation sample.....	194

List of figures

Figure 1.1: Schematic diagram of HVDC transmission line technology.	2
Figure 1.2: Schematic of LCC at HVDC system.	2
Figure 1.3: Schematic of VSC at HVDC system.	3
Figure 2.1: Schematic representation of traps in energy band diagram.	17
Figure 2.2: Hopping conduction mechanisms: (i) hopping process in the insulation material, (ii) Potential barriers before and after the application of electric field[18].	18
Figure 2.3: Basic principle of the PEA [70].	27
Figure 2.4: PEA system for thin sample.	28
Figure 2.5: The equivalent circuit of high pass filter (detecting circuit).	30
Figure 2.6: The equivalent circuit of low pass filter.	30
Figure 2.7: Effect of homo-charge on electric field E [20], X is the distance in to the dielectric measured from the anode.	32
Figure 2.8: Effect of hetero-charge on electric field E [20], X is the distance in the dielectric measured from the anode.	33
Figure 2.9: dielectric-dielectric interface between two different materials.	34
Figure 3.1: Typical raw output signal of PEA measurement.	41
Figure 3.2: Base line correction for PEA output signal.	42
Figure 3.3: De-noising of raw output signal of PEA measurement.	42
Figure 3.4: Schematic representation of the deconvolution technique [20].	44
Figure 3.5: Processed output signal of PEA measurement after deconvolution.	45
Figure 3.6: Space charge recovery profile of PEA output signal.	49
Figure 3.7: (a) Charge density, (b) Electric field, (c) Electric potential, distribution in LDPE sample at different aging time.	53
Figure 3.8: Space charge decay in LDPE after removing external voltage. Arrows indicate the time evaluation of the signals.	54
Figure 3.9: (a) Space charge, (b) Electric field,(c) Electric potential distribution in XLPE sample at different aging time.	56
Figure 3.10: A net charge density accumulation in XLPE sample at different aging time.	57
Figure 3.11: (a) Space charge, (b) Electric field distribution in two ‘as received’ LDPE layers during polarization.	59
Figure 3.12: (a) Space charge, (b) Electric field distribution in two layer sample during polarization.	61
Figure 3.13: (a) Space charge, (b) Electric field distribution in two layer sample during depolarization.	62
Figure 3.14: Electrode system for DC conduction measurement.	63
Figure 4.1: Conductivity modification based on equation 4.9.	71
Figure 4.2: Discretised 1D thin film sample based on FDM.	72
Figure 4.3: Schematic representation of two layer thin film sample.	74
Figure 4.4: Schematic representation of 2D thin film sample used for the simulation. .	75
Figure 4.5: Flowchart of the numerical procedure of calculation the space charge due to the field dependent conductivity.	78
Figure 4.6: (a) Electric field, (b) Charge density, (c) conductivity profiles as a function of position in a thin film sample when the conductivity is field dependent.	80

Figure 4.7: Numerical procedure of calculation the space charge due to the field dependent conductivity and temperature (Joule heating) dependent conductivity.....	82
Figure 4.8:(a) Temperature,(b) conductivity,(c) electric field, (d) charge density distribution in a thin film sample when the conductivity when the DC heat generation is considered.....	85
Figure 4.9: Numerical procedure of calculation the space charge due to the field dependent conductivity and temperature (conductor heating) dependent conductivity.....	87
Figure 4.10: (a) electric potential, (b) electric field, (c) conductivity, (d) charge density distribution in a thin film sample when the conductivity is temperature dependent.	89
Figure 4.11: (a) electric potential, (b) electric field, (c) charge density, (d) Conductivity distribution in a thin film sample due to the homocharge and/or heterocharge injection from electrode (s).	92
Figure 4.12: (a) Space charge, (b) Electric field, (c) conductivity distribution in two layer thin film insulation when they have different conductivity.	95
Figure 4.13: Schematic representation of 2D thin film sample used for the simulation.	97
Figure 4.14: (a) Potential, (b) Charge density, (c) Electric field distribution profiles as a function of position first without defect, second with defect at the middle of the sample for different instants of time.	100
Figure 4.15: (a) Charge density, (b) Electric field distribution at different times when defect located at the middle of the sample is under polarity reversal.	100
Figure 4.16: (a) Electric potential, (b) Space charge, (c) Electric field distribution under polarity reversal and depolarization with defect located at the middle of the sample.	101
Figure 4.17: (a) Space charge, (b) Electric field, (c) Temperature distribution around the defect at different applied voltages. The dotted lines represent the results of field dependent conductivity, whereas the solid lines represent the results of field and temperature dependent conductivity.	105
Figure 5.1: The shape of Gaussian voltage pulse with a width of 25ns and a pulse delay of 100nS.	110
Figure 5.2: Discretised PEA layers based on FDM.	115
Figure 5.3: Procedure of generation, propagation of acoustic pressure wave in PEA system.	118
Figure 5.4: Acoustic pressure wave at time=0.....	121
Figure 5.5: Applied pulse voltage on PEA system.	121
Figure 5.6: (a)-(f) Pressure wave propagating through the PEA layers at various times. The direction of propagation is shown by the arrows.....	124
Figure 5.7: (a) Acoustic pressure wave in a total domain,(b) PVDF output voltage, (b) PVDF output electric field distribution, of ideal (lossless) sample in PEA simulation model.....	125
Figure 5.8: (a) Acoustic pressure, (b) PVDF output voltage, (c) PVDF output electric field distribution, of ideal (lossless) sample when it is the impedance mismatch between PVDF and PMMA.	128
Figure 5.9: Effect of Electrode properties on PEA acoustic signal.	129

Figure 5.10: Propagation the acoustic wave in a lossy and dispersive medium.	131
Figure 5.11: Typical experimental PEA output signal.	134
Figure 5.12: (a) attenuation-dispersion correction, (b) attenuation-dispersion and reflection corrections, (c) attenuation-dispersion, reflection and PVDF-buffer amplifier corrections.	136
Figure 5.13: The result of PEA simulation compared with the PEA output data in XLPE sample.	137
Figure 5.14: Influence of top electrode on PEA acoustic wave.....	138
Figure 5.15: Temperature profile across the PEA layers in case of 40 °C temperature gradient across the semicon and the sample.	139
Figure 5.16: Simulation procedure of temperature gradient in a PEA system.	141
Figure 5.17: PEA acoustic wave at different temperature gradients.	143
Figure 6.1: Procedure of combining the simulation models and comparing with the PEA raw data.	147
Figure 6.2: The PEA output data of LDPE sample at different voltage stressing time.	149
Figure 6.3: Conductivity enhancement due to impurity diffusion from the electrodes after 30minutes.....	150
Figure 6.4: (a) voltage, (b) charge density, (c) Electric field distribution that obtained from the simulation models of LDPE sample to be able to compare with the experimental result (Figure 6.2) at different ageing time.	152
Figure 6.5: (a) PEA measurement data, (b) PEA simulation data, (c) Charge density profile,(d) Electric field distribution, in LDPE sample after removing the applied voltage.	155
Figure 6.6: (a) Measurement PEA raw data, (b) simulation PEA data, (c) charge density profile, (d) electric field distribution, under 40kV/mm of DC applied voltage.....	158
Figure 6.7: (a) PEA measurement result, (b) PEA simulation result, (c) charge density profile, (d) Electric field distribution during depolarization.....	161
Figure 6.8: (a) PEA measurement result, (b) and (c) simulation result of space charge distribution in case of temperature gradient [75].	164
Figure 6.9: (a), Space charge distributions from the charge transport model under different temperature gradients (b) Electric field profiles and (c) Final PEA simulation results.	167
Figure 6.10: Experimental PEA raw data under polarisation.	169
Figure 6.11: (a) PEA simulation voltage, (b) Electric field, (c) Space charge distribution in double layer LDPE under -7kV.	172
Figure 6.12: Experimental PEA raw data during depolarization period.....	173
Figure 6.13: (a) PEA raw output simulation, (b) electric field distribution, (c) space charge distribution under depolarisation.....	174
Figure 7.1: AC ripple voltage that superimposed on DC voltage wave form.	178
Figure 7.2: Experimental setup for measuring space charge accumulation under HVDC superimposed with AC ripple voltage.....	180
Figure 7.3: PSpice simulation model for choosing the input resistance of the PEA system.	180
Figure 7.4: PEA raw data in case of pure DC voltage.	181

Figure 7.5: PEA raw data when, (a) %10, (b) %20, AC ripple superimposed on DC applied voltage.	182
Figure 7.6: PEA raw data under -6kV DC voltage in two layer LDPE samples.	183
Figure 7.7: PEA measurement result, under -6kV and %10 ripple voltage in two layer LDPE samples.	184
Figure 7.8: (a) PEA simulation, (b) Space charge, (c) Electric field distribution under -6kV voltage in 150 μ m LDPE sample.	186
Figure 7.9: (a) PEA simulation, (b) Space charge, (c) Electric field distribution under -6kV and %10 ripple voltage in 150 μ m LDPE sample.	189
Figure 7.10: (a) PEA simulation, (b) Space charge, (c) Electric field distribution under -6kV and %20 ripple voltage in 150 μ m LDPE sample.	190
Figure 7.11: (a) PEA measurement, (b) PEA simulation, (c) Electric field, (d) space charge distribution under -6kV voltage in two layer LDPE.	192
Figure 7.12: (a) PEA measurement, (b) PEA simulation, (c) Electric field, (d) space charge distribution under -6kV and %10 ripple voltage in two layer LDPE.	193
Figure 7.13: (a) Electric field, (b) space charge, (c) temperature distribution in 1-D insulation sample under 40kV/mm DC with different ration of ripple voltage.	196
Figure 8.1: As supplied LDPE material.	202

Definition and Abbreviations

DC/HVDC	Direct current/High voltage direct current
AC/HVAC	Alternative current/High voltage alternative current
LCC	Line commutated convertor
VSC	Voltage source convertor
GTO	Gate turn off thyristor
IGBT	Insulated gate bipolar transistor
LPOF	Low pressure oil fill
SCFF	Self-contained fluid field
MI	Mass impregnated
MIND	Mass impregnated non draining cable
PE	Polyethylene
LDPE	Low density polyethylene
MDPE	Medium density polyethylene
HDPE	High density polyethylene
XLPE	Crosslinked polyethylene
DCP	Dicumyl peroxide
TSM	Thermal step method
TPM	Thermal pulsed method
PWP	Pressure wave propagation
PEA	Pulsed electro acoustic method
SCLC	Space charge limited conduction
PVDF	Polyvinylidene fluoride
PMMA	Polymethylmethacrylate
PML	Perfectly matching layer
FDM	Finite difference method
FFM	Fast Fourier transform
IFFT	Inverse fast Fourier transform

❖ **Definition of electrical parameters:**

E	Electric field
V	Electric potential
J	Current density
ρ	Charge density
σ	Electric conductivity
∇	Gradient
ε_o	Permittivity of air
ε_r	Relative permittivity
t	Time constant
d	Distance
E_0	Reference field
a	Distance between two traps
K_{cal}	Calibration factor
Δx	Spatial step
Δt	Time step
n_a	Conductivity enhancement factor near Al electrode
n_b	Conductivity enhancement factor near semicon electrode
d_a	Depth of conductivity enhancement near Al
d_b	Depth of conductivity enhancement near semicon
x	Position
γ	Field power index
e	Electron
C	Capacitance
R	Resistance
$k(t)$	Time dependent surface charge
σ_0	Conductivity reference
$V_s(t)$	Attenuated and dispersed signal
$C'E^{2b}$	Field assisted crossing of free energy barrier

❖ **Definition of mechanical parameters:**

F	Force
M_{ij}	Maxwell's tensor
a	Electrostriction coefficient of the material
c	Speed of sound
C	Young's modules
t_p	Pulse delay time
t_w	Pulse width of the half peak height
P	Pressure wave signal of PEA
$\alpha(i), \gamma(i)$	Attenuation coefficients in PML layer
ρ_m	Mass density
ρ	Density
k_f	Forward reaction rate
k_b	Backward reaction rate
k	Boltzmann constant
h	Plank constant
X	Reaction progress
A^*	Critical fraction
ΔH	Activation enthalpy
ΔS	Activation entropy
Δ, C', b	Generic parameters

❖ **Definition of thermal parameters:**

T	Temperature
C_p	Specific heat
k	Thermal conductivity
S_{heat}	Source of heat
S_{insul}	Heat that originated inside the insulation
S_{cond}	Heat that comes from the electrode (conductor)
S_{Joule}	Joule heating due to applied DC voltage

S_{Diel}	Dielectric heating due to applied AC voltage
T_0	Reference temperature
α	Temperature coefficient
ϑ	Thermal activation energy

1 Introduction

1.1 HVDC transmission system

Ultra-high voltage power transmission is now being developed world-wide. However, the importance for a stable and reliable transmission system must be maintained and guaranteed. The choices for transmission of electric power are basically defined through either overhead lines or underground cables. However, the capacitive and inductive elements in the cable and overhead lines have great impact on limiting the distance and capacity of existing technology of HVAC transmission lines. Therefore, in HVAC, power can only be transmitted efficiently over distances of up to (40-100km), this due to the increase of the capacitive charging current with increasing line distance [1]. Capacitive charging current reduces the ability of the transmission line to deliver active power to the load and requires reactive power compensation to overcome the line capacitance. Transmission of power over a long distance using HVAC lines is therefore not practical and expensive. In order to overcome this problem, HVDC based transmission system are being developed and deployed world-wide. The length of HVDC lines are not restricted by charging current and therefore the reactive power compensation is not required. HVDC power transmission lines also have the advantages of being able to interconnect two asynchronous AC power grids with controlled bi-directional power flow and for distributed connection of local renewable energy services to an existing AC power grid. HVDC technology therefore offers greater flexibility in the management of reliable power systems.

Different types of configuration have been used for HVDC links such as mono-polar, bi-polar, back-to-back and multi-terminal converters. The location, voltages range, power capability and chosen cable technologies are the main factors that are used to decide which types of configuration to use. Conversion between AC and DC power can be achieved using the traditional technology named current source converter (CSC), which is also called line commutated converter (LCC) or by using a voltage source converter (VSC) which is a more recent development [2, 3]. In a HVDC system, these converters operate as a rectifier at the sending end point (by changing HVAC to HVDC), while at the receiving end they are working as an inverter (by changing HVDC to HVAC), as shown in figure 1.1 [4]. LCC uses half- controllable thyristor valves to perform the conversion from AC to DC and from DC to AC in both rectifier and inverter stations.

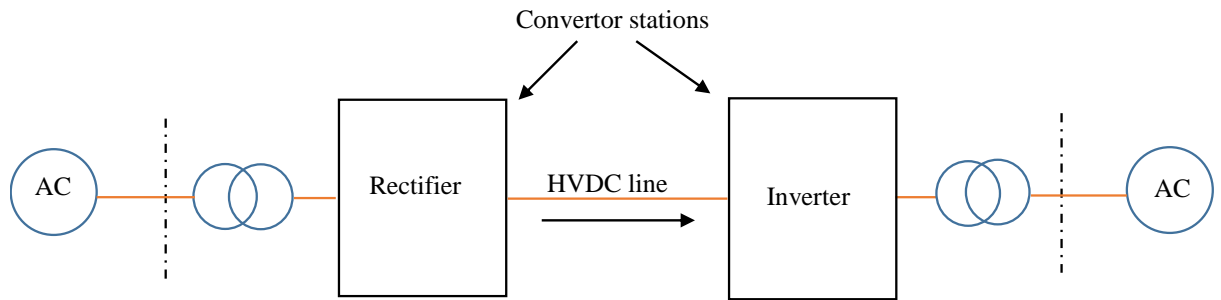


Figure 1.1: Schematic diagram of HVDC transmission line technology.

In order to reduce the ripple current/voltage superimposed on the DC voltage and to limit the transient current surges that result from lightning strikes, LCC-HVDC transmission system uses DC smoothing reactors at both ends as shown in figure 1.2. However, the switching timing of the thyristors rely on the voltage phase of the connecting AC network, which means a strong AC system is required to operate them satisfactory [5], that is why thyristor based converter is known as line commutated converter. Furthermore, both converter and inverter stations consume reactive power; therefore in both stations reactive power compensation is required.

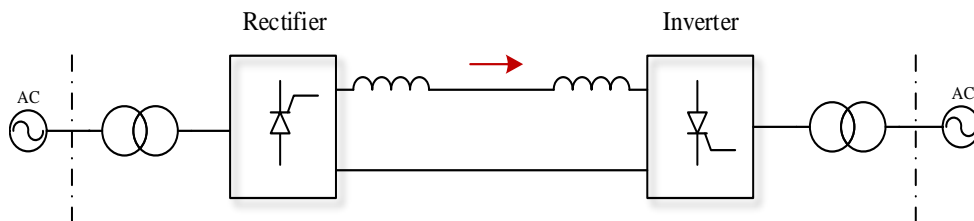


Figure 1.2: Schematic of LCC at HVDC system.

Converse to the thyristor based LCC converter in which the individual thyristors can only conduct when it receives a trigger pulse to the gate, VSC uses fully controllable devices such as gate turn off thyristor (GTO), or insulated-gate bipolar transistor (IGBT) [6]. IGBT is self-commutating, which means it can turn off and turn on without the requirement of current flow through it being interrupted for example at a zero crossing of the voltage applied across it [7]. The abilities of IGBT to turn off and turn on many times per cycle leads to a greater flexibility in controlling the current through these devices in order to deliver AC power. Thus VSC technology offers the advantage of reduced AC harmonics along with operation of the VSC converter in a self-commutated mode and no longer relies on a strong AC system for operation. In IGBT based converters, instead of smoothing reactors, DC capacitors are used in the DC side of the transmission system to reduce the ripple voltage originating from the switching of the power electronic devices.

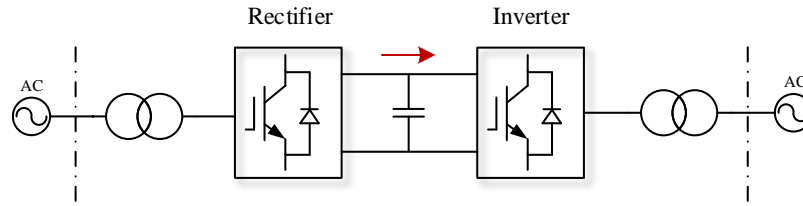


Figure 1.3: Schematic of VSC at HVDC system.

Even when installing DC capacitor banks in VSC and smoothing reactors in LCC in order to filter out the ripple voltage, the voltage in the HVDC cable which interconnects with the converter stations is not a pure steady DC voltage. Due to imperfect filtering, a residual high frequency ripple AC voltage remains superimposed on the nominal DC voltage. The degree of filtering depends on the amount (and therefore cost) of the capacitor filter banks and/or smoothing reactors. The amount of ripple voltage therefore depends on the number and size of capacitor filters that are installed on DC side of the VSC, while in LCC the ripple voltage is due to the rectification of the AC and it is filtered on DC side by a smoothing reactor. Typically the ripple voltage has a peak to peak voltage of 1-10% of the nominal DC voltage value [8, 9] and has frequency components ranging from 600Hz to tens of kilohertz. Polarity reversal of the cable voltage is another important consideration that usually occurs in DC transmission system. In LCC, the polarity reversal is a functional requirement. The direction of power flow cannot be changed by only changing the direction of current flow, it also needs to change the polarity of the two pole conductors in the transmission network. In VSC, polarity reversal is not an issue, because changing the direction of current flow causes the change of direction of power flow without the necessity of changing the polarity of the two pole conductors [1]. Therefore, polarity reversal presents another stress hazard for LCC systems.

1.2 HVDC insulators

In both AC and DC cable transmission systems, the high electric potential is insulated using dielectric materials. Nowadays, the insulation system of power cable need to withstand extremely high voltages up to 1000kV with reliable long-term operation (up to 40 years) and insulation thicctt as thin as possible to reduce cost [10]. Any insulation defects in power cables can cause the insulation to breakdown leading to power failure, which subsequently results in significant economic losses including power outage cost, compensation cost, replacement cost and safety cost. This is particularly the case for undersea cables as failure would require the lease of a specialised lifting vessel to bring the cable to the surface in order to perform a repair. Therefore, the study of and

improvements to the insulation system of power cables has a great benefit to the cable manufacturing industry as well as end users such as the grid operators. Different types of cable insulation materials have been used in DC system, however, paper/oil based insulation and polyethylene based insulations are the two most common.

1.2.1 Paper based insulation

The paper based insulation cable is the most used insulation which have been widely used in DC cable system. In the beginning, low-pressure oil-filled (LPOF), self-contained oil-filled (SCOF) and self-contained fluid-filled (SCFF) were the three most common types of paper insulation material [11]. However, due to environmental issues and their limitations for long distance the mass impregnated (MI) design became a practical alternative. Nowadays, the mass impregnated non draining cable (MIND) is the most used insulation material compared with the other types of paper insulations; even compared with the polymeric materials for HVDC applications [1, 12, 13]. Although paper - oil has a good reliability, high electrical breakdown strength, and service history, it does not withstand a high temperature when it is in service (hence low transmission capacity) and it is still susceptible to oil leakage that can cause environmental damage and is a major concern for the maintenance of good marine habitats. This limits the achievable cable rating and therefore the power capacity of the HVDC link. Besides that, paper oil insulator cable is expensive and has a complicated manufacturing process [1]. Today, the trend is towards polymeric materials especially cross-linked polyethylene (XLPE) as the primary insulation in both HVDC and HVAC systems.

1.2.2 Polyethylene based cable

Polyethylene is a hydrocarbon based polymeric material that comprises of many ethylene (C_2H_4) monomers that are treated under high pressure and temperature to produce long chain molecules (polymerisation). Polymerisation occurs when the ethylene monomers link with others to produce large polymer chains ($C_{2n}H_{4n}$), where n represents the number of repeat units called the degree of polymerisation. The degree of polymerisation, n, can be large, 10^3 to 10^5 and sometimes more [14]. Dependent on pressure and temperature, the polymerisation reaction can yield long linear chains or branched chains. Linear chains can fold along itself to produce crystals called lamellae, while the branched polyethylene can remain in a disordered state called the amorphous phase.

Polyethylene (PE) is therefore a semi-crystalline polymer [14], which means that linear molecular chains in this type of polymer are arranged as lamellae in crystalline regions, whereas in other regions branched chains are disordered and randomly tangled by each other. The solid polymer is held together by molecular entanglement of the amorphous polymer. For electrical insulations the PE has been manufactured with different density ranges (dependent on the branch content) such as low density polyethylene (LDPE), medium density polyethylene (MDPE) and high density polyethylene (HDPE). However, the density of all three types is usually between 0.9 to 0.97 g/cm³[15].

Normally, for low power applications, LDPE is more widely used as cable insulation material compared with the other two polyethylene types. The maximum operating temperature for PE materials is between 70 to 80 °C (70 °C for LDPE and 80 °C for HDPE) [16], increasing the temperature more than this range leads to aging and melting of the polymeric material and as a consequence it will no longer mechanically support the conductor of the cable. In order to increase the maximum operating temperature, the LDPE polymer molecules are chemically crosslinked together. The crosslinks hold the individual polymer chains together and largely prevent flow. This allows cables to have a higher operating temperature to 90 °C. The crosslinking process to produce XLPE was first developed in 1963 at the general electrical research laboratory in Niskayuna, New York [17]. XLPE is obtained by mixing LDPE with particular chemically reactive crosslinking agents. Dicumyl peroxide (DCP) is the most common organic peroxide agent that has been used in the crosslinking process. The cable manufactures also employ water-tree retardants and anti-oxidation agents as additives for limiting the water tree and oxidation inside the insulation [18]. The process of crosslinking can be conducted using peroxide curing technique.

After the crosslinking reaction has completed a degassing stage is required to remove the crosslinking by-products from within the insulation. This is because after peroxide crosslinking, there remains some decomposition by-products such as acetophenone and cumyl alcohol trapped inside the insulation structure. The triple extrusion stage of the cable electrical insulation (before cross-linking stage) has to be conducted by co-extruding the conductor shield, insulator and insulator shield simultaneously to prevent any defects and voids and to increase the reliability of cable. The process of crosslinking and subsequent degassing makes the XLPE to have a good thermal performance with excellent mechanical and electrical properties, and thus it is highly preferable for use in AC and DC cable systems [4, 12, 19].

In comparison with paper, the cost, maintenance and environmental impact are the main advantages of XLPE polymer compared with oil paper cable [1, 12, 20]. Therefore, this study will focus on XLPE and its precursor, low density polyethylene (LDPE) for both simulation and experimental tests.

1.3 Space charge accumulation in DC voltage system

Today polyethylene polymer especially XLPE due to its low permittivity and dielectric loss is the preferred insulation material in power industry. However, it is far from perfect particularly given the more and more demanding requirements for the insulation systems of power cable. Although XLPE is commonly and successfully used as a cable insulation in AC systems, where the rapid field reversal of alternating supply voltage (50Hz) prevents long-term charge accumulation. In HVDC insulation, continued application of voltage of a single polarity can cause space charge to accumulate within the insulation [4], and this results in local electric field enhancement within the insulation that will contribute to the processes of electrical ageing and degradation and premature electrical breakdown in worst case. Therefore, the formation of space charge in insulation materials, especially in polymers under DC voltage is of serious concern for HVDC cable manufactures and end users. Under DC voltage, the space charge can accumulate due to charge injection from electrode/insulation interfaces, inhomogeneity of insulation materials, dielectric/dielectric interfaces and/or due to the transport of ionized impurities (including the remaining crosslinking by-products) within the bulk of the insulation [21]. The accumulation of space charge in solid polymers can also be the consequence of the non-linear dependency of electric field and temperature on the electrical conductivity, particularly under a divergent electric field condition such as in cable insulation that has a cylindrical geometry. The space charge distribution inside the insulation that forms is determined by the electric field and electro-thermal properties of the insulation material. Therefore, a distribution of electrical conductivity can be formed due to the distribution of electric field and/or gradient of temperature distribution in a specific thickness of insulation material which will result in the accumulation of space charge. Space charge accumulation will also occur in flat plane samples, when there is a defect or a non-uniform distribution of impurities inside the insulation material, multi-layer samples of different electrical conductivity or when a temperature gradient is applied across the sample. In these cases the space charge can easily accumulate due to the non-homogeneous conditions that exist across the insulation material.

The accumulation of space charge can be reversed to some extent when the external applied field is removed. However, the decay of space charge can take a long time compared with the time to charge, depending on the type of insulation and temperature [22]. For example, the depletion of space charge in polymeric (XLPE) material takes longer time than the oil-paper insulation cable due to the higher inherent low field conductivity of the paper-oil insulation. Therefore, in certain materials, the space charge may remain within the insulation after removing or changing the value of applied voltage. As mentioned in 1.1, VSC produce high frequency ripple as the result of switching power electronic components. The presence of a ripple voltage on the nominal DC voltage may also have consequences for the accumulation of space charge inside the insulation and hence can affect the life time of the cable.

1.4 Space charge measurements

In order to understand the mechanism of space charge phenomena, considerable research has been conducted for developing measurement techniques of the space charge distribution inside the insulating material. Generally, there are two types of space charge measurements, destructive and non-destructive. In the early years the destructive methods of space charge detection was used such as the dust figure method [1]. In this method the sample was cut in to slices and the distribution of charge on the surface of the cut slices was detected. The destructive techniques are difficult to execute and interpret as cutting could cause the discharge of space charge. Later on, different types of non-destructive method have been developed to measure the space charge inside solid dielectrics. The non-destructive measurement method is usually divided in to two different categories which are [1, 23]:

- Thermal methods such as the Thermal Step Method (TSM) and Thermal Pulsed Method (TPM).
- Pressure pulse based methods such as Pressure Wave Propagation (PWP) and the Pulsed Electro-Acoustic method (PEA).

One of the significant advantage of the non-destructive method compared with the destructive method is that space charge is not formed during sample preparation [24]. Instead, space charge only forms on application of an applied voltage. Nowadays, the most popular and most straight forward method for the measurement of the space charge profile in dielectrics is the PEA method due to its low cost and simplicity. Therefore, in

this study the PEA technique will be used to measure space charge inside polymer samples.

1.5 Justification for the proposed work

Prolonged application of DC voltages causes space charge accumulation within insulating polymers, and results in local electric field enhancement that will contribute to electrical ageing resulting in premature breakdown of the insulation material in the worst case. Although a considerable amount of research has been performed in a last few decades to investigate the space charge phenomena inside electrical insulation materials and its consequences for electrical breakdown, only a few researchers have been carried out and reported on the effect of space charge accumulation in double layer samples which are used in cable joints [25, 26] and temperature gradients that come from the cable conductors[27]. Besides that, there is no research in the literature to show the effect of AC ripple voltage on space charge accumulation, although in some work the effect of ripple voltage on partial discharge and degradation of insulation material have been conducted [8, 28].

The mechanism of space charge accumulation in polymer insulation is not well understood. This is due to two main difficulties. The first one is due to the dependency of space charge formation on many factors such as, the material electrical conductivity (which for most materials is field and temperature dependent), the permittivity, the physical morphology of the insulation, impurities contained within the insulation material, dielectric interfaces and electrode materials. On the other hand the amount and the dynamics of space charge expected to be different when the DC voltage is superimposed with AC ripple compared with the pure DC voltage. The original source of AC ripple voltage is the transients produced when switching of the power electronic devices of the converter stations. However, even when the electrical conductivity of insulation material is assumed only field dependent (the temperature difference between the electrodes is neglected), the temperature gradient inside the sample is still expected due to the joule heating (operative when pure DC voltage is applied) and dielectric heating [29] (operative when AC ripple voltage is applied); thus their effect needs to be considered. Therefore, in order to observe the space charge dynamics inside the insulation material more accurately, the above factors need to be included. These complications have resulted in the lack of progress toward a complete physical understanding of conduction and space charge accumulation in the literature.

The second difficulty relates to the reliability and accuracy of measuring the space charge distribution inside dielectric materials. Much work in the literature has been conducted in developing space charge measurement systems based on the pulsed electroacoustic (PEA) technique. However, the main approach which has been adopted in the literature for the interpretation of the PEA output signal data and the reconstruction of the space charge profile in both thin film and cable geometries is to work backward from the PEA raw data. Although the PEA raw data contains information regarding the space charge distribution, this information is degraded due to various PEA system imperfections such as acoustic reflections, attenuation and dispersion of the acoustic signal and the frequency response of the acoustic sensor/amplifier response. Theory of dielectric electrostatic forces also highlights that it is not just space charge that can produce acoustic waves inside the sample under test. In addition mechanical forces can also be generated in cases where the electric field is divergent such as in the case of cable insulation exhibiting cylindrical geometry and in samples where the permittivity is not constant. The deconvolution of the various instrument responses, acoustic attenuation, dispersion correction and calibration are the three main steps which usually have been used to recover the space charge distribution from the PEA output signal. Attenuation and dispersion of the propagating acoustic waves is also usually required even for thin film samples as correction is still need to be done for reduction of the signal amplitude as the acoustic wave propagates through the insulating material. The signal processing methods used for reconstructing the original acoustic wave have been proposed in [30, 31]. The basis of these techniques is the use of deconvolution algorithms. Unless care is taken in applying these techniques, the solutions can be unstable and lead to the generation of false data that could potentially be misinterpreted as space charge. It is also difficult in practice to apply computer algorithms to correct the PEA signal for acoustic attenuation and dispersion. This is because of the inherent instabilities in applying matrix inversion on ill-conditioned matrices that the technique depends. Because of this difficulty, many workers usually ignore the effect of acoustic attenuation and dispersion when processing to recover the space charge distributions from PEA measurements. The limitations of the space charge recovery process is that the data processing can lead to a family of solutions for the recovered space charge profile dependent on the precise parameter values chosen in the analysis. The lack of a unique solution for the resultant space charge profile has the danger of making the technique subjective rather than analytical. The space charge recovery process as detailed above is usually employed in

the literature in the case of simple homogeneous dielectric films. However it is unclear if this technique could be extended to more complex situations such as multi-layer insulation samples where each layer has different electrical and mechanical properties or in cases of divergent field situations such as HV cable insulation.

In addition to the technical issues raised above, The PEA method also suffers from a number of other limitations that limit its effectiveness in the measurement of the electric fields at the electrodes. The PEA is responsive only to the net space charge density within a sample material. In addition the PEA instrument has a spatial resolution limit set by the applied pulse duration, the thickness of the acoustic sensor and the bandwidth of the amplifier and oscilloscope combination. These factors mean that the space charge information that can be obtained from the raw data is limited to the net average charge over a region of space equal to the resolution of the instrument. In the case of space charge accumulation in the insulation close to the electrodes, this charge will induce charge of opposite charge carriers at the surface of the electrode. The PEA instrument will only see the net charge of near zero in the regions of the interface as the overall net charge will be near zero. The PEA technique is therefore not responsive to charge close to the electrodes (within the spatial resolution limit). Hence it is not possible to usefully employ the PEA technique to probe the electric fields in the material adjacent to the electrodes in order to identify particular charge injection mechanisms.

The broad objective of the current study is to obtain a better understanding of space charge accumulation phenomena and its effect on electric field distribution in both one layer and two layer thin film insulation materials subject to HVDC (both steady DC and with superimposed ripple voltage). This will be accomplished by developing a new approach for the analysis of PEA raw data that overcomes many of the issues raised above. This will include the development of an electro-thermal simulation model for space charge accumulation under pure DC voltages and DC voltages containing an AC ripple voltage component. The output of this simulation will then be fed into a combined electro-acoustic simulation model of the PEA apparatus. This simulation will include all factors that degrade the space charge information and generate raw data to compare directly with experimental PEA raw data. Performing the analysis in this way avoids the use of deconvolution and matrix inversion techniques that can lead to unstable and non-unique solutions. Provided that the simulation results match the raw experimental PEA

output data then space charge and electric field profiles are directly obtainable from the electro-thermal charge transport simulation.

This approach to space charge recovery was first applied to the understanding of space charge accumulation in single layer mini cable insulation samples where it was used to interpret the experimental space charge distributions across the mini cable insulation in samples having isothermal temperature [23]. However, in this study the approach will be extended to include the effects of temperature on space charge accumulation and in the PEA technique for the measurement of space charge in single layer and double layer thin film insulation polymers under different electrical and thermal conditions.

This approach overcomes the limitation of PEA spatial resolution on determining the actual space charge and electric fields at the insulation electrodes as these are calculated by the electro-thermal transport model. If correspondence between the simulated and the raw PEA data cannot be achieved then a more developed electro-thermal charge transport model will need to be introduced. This proposed methodology provides a robust analytical tool linking PEA based space charge measurements with theoretical models and offers a considerable advance on that currently in the literature. Successful correspondence between the simulation and the raw PEA output will allow the simulation models to be applied to 2-layer insulation systems, the assessment of the effect of ripple voltage and temperature gradient on the accumulation of space charge and the adaption of the electro-thermal charge transport simulations to 2-D in order to examine the effect of space charge accumulation and electric field around electrically conducting defects.

To achieve these goals the following steps are required:

- Build and develop a one-dimensional (1-D) finite difference numerical electro-thermal charge transport model for calculating the space charge accumulation within the insulation material. A charge transport model will be selected at the start. The model will be required to have the capability to evaluate the electric field and space charge distributions as a function of applied voltage, applied ripple voltage, temperature gradient, interfaces (both electrode/dielectric interfaces and dielectric/dielectric interfaces) and include the processes of Joule and dielectric heating. The model should also be extended to 2 dimensions (2-D) in order to evaluate the space charge accumulation around electrically conductive defects.

- Develop a 1-D simulation model for the PEA apparatus including acoustic wave generation, propagation and detection. The model should accommodate the imperfections of the PEA apparatus including acoustic reflections at materials of different acoustic properties, acoustic attenuation and dispersion of the acoustic waves as they propagate in an absorbing and dispersive medium and the effect of the detector amplifier and oscilloscope frequency responses. Provision should be made for acoustic wave propagation in materials having a temperature gradient.
- Combine the above two simulation models to obtain the quantitative model of space charge accumulation in thin film samples and to simulate the PEA output raw data.
- Verify the new proposed model by comparison with experimental PEA results in cases of one layer and two layer insulation samples under charging and discharging.
- Identify the characteristic of thin film LDPE insulation sample under different electrical and thermal experimental conditions and interpreting the results using the proposed simulation models.
- Apply simulations to investigate the effect of ripple voltage superimposed on a steady DC applied voltage. Verify with PEA experiments.
- Apply the proposed model to cases in which a temperature gradient exists across the sample and compare with experimental PEA results from the literature in cases of a temperature gradient within insulation samples under pure DC voltage.
- Examine simulations of the effects of including dielectric heating losses under DC voltage superimposed with AC ripple and comparing with the effect of Joule heating that is obtained under pure DC voltage.
- Develop the model to calculate the space charge accumulation around the defects in a two dimensional (2-D) thin film geometry in cases of field and temperature dependent conductivity. Examine the resultant space charge behaviour.

1.6 Outline of the thesis

The Chapters of this thesis are organised as follows:

Following the introduction chapter, Chapter 2, contains the basic background theory on space charge, a detailed literature survey on macroscopic approach models of space charge, charge transport model and a principle work of PEA measurement technique. In Chapter 3, the space charge measurement in thin film LDPE and XLPE samples under voltage on and voltage off (the DC voltage is absent and the test subject is short circuited) conditions have been performed. One layer and two layer thin film sample are tested. In this chapter, the traditional approach for the recovery of the space charge accumulation and electric field distribution is taken for comparison later with the new proposed approach.

The electro-thermal model of calculation of the space charge and electric field distribution in cases of field and temperature dependent conductivity is developed in Chapter 4. The developed model is then applied to 1-D and 2-D flat plane samples. In Chapter 5, an electro-acoustic-thermal simulation model for the PEA measurement system is developed. This will be developed based on the theory behind the PEA pressure wave generation and propagation and detection including the influence of temperature. The process of combining the charge transport model with the PEA simulation model and then comparing with the PEA measurement raw data in one layer and two layer thin film LDPE are described in Chapter 6.

In Chapter 7, the effect of AC ripple superimposed on DC voltage on space charge accumulation will be accessed using the simulation models and experimentally using PEA technique in one layer and two layer thin film (LDPE) samples. The effect of AC ripple voltage on dielectric heating and subsequent space charge accumulation is also considered. Chapter 8, gives the overall discussion of the work. Chapter 9 includes the conclusions, main contributions of the study and suggestion for future work.

2 Background

2.1 Overview

This chapter introduces and reviews the physical background related to the process of charge transport and space charge accumulation inside electrical insulation materials as used in HVDC power transmission systems. The chapter also introduces the principles behind the measurement of space charge using the PEA method and the PEA system responses. Finally the basic principle of the finite difference method (FDM) is described which will be used to solve the equations of the electro-thermal transport model.

2.2 Theory and fundamental concepts

In order to understand the electrical properties of materials it is necessary to introduce a number of basic concepts which are:

2.2.1 Electrical materials

Materials are made of atoms that are configured in a way determined by chemical bonding. The atoms consist of positive charge particles, + proton (1.6×10^{-19} C), negatively charged particles, electrons (-1.6×10^{-19} C) and neutral particles, neutrons [32]. Charge is a property of the sub-atomic particles that account for the forces of electrostatic interaction between particles (excepting gravity and nuclear interactions). The force acting between particles is expressed by Coulomb's law as given by equation 2.1[33].

$$F = \frac{q_1 q_2}{4\pi\epsilon_0 d^2} \quad (2.1)$$

Where, q_1 and q_2 are the charges on the particles and d is the distance between them.

Based on equation 2.1, the force acting is proportional to the product of the charges of the two particles and inversely proportional to the square of the distance between them. If the charges are of different polarity, the force will be attractive, while if the polarities of the charge are the same, the force will be repulsive. Atoms are formed by a nucleus of closely bound protons and neutrons and hence are positively charged. The atomic number of a particular element is defined by the number of protons contained within the nucleus. Surrounding the positive nucleus are shells of electron orbits of different energy. For charge neutrality, an atom has the same number of electrons orbiting as there are protons within the nucleus. The electrons in the outermost orbit have the highest energy and are responsible for chemical bonding as well as the resultant electrical properties of the material. These outermost electrons are called valence electrons. Metals are formed by elements comprising of atoms with one or two valence electrons. As atoms condense into

a solid crystalline lattice structure, the valence electrons surrounding each atom have sufficient energy to escape from their orbit and become free to move through the crystal lattice. As the individual atoms lose their valence electrons, the atoms become positive ions. The positive ions are effectively bonded to the lattice structure due to the negative charge of the electrons that freely roam around the space between them. The free electrons are effectively mobile within the crystal structure and they can be considered as the charge carriers that contribute to the flow of charge (an electrical current). Hence metallic bonding leads to materials with good electrical conductivity. In covalently bonded materials such as many polymers, the situation is very different. Covalent bonding involve the sharing of valence electron between adjacent atoms. At absolute zero temperature, 0 K, the valence electron occupy the space of bonds between atoms. Consequently, there are no free charges and the material will act as perfect electrical insulator. In order to account for the small level of electrical conduction in covalent bonded materials, additional factors need to be introduced and these will be considered in the following sections.

2.2.2 Origin of charge carriers in insulating materials

Charge carriers are particles that can convey electrical charge within the material under the action of diffusion (diffusion current) or the application of an applied electric field (drift current). The particles must be unbound from the insulator molecular structure such that the particles can carry their charge from one region to another within the material. Possible charge carriers in insulation material include electrons and holes that are formed when a valence electron is removed from its bond position. This results in a free electron and a positive charge at the bond position from which the negatively charge electron was removed. In order for a free electron and hole to form, valence electrons must acquire sufficient thermal energy to overcome the band gap energy of the material. Hence the numbers of the electrons and holes formed depend on temperature. An alternative possible source of electrons and holes are from the electrodes attached to the material. If the applied electric field is sufficiently high, electrons/holes may be injected/extracted. Alternatively, positive and negative impurity ions may be present in the insulating material. Again these ions may migrate through the insulating material under the action of an applied voltage.

2.3 Charge transport mechanism in dielectric materials

Charge diffusion is often neglected in the field of charge transport in insulators as the carrier concentrations are usually low [34]. From a macroscopic point of view, the drift of charge carriers is often made proportional to the applied electrical field, Ohms law, $J = \sigma E$ where σ is a constant of proportionality called the electrical conductivity of the material. J is the current density and E is the applied electric field.

There are two different processes of charge transport which are electrode process and bulk process [1]. The electrode process occurs at the interface between the conductor and insulation material, in which the injection of charge carriers occurs under an applied electric field. In order for the charge carriers to leave the metal and enter the insulation material they have to pass across a potential barrier. The mechanism of passing the barrier is governed by either Schottky injection, which depends on height of the potential barrier and the available thermal energy, or tunnelling (Fowler-Nordheim) injection, which depends on the width of the potential barrier at the interface [35]. Thus, the Schottky injection occurs under low fields and high temperature, in which the potential barriers are reduced by the applied field and the electron can pass over the barrier easily provided they have enough thermal energy, while tunnelling occurs under high electric field, in which the width of the potential barrier is decreased sufficiently for the quantum mechanical process of tunnelling through these narrow potential barriers. Moreover, three conduction mechanisms in the bulk of insulation material have been investigated which are space charge limited conduction (SCLC), Pool-Frenkel conduction and hopping conduction [1]. It should be noted that both electrode process and bulk process of charge transport mechanism are dependent on the availability of trap centres, in which the charge carrier becomes immobile. The charge can be accumulated inside the insulation sample either due to charge injection from the electrodes or due to the impurity diffusion from the semicon electrodes into the sample.

The structure and chains of polymer insulation materials are disordered that lead to changing the band gap and the result of producing localized states which are called the trap centres. Therefore, the trapping centres originate at defects of chemical and physical aspects. Traps which are localised at different energy levels within the band gap between valence band and the conduction band. Based on energy levels and depth, traps are classified as shallow traps or deep traps [36]. The shallow traps are localized at the edge of both bands with the depth range of 0.15-0.3eV. The residence time of charge carriers

in the shallow trap is about 10^{-12} s. However, the deep traps are localized between both bands in the depth range of 0.04-1.5eV, in which the charge carriers might be residence for extremely long periods of time [37]. The charges trapped in deep levels therefore move relatively slower than those at shallow trap levels. Figure 2.1 shows the energy diagram of traps, in which the electron traps are located under the conduction band above the Fermi level, whereas the hole traps are located above the valence band and under the Fermi level. In the bulk of the dielectric, traps in the band gap at various energy levels capture electrons and holes and by this cause to limit charge transportation [38]. The movement of the captured charge is restricted by the depth of the trap. In order for a charge to continue to migrate through the dielectric, a hopping mechanism must take place, where the charge carrier gain sufficient energy through random thermal motion [38] to escape from one trap to another. Figure 2.2 shows a hoping mechanism that can occur inside the insulation sample. As can be seen when the electric field applied, the potential barrier decreases. The extra energy that aids the charge to move from the bottom of the trap to the top of the barrier is equal to, $eEa/2$, where a is the distance between two traps. As a result jumping of charge carriers to the left side become difficult due to requiring a higher energy comparing to the jumping to the right side[38]. Therefore in the case of hopping transport the effective conductivity of the material will be both field and temperature dependent and ohms law must be modified to, $J = \sigma E(E, T)$.

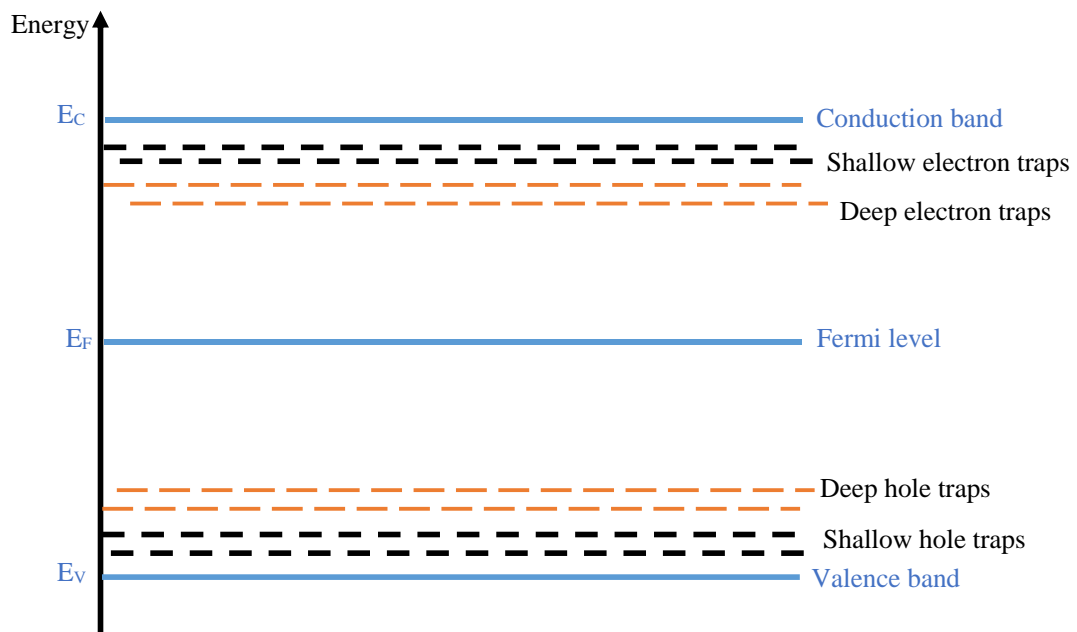


Figure 2.1: Schematic representation of traps in energy band diagram.

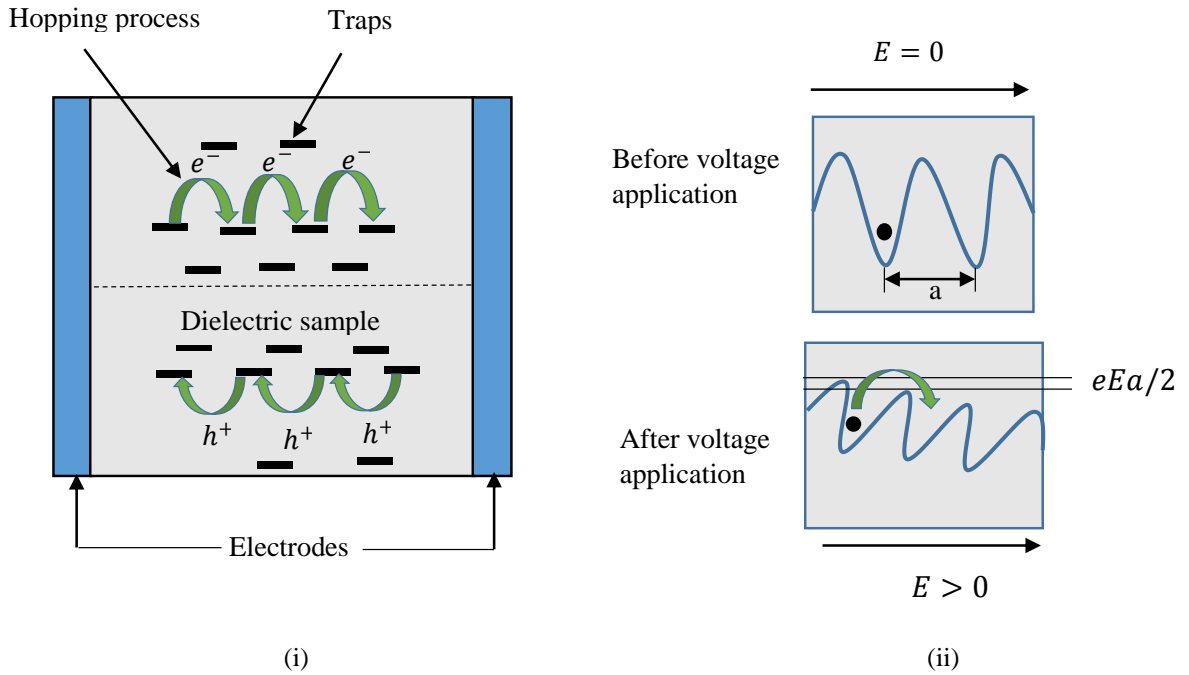


Figure 2.2: Hopping conduction mechanisms: (i) hopping process in the insulation material, (ii) Potential barriers before and after the application of electric field[18].

2.4 Fundamental equations that represent space charge accumulation in DC system

As it is well known, one of the properties of insulation polymers under HVDC is their tendency to accumulate space charge [39]. Theoretically, there are a number of important electrostatic and thermal equations that can be used to calculate the space charge accumulation inside the insulation materials which are described in the following sub sections.

2.4.1 Electrostatic model

The first and main electrostatic equation that can be used to represent the space charge accumulation inside the insulation samples is Gauss' law, equation 2.2. It enables the space charge density to be obtained from the divergence of the product of electric field vector and permittivity inside the insulation [33].

$$\nabla \cdot (\epsilon_0 \epsilon_r E) = \rho \quad (2.2)$$

Where, ρ is space charge density in (C/m^3), ϵ_0 is the vacuum permittivity and ϵ_r is the relative permittivity of the material. In a free charge region ($\rho = 0$) and when the permittivity is constant the divergence of electric field satisfies the Laplace equation ($\nabla \cdot (E) = 0$) [1].

The second equation is the transport equation. This is based on the vector of current density through an isotropic and homogenous insulation material is equal to the scalar conductivity multiplied by the vector electric field [40].

$$J = \sigma E \quad (2.3)$$

Where, J is current density in (A/m^2), σ is conductivity in (S/m). In an ideal (Ohmic) isotropic and homogeneous medium, the conductivity can be treated as a scalar constant. However, the conductivity of insulation material is non-linear under DC voltage, due to its dependency on electric field and temperature [41]. The non-linearity of conductivity of insulation material can have a significant effect on space charge accumulation when the electric field inside the insulation is non-uniform as is the case with cylindrical geometry. The accumulation of space charge can be represented using the continuity equation that has form of equation 2.4 [1]:

$$\nabla \cdot J = \frac{-\partial \rho}{\partial t} \quad (2.4)$$

This equation states that, the space charge will be accumulated, when there exists a net imbalance of charge flow into a region to that out of that region, [1]. Therefore, any situation where the current density differs in space (has divergence) will necessarily result in the generation of space charge. The build-up of space charge proceeds such as to reduce the gradient of the current density and eventually will bring the system to a steady state, in which the charge density will no longer change with time.

When the voltage is first switched on, it is often assumed that there is no space charge inside the insulation ($\rho=0$), hence equation 2.2 becomes

$$\nabla \cdot (\epsilon_0 \epsilon_r E) = 0 \quad (2.5)$$

By this, the initial field distribution is only dependent on the permittivity variation inside the material [1, 42]. Moreover, after applying the voltage for a long time, the current density will achieve a steady state value, and equations 2.3 and 2.4 become:

$$\nabla \cdot J = \nabla \cdot (\sigma E) = 0 \quad (2.6)$$

Based on equation 2.6, the electric field distribution is dependent on conductivity variation inside the material [1, 42, 43]. Furthermore, according to equations 2.5 and 2.6, space charge can be accumulated in the insulation material in steady state condition due

to the variation of conductivity. As a result, by combining equation 2.2, 2.3 and 2.6, the equation for determining space charge in steady state condition can be written:

$$\begin{aligned}\nabla \cdot (\varepsilon_0 \varepsilon_r E) &= \nabla \cdot \left(\varepsilon_0 \varepsilon_r \frac{J}{\sigma} \right) = J \cdot \nabla \left(\frac{\varepsilon_0 \varepsilon_r}{\sigma} \right) + \frac{\varepsilon_0 \varepsilon_r}{\sigma} \nabla \cdot J \\ &= J \cdot \nabla \left(\frac{\varepsilon_0 \varepsilon_r}{\sigma} \right) = \rho\end{aligned}\quad (2.7)$$

Or it can be written,

$$\rho = \sigma E \cdot \nabla \left(\frac{\varepsilon_0 \varepsilon_r}{\sigma} \right) \quad (2.8)$$

This means, that space charge can accumulate in regions where the ratio of $\varepsilon_0 \varepsilon_r / \sigma$ varies with position [12, 44].

The purely resistive (DC) steady state space charge distribution will be obtained after a period of time [45]. Determining the time to reach the steady state is therefore vital when determining the effects of a change in the operation conditions of DC cables. For instance, loading the cable will cause a temperature variation to exist inside the cable [46]. The electrical conductivity depends on both the local temperature and electric field and both these factors will have a role for determining the time to reach the steady state operation. The conductivity gradient causes the space charge accumulation which alters the electric field distribution and non-uniformity over the insulation thickness [47].

Following reference [40], the transient form of space charge accumulation can be expressed in terms of electric current density and material properties by substitution of equations (2.3) and (2.4) into equation (2.2).

$$\rho = -\frac{\varepsilon_0 \varepsilon_r}{\sigma} \frac{\partial \rho}{\partial t} + J \cdot \nabla \left(\frac{\varepsilon_0 \varepsilon_r}{\sigma} \right) \quad (2.9)$$

Based on equation (2.9), the space charge can accumulate if the permittivity or the electrical conductivity of the material is not uniform. Steady state is achieved, when the time differential of charge density goes to zero $\left(-\frac{\varepsilon_0 \varepsilon_r}{\sigma} \frac{\partial \rho}{\partial t} = 0 \right)$, then the electric field distribution and the space charge will attain the steady state condition $\left(\rho = J \cdot \nabla \left(\frac{\varepsilon_0 \varepsilon_r}{\sigma} \right) \right)$. The time to achieve steady state can be represented by a parameter τ , where τ is the time constant and is equal to $\varepsilon_0 \varepsilon_r / \sigma$.

In calculating the internal electric field inside the insulator when space charge is present, inside the insulation material, the value of the internal electric field is equal to summation of two contribution fields which are the space charge field and the external applied field (Laplacian field)[22, 48].

$$\vec{E} = \vec{E}_0 + \vec{E}_\rho \quad (2.10)$$

2.4.2 Thermal model

As electrical conductivity is temperature (and field) dependent, in order to model space charge accumulation, it is critical to establish a model for the temperature gradient in DC cables. The main source of heat is from the Joule heating of the cable under load conditions. For example in HVDC power cables, when full load current flows through the central conductor of the cable, the thermal (Joule) energy that is generated is transferred through the insulation. However, the outer surface temperature of the cable is dependent on the environment situation in which the cable is laid. The heating of the conductor will therefore give rise to a temperature distribution inside the cable insulation. The greater the conductor current, the greater the inside temperature and temperature profile obtained. Other sources of heat include resistive heating due to the very small conduction current inside the insulation material and dielectric losses due to the application of a ripple voltage superimposed on the DC voltage. The value of Joule heating is small, due to the very high resistivity and low dielectric loss of the insulation material.

The fundamental equation that can be used to deduce the temperature distribution inside the cable insulation is the heat conduction equation [49],

$$\rho_m c_p \frac{\partial T}{\partial t} = \nabla \cdot (k \nabla T) + S_{heat} \quad (2.11)$$

Where, ρ_m is the mass density, c_p is specific heat, k is thermal conductivity of the insulating material, T is the temperature and S_{heat} is the source term which represents a number of different sources; the resistive heating due to the leakage current through the insulation S_{Joule} , dielectric heating due to applied AC component (ripple), S_{Diel} , and also the resistive losses of the cable high voltage cable conductor, $S_{conductor}$ [50],

$$S_{heat} = S_{insulation} + S_{conductor} \quad (2.12)$$

where, $S_{insulation} = S_{Joule} + S_{Diel}$.

When a DC cable is first energized (voltage on) at the beginning, with zero load current through the central conductor such that there is no temperature gradient across the cable, at that time the field distribution would be classified as ‘quasi-capacitive’ or ‘quasi-Laplacian’ [43] and no space charge exists. After the cable is loaded, the Joule heating will occur in the conductor which leads to the establishment of a thermal gradient in the insulation. The internal electric field will then change from ‘quasi-capacitive’ to ‘quasi-Poisson’ as space charge accumulates. The internal temperature and electric field changes with time until a steady state is achieved. The steady state electric field distribution is then called ‘quasi resistive’ as the electric field now depends on the non-homogeneous distribution of electric conductivity. In regions of the insulation where the temperature is high, the high electrical conductivity will cause the electric field to reduce. Conversely, the electric field will increase in regions of low temperature.

2.5 Conductivity model in DC system

As mentioned in section 2.4.2, a temperature gradient will exist in HV cable insulator material mostly due to the joule heating losses originated from the central conductor [1, 18, 20, 51]. This occurs when cables are loaded under HVDC [52, 53], while the outer surface temperature of the cable is determined by the environment. The temperature gradient leads to a gradient of electrical conductivity within the insulation. The ratio of $\varepsilon_0 \varepsilon_r / \sigma$ will therefore change across the insulation thickness and space charge will build up in the material based on equation 2.13 [1].

However, even in cables at zero load, the ‘Laplacian’ field is not uniform inside the insulation material due to the cylindrical shape of the cable. It depends on $\frac{1}{r}$, where r is the radius of the cable insulation position. Therefore, when the conductivity is field dependent, the steady state space charge distribution can be determined by:

$$\rho = J \cdot \nabla \left(\frac{\varepsilon_0 \varepsilon_r}{\sigma} \right) \quad (2.13)$$

Where, J is the current density that flows within the insulation material, ε and σ are the permittivity and electrical conductivity of the insulation material respectively.

In case of thin film samples under isothermal temperature, no space charge will accumulate owing to the uniform electric field and current density across the sample. When the electrical conductivity becomes non-uniform, due for example to a temperature gradient across the sample, space charge will be accumulated.

Conductivity gradient and its effect on space charge accumulation has been investigated by researchers. Bodega in [54] stated that the first work on time dependent accumulated space charge due to the gradient of conductivity was done by Lau in 1970. In that research, the space-charge dynamics due to the thermally induced conductivity gradient in a cable stressed at constant voltage after it is connected to its load has been considered. In this work it was assumed that the thermal time constant of the cable insulation is so short compared to its dielectric time constant that the steady temperature profile can be regarded as quasi- instantaneous. However, in that work the field dependency of conductivity was not considered [54, 55]. Lau's model was extended by Coelho in [55] by including in the calculation the field dependency of electrical conductivity.

On the other hand, Jeroense in [13, 46] defined a numerical procedure for calculating the electric field and space charge in paper-insulated cables. In this work a one dimensional time dependent field distribution was calculated over an interval of time for charging and polarity reversal which was divided into seven different voltage application stages. In the initial voltage application stage which is a capacitive stage (first time when the voltage applied and ramped) the calculation could be done analytically. However, for the subsequent time stages (resistive stages) the field and space charge had to be calculated numerically. Therefore, the field and temperature dependencies on conductivity gradient were calculated in the resistive stages.

After that, Boggs et al. [41, 51] using a charge transport model based on hopping conduction, in which the significance of thermal activation energy and the importance of field and temperature gradients on conductivity measurements that directly influence upon the field distribution in insulation materials was demonstrated. The key point of Boggs research was that the activation energy determines the amount by which conductivity changes with changes in temperature.

Moreover, in [39, 52, 53, 56] COMSOL Multiphysics software was used to calculate the electric field distribution in XLPE by considering both effects of temperature and field on conductivity of the material. In all of these research works, the space charge was accumulated due to the conductivity gradient of insulation.

In order to take into account the dependencies of electrical conductivity on temperature and electrical field, different equations for the electrical conductivity have been used in the literature. However equations 2.14, 2.15 and 2.16 are the most common. Equation

2.14 is derived from the charge hopping theory model of conduction in the dielectric material [41, 51], in which the charge hopping process is thermally activated [54]. This means that the electrons must have sufficient thermal energy to overcome the potential barrier or through tunnelling from side to side if the electric field is sufficiently high [14, 38, 57], while equations 2.15 and 2.16 are both empirical equations [1, 13, 42]:

$$\sigma(E, T) = A \exp\left(\frac{-\vartheta \cdot e}{K \cdot T}\right) \frac{\sinh(B|E|)}{|E|} \quad (2.14)$$

$$\sigma(E, T) = \sigma_0 \exp(\alpha T) \exp(\gamma|E|) \quad (2.15)$$

$$\sigma(E, T) = \sigma_0 \exp(\alpha(T - T_0)) \left(\frac{E}{E_0}\right)^\gamma \quad (2.16)$$

From equation 2.14, A and B are constants; ϑ is thermal activation energy in eV; e is elementary charge; T is temperature in Kelvin; E is electric field in V/m and K is Boltzmann constant.

In equation 2.15, σ_0 , α and γ are empirical constants which represent the proportionality, temperature and field dependency coefficients of electrical conductivity [13]. Equation 2.16 is nearly similar to equation 2.15, in which σ_0 is a proportionality coefficient, and E_0 , α and γ are empirical constants. In this study equation 2.16 will be used in the numerical calculations. The reason of choosing this equation is because it is widely used in the literature [1, 23, 48, 54], and it has a superior fit with the experimental data that obtained in this study compared with the other two equations.

On the other hand, additives and impurities within the insulation material can have a significant impact on electrical conduction, electric field and space charge distribution [58]. The existence of impurities could be a function of temperature or chemical related parameters and they can be dependent on their diffusion time [59]. By this the electrical conductivity can be a function of composition, temperature and electric field, which can be demonstrated mathematically as described below:

$$\sigma = \prod_i f_{c_i}(c_i) f_T(T) f_E(E) \quad (2.17)$$

Where $f_{c_i}(c_i)$ is a function depending on the i^{th} impurity type as a function of its distribution, c_i , across the insulator, $f_T(T)$ a function of temperature and $f_E(E)$ a function of the electric field across the insulator.

2.6 PEA measurement technique

To measure space charge distributions in insulating materials, the pulsed electro-acoustic (PEA) technique can be used [60, 61]. This method requires the application of a fast pulsed variation of the applied voltage across its electrodes. The change in applied field due to the pulsed voltage produces a variation of the electrostatic force acting on each charge and thus creates elastic pressure waves that propagate in the insulation having amplitude proportional to the charge density. These elastic pressure waves travel through the insulator and the electrodes of the PEA apparatus at the velocity of sound and can be measured by transducers. The PEA method is a successful technique that has been widely used for measuring space charge distributions in thin film, mini –cables and full size cable samples [23, 62]. The PEA was first developed in Japan in the 1980s [63]. By the 1990s, it was routinely applied in the lab internationally [64].

2.6.1 Basic theory behind PEA

The basic principle of PEA technique is schematically represented as shown in figure 2.3. The technique is based on the Coulombic force, in which, an external applied electric field induces a mechanical force on space charge $q(x)$. A sudden change in the applied field $E + \Delta E$, will lead to the production of acoustic (pressure) waves $P(x, t)$ in the insulation material which, as a function of time, propagate towards the piezoelectric sensor through the aluminium base plate. These acoustic waves are detected and transformed in to an electrical signal $V_S(t)$ by a piezoelectric transducer which is mounted on the reverse side of one of the electrodes (usually the ground electrode). The amplitude of the signal that is detected by PEA after correction for the high pass response of the piezo transducer (capacitor) and the input resistance of the amplifier (50Ω) is assumed to be directly proportional to the space charge distribution inside the insulator, $q(x)$. The electric signal is then amplified before recording by using an oscilloscope.

In general there are a number of sources of acoustic waves in dielectric materials when a pulsed electric field is applied. These can be derived from the following expression for the force density. Force density is the force acting per unit volume of the dielectric. The total vector force density that acts on an insulation body is [65, 66]:

$$\vec{f} = \rho \cdot \vec{E} - \frac{\epsilon_0}{2} \cdot E^2 \cdot \nabla \epsilon_r - \frac{\epsilon_0}{2} \cdot \nabla (E^2 \cdot a) \quad (2.18)$$

Where the arrows placed above certain parameters, force density, f , and electric field, E are vector quantities. ρ is a scalar quantity representing the space charge density, ϵ_0 is

the permittivity of free space, ϵ_r is the relative permittivity of the dielectric and a is the electrostriction coefficient of the insulator material. The first term on the right hand side represents the columbic force acting on space charge due to the applied electric field, $E(x)$. The second term is called the electrophoretic force, it generates acoustic waves when the dielectric is inhomogeneous in that it has boundaries of different permittivity. Therefore the second term must be counted when the two-layer insulation material samples are tested which have different permittivity. The third term is called the electrostrictive force which is the force due to a dimensional change of the dielectric leading to a change in the relative permittivity of the dielectric on applying an electric field on that dielectric.

Assuming that the polling field, $E(x)$, is uniform due to the plane geometry of electrode/dielectric materials, the electrostriction term is often neglected and only the first two terms of equation 2.18 contribute to the force density in the simulated configuration [67] , the total force vector can be written as:

$$\vec{f} = \rho \cdot \vec{E} - \frac{1}{2} \cdot E^2 \cdot \nabla \epsilon \quad (2.19)$$

However, the calculation of force density can be simplified, if the force density is expressed as the divergence of Maxwell's tensor M_{ij} . The main advantage of this method of calculation is that the force vector can be written in terms of the vector electric field without requiring the calculation of the interfacial surface charge densities at each of the two PEA electrodes [68]. Therefore, by using Poisson's equation to eliminate charge density (ρ), in equation 2.19, the force density vector can be written as following equation [69]:

$$f_i = \frac{\partial M_{ij}}{\partial x_j} = \frac{\partial(\epsilon E_i E_j)}{\partial x_j} - \frac{1}{2} \frac{\partial(\epsilon E^2)}{\partial x_i} \quad (2.20)$$

Where the indexes, i and j refer to the components of the 3-D vector [23].

In fact, when a sudden change in electric field occurs, two kinds of pressure wave (compression and rarefaction) are generated by space charge at each point in space, these two pressure waves propagate in opposite directions (one moves towards the ground electrode while the other moves towards the upper electrode). The pressure wave that moves towards and through the ground electrode is detected using the piezoelectric sensor. However, the part of the acoustic pressure waves that moves towards the top electrode may be reflected back from the free surface above the semicon layer and then

move towards the piezo-electric sensor. However, this pressure wave undergoes a longer propagation distance and this unwanted signal occurs later in time. Correction to the detected raw output data is required to obtain the real space charge that accumulated inside the insulation sample.

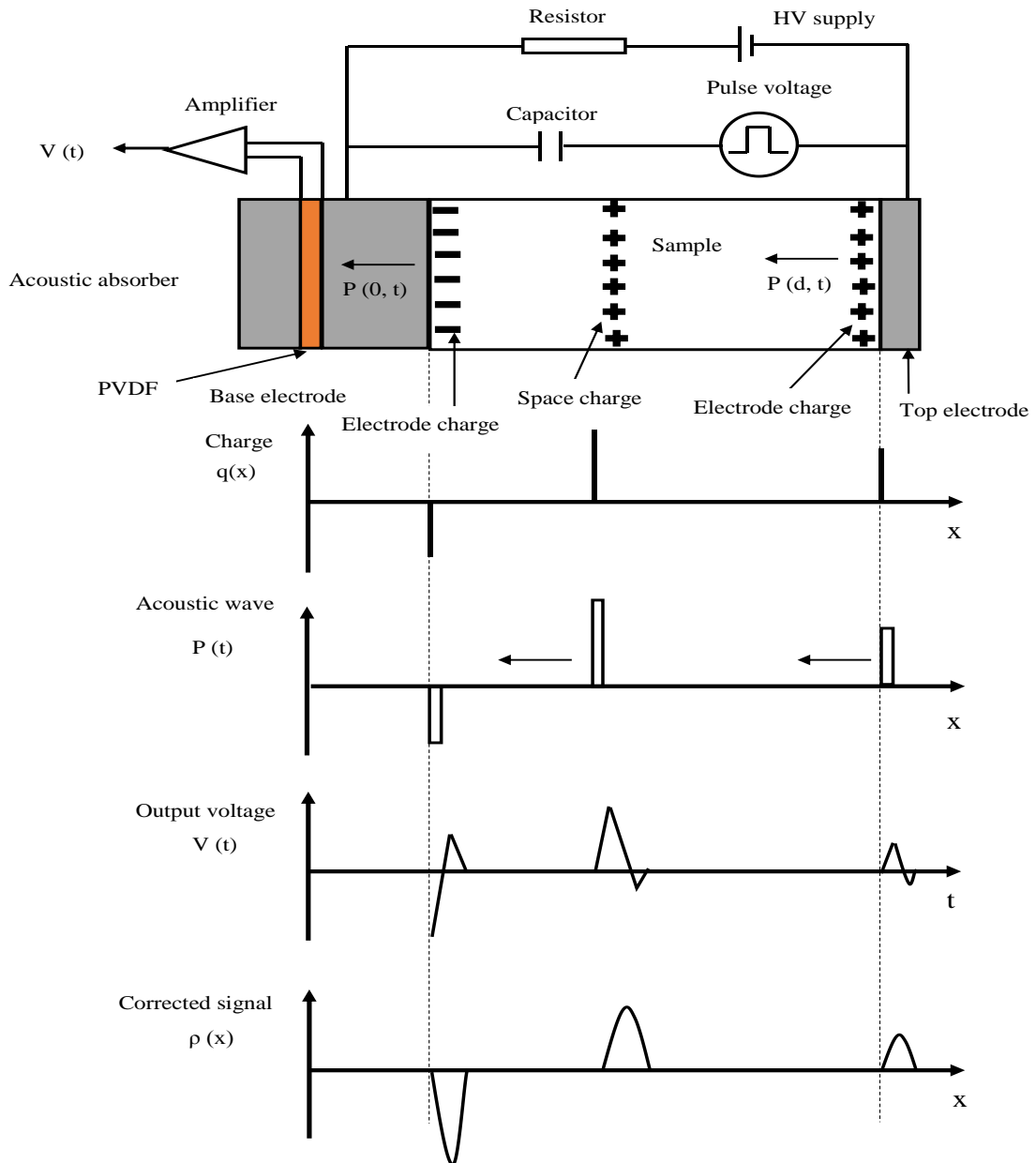


Figure 2.3: Basic principle of the PEA [70].

2.6.2 Typical setup of PEA for thin film sample

Typical schematic diagram of a PEA setup is shown in figure 2.4. The typical PEA system consists of a top electrode, a ground electrode, a piezoelectric sensor (PVDF), PMMA, absorber and amplifier. The sample is sandwiched between the top and ground electrode. The DC voltage is supplied to the top electrode and the ground electrode is

earthed to produce the HVDC field to the sample. To measure the space charge, a pulsed voltage is applied to the top electrode to momentarily change the polarization field. Due to the changing field, mechanical pressure (acoustic) waves are generated by space charge that are detected by the PVDF sensor. In order to have a good match of acoustic impedance between the top electrode and the insulation sample, a semi-conducting (carbon loaded) polymer is usually selected (called semicon) as the top electrode material, while Al material is selected as a ground electrode. The ground plane electrode serves two functions; the first is to provide a zero equipotential on one surface of the sample. The second function is to act as an acoustic transmission line to couple acoustic pressure waves generated by space charge in the sample to the PVDF detector. The DC voltage and pulsed voltage are applied from the top electrode to the sample through protecting resistance and coupling capacitance. The PVDF sensor is connected under the bottom electrode to detect the acoustic wave and produce the electrical signal. An absorber with same acoustic properties as a PVDF sensor is used to absorb the acoustic waves that transfers through the PVDF in order to prevent the acoustic reflection. The output signal of the PVDF is amplified by using amplifier. The amplifier is connected to a digital storage oscilloscope.

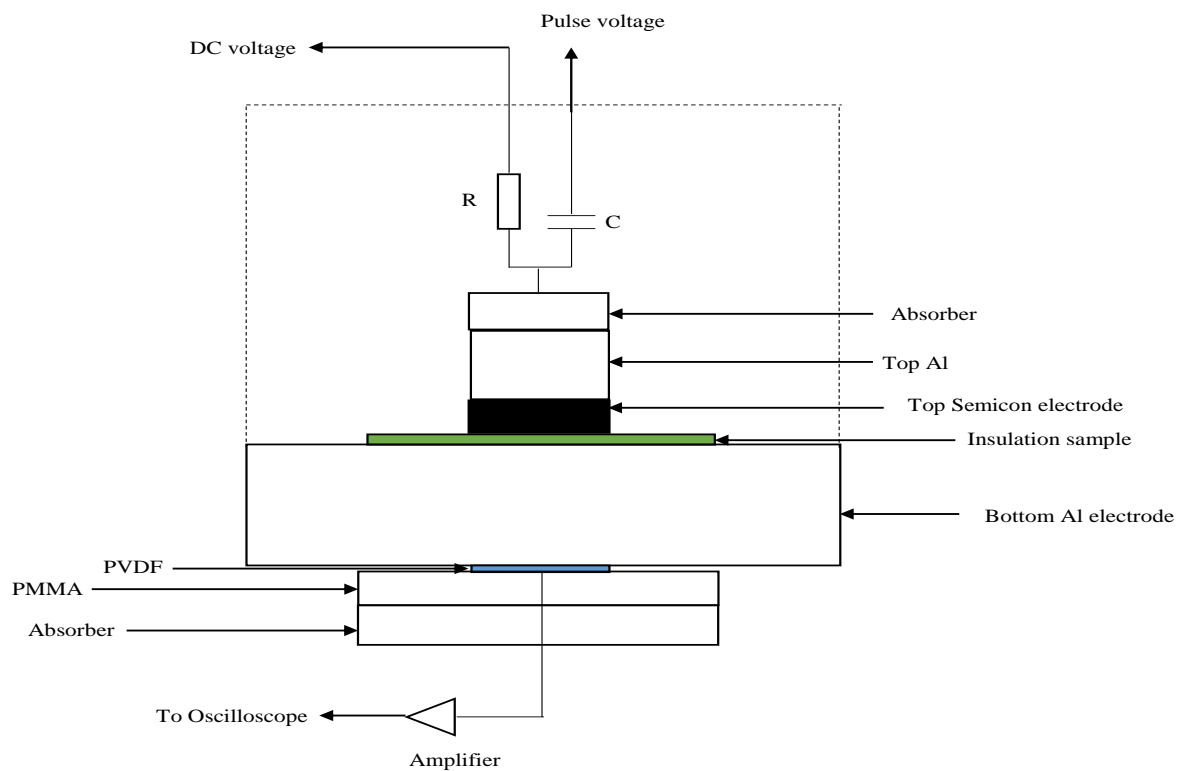


Figure 2.4: PEA system for thin sample.

2.6.3 PEA system responses

In the PEA system, the space charge distribution can be obtained after correction for several system imperfections and responses, such as pressure wave attenuation and dispersion, acoustic reflections, the distortion of the electric signal due to the sensor capacitance and input resistance of the amplifier and the limited bandwidth of the oscilloscope. All of these processes has an influence on the measured space charge signal. To be able to reconstruct the space charge correctly, the transfer function of all these non-ideal system responses are required, such as the transfer function of the PVDF and amplifier which works as high pass filter and the transfer function of the oscilloscope which works as a low pass filter. Explanation of these two latter transfer functions are given below.

2.6.3.1 RC detected circuit (High pass filter (HPF))

The PVDF sensor is essentially a capacitor of capacitance, C , and directly connected with the amplifier having a resistive input impedance, R of 50Ω as shown in figure 2.5. The frequency response of the amplifier is from 1MHz to 1GHz. The equivalent circuit of PVDF can be considered as a voltage source in series with a capacitance of the sensor C . The capacitance of the sensor (C) is given by:

$$C = \frac{\epsilon_0 \epsilon_r A}{d} \quad (2.21)$$

Where, ϵ_0 is vacuum permittivity its equal to $8.854 \cdot 10^{-12}$ F/m, ϵ_r is the relative permittivity of PVDF and equal to 8.5 [67], A is the area of the PVDF sensor and is typically equal to 1 cm^2 , d is the PVDF thickness and is typically equal to $9 \mu\text{m}$ given a capacitance of $8.4 \cdot 10^{-10}$ F. The input impedance of the amplifier, $R = 50 \Omega$ and hence the cut off frequency of HPF is, $F = \frac{1}{2\pi RC} = \frac{1}{2\pi \cdot 50 \cdot 8.4 \cdot 10^{-10}} = 3.8 \text{ MHz}$.

The transfer function of the high pass filter in the frequency domain is given by equation 2.22. The detailed derivation of this equation is given in appendix (B1)

$$\begin{aligned} H_h(f) &= \frac{V_o(f)}{V_i(f)} = \frac{j\omega\tau}{1 + j\omega\tau} \\ &= \frac{j2\pi fRC}{1 + j2\pi fRC} \end{aligned} \quad (2.22)$$

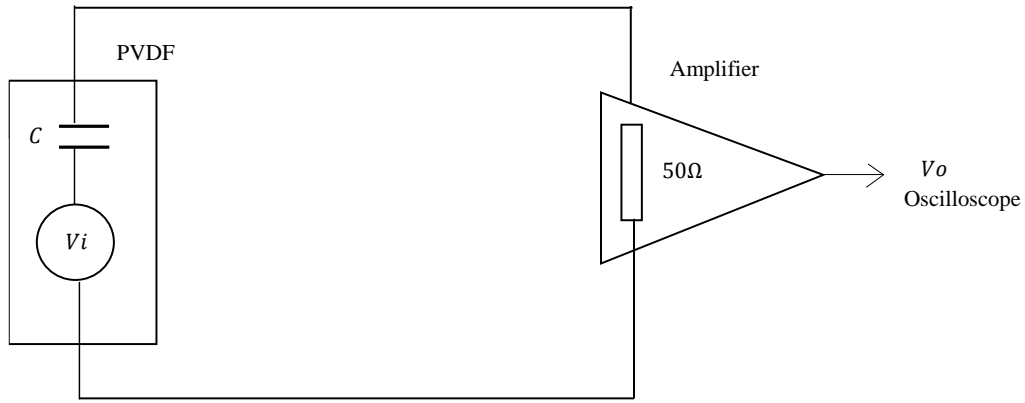


Figure 2.5: The equivalent circuit of high pass filter (detecting circuit).

This high pass filter will lead to some distortion in the original signal. Therefore, to reconstruct the PEA data it should be considered and accounted for using deconvolution techniques.

2.6.3.2 Oscilloscope frequency response (Low pass filter)

The frequency response of the oscilloscope is approximately 500MHz [46], and can be considered to work as a low pass filter. The time constant of the low pass filter is much smaller than the high pass filter ($\tau_r = 1/f$) about 2ns. The low pass filter will also cause some distortion in the original signal by removing high frequency components in the output signal. Therefore, to reconstruct the data correctly, it should also be considered. Here, the output of the amplifier will be the input for the oscilloscope as shown in figure 2.6. Therefore, the equivalent circuit of the input stage of the oscilloscope amplifier can be considered as a capacitance C in parallel with a 50Ω resistor. The time constant τ_r can be considered equivalent to the reciprocal of the oscilloscope amplifier band width.

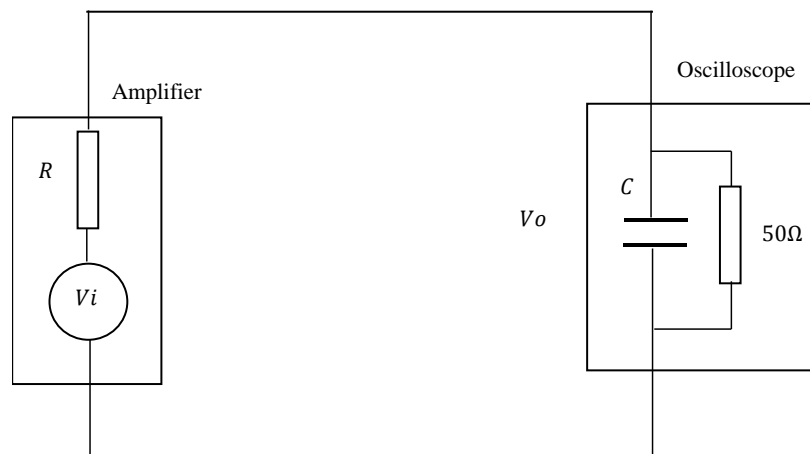


Figure 2.6: The equivalent circuit of low pass filter.

The transfer function of the low pass filter in the frequency domain is given by 2.23. The detailed derivation of equation 2.23 is given in appendix (B2)

$$H_l(f) = \frac{V_o(f)}{V_i(f)} = \frac{1}{1 + j\omega\tau_r} \quad (2.23)$$

2.7 Space charge observations

The space charge that accumulates inside the insulation material is often found to be formed in regions of the insulation close to the electrodes in the form of homocharge or heterocharge. Reasons of these observations are: (1) Imbalance between charge injection from the electrodes and charge transport in the bulk of the sample [20, 71, 72]. (2) In case where the sample contains impurities that have diffused into the sample or cross-linking reaction by-products where charge forms due to the ionisation process [73, 74]. (3) In case of temperature gradient, either due to the temperature difference between the electrodes or due to the joule heating that originated inside the sample [75, 76]. (4) In case of a non-homogenous material, such as material containing defects or in case of double layer insulation samples when the layers have different permittivity and/or different conductivity [77-79].

According to literature, the two most common places that lead to divergence of current density which leads to space charge accumulation are the following:

2.7.1 Electrode-dielectric interface

The flow of charges through the electrode- dielectric interface is governed by the nature of charge injection / extraction processes and their dependency on electric field and temperature [14]. The charge transport mechanisms that lead to the flow of charges through the insulation bulk is also dependent on electric field and temperature. When there exists a difference between the flows of charge across the electrode-dielectric interface, $J_{inj}(E, T)$, which named charge injection or extraction, and the flow of charge through the dielectric material, $J_{trans}(E, T)$, which named charge conduction or charge transport, space charge will build up at the electrode–dielectric interface as a consequence of these two flows. The net imbalance of charge density, $\Delta J_{inj}(E, T)$, as shown in equation 2.24, gives rise to the accumulation of charge. The charges that flow in both cases depends on temperature and electric field as well as the electrode and dielectric material [35].

$$J_{inj}(E, T) - J_{trans}(E, T) = \Delta J_{inj}(E, T) \quad (2.24)$$

The build-up of space charge can be divided in to three cases [20, 35]:

- 1- In the first case which is usually named ohmic, $J_{inj}(E, T) = J_{trans}(E, T)$. It means, the injected current charge is just enough to replenish the charge that has been transported away from the interface. Therefore, the difference between the two flows is zero and there is no build up of space charge.
- 2- In the case where the injection current is higher than the transport current, $J_{inj}(E, T) > J_{trans}(E, T)$, a positive homocharge (of the same sign) accumulates near the anode and negative homocharge accumulates near the cathode as demonstrated in figure 2.7. The generated homocharge leads to an increased electric field in the bulk of the insulator and increasing the bulk transport, and it causes a decrease in the electric field at the electrode interface and hence decrease injection current. When the injection current and the transport current are in balance a steady state condition can be achieved.

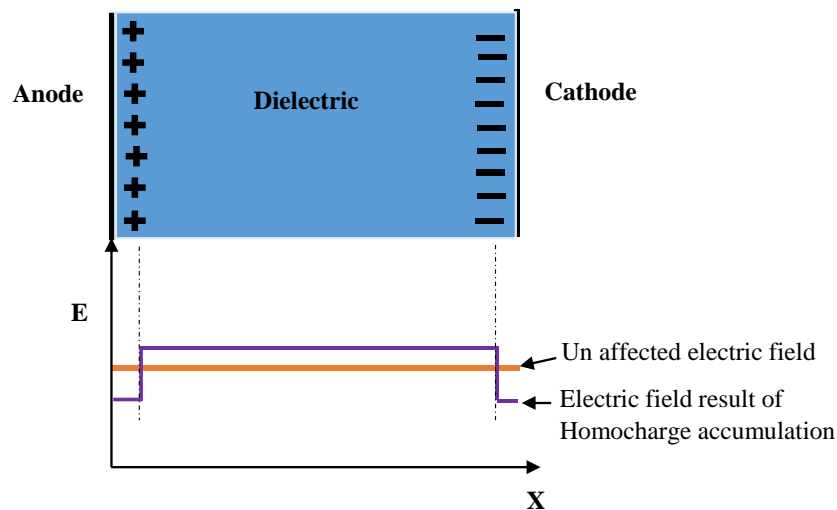


Figure 2.7: Effect of homo-charge on electric field E [20], X is the distance in to the dielectric measured from the anode.

- 3- On the other hand, if the injection current is smaller than the transport current $J_{inj}(E, T) < J_{trans}$, then negative heterocharge will be accumulated near the anode and positive heterocharge accumulated near the cathode. The heterocharge leads to a reduction of the electric field in the bulk and reduction of the bulk transport current, whereas at the electrodes it causes an increase in the electric field and hence increasing injection current as shown in figure 2.8. When the injection current and the transport current are in balance a steady state condition is achieved.

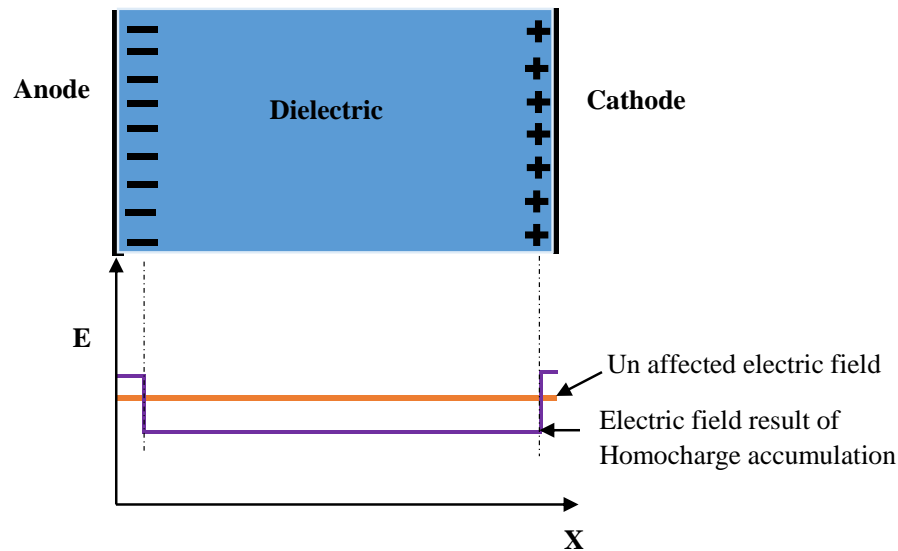


Figure 2.8: Effect of hetero-charge on electric field E [20], X is the distance in the dielectric measured from the anode.

An alternative explanation for the origin of homocharge layers is given in references [58, 80, 81]. In HV cables, homocharge can build up due to the diffusion of impurities from the semicon layers into the insulation which modifies the local electrical conductivity in the insulation material adjacent to the semicon. This modification of electrical conductivity near the semicon layers can be included in the electro-thermal charge transport model as a spatial function of impurity concentration. In this case, parameters are required to represent the concentration and depth of impurity diffusion from the surfaces of the insulation sample. This principle of representing the space charge accumulation is therefore easier and it's more straightforward than using the theory to determine the space charge accumulation due to the imbalance between charge injection and extraction from the electrodes. In this thesis, the space charge measurement data will be analysed and interpreted based on this method.

2.7.2 Dielectric – Dielectric interface

HVDC insulation systems may contain dielectric – dielectric interfaces, such as in joints and terminations of HV cable [82]. These interfaces which are unavoidable in cable accessories are often considered as the weakest part of the insulation material [83, 84]. The effect of these interfaces is assumed to be more important in DC systems due to the fact that material conductivities can vary over an extremely large range while material permittivities vary much less. It is expected that the permittivity and conductivity of two different dielectrics are different. The permittivity difference between two dielectrics would produce a discontinuity of electric field at the moment of field application at the

interface and causes a difference of electric field to exist in each dielectric. The difference of electric field leads to a difference in current density within the two materials and this causes the build-up of space charge at the interface [54]. In addition, according to transport equation ($J = \sigma E$), the conductivity difference between the two dielectrics would initially cause a divergence of current density to exist at the interface between them [20]. The divergence of current density at the interface leads to accumulation of space charge at the interface. However, as the charge accumulates at the interface, the electric field in the two dielectrics change as to reduce the divergence of current density at the interface. Steady state is achieved when the electric field has been modified by space charge such that $\nabla \cdot J = 0$ at the interface.

The accumulated space charge at the interface between two different dielectrics can be analysed using the Maxwell–Wagner (MW) theory [20, 83, 85]. For example, for two different dielectrics, A and B, that shown in figure 2.9, and where ϵ_A , σ_A and d_A are the permittivity, conductivity and the thickness of dielectric A, and ϵ_B , σ_B and d_B are the permittivity, conductivity and the thickness of dielectric B, a space charge surface density at the interface is given by [89, 90][86, 87]:

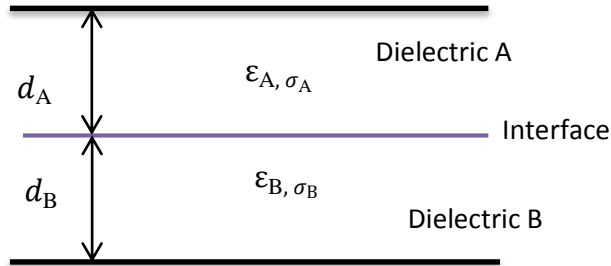


Figure 2.9: dielectric-dielectric interface between two different materials.

$$k(t) = \frac{\epsilon_A \sigma_B - \epsilon_B \sigma_A}{\sigma_A d_B + \sigma_B d_A} \cdot U_0 \left(1 - e^{-t/\tau_{MW}} \right) \quad (2.25)$$

$$\tau_{MW} = \frac{d_A \epsilon_B + d_B \epsilon_A}{d_A \sigma_B + d_B \sigma_A} \quad (2.26)$$

Where $k(t)$ is a time dependent of surface charge density at the interface. τ_{MW} is the Maxwell Wagner time constant. From equation 2.25 the interfacial charge can be

calculated directly from the knowledge of insulation properties and insulation thicknesses. After finding the interfacial charge density, the electric field in each dielectric can then be found using:

$$E_{A(B)} = \frac{U - \frac{k(t) \cdot d_{B(A)}}{\epsilon_{A(B)}}}{d_{A(B)} + d_{B(A)} \cdot \frac{\epsilon_{A(B)}}{\epsilon_{B(A)}}} \quad (2.27)$$

These findings of interfacial charge density and electric field are the main advantages of MW approach [54, 83]. However, when the electric field and/or temperature dependent conductivity are taken in to account, the MW theory is no longer valid to calculate interfacial charge, because in the simple MW theory, the temperature and electric field are discounted for the insulation conductivity [54, 78, 83, 86]. Therefore, for calculating the influence of temperature and field on the electrical conductivity, the interfacial space charges have to be calculated numerically.

Bodega et al. in [83] used a numerical iterative method to calculate the field dependent conductivity based on the macroscopic properties of the insulation which was named ‘Numerical Maxwell Wagner’ (NMW) theory. After comparing the NMW and MW results with the experimental results, they found that the numerical approach indicates a better agreement with the experimental result.

Later on, based on MW and NMW theories, the dynamic model (DM) was proposed by Leroy et al. [78] which was a computer simulation model for calculating the interfacial charge for XLPE/ ethylene propylene rubber (EPR) sandwich system. In this work, the DM model used a bipolar transport approach to simulate the charge transport in a XLPE/EPR sandwich system. After comparing the results of NMW and DM, they found that, the accumulated charge at the interface calculated by DM was higher compared to NMW and better reproduced the experimental results [78].

Furthermore, in [88], the estimation of electric field distribution and interfacial charge between XLPE and EPR has been described at different values of temperature using COMSOL software. As a result, the interfacial charge between these two dielectrics changes between positive and negative, due to the variation of field and temperature dependencies on conductivity.

After that, some other simulations and experiments were conducted for materials that exhibit field and / or temperature dependent conductivity to determine the space charge

accumulation at the interface between two dielectrics either with the same or different insulation polymers [77, 89, 90].

2.8 Finite Difference Method (FDM)

It is known that most of engineering field equations are partial differential equations such as the electrostatic and thermal equations (see section 2.4). These equations cannot be solved by analytical method, when non-linear models and complex geometries are involved. Therefore, numerical techniques are used to solve these equations. Although there are variety of numerical methods which have been used to achieve this goal, FDM is a simple and practical one [91]. FDM is a numerical method for converting partial differential equations into a set of algebraic equations [92], and is based on the properties of the Taylor series expansion [93] of the differential operators. By using this method, PDEs can be discretised to a finite number of points and meshing these points in the physical domain [94, 95]. These mesh points are named nodes. The number and distance between nodes have a great influence on accuracy and resolution of the numerical solution [94]. The PDEs can be solved using FDM by changing the derivatives to finite difference between neighbouring points. In this study FDM method is used to solve the equations of the simulation model.

To familiarize with the steps of changing from PDE equations to the formula of FDM equations, the Cartesian Laplace PDE equation is considered for one dimension (1-D) and two dimensions (2-D). In 1-D, three neighbouring points are considered on the x-axis separated by Δx which are $x - \Delta x$, x and $x + \Delta x$. These points can be labelled as $i - \Delta x$, i and $i + \Delta x$. Consider V as a function of i at these points, $V_{(i-\Delta x)}$, $V_{(i)}$ and $V_{(i+\Delta x)}$. The Taylor series expansion for $V_{(i-\Delta x)}$ and $V_{(i+\Delta x)}$ can be written as follows [91-93]:

$$V_{(i-\Delta x)} = V_{(i)} - V'_{(i)}\Delta x + \frac{1}{2} V''_{(i)}(\Delta x)^2 - \frac{1}{6} V'''_{(i)}(\Delta x)^3 + \dots \quad (2.28)$$

Where $V'_{(i)}$ represents the first spatial derivative of (i) , $V''_{(i)}$ the second spatial derivative of $V_{(i)}$ and so on.

Equation 2.29 can be obtained from equation 2.28

$$V'_{(i)} = \frac{V_{(i)} - V_{(i-\Delta x)}}{\Delta x} + O(\Delta x) \quad (2.29)$$

Where $O(\Delta x)$ means all the remaining terms that contain $(\Delta x)^n$ with $n > 1$. Equation (2.29) indicates the first order accurate 'backward difference' formula. 'Backward'

means decreasing the value of (i) by small value of (Δx) . Similarly, from the Taylor series theorem of equation 2.30, the equation 2.31 can be obtained.

$$V_{(i+\Delta x)} = V_{(i)} + V'_{(i)}\Delta x + \frac{1}{2} V''_{(i)}(\Delta x)^2 + \frac{1}{6} V'''_{(i)}(\Delta x)^3 + \dots \quad (2.30)$$

$$V'_{(i)} = \frac{V_{(i+\Delta x)} - V_{(i)}}{\Delta x} + O(\Delta x) \quad (2.31)$$

Equation 2.31 indicates the first order accurate ‘forward difference’ formula and ‘forward’ means increasing value of (i) by small value of (Δx) . Furthermore, equation 2.32 can be obtained by subtracting equation 2.28 and 2.30.

$$V'_{(i)} = \frac{V_{(i+\Delta x)} - V_{(i-\Delta x)}}{2\Delta x} + O(\Delta x)^2 \quad (2.32)$$

Equation 2.32 indicates the second order accurate ‘central difference’ formula for the first derivative. Moreover, the second derivative central difference formula (equation 2.33) can be obtained by adding equation 2.28 and 2.30.

$$V''_{(i)} = \frac{V_{(i+\Delta x)} - 2V_{(i)} + V_{(i-\Delta x)}}{(\Delta x)^2} + O(\Delta x)^2 \quad (2.33)$$

Similarly, if the points $j - \Delta x$, j and $j + \Delta x$ along y-axis are taken, by adding and subtracting the Taylor series equations and arranging as before, the following difference equations can be obtained.

$$V'_{(j)} = \frac{V_{(j+\Delta y)} - V_{(j-\Delta y)}}{2\Delta y} + O(\Delta y)^2 \quad (2.34)$$

$$V''_{(j)} = \frac{V_{(j+\Delta y)} - 2V_{(j)} + V_{(j-\Delta y)}}{(\Delta y)^2} + O(\Delta y)^2 \quad (2.35)$$

Equations 2.34 and 2.35 are the central difference formula for first and second derivatives of the finite difference method along the y-axis. The two dimensional finite difference methods can be obtained, by combining equations 2.33 and 2.35

$$V''_{(i)} + V''_{(j)} = \frac{V_{(i+\Delta x)} - 2V_{(i)} + V_{(i-\Delta x)}}{(\Delta x)^2} + \frac{V_{(j+\Delta y)} - 2V_{(j)} + V_{(j-\Delta y)}}{(\Delta y)^2} \quad (2.36)$$

When $V''_{(i)} + V''_{(j)} = 0$, the two dimensional Laplace equation is achieved which can easily be described using 5-points along x-axis and y-axis.

Equation (2.36) can then be arranged as below

$$V_{(i+1,j)} - 2V_{(i,j)} + V_{(i-1,j)} + V_{(i,j+1)} - 2V_{(i,j)} + V_{(i,j-1)} = 0 \quad (2.37)$$

This is usually written:

$$V_{(i,j)} = \frac{1}{4} (V_{(i+1,j)} + V_{(i-1,j)} + V_{(i,j+1)} + V_{(i,j-1)}) \quad (2.38)$$

Equation 2.38 states that for solution of the Laplace equation the value of $V_{(i,j)}$ takes the value of the average value of the four node points surrounding it.

3 Space charge measurements using traditional PEA methodologies

3.1 Overview

In this chapter the traditional approach of using the pulsed electroacoustic method is described. In order to measure space charge it is necessary to take into account the imperfections and non-ideal response characteristics of the system in order to recover the space charge profile inside thin film polymer samples. The aim here is to show the current state-of-the-art signal processing steps of this approach that need to be conducted in order to correct the system imperfections and determine the real space charge distribution. The system imperfections to be corrected for were outlined in chapter 2. The main steps of traditional approach of space charge recovery will be introduced in more detail and demonstrated using raw PEA data in section 3.2. The other aim of this chapter is to employ the PEA technique using single and double layer specimens of LDPE and XLPE to assess how the impurity levels and chemical structure of the material affect the electrical conduction process and the amount of space charge that accumulates. Based on Hjerrild and Boggs models [58, 80], the effect of impurity diffusion into the insulation sample surfaces is to locally increase the electrical conductivity leading to the build-up of a homocharge layer at each surface. These effects will be assessed during voltage-on and voltage-off measurements using single layer LDPE and XLPE samples and then double layer LDPE thin film samples in which one of the two material layers has been heat treated in an attempt to remove these impurities as described in section 3.3 and 3.4. Section 3.5 contains the summary of this chapter.

3.2 Traditional signal processing approach for recovery of space charge distribution measured by PEA

The PEA output electrical signal is not a direct representation of the space charge distribution within the sample due to the various imperfections of the measurement system. In the case of a space charge free sample under an applied voltage, the PEA system will produce two acoustic pressure waves generated by the electrode surface charges. These charges occupy a narrow range of space situated at each electrode boundary. However, due to the width of the pulsed voltage, typically 5-10 nanoseconds, the acoustic waves generated at the electrodes are smeared out in time. Since longitudinal acoustic velocity in a typical LDPE specimen is around 2000ms^{-1} , this limits the spatial

resolution of the instrument to around $20\mu\text{m}$. The spatial resolution of the instrument is further reduced as the acoustic pressure waves are integrated over the thickness of the PVDF sensor typically $9\mu\text{m}$. The theoretical resolution of a typical PEA instrument is therefore of the order of $30\mu\text{m}$. The acoustic pressure waves are further distorted due to attenuation and dispersion of the pressure waves as they traverse the sample thickness. Further distortion of the pressure signal occurs when the pressure waves are detected by the PVDF transducer/amplifier and oscilloscope frequency responses which work as a high pass filter and low pass filter respectively. The signal can also be distorted by acoustic reflections from boundaries of different materials having different acoustic properties. Figure 3.1 shows a typical raw output signal (taken as soon as possible after the application of a low applied voltage to minimise the accumulation of space charge) which is a voltage profile without any corrections. The PEA signal consists of a number of time separated events. The initial negative going peak is due to the pressure wave from the electrode charge at the aluminium base plate/sample interface. The duration of this peak is approximately 13ns corresponding to a spatial resolution of $26\mu\text{m}$. This is immediately followed by a small positive going peak due to a reflection of the pressure wave at the PVDF sensor/ PMMA absorber interface. PVDF and PMMA materials have slightly different acoustic impedances and cause part of the incident acoustic wave to reflect back towards the aluminium base plate. This reflection therefore does not represent the formation of real positive charge inside the sample but represents part of the non-ideal response function of the instrument. Following the first peak there is an extended period over which the voltage decays due to the PVDF/amplifier high –pass frequency response. Again, this represents part of the non-ideal response of the system which will need to be corrected. Finally there is a positive going peak due to the pressure wave generated by the electrode charge at the top electrode/sample interface. In a thin film sample in which no space charge had formed, the detected peaks corresponding to the electrode charges at the Al base plate and the top electrode should be in principle equal in magnitude but opposite in polarity. The example shown here shows the top electrode charge has a lower magnitude and a longer duration than the Al peak indicating that either:

Absorption and dispersion of the acoustic waves occurs as it propagates through the sample before entering the aluminium base plate.

Or:

The existence of an acoustic interface mismatch between the sample and the top electrode. This causes an immediate reflection of the acoustic wave as it is generated at the top electrode with the reflected wave either adding to or subtracting from the direct acoustic wave. Whether it adds or subtracts depends on the actual acoustic impedance difference between the two materials.

Or:

If, in addition, the sample surfaces are not quite parallel with each other this would account for the slight broadening of the peak as the generated acoustic wave would not be aligned with the principal axis of the PEA instrument.

The traditional method that has been used to correct the raw PEA output signal and to reconstruct the space charge profile consists of the following steps [20, 23, 35, 96]:

First, the PEA raw data is obtained under a low DC applied voltage to avoid the accumulation of space charge within the sample. The small PEA output signal needs to be averaged over many acquisitions (typically in excess of 500) to give a good signal to noise ratio. Typical raw PEA data suitable for demonstration of all the system corrections is shown in figure 3.1.

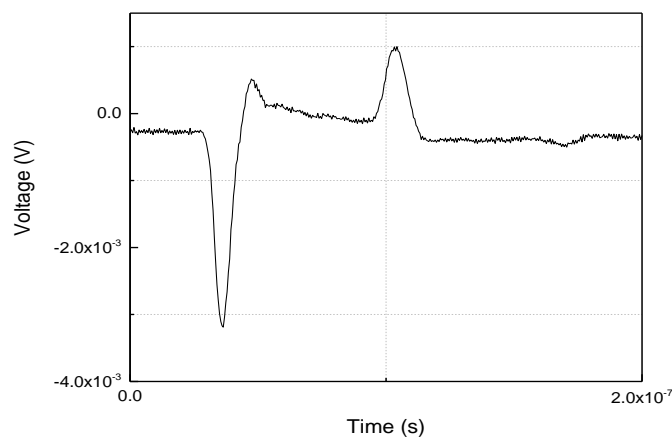


Figure 3.1: Typical raw output signal of PEA measurement.

3.2.1 Base line correction:

A base line correction is employed to correct for any DC off-set drift in the detected averaged signal. This off-set voltage is due to signal pick-up of the PEA pulse voltage as well as drift in the DC levels of the amplifier and oscilloscope. The zero voltage baseline can be corrected by selecting the raw PEA data ahead of the first peak corresponding to

the earth electrode charge (zero) which is then averaged. The average value is then subtracted from each point in the PEA raw data set. Figure 3.2 shows the raw output signal after base line correction. Here the signal before the first peak is now aligned with the zero on the y-axis.

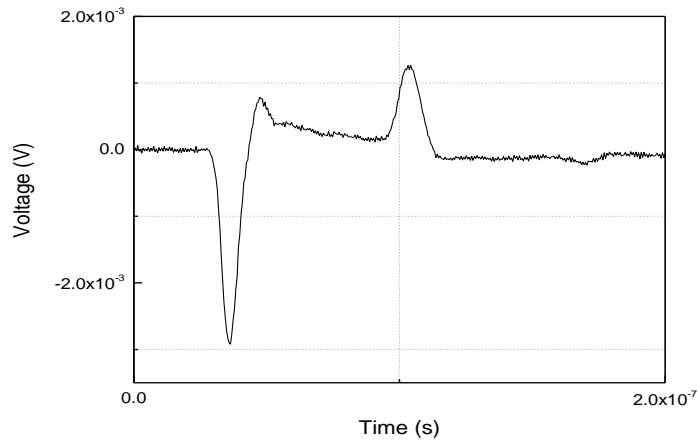


Figure 3.2: Base line correction for PEA output signal.

3.2.2 De-noising:

Even after signal averaging of the detected raw PEA signal a significant amount of noise is still present in the PEA output signal. This is especially the case under low applied voltage and for voltage-off measurements. To reduce this noise, different values of frequency were tried to eliminate the noise on the PEA raw data without affecting on the shape of the signal. It was found that a 125 MHz low pass filter is best value that can be used for this purpose and therefore it is applied to the averaged and base line corrected PEA raw data. A MATLAB program has been written to perform this filtering of the data. Figure 3.3 shows the filtered output signal after de-nosing the raw PEA signal shown in figure 3.2.

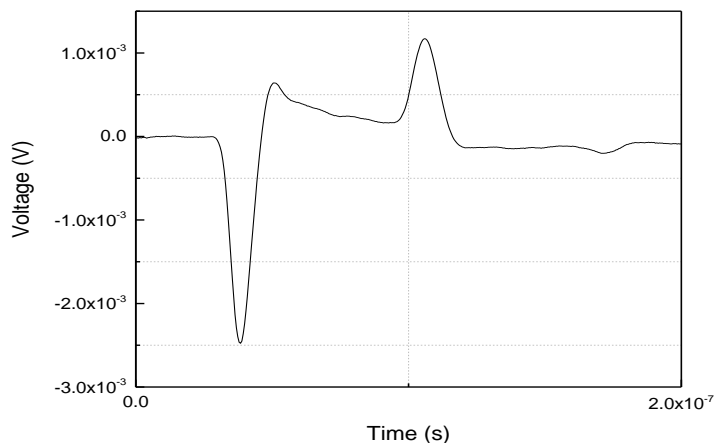


Figure 3.3: De-noising of raw output signal of PEA measurement.

3.2.3 Deconvolution:

In order to correct for non-ideal system responses of the PEA (acoustic reflections at the PVDF/PMMA interface and the HPF response of the PVDF detector and amplifier) the deconvolution technique is employed. Based on the convolution theorem, if the signal response of the linear system is known, then the relationship (transfer function) between the input and output of that system can be calculated. For the PEA system, the relationship between the original signal, $V_{origin}(t)$, in this case representing the actual space charge distribution inside the sample and the raw detected output signal at the oscilloscope, $V_{detected}(t)$, can be defined by the system response function, $H(f)$, where f represents frequency. Once $H(f)$ and the detected signal are known in the frequency domain, the original signal in the frequency domain can be calculated as equal to the inverse of $H(f)$ multiplied by the detected signal.

$$V_{origin}(f) = H(f)^{-1}V_{detected}(f) \quad (3.1)$$

By using the inverse Fourier transform (*IFFT*), the time domain for the original signal representing the space charge distribution can then be obtained as

$$V_{origin}(t) = IFFT(V_{origin}(f)) \quad (3.2)$$

However, if the system response, $H(f)$, is not known, then equation (3.2) cannot be applied directly. Therefore, in practice, an approximation of $H(f)$ is obtained by comparison of the measured response with an ideal response representing the pulsed PEA voltage as illustrated in figure 3.4. A representative signal, $V_{earth}(t)$, is extracted from the filtered de-noised PEA data. This is achieved by extracting from the de-noised data, the data points between the start of the first electrode peak until just before the second electrode peak. The extracted data which represents the signal from the ground electrode charge, was then used to determine the system response. In addition, an ideal signal $V_{ideal}(t)$ was used, which had the same duration as the voltage pulse with the height of one unit. The time domain signals, $V_{earth}(t)$ and $V_{ideal}(t)$, were transformed to the frequency domain, $V_{earth}(f)$ and $V_{ideal}(f)$, using the Fast Fourier transform (FFT). An estimate of the inverse of the system response, $H(f)^{-1}$, can then be found from dividing $V_{ideal}(f)$ by $V_{earth}(f)$. In order to eliminate the high frequency components that are often introduced using this deconvolution technique a Gaussian low pass filter is usually applied before calculating the final estimate of $H(f)^{-1}$. The deconvolution signal, $V_{decon}(t)$, can then be obtained using equations 3.3 and 3.4.

$$V_{decon}(f) = H(f)^{-1}V_{detected}(f) \quad (3.3)$$

$$V_{decon}(t) = IFFT(V_{decon}(f)) \quad (3.4)$$

It should be noted that the deconvolution signal $V_{decon}(t)$ is an approximation and therefore does not necessarily give us the correct space charge distribution. This is because, despite the Gaussian filter, zeros in the FFT of the $V_{earth}(f)$ signal can cause infinities (large values following the division) in the deconvolution signal. This is observed as unwanted frequency components and false detail appearing in the deconvolved signal that would be misleading for space charge accumulation and interpretation. In practice this makes the deconvolution procedure used to eliminate the non-ideal system responses subjective as small changes to the choices for the truncation limits of the original de-noised data to obtain $V_{earth}(t)$ can lead to large changes in the deconvolved data set and potentially lead to significant errors when recovering the space charge distributions. Figure 3.4, shows the complete procedure of deconvolution for the correction of the non-ideal PEA system responses. Figure 3.5, is an example of the raw output signal after deconvolution technique which was applied to the de-noised data of figure 3.3.

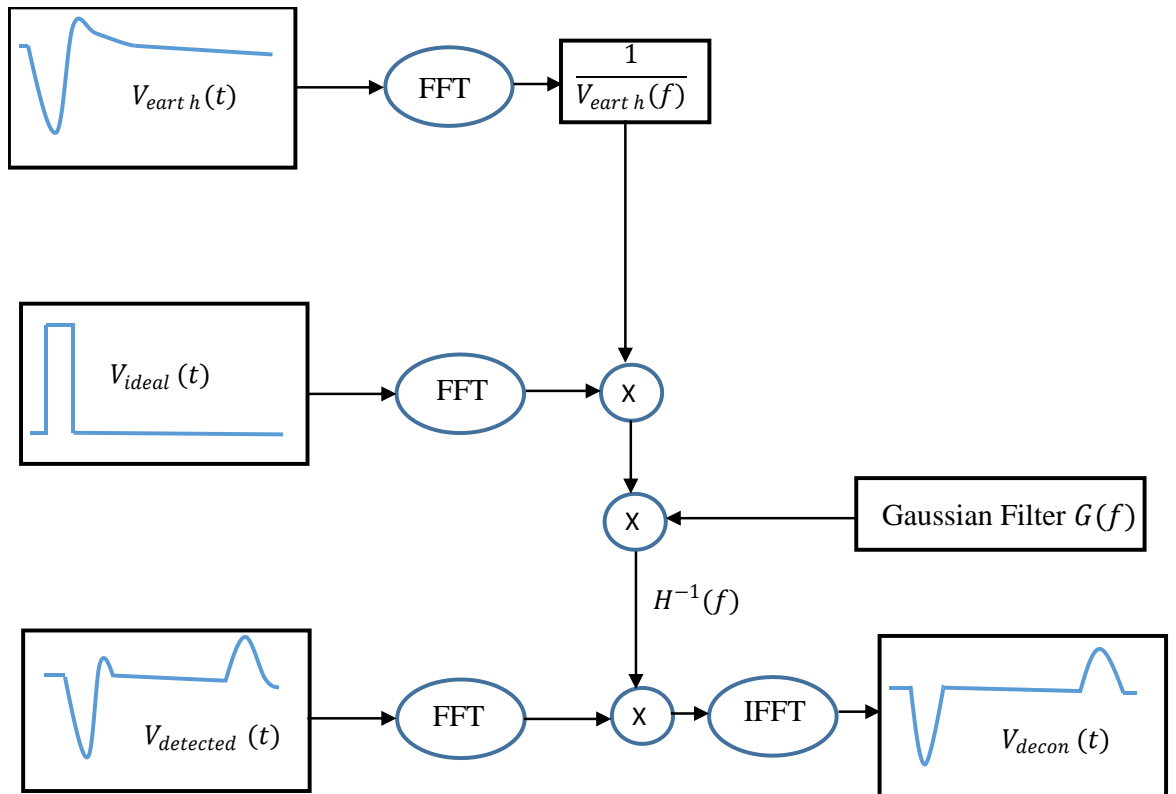


Figure 3.4: Schematic representation of the deconvolution technique [20].

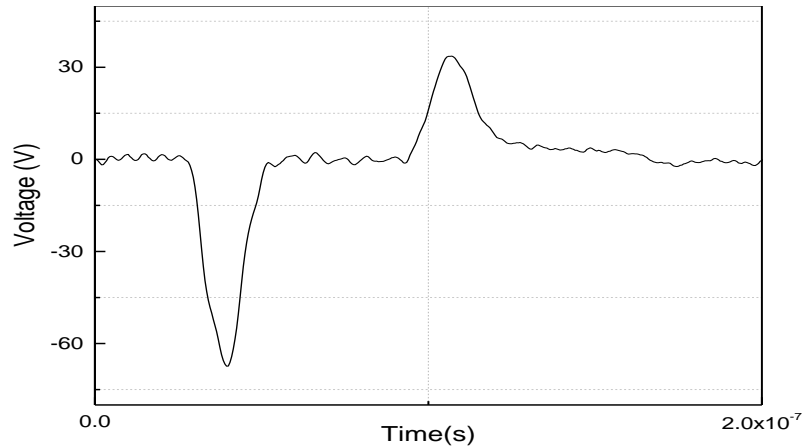


Figure 3.5: Processed output signal of PEA measurement after deconvolution.

The processed output corrected for acoustic wave reflection and amplifier/PVDF contains artefacts such as ripple in the signal and distortion of the peak shapes. The spatial resolution of the technique also degrades significantly following deconvolution. The deconvolution technique therefore has significant limitations for the process of reconstructing the space charge distribution.

3.2.4 Attenuation and Dispersion Correction

In theory, for plane-plane samples, the two electrode peaks shown in figure 3.5 should be equal in area if they are to represent the surface space charge densities at the two electrodes. In fact the signal from the upper semicon electrode has a smaller amplitude and slightly wider peak width. The effect of attenuation and dispersion of the pressure wave in an acoustic lossy medium should therefore also be corrected during the signal recovery process as the acoustic pressure wave is distorted when it propagates due to the effect of attenuation and dispersion. Attenuation is due to the absorption of acoustic energy as the pressure wave propagates in the medium. While dispersion is due to the frequency dependent acoustic velocity of the pressure wave frequency components as they propagate through the medium. The amount of distortion depends on the thickness of the sample, the attenuation coefficient and the dispersion coefficient of the medium. The thicker the sample the larger the distortion. Different methods have been used to analyse the extent of signal distortion during acoustic wave propagation within the insulation sample [30, 31, 97]. The detailed information of how the acoustic attenuation and dispersion in a plane sample is determined is described in [31]. The summary of this is explained below using the following theories.

A typical equation that describes the wave propagation across a lossy medium is given by:

$$v_s(t) = C \int_0^t \rho(\tau) G(t - \tau) dt \quad (3.5)$$

Where, $v_s(t)$ represents the attenuated and dispersed signal, C is a constant, $G(t - \tau)$ represents a transfer function in a medium associated with attenuation and dispersion at every time step, τ , as the pressure wave propagates along the sample thickness. $\rho(t)$ is the ideal space charge profile (i.e. without attenuation and dispersion). Therefore to recover the space charge profile from the detected signal $v_s(t)$ it is necessary to calculate the inverse of $G(t - \tau)$.

From equation (3.5), to get the space charge profile, first it is necessary to define the attenuation and dispersion factors correctly. These values can be estimated from the comparison of the detected acoustic pulses that originated at two given points (position $x=0$ (original pulse generated from the Al electrode of the PEA)) and (position $x=z$ (transmitted pulse generated from the semicon electrode that had propagated through the sample to the aluminium electrode)). In the frequency domain, the transfer function describing the propagation of the pressure wave between the point z and point 0 can then be determined by

$$G(f, z) = \frac{P(f, z)}{P(f, 0)} = e^{-\alpha(f)z} e^{-j\beta(f)z} \quad (3.6)$$

Where, $P(f, 0)$ is the FFT of the original time domain pulse signal located at the aluminium base electrode, $z=0$, and $P(f, z)$ is the FFT of the transmitted time domain pulse signal from the semicon interface at position z , $\alpha(f)$ is a frequency dependent attenuation factor, $\beta(f)$ is a frequency dependent dispersion factor. These propagation parameters can be found from the magnitudes and phase angles, ϕ , of $G(f, z)$:

$$\alpha(f) = -\frac{1}{z} \ln[|P(f, z)|/|P(f, 0)|] \quad (3.7)$$

and

$$\beta(f) = -\frac{1}{z} [\phi(f, z) - \phi(f, 0)] \quad (3.8)$$

The transfer function $G(f, x)$ representing the propagation of a pressure wave at arbitrary position x to position 0 can then be obtained by

$$G(f, x) = e^{-\alpha(f)x} e^{-j\beta(f)x} \quad (3.9)$$

The transfer function in the time domain at any point x can then be found from the inverse Fourier transform:

$$G(t, x) = IFFT(G(f, x)) \quad (3.10)$$

From equation 3.5, the space charge profile $\rho(t)$ can be found from the PEA output signal $v_s(t)$, and the inverse of the transfer function, $G(t - \tau)$. Equation 3.5, can be discretised into M position points and N time points. In this case equation 3.5 becomes:

$$v_s(i) = C' \sum_{j=1}^N G(i - j)\rho(j) \quad (3.11)$$

Where, C' is a constant. In a computer program $v_s(t)$ is defined by certain time duration (measurement time), whereas $\rho(t)$ is defined by a certain position interval enclosed by the boundaries of the sample. $G(i - j)$, represents the matrix of transfer functions representing the propagation of the pressure wave from an arbitrary point, i , between 1 and M and position $i = 1$ representing the position of the aluminium base plate. Equation 3.12 is therefore a set of simultaneous linear equations which describe the relation between the PEA output signal, $v_s(i)$, and the space charge profile, $\rho(j)$, when the acoustic pressure waves are propagating in an absorbing and dispersive medium.

$$\begin{bmatrix} v_s(1) \\ v_s(2) \\ \vdots \\ v_s(i) \\ \vdots \\ v_s(N) \end{bmatrix} = C' \begin{bmatrix} g(1,1) & g(1,2) & \cdot & \cdot & g(1,j) & \cdot & \cdot & g(1,M) \\ g(2,1) & g(2,2) & \cdot & \cdot & g(2,j) & \cdot & \cdot & g(2,M) \\ \vdots & \vdots & \cdot & \cdot & \vdots & \cdot & \cdot & \vdots \\ g(i,1) & g(i,2) & \vdots & \vdots & g(i,j) & \vdots & \vdots & g(i,M) \\ \vdots & \vdots \\ g(N,1) & g(N,2) & \cdot & \cdot & g(N,j) & \cdot & \cdot & g(N,M) \end{bmatrix} \begin{bmatrix} \rho(1) \\ \rho(2) \\ \vdots \\ \rho(j) \\ \vdots \\ \rho(M) \end{bmatrix} \quad (3.12)$$

Equation 3.12 can be written in matrix form as given below:

$$v_s = C'G\rho \quad (3.13)$$

Where v_s is the column matrix of output voltage $v_s(i)$, G is the matrix of transfer functions $G(i, j)$, and ρ is a column matrix representing the space charge distribution inside the sample. Finally, the space charge profile can be calculated by taking the inverse of the G matrix:

$$\rho = \frac{1}{C'} G^{-1} v_s \quad (3.14)$$

Where G^{-1} is the inverse of the matrix G .

However, realizing the value of transfer function coefficients from the raw PEA data is not straight forward. The calculation of $\alpha(f)$ and $\beta(f)$ suffers the effects of zeros in the denominator leading to infinities and unstable solutions. The resultant G matrix is often ill-conditioned making obtaining the inverse problematic due to the accuracy of the numerical procedure employed. As a result oscillations and instability may occur in the recovered signal leading to large errors in the recovered space charge distribution, $\rho(z)$. The success of the technique is also related to the assumptions that no space charge accumulation occurs when obtaining the initial space charge data and that the differences between the detected space charge peaks at the aluminium electrode and at the top semicon electrode are due entirely to absorption and dispersion and not due to other factors such as an acoustic impedance difference between the sample under test and the top semicon electrode material. For these reasons, most researchers tend to avoid correcting the PEA signal for attenuation and dispersion during the data processing for recovery of the space charge profile. In chapter 5 of this thesis an alternative technique will be developed for the interpretation of PEA output signals from thin film sample materials exhibiting attenuation and dispersion, in which calculation of the inverse of transfer function $G(t, z)^{-1}$ is not required.

3.2.5 Calibration

After deconvolution and the optional attenuation/dispersion correction of the PEA output signal, calibration of the PEA output signal is required in order to find the quantitative determination of space charge density in C/m^3 . In order to do this, the time signals need to be converted to distance by multiplying time by the velocity of longitudinal pressure wave propagation in the sample material. A calibration factor K_{cal} is also required, which can be obtained by considering the charge at the base electrode only and assuming that the PEA data was acquired when no space-charge had formed within the insulation.

First it is necessary to convert the time dependent PEA output signal, $V_{final}(t)$, to the corresponding distance inside the sample, $V_{final}(x)$. Where, $x = vt$, v is the speed of the acoustic waves in the insulation. The speed of sound in the sample material can easily be found from the measured thickness of the sample and the measured time interval between the two PEA electrode peaks from the oscilloscope trace. Typical value for LDPE is approximately 2000 ms^{-1} .

In the case of the measured electrode charge at the base electrode, the electrode surface charge density, σ , is proportional to the area under the signal peak, $\int_{x_1}^{x_2} V_{final}(x)dx$. This is to be compared with the expected surface charge density that would appear when a known voltage is applied. Hence, in order for the calibration factor to be calculated, a certain DC voltage V is applied to an initially space charge free sample. The calibration factor can then be calculated according to equation (3.15):

$$K_{cal} = \frac{\int_{x_1}^{x_2} V_{final}(x)dx}{\sigma} \quad (3.15)$$

Where x_1 and x_2 are denoted the starting and ending point of earth electrode, σ is the surface charge density which can be found from below equation :

$$\begin{aligned} \sigma &= \varepsilon_0 \varepsilon_r E \\ &= \varepsilon_0 \varepsilon_r \frac{V}{d} \end{aligned} \quad (3.16)$$

Where σ is a surface charge density, Cm^{-2} , V is the applied voltage, ε_r is the relative permittivity of the sample and d is the sample thickness. After finding the calibration factor, K_{cal} , the space charge density, $\rho(x)$ can be found from dividing the final deconvoluted signal $V_{final}(x)$ by the calibration factor K_{cal} :

$$\rho(x) = \frac{V_{final}(x)}{K_{cal}} \quad (3.17)$$

Figure 3.6 shows the recovered space charge profile of the PEA measurement after correction and calibration. The thickness of the sample is the distance between the two interfacial charge peaks which are shown by the two dotted lines in figure 3.6.

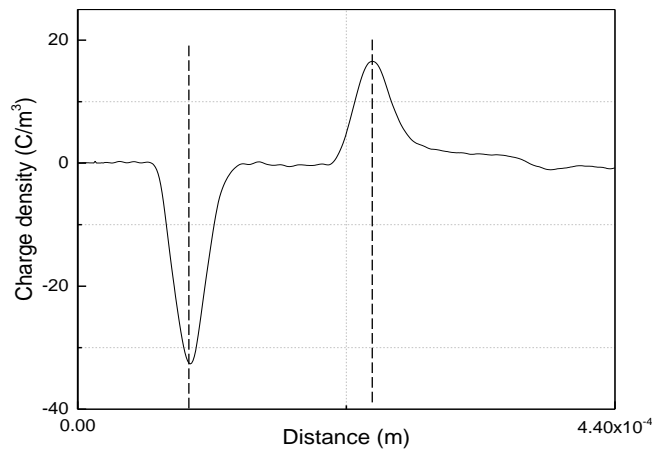


Figure 3.6: Space charge recovery profile of PEA output signal.

In order to verify the calibration procedure, the electric field distribution, $E(x)$, and electric potential distribution, $V(x)$, across the sample can be found from equations (3.18) and (3.19).

$$E(x) = \frac{1}{\epsilon_0 \epsilon_r} \int_0^d \rho(x) dx \quad (3.18)$$

$$V(x) = - \int_0^d E(x) dx \quad (3.19)$$

Where, d is the thickness of the sample. From equation 3.19, if the calibration is correct the value of $V(x)$ at point d , should be equal to the external applied DC voltage. Due to the integrations in equations 3.18 and 3.19, small errors in the recovered space charge density distribution can therefore lead to significant errors accumulating in the calculation of the electric field and electric potential profiles.

In order to demonstrate how the traditional analysis proceeds, experimental PEA space charge measurements were undertaken on single and double layer specimens of LDPE and XLPE subject to different thermal conditioning and under initial voltage application (charging) and zero voltage (discharging) as described in the following sections.

3.3 Space charge measurement under voltage-on and voltage-off conditions

Preliminary space charge measurements using the PEA technique with the traditional technique of space charge distribution recovery were performed on single layer and double layer flat plane samples. Cable grade cross-linked polyethylene (XLPE) and low density polyethylene (LDPE) thin films were used as test samples.

The PEA electrodes are configured as a parallel plane. The top (HV) electrode was semicon (Carbon loaded) LDPE material and the bottom ground (0V) electrode is made from aluminium (Al). The thickness of the samples was measured using a digital micrometre to an accuracy of +/- 2µm. The spatial resolution of the PEA was determined by the pulse width, acoustic speed in the sample and the thickness of PVDF [98]. In this study, the amplitude of the applied pulse voltage was between 500V-700V with duration of 8ns, which was applied to the sample to generate the acoustic signal. The PVDF material used as a sensor had a thickness of 9 µm. The thickness of the single layer LDPE sample was approximately 150 µm and for two layers was approximately 300 µm, while the thickness of the single layer XLPE samples were 200 µm.

3.3.1 Experiment protocol

The same experimental protocol was used for single layer and double layer measurement samples. After sandwiching the sample or layered samples between the PEA electrodes, the pulse voltage was applied along with a low DC voltage, of 1kV, for about 10 seconds. This was done to obtain reference data in which the sample or samples is/are assumed to be free of space charge and hence data that is suitable for calibration [99] of the PEA apparatus. After recording the reference data, the DC voltage was raised and kept constant for the remaining period of the experiment. In addition, the space charge evolution after the removal of the applied DC voltage (set to zero) was also measured over the same time interval as the polarization period. In both polarization and depolarization process, PEA space charge measurements were taken at regular time intervals.

3.3.2 Space charge measurement inside one layer thin film samples

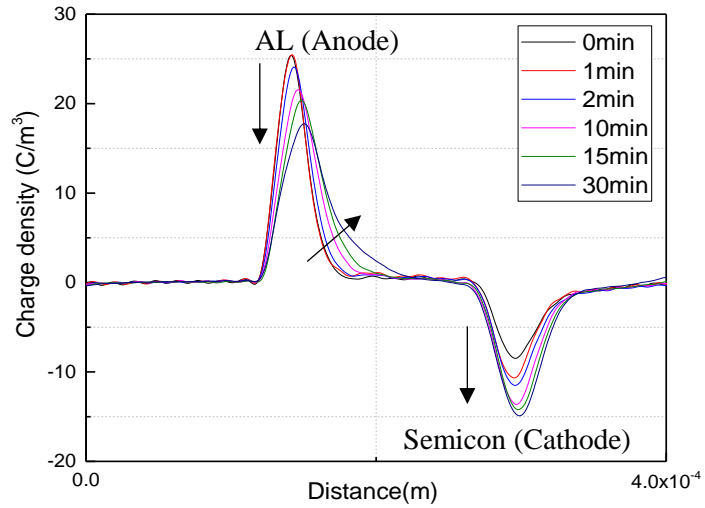
In order to investigate the charge accumulation at the electrode/ dielectric interfaces, single layer LDPE and single layer XLPE samples were used. The details of experiments and measurements are explained in the following sub sections.

3.3.2.1 Low density polyethylene (LDPE)

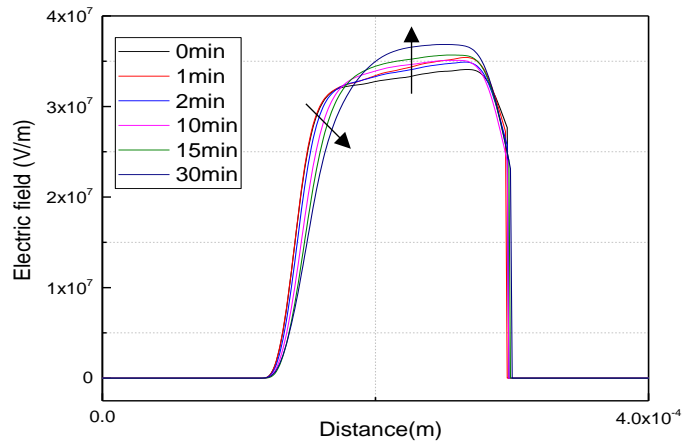
The experiments described in this section used LDPE film which had been stored in the laboratory for many years. The reason for using LDPE is due to its wide use as a cable insulation and because it has a simple chemical structure [100]. As the sample is a thin film, the possibility of space charge formation in the bulk is very weak due to the homogeneous morphology and uniform applied electric field. However, impurity diffusion, either introduced during the manufacturing process of the thin films or during the long length of time the thin film samples were stored in the laboratory, may lead to the possibility of space charge accumulation. Following the calibration measurements at low applied voltage, a DC voltage of -5kV was then applied to the top (semicon) electrode for 30 minutes at ambient temperature (18°C) with the PEA raw data (carrying the accumulated space charge distribution) being measured after times from 0 to 30 minutes. After the voltage-on test, the applied DC voltage was removed (set to zero) and the space charge that had accumulated in the sample was allowed to decay until it became reasonably stable. The PEA raw data was measured at different time intervals during the decay. The raw PEA data was then corrected to recover the space charge distribution using the methods described in the previous section. Corrections for base-line, denoising,

acoustic reflections and the buffer amplifier HPF response were applied to the raw PEA data. However, for the reasons described in the previous section, corrections for attenuation/dispersion were not carried out. Finally the processed data was calibrated.

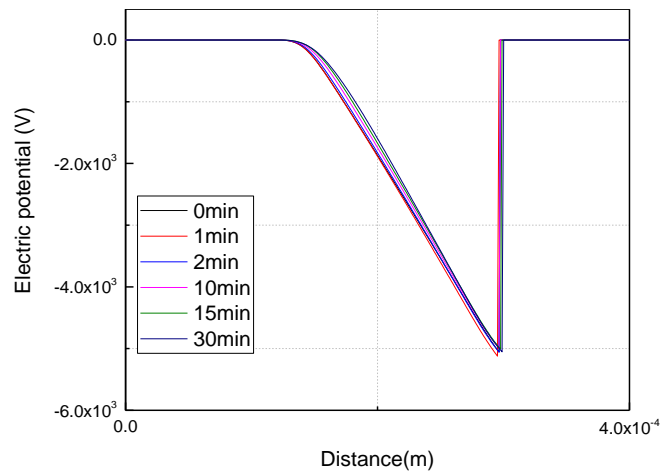
The processed measured space charge distributions during initial charging are shown in figure 3.7 along with the calculation of electric field and electric potential distributions. Figure 3.7(a) clearly shows that the distribution of charge is dominated by positive charge accumulation adjacent to the positive Al electrode and only a small negative space charge accumulation in the sample adjacent to the negative semicon electrode which indicates homocharge build up at the vicinities of both electrodes. The origin of these homocharge may be due to the charge injected and subsequently accumulated in the insulation close to the electrodes or due to the diffusion of impurities into the surfaces of the sample modifying the local electrical conductivity. The positive homocharge induces opposite (negative) charge on the aluminium electrode which causes the total electrode charge at the Al/sample interface to reduce from its initial value and to increase it slightly at the sample/semicon interface. Therefore, the peak of space charge at the aluminium electrode decreased with time as homocharge accumulates within the sample, whereas at the semicon electrode, the peak of space charge was increased as demonstrated in figure 3.7(a). At the same time, the electric field decreased at the aluminium electrode but increased in the bulk of the sample. This is shown in the calculation of electric field distribution in figure 3.7(b) (obtained from integrating the space charge density across the sample thickness). Integration of the electric field profile across the thickness of the sample results in the electric potential profile. As can be seen in figure 3.7 (c), the voltage across the sample was -5kV, which is the same as the DC applied voltage. This demonstrates that the calibration procedure was applied correctly to the raw PEA data.



(a)



(b)



(c)

Figure 3.7: (a) Charge density, (b) Electric field, (c) Electric potential, distribution in LDPE sample at different aging time.

The calibrated and processed PEA space charge decay measurements are shown in figure 3.8. This was conducted after setting the DC applied voltage to zero and the space charge

profiles measured and recorded at different times. It can be seen that there is a significant decay in the homocharge that had accumulated in the sample during the previous polling time and corresponding decay in the induced charge on the electrodes. Even after 30 minutes, significant amount of space charge remains in the sample. Hence the decay of space charge is much slower than that for the initial charging.

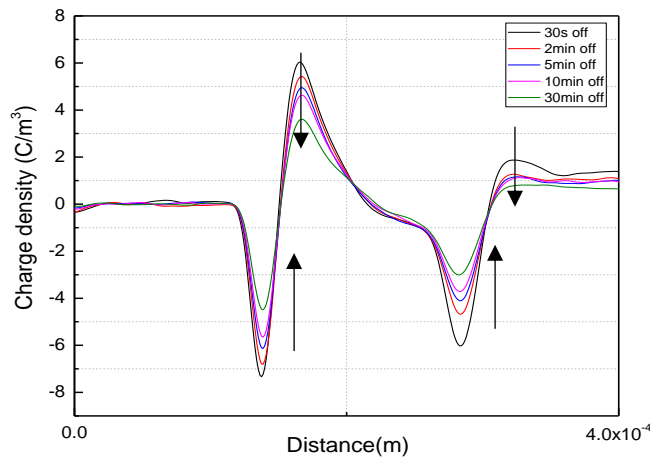


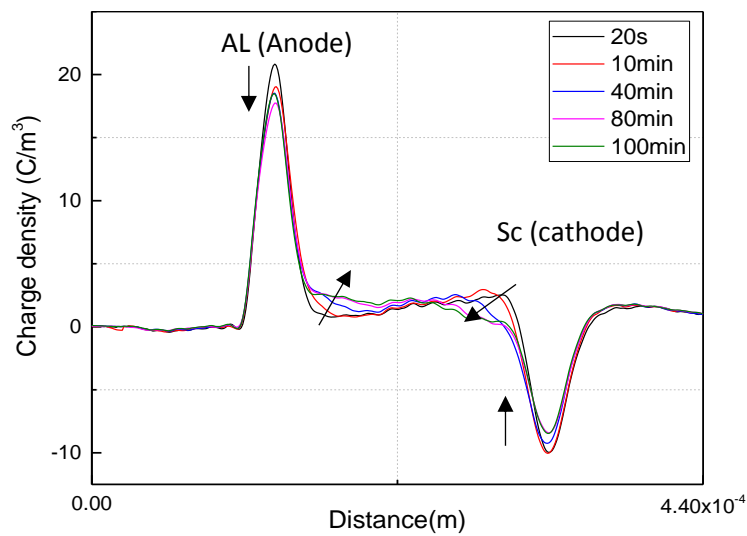
Figure 3.8: Space charge decay in LDPE after removing external voltage. Arrows indicate the time evaluation of the signals.

3.3.2.2 Cross-linked polyethylene (XLPE)

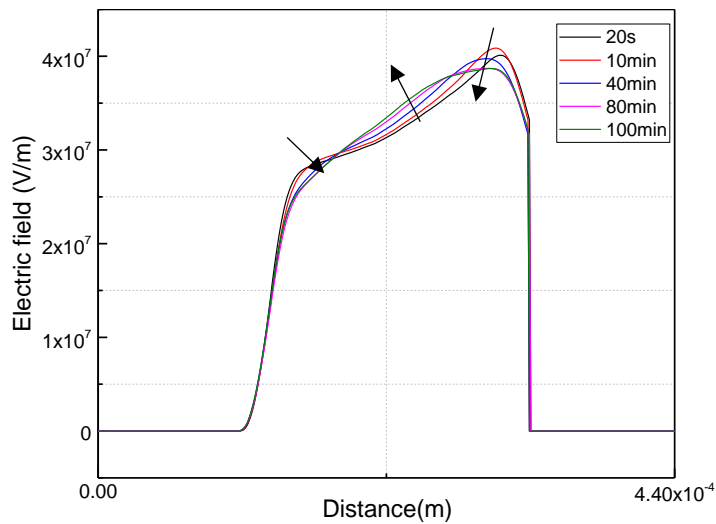
The XLPE thin film samples were manufactured and cross-linked in the laboratory and used directly to measure the space charge accumulation. Pellets of uncured material containing the crosslinking agent were melted and compressed in a compression mould at 120 °C for 20 minutes at a pressure of 2 MPa. The temperature was then raised to 180 °C to initiate the crosslinking reaction at an increased pressure of 15MPa. After 10 minutes of crosslinking, the temperature was slowly reduced to room temperature and pressure released [101]. The cross-linked sample was then placed in the PEA apparatus and -7kV DC voltage was applied at ambient temperature for a time of 100 minutes. Space charge measurements were recorded at various times during the voltage application and the experimental results are shown in figure 3.9.

The calibrated space charge measurements are shown in figure 3.9(a). The result that was obtained from fresh XLPE sample clearly shows that homocharge accumulated adjacent both electrodes (positive charge injected from anode and negative charge injected from cathode), which results in the reduction of interfacial electric field near the electrodes and enhanced the electric stress in the bulk of the dielectric as shown in figure 3.9(b). These

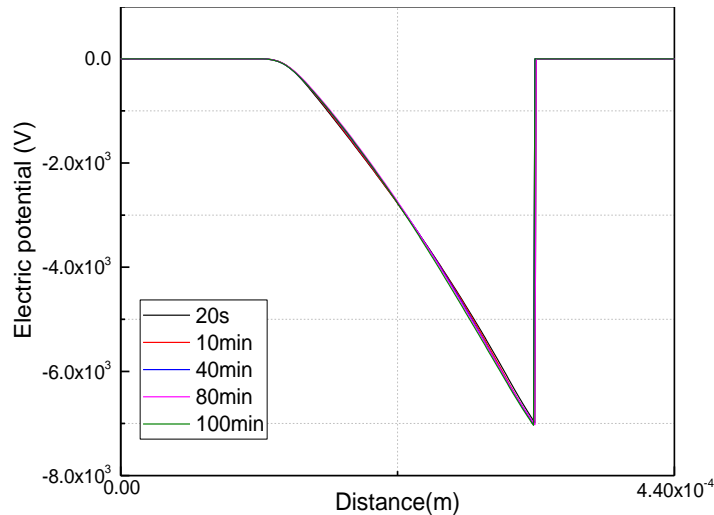
results clearly contradict the observations of Li and Takada in [102] who stated that hetero-charge is formed in fresh XLPE sample (containing cross-linking by-products) and the formation of homo-charge occurred in a degassed sample. This observation implies that the cross-linking by-products such as acetophenone and cumyl-alcohol were dissipated from the sample to the environment during the heating cycle of the manufacturing process of the XLPE samples. The electric potential distribution obtained from the electric field profile is shown in figure 3.9(c) and shows that the voltage difference between the electrodes was -7kV the same as the applied voltage.



(a)



(b)



(c)

Figure 3.9: (a) Space charge, (b) Electric field,(c) Electric potential distribution in XLPE sample at different aging time.

After the polarization (voltage on) measurements, the DC supply was set to zero and the decay of space charge was monitored using the PEA apparatus at different time intervals. Similar to the LDPE samples, the accumulated homocharge decayed with time until a reasonable steady state obtained (after 100 minutes). Even after 100 minutes, a substantial amount of space charge was still present in the sample. As with LDPE, the decay of space charge is much slower than for the initial charging in XLPE.

Although, the polarization time of XLPE was 100 minutes, three times longer than LDPE, the amount of space charge that accumulated in LDPE was higher by more than a factor of two (see figure 3.8). This result is in agreement with the results of [103], in which it is shown that the threshold electric field for the detection of space charge in LDPE was 5kV/mm, whereas the threshold electric field of XLPE was 10kV/mm. It was also shown the space charge in LDPE was twice that found for XLPE under an applied electric field of 60kV/mm. The reduction of space charge in XLPE can be explained to be due to the presence of antioxidant within the sample, or a difference in the density of localized states of charge traps, at least of traps deeper than those present in LDPE and participating in charge transport and trapping [103], or more likely due to the greater level of impurity inside the laboratory stored LDPE compared with the freshly manufactured and de-gassed XLPE.

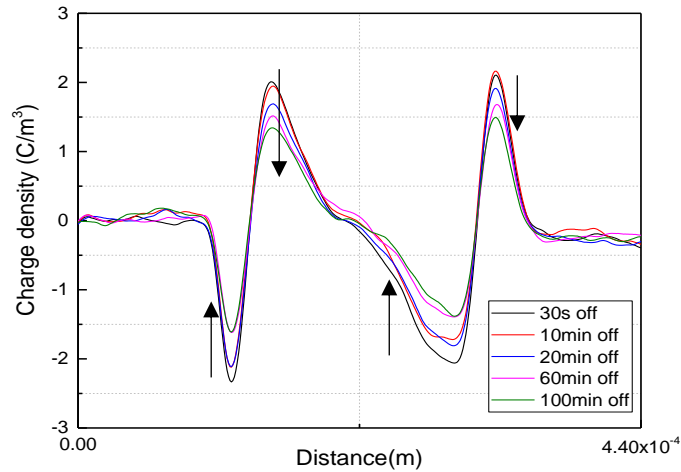


Figure 3.10: A net charge density accumulation in XLPE sample at different aging time.

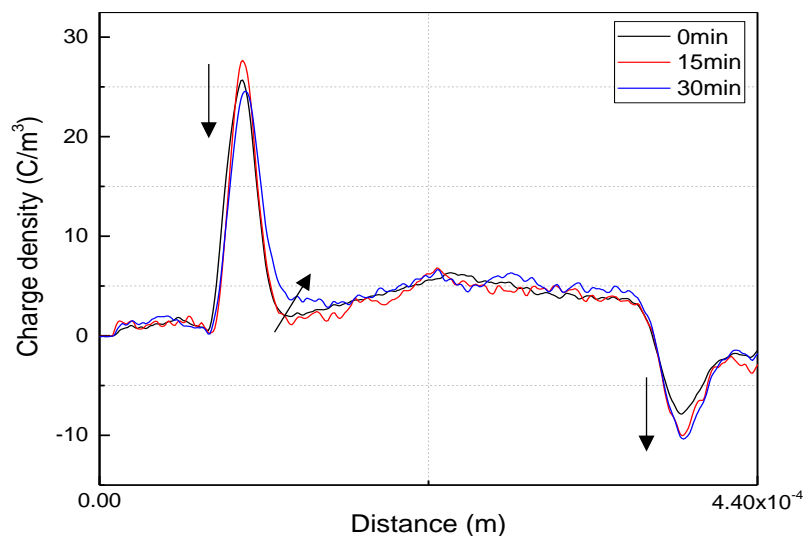
3.3.3 Space charge measurement inside double layer thin film samples

Another active area of research into reliable HVDC insulators concerns the use of different insulating materials to control (grade) the internal DC electrical field. By using layers of materials of different electrical conductivity, it is possible to reduce the steady state DC electric field in regions which would have high field divergence. Practical cases involve the design of reliable cable accessories such as cable joints and end terminations [67, 104, 105]. Here materials of higher conductivity are used in regions where the electric field is expected to be enhanced due to the electrode geometry. Charging of the interface between the two materials results in a lower electric field in the original high field region and the reverse taking place in the original low field region. Laboratory based experimental work on layered materials usually involves measurement of the space charge dynamics of thin film sandwiches of two insulating materials in general having different permittivity and resistivity. In the work to be described here, first two untreated LDPE sample are tested while in the second case untreated and thermally treated LDPE was used to assess the effect of material impurity on the DC conductivity.

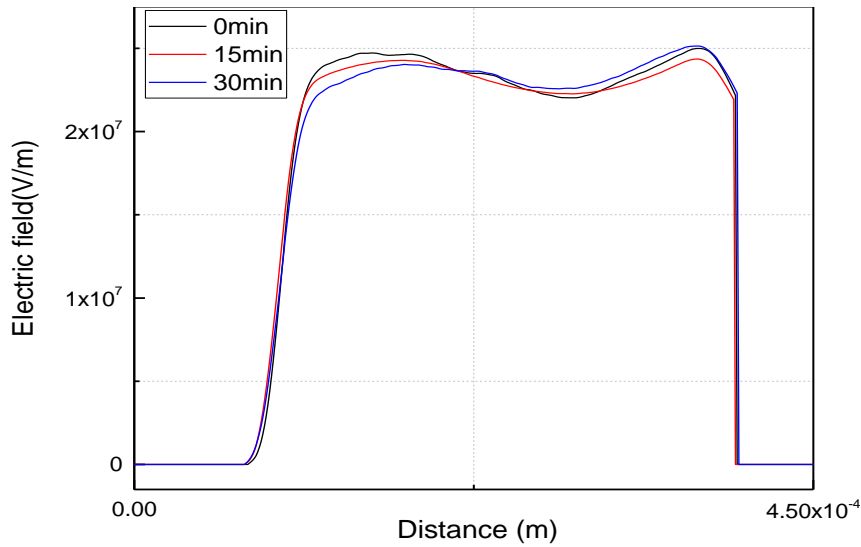
In the first case, a double layer specimen formed from two 150 μm thin film ‘as received’ layers of LDPE thin film sample which had the same permittivity. The total thickness of the double layer sample was 300 μm . The double layer sample was sandwiched between the base electrode and the semicon top electrode of the PEA system measurement apparatus. A -7kV DC voltage were applied on the top semicon electrode for 30 minutes and PEA raw data was measured at three different times (0 minute, 15 minutes and 30 minutes). To correct the signal and reconstruct the space charge profile, the traditional

method of space charge recovery was used as described for the single layer sample in section 3.1. This was possible because the same material was used for both layers and therefore there was no acoustic impedance mismatch between the two LDPE layers. The steps taken to correct the raw PEA data and to calibrate the resultant space charge profile therefore included, baseline correction (to obtain the zero base-line value), de-noising (to reduce the noise on the PEA raw data), deconvolution and finally calibration in order to get the quantitative amount of space charge in C/m^3 . In order to avoid oscillations and instability due to inaccuracy of finding the inverse of the $G(t, z)$ matrix, the effect of attenuation and dispersion was neglected.

Figure 3.11 (a) and 3.11(b) shows the recovered space charge and electric field distribution profiles obtained during the 30 minutes of polarisation. As can be seen from figure 3.11(a) a positive homocharge is accumulated near the positive Al electrode which itself induces negative charge at the Al and semicon electrodes. This led to a reduction in the electric field adjacent to the Al electrode and enhancement in the bulk of the samples as shown in figure 3.11(b). However no interface charge can be seen at the interface between the two sample layers. This is because both LDPE layers have the same electrical conductivity and the same permittivity. This result is expected from Maxwell-Wagner theory [85] where interfacial charge is obtained between the two material only if the permittivity and/or the conductivity of the materials are different. The absence of interface charge shown in figure 3.11 contradicts the observations of [79], in which interfacial charge was observed between the two free additive LDPE layers in which it was assumed that they have the same properties.



(a)



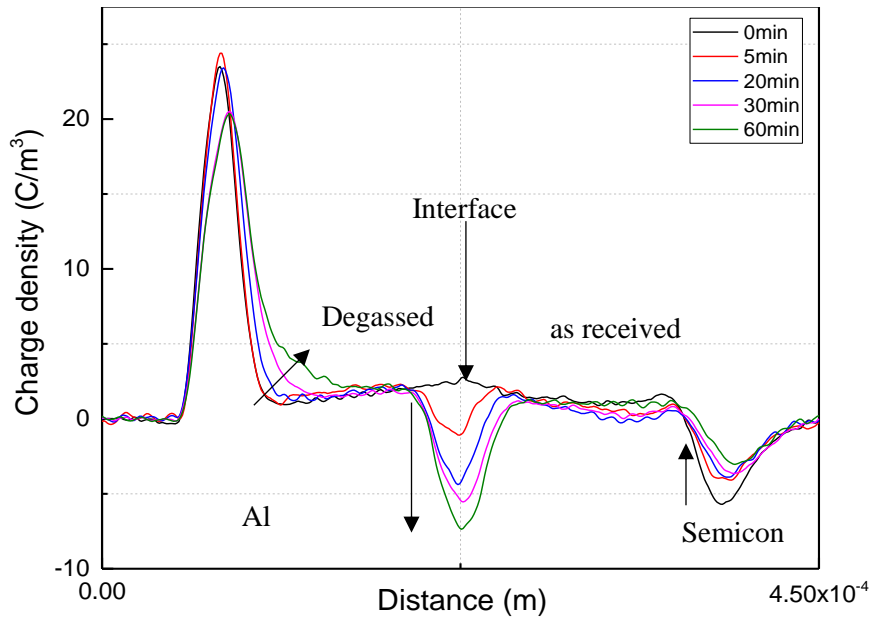
(b)

Figure 3.11: (a) Space charge, (b) Electric field distribution in two ‘as received’ LDPE layers during polarization.

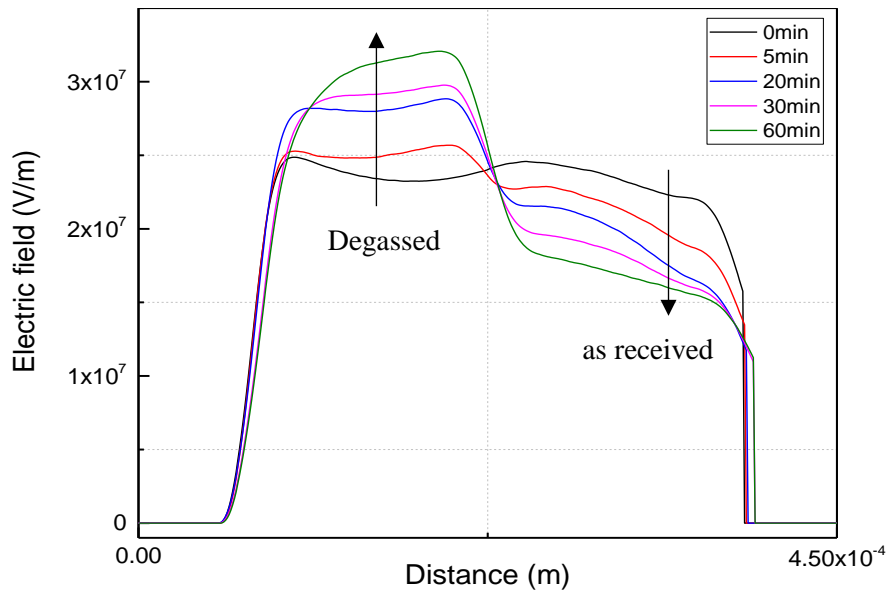
In the second case, in order to assess if impurities in the LDPE alters the DC conductivity, the thin film LDPE layer attached to the Al electrode was first vacuum degassed in an oven under a temperature of 50 °C for 24 hours. The top layer of LDPE in contact with the semicon electrode was in ‘as received’ condition and potentially includes impurities introduced during manufacture or storage. In this case, the two samples are not identical and they may have different electrical conductivity. Again, both samples were sandwiched between the base electrode and the semicon top electrode of the PEA system measurement apparatus. The total thickness of the samples were typically 300 μm. A -7kV DC voltage was applied to the top semicon electrode for 60 minutes duration and PEA raw data was recorded at different time intervals between 0 and 60 minutes.

Figure 3.12(a) and 3.12(b) show the corrected and calibrated space charge and electric field distributions during the initial 60 minute polarization period. Figure 3.12(a) shows that positive homocharge forms adjacent to the positive aluminium electrode. At the same time, negative space charge accumulated at the interface between the two layers. A negative homocharge also formed within the layer adjacent to the negative semicon electrode. As was the case with a single layer, (see section 3.2.2), the origin of these homocharge may be due to electrical conductivity modification due to the presence of diffused impurities that had formed either during manufacture of the thin films or occurred during storage of the films in the laboratory. Alternative explanations are often cited in the literature for the origin of homocharge as due to charge injection at the

electrodes which is then trapped in the insulation close to the electrodes [79, 106]. The net negative charge accumulation at the interface of the two thin films is a consequence of the different electrical conductivities of the ‘degassed’ layer and the ‘as received’ layer. The degassing stage removes impurities from the sample reducing its electrical conductivity compared with the ‘as received’ condition. Negative charge from the ‘as received’ layer adjacent to the negative semicon electrode propagates to the interface where it builds up. The consequence of this is to reduce the electric field in the ‘as received’ layer and to increase the electric field in the ‘degassed’ layer as shown in figure 3.12(b). At time $t=0$, the electric field distribution is approximately uniform and corresponds to the Laplacian applied electric field of -7kV applied across $300\mu\text{m}$, equivalent to 23kV/mm . During polling, the electric field in the ‘as received’ material decreases whilst at the same time the electric field increases in the degassed layer. A steady state charge distribution will occur when the current density ($J=\sigma E$) is the same in both layers and no further build-up of charge can occur at the interface as charge migrating to the interface in the ‘as received’ layer is balanced by charges migrating from the interface to the aluminium electrode in the ‘degassed’ layer. The negative charge at the interface would normally induce additional positive charge on both the aluminium and semicon electrodes. However, the increased electric field in the ‘degassed’ layer, enhances the formation of positive homocharge adjacent to the aluminium electrode in the degassed layer and this causes the charge density at the aluminium electrode to decrease slightly owing to the positive homocharge inducing negative charge on the aluminium electrode. Therefore, the peak of space charge at the anode electrode decreased slightly with time as the homocharge accumulates. At the semicon (electrode (cathode)) the space charge peak steadily decays due to the reduced electric field within the ‘as received’ layer.



(a)



(b)

Figure 3.12: (a) Space charge, (b) Electric field distribution in two layer sample during polarization.

After the polarization test, the voltage was removed (set to zero) and the space charge that had accumulated in the two layers and at the interface was allowed to decay for a further 60 minutes. The PEA processed data was measured and recorded at different time intervals from 10 second to 60minutes during the depolarisation experiment.

The corrected PEA space charge profile and electric field distribution under voltage-off (depolarisation) conditions are shown in figure 3.13. After 10 seconds of depolarisation, the negative interface charge that had formed during the polling experiment induces

positive charge at both electrodes and gives rise to a positive electric field in the ‘degassed’ layer and a negative electric field in the ‘as received’ layer. The interface charge slowly decreased with time causing the magnitudes of the electric field in both layers to decrease with time. Even after 60 minutes of depolarisation, significant amount of space charge remained in the sample at the interface between the dielectrics of 4.5 C/m^3 . This can be explained as due to the interface between the dielectrics providing deeper traps for electrons than are present in the bulk of the material. Larger amounts of energy are therefore required to free the trapped electrons at the interface. In that case, the time required for the decay of space charge would be much longer than those required for accumulation [89]. Alternative explanations exist in the literature to explain this phenomena for example if the materials have a field dependent electrical conductivity. LDPE is a material that has been identified as exhibiting a field dependent conductivity [58].

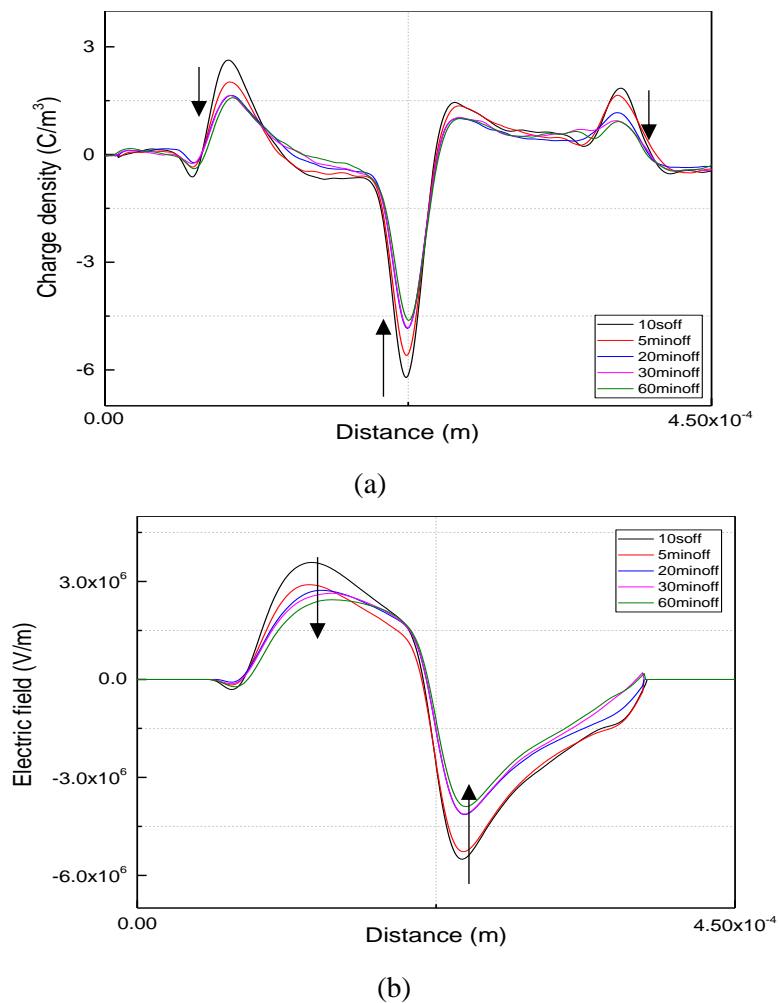


Figure 3.13: (a) Space charge, (b) Electric field distribution in two layer sample during depolarization.

3.4 Conductivity measurement

In order to be sure if the LDPE sample that was used in the experiment is contained the impurities and how these impurities are affected on the conduction of the material, the LDPE samples were sent to China for measuring the electrical conductivity. The conductivity were measured in two different cases. In the first case, the ‘as received’ sample was used, while in the second case, prior to the measurement, the sample was vacuum degassed under 50 °C for 24 hours. In both cases the electrical conductivity of the samples was measured using the high field DC conductivity measurement setup that shown in figure 3.14, in which the electrodes are made of brass and the measurement electrode has a diameter of 50 mm. The guard electrode surrounds the measurement electrode and insulated from it by Teflon insulation; in this way, the guard also shields against stray capacitances. A thin stainless steel film was put between the sample and the high voltage electrode to provide better electrical contact and a better diffusion barrier. The DC voltage was supplied by a Keithley 2290-10 10 kV power supply and the leakage current was measured using a Keithley KE6514 Pico ammeter. The temperature was controlled using an oven.

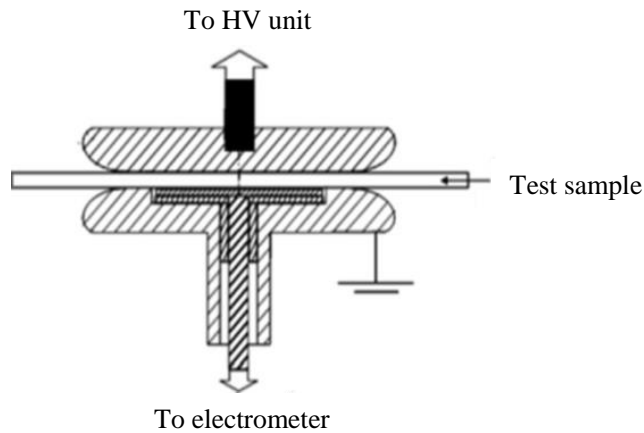


Figure 3.14: Electrode system for DC conduction measurement.

In both cases the applied voltage were 13kV/mm. The apparent DC conductivity of the samples was calculated using the measured leakage current I , applied voltage U , sample thickness d , and measurement area A as shown in equation 3.20:

$$\sigma = \frac{I}{V} * \frac{d}{A} \quad (3.20)$$

From the measurement results, it was found that the conductivity of the ‘as received’ sample was 1.37×10^{-15} S/m, whereas the conductivity of the degassed sample was 7.88×10^{-16} S/m, which means degassing the sample led to reduction the electrical

conductivity. This result proves the results of space charge measurement which were found in previous section in non- degassed and degassed sample and also shows the LDPE material which were used in this study contained impurities.

3.5 Summary

The traditional approach of signal processing to reconstruct the space charge distribution in thin film single and double layer samples has been discussed in detail in this chapter. The signal processing steps consists of base line correction, denoising, deconvolution of the non-ideal instrument response characteristics and calibration techniques of the PEA raw data. The corrections for attenuation and dispersion of the acoustic waves were considered but not attempted owing to the difficulties of the technique. Below are the summarised points and some drawbacks relating to the data processing to reconstruct the space charge distribution:

- 1- In order to get the space charge profile from the PEA raw data, baseline line correction, de-noising, deconvolution, attenuation/dispersion and finally the calibration are required.
- 2- Unwanted frequency components and false detail may appeared in the deconvoluted signal due to zeros in the FFT of the PEA system response ($V_{earth}(f)$) that would be misleading for space charge accumulation and interpretation.
- 3- Attenuation and dispersion correction of the PEA output signal is usually avoided by researchers. This method of space charge recovery is difficult in finding the attenuation and dispersion coefficients and in performing inversion to an ill conditioned G matrix which can results in instability.
- 4- The electric field distribution can be found by integrating the space charge profile, whereas the electric potential can be found by integrating the electric field profile. Therefore, any errors in the recovered space charge density distribution can therefore lead to significant errors in the calculation of the electric field and electric potential profiles.
- 5- The electric fields in space charge free regions should be constant but the results show that this is often not the case when reconstructing the space charge profiles.

Based on the traditional approach of space charge recovery, space charge accumulation has been characterised in one layer and two layer thin film samples under voltage on and voltage off conditions. Space charge behaviour of double layer

samples in which one layer had undergone a heat treatment to remove impurities has also been discussed. The following main points were concluded:

A- Single layer:

- 1- In both LDPE and XLPE single layer samples homocharge was observed to accumulate adjacent to the electrodes. However, the amount of homocharge that accumulated in LDPE was higher than that accumulated in XLPE by more than a factor of two. This is likely to be due to their differences in impurity level, morphology and chemical structure.
- 2- The electrical conductivity of the degassed LDPE sample was found much smaller than the 'as received' LDPE sample. This is in agreement with Hjerrild and et al in [58], in which they state that the impurity diffusion from semicon into polymer can take place and leads to an enhanced electrical conductivity and by which will cause the formation of homocharge regions within the insulation.

B- Double layer:

- 1- When the two 'as received' LDPE samples were tested, no interfacial charge was found between the two layers. This is because both LDPE layers had the same permittivity and the same conductivity.
- 2- In two layer LDPE samples, when the sample attached with the Al electrode degassed under 50 °C for 24 hours and used with the as received sample, under negative applied voltage the positive homocharge forms adjacent to the positive aluminium electrode. At the same time, negative space charge accumulated at the interface between the two layers. A negative homocharge also formed within the layer adjacent to the negative semicon electrode. The origin of these homocharges again may be due to electrical conductivity modification due to the presence of diffused impurities that had formed either during manufacture of the thin films or occurred during storage of the films in the laboratory.
- 3- The net negative charge accumulation at the interface between the layers is a consequence of the different electrical conductivities of the 'degassed' layer and the 'as received' layer.

- 4- Due to different electrical conduction in the layers, during polling time, the electric field in the ‘as received’ material decreases whilst at the same time the electric field increases in the degassed layer.
- 5- When the applied voltage was removed, the interface charge slowly decreased with time causing the magnitudes of the electric field in both layers to decrease. However, even after 60 minutes of depolarisation, a significant amount of space charge remained in the sample at the interface between the dielectrics which is about 4.5 C/m^3 . This result supports the hypothesis of a field dependent electrical conductivity in LDPE.

In order to provide a more robust and objective methodology for the interpretation of experimental PEA data a package of simulation models will be developed. An electro-thermal charge transport model with field and temperature dependent electrical conductivity (as described in the next chapter) will be combined with a simulation model for the PEA measurement system (described in chapter 5) to generate raw PEA data that can be compared directly with experimental raw data without the need to perform all the signal corrections for recovery of the space charge distributions. This will provide an alternative methodology for the interpretation of raw PEA data in terms of physical models for charge transport in insulating materials and avoid the use of numerically unstable techniques that could lead to false detail in the recovered space charge distributions.

4 Electro-Thermal Charge Transport Model for Space Charge Formation inside a Dielectric

This chapter describes the development of an electro-thermal charge transport model for calculating the space charge accumulation and electric field distribution in single layer and double layer thin film insulation samples. The aim of this model is to aid the interpretation of space charge measurement data within the context of a physical model based on sound electrostatic principles.

The fundamental equations of the developed charge transport model are described in section 4.2 which consist of electrostatic and thermal equations. These equations are used to calculate the effect of nonlinear dependence of electric field, temperature and distance on the electrical conductivity of the insulation material. Implementation of the model is based on the FDM method in one dimension (1-D) for single and double layer samples, and two dimensions (2-D) for samples containing defects as explained in section 4.3. In section 4.4, the space charge accumulation under the effect of electric field, temperature gradients and distance dependent conductivity are considered in single layer 1-D plane-plane geometry. The temperature gradients due to the joule heating inside the dielectric and/or due to the temperature difference between the electrodes are considered. While the distance dependent conductivity was calculated based on Boggs model [58, 80], in which stated that the homocharge and/or hetero charge can be accumulated inside the insulation sample due to the effect of impurities that have diffused in to the sample from the sample surfaces after voltage application. In the final part of section 4.4, the space charge accumulation at the interface between two different dielectrics is simulated under the effect of field dependent conductivity. In section 4.5 the model is extended to 2-D and the space charge accumulation around the defect under the effect of field and temperature dependent conductivity are considered. The source of heat is considered to be Joule heating originating inside the sample. The developed charge transport model cannot interpret the space charge data obtained from experimental PEA measurement data directly; it will require another simulation model to calculate the generation, transmission and propagation of acoustic pressure waves and their detection as they occur in real PEA measurement system. The details of the PEA simulation model will be described in chapter 5.

4.1 Electro-thermal charge transport model

Space charge accumulation in dielectrics can be considered from the point of view of the transport of charge carriers within the insulation material on application of an applied electric field. There are two different approaches, which are the macroscopic approach and microscopic approach. The bipolar charge transport model can be used to represent the microscopic approach of space charge accumulation [54]. In bipolar charge transport model two types of charge carrier are considered, electrons and holes[107]. The charge carriers are usually considered trapped at trapping centres related to the morphology of the material and transport occurs due to charge carriers hopping from one trap centre to another. The outcome of such models is that the electrical conductivity of the material is a non-linear function of the electric field. In this work, an alternative macroscopic approach is taken. Here, an electro-thermal model that can be described as a non-polar charge transport model is developed in which the electrical conductivity of the material is determined from an empirical function of electric field and temperature. The advantage of this approach is that only a few parameters (such as, permittivity and conductivity) are required for characterizing the material [54]. Hence the model can be used for variety of situations without structure modification and does not require too many assumptions for parameters. Another main advantage of this model is simplicity for application in practical cases. However, as this model is based on a macroscopic approach, it cannot provide any information about the injection, extraction, trapping, detrapping and recombination of charge carriers; as this involves the understanding of the interaction of charge carriers with the atoms and molecules of the host polymer [108]. Therefore, bipolar charge transport model requires an advanced simulation model to calculate and solve the set of convection equations[109, 110]. The information about these processes of space charge can be obtained in microscopic approach which explained extensively in [36, 71, 111]. In this study, to avoid the complexity and parametrisation of bipolar charge transport model, an electro-thermal model of charge transport which encompasses field and temperature dependent conductivity will be used instead.

On the other hand, the space charge measurements have often shown the presence of space charge accumulation localised at one or at both interfaces of the sample. This build-up of space charge is often termed homocharge if the space charge has the same polarity as the adjacent electrode polarity or heterocharge if the polarity of the space charge is opposite that of the adjacent electrode. Heterocharge/homocharge may form due to a

number of reasons. In the case of homocharge, this may be due to the injection of excess charge carriers from the electrode having the same polarity. The effect of this space charge is to reduce the electric field at the injecting electrode and a steady state homocharge distribution results when the charge injected is balanced by charge transport into the bulk of the material. The formation of homocharge may also be the result of enhanced electrical conductivity caused by impurity diffusion from the surfaces of the sample during manufacture or during storage of the material following manufacture [58]. In this case, the presence of impurity can enhance the electrical conductivity in the material close to the surface and the enhanced conductivity leads to the formation of homocharge. Heterocharge accumulation can occur in a similar manner if impurities from the material diffuse to the environment leading to a decrease in the electrical conductivity close to the surfaces of the material. Alternatively, heterocharge can be explained as due to the transport of ionised impurities within the material drifting towards the electrodes when an electric field is applied [102, 112, 113]. In this study the homocharge and heterocharge accumulation is considered by modifying the local electrical conductivity due to impurity diffusion at the electrode/insulation interface [58, 80].

4.2 Electro-thermal conductivity model

4.2.1 Electrostatic part

The fundamental set of equations for time dependent space charge accumulation and electric field distribution inside the dielectrics that are relevant for the weakly electrical conductive material are [40, 114]:

$$E = -\nabla V \quad (4.1)$$

$$J = \sigma E \quad (4.2)$$

$$\frac{\partial^2 V}{\partial x^2} = -\frac{\rho}{\epsilon_0 \epsilon_r} \quad (4.3)$$

$$\nabla \cdot J = -\frac{\partial \rho}{\partial t} \quad (4.4)$$

Where, V is electric potential, E is electric field vector, ϵ_0 is the permittivity of vacuum, ϵ_r is relative permittivity of the dielectric, σ is electrical conductivity, J is the current density vector and ρ is the charge density. Equation 4.1 establishes the relationship between the vector electric field and the scalar electric potential distribution. Equation 4.2, is ‘Ohms’ law relating the current density vector J to the electric field vector E . Equation 4.3, is Poisson’s equation which describes the spatial dependence of electrical potential in terms of the charge density distribution, ρ , inside the insulator. Equation 4.4

is the continuity equation which states that the charge density within a region of space will change with time if the divergence of the current density is not zero.

The transient form of space charge accumulation can be expressed in terms of electric current density and material properties by inserting (4.2) and (4.4) into equation (4.3).

$$\rho = -\frac{\varepsilon_0 \varepsilon_r}{\sigma} \frac{\partial \rho}{\partial t} + J \cdot \nabla \left(\frac{\varepsilon_0 \varepsilon_r}{\sigma} \right) \quad (4.5)$$

4.2.2 Thermal part

In an ideal (Ohmic) isotropic and homogeneous medium, the conductivity can be treated as a scalar constant [1]. However, the electrical conductivity of insulation material, such as LDPE and XLPE, is strongly dependent on both temperature and electric field. As mentioned in chapter 2, different empirical equations have been suggested in the literature in order to take into account the dependencies of electrical conductivity on temperature and electric field. In this study an empirical equation involving a power-law function of electric field and exponential temperature dependence [23, 48, 54] for field and temperature dependent conductivity (4.6) is used.

$$\sigma(E, T) = \sigma_0 \left(\frac{E}{E_0} \right)^\gamma \exp\left(\alpha \left(\frac{T}{T_0} \right)\right) \quad (4.6)$$

Here; σ_0 , E_0 , α , T_0 and γ are empirical parameters to describe the dielectric's electrical conductivity as a non-linear function of the electric field (E) and temperature (T).

The temperature distribution inside the sample is governed by the heat conduction equation [49],

$$\rho_m c_p \frac{\partial T}{\partial t} = \nabla \cdot (k \nabla T) + S_{heat} \quad (4.7)$$

Where, ρ_m is the mass density, c_p is specific heat capacity, k is the thermal conductivity of the material, T is the temperature and S_{heat} is the source of heat generation. As mentioned in chapter 2 (subsection 2.4.2), S_{heat} represents a number of different sources S , including the resistive heating due to the leakage current through the insulation S_{Joule} , dielectric heating due to applied AC component (ripple), S_{Diel} , and also the resistive losses of the cable high voltage cable conductor, $S_{conductor}$ [50],

$$S_{heat} = S_{Joule} + S_{Diel} + S_{conductor} \quad (4.8)$$

4.2.3 Inclusion of homocharge or heterocharge accumulation

To be able to calculate the heterocharge/homocharge accumulation behaviour, the conductivity of the insulation material (equation 4.6) is modified artificially. Steve Boggs in [58, 80] and further Zheng in [23] explained this modification by the diffusion of impurities from the inner and outer semicon layers into the insulator, such as to produce an exponential dependence of electrical conductivity close to the electrodes. The original electric field and temperature dependent conductivity, $\sigma(E, T)$ is modified by multiplying it with a distance dependent function that either enhances or reduces the local electrical conductivity. Hence the local electrical conductivity becomes distance, electric field and temperature dependent, $\sigma(E, T, x)$. In thin film samples, the conductivity is therefore expressed as:

$$\sigma(E, T, x) = \sigma(E, T) \left(1 + (n_a - 1) \cdot e^{\frac{x_{min} - x_i}{d_a}} \right) \left(1 + (1 - n_b) \cdot e^{\frac{x_i - x_{max}}{d_b}} \right) \quad (4.9)$$

Where $n_{a,b}$ are the enhancement ($n_{a,b} > 1$) or reduction ($n_{a,b} < 1$) terms for the conductivity in the homocharge/heterocharge region adjacent to the inner electrode interface at axial position x_{min} and outer electrode interface x_{max} ; d_a and d_b are the distance constants which characterise the thicknesses of homocharge and/ or heterocharge regions at the interface and the outer interface respectively (depth enhancement). x_i is the nodal distances in the insulation. Figure 4.1 shows the electrical conductivity modification based on equation 4.9.

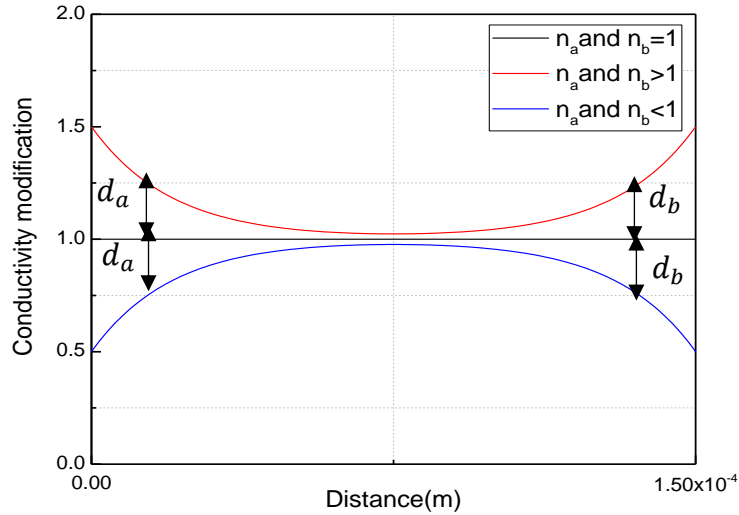


Figure 4.1: Conductivity modification based on equation 4.9.

4.3 Model implementation

The above coupled set of time dependent differential equations cannot be solved by analytical methods. Therefore, a numerical simulation for the electrostatic and thermal behaviour based on the finite difference method (FDM) was implemented using MATLAB. As mentioned in chapter 2, the principle of FDM method is to express the partial differential equations (PDE) in terms of a set of algebraic equations. To achieve this, the PDEs are discretised to a finite number of mesh points in the physical domain [95]. In this study the charge transport model is implemented for 1-D and 2-D thin film samples in different situations. A thin film PEA space charge measurement system is effectively a 1-D measurement through the thickness of the sample or layered sample. It assumes that the space charge profile is essentially uniform over the area of the dielectrics. In this case 1-D FDM models are suitable for the interpretation of PEA measurements. In order to extend the model to take into account defects within the insulation then 2-D FDM models have to be used. In the following sections the FDM models will be developed and described in 1-D and 2-D plane- plane geometries.

4.3.1 FDM formula for 1-D thin film sample

In order to simulate the space charge accumulation in 1-D single layer and double layer thin film samples, it is necessary to discretise the space domain and to convert equations, 4.1-4.9 to FDM form. The external HVDC voltage is applied on the insulation at $x=0$ and is grounded at the end ($x= d$). In order to differentiate the two surfaces of the thin film insulator, the term ‘inner’ represents the surface at position $x=0$ and the term ‘outer’ represents the surface at position $x=d$. Figure 4.2 shows the 1-D single layer insulation domain which is discretised by n nodes with equal spatial intervals of distance, Δx .

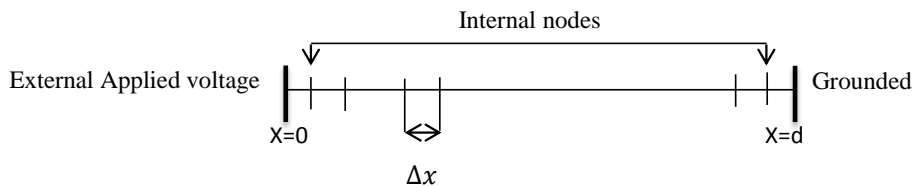


Figure 4.2: Discretised 1D thin film sample based on FDM.

The final FDM formula to equations 4.1, 4.3, 4.5 and 4.7 are given as 4.10, 4.11, 4.12 and 4.13 respectively. The FDM equations 4.11 and 4.13 are derived in detail in appendix C1 and C2 respectively.

$$E_{(x)} = \frac{V_{(x+\Delta x)} - V_{(x)}}{\Delta x} \quad \text{at } x = 0$$

$$E_{(x)} = \frac{V_{(x)} - V_{(x-\Delta x)}}{\Delta x} \quad \text{at } x = d$$

$$E_{(x)} = \frac{V_{(x+\Delta x)} - V_{(x-\Delta x)}}{2\Delta x} \quad \text{at } x > 0 \text{ \& } x < d \quad (4.10)$$

$$V_{(x)} = 1/2 \left(V_{(x+\Delta x)} + V_{(x-\Delta x)} + \frac{(\Delta x)^2}{\epsilon_0 \epsilon_r} \rho_{(x)} \right) \quad (4.11)$$

With the electrostatic boundary conditions; $V(0)$ = applied voltage and $V(d)$ =0V.

Equation 4.5 expressed in finite difference form is given below where ρ_{new} (updated) charge density at time $t+\Delta t$.

$$\rho_{new(x)} = \sigma_{(x)} J_{(x)} \cdot \frac{\Delta t}{2\Delta x} \left(\frac{1}{x+\Delta x} - \frac{1}{x-\Delta x} \right) - \rho_{(x)} \left(\frac{\sigma_{(x)}}{\epsilon_0 \epsilon_r} \Delta t - 1 \right) \quad (4.12)$$

And equation 4.7 expressed in finite difference form is given below and where

T_{new} refers to the new (updated) temperature at time $t+\Delta t$.

$$T_{new(x)} = \frac{k\Delta t}{\rho_m c_p \Delta x^2} (T_{(x+\Delta x)} + T_{(x-\Delta x)}) + \left(1 - 2 \frac{k\Delta t}{\rho_m c_p \Delta x^2} \right) T_{(x)} + \frac{\Delta t S_{heat(x)}}{\rho_m c_p} \quad (4.13)$$

With thermal boundary conditions; $T(0)$ = temperature of the high voltage electrode and $T(d)$ set to temperature of the ground electrode. In a double layer thin film sample, the same governing equations as single layer sample are used. Again, the external voltage was applied on the insulation at $x=0$ and grounded at the end ($x= d$) as shown in figure 4.3. In figure 4.3, ϵ_1 , σ_1 and x_1 are the permittivity, conductivity and thickness of the first layer (layer that is in contact with the high voltage electrode), whereas ϵ_2 , σ_2 and x_2 are the permittivity, conductivity and thickness of the second dielectric layer (the layer in contact with the ground electrode). The spatial intervals between the nodes of both samples were assumed equal, $\Delta x_1 = \Delta x_2$.

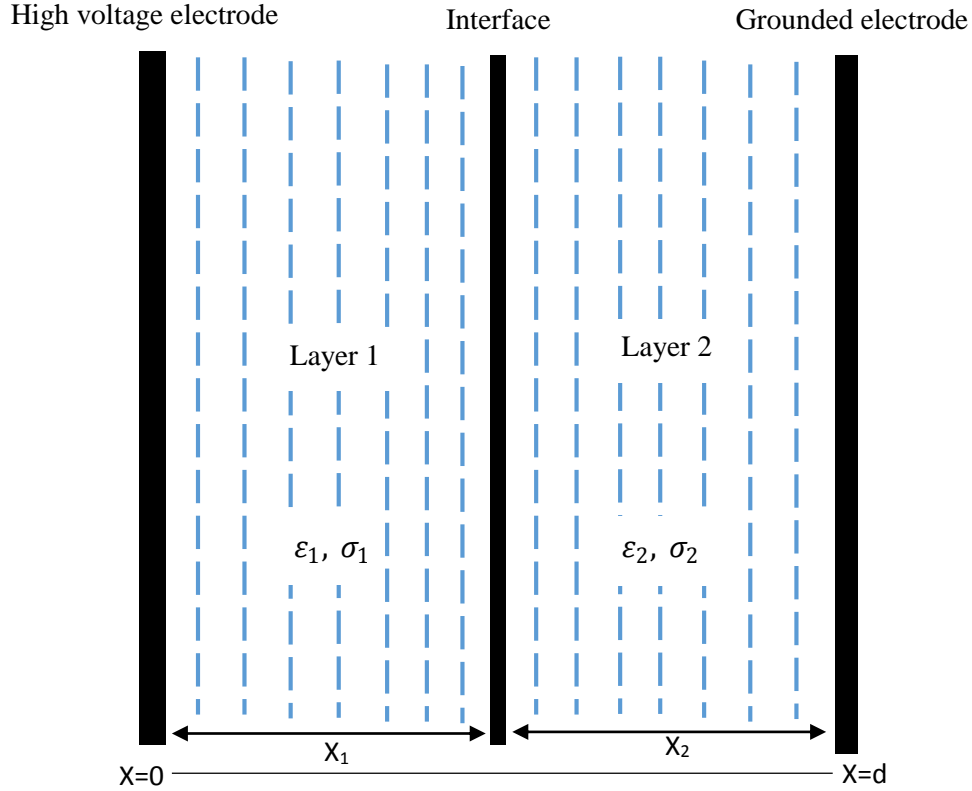


Figure 4.3: Schematic representation of two layer thin film sample.

4.3.2 FDM formula for 2-D thin film samples

For the insulation samples containing defects, a 2-D domain is required to calculate the space charge accumulation around the defect and in the rest of the sample. In that case the space domain is discretised along X and Y axis to satisfy a 2-D square and these are divided into a number of nodes along each direction to produce a mesh. The distance between two nodes along both X and Y axis is set equal ($\nabla x = \nabla y$). The Dirichlet boundary conditions are set on the top and bottom of the sample (external DC voltage is applied on the top electrode and the bottom electrode boundaries is grounded), whereas Neumann boundary conditions ($\frac{\partial V}{\partial x} = 0$) is set on the right and left edges of the sample. In order to calculate the temperature distribution inside the sample, again the Neumann boundary condition is set on the left and right edges ($\frac{\partial T}{\partial x} = 0$) as the same as in case of voltage distribution, and Dirichlet boundary condition is set up on the high voltage and ground of electrodes. For simulations involving the effect of Joule heating, the value of temperature of the ground electrode will be the same as the value of temperature at the high voltage electrode. However, different temperatures of the electrodes will be used for

simulations involving a temperature gradient inside the sample. Figure 4.4 shows the schematic representation of 2-D domain based on FDM.

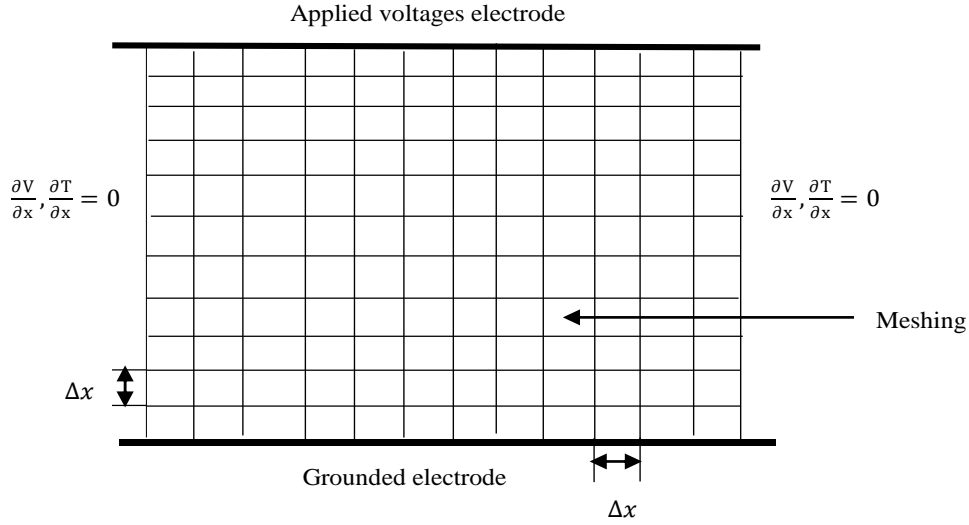


Figure 4.4: Schematic representation of 2D thin film sample used for the simulation.

Based on the above assumptions, in 2-D, the electric potential at each internal node is determined by solving Poisson's equation (equations (4.1) and (4.3)) and in the absence of space charge, is equal to the average of potential of the four adjoining nodes as given by equation below which is the FDM formula of Laplace equation:

$$V_{(x,y)} = \frac{1}{4}(V_{(x+\Delta x,y)} + V_{(x-\Delta x,y)} + V_{(x,y+\Delta y)} + V_{(x,y-\Delta y)}) \quad (4.14)$$

However, when space charge accumulates in the sample, Poisson's equation must be used to determine the electric potential of the internal nodes. The FDM formula for Poisson's equation is used as shown in equation 4.15 (the detailed derivation of Poisson's equation in 2-D is shown in appendix D1):

$$\frac{V_{(x+\Delta x)} - 2V_{(i)} + V_{(x-\Delta x)}}{(\Delta x)^2} + \frac{V_{(y+\Delta y)} - 2V_{(y)} + V_{(y-\Delta y)}}{(\Delta y)^2} = -\rho / \epsilon_0 \epsilon_r \quad (4.15)$$

Where, Δx is a distance between two adjacent nodes along X-axis, Δy is the distance between two adjacent nodes along Y-axis. If $\Delta x = \Delta y$, equation 4.15 becomes:

$$V_{(x,y)} = \frac{1}{4}(V_{(x+\Delta x,y)} + V_{(x-\Delta x,y)} + V_{(x,y+\Delta y)} + V_{(x,y-\Delta y)}) + \frac{(\Delta x)^2}{\epsilon_0 \epsilon_r} \rho \quad (4.16)$$

for simplicity equation 4.16 can be written:

$$V_0 = 1/4 \left(V_1 + V_2 + V_3 + V_4 + \frac{(\Delta x)^2}{\epsilon_0 \epsilon_r} \rho \right) \quad (4.17)$$

For the nodes which occupy the left and right edges, the two equations shown below were used [115] in order to satisfying the Neumann boundary conditions:

$$V_0 = 1/4 \left(2V_1 + V_2 + V_3 + \frac{(\Delta x)^2}{\varepsilon_0 \varepsilon_r} \rho \right) \text{ for left edge} \quad (4.18)$$

$$V_0 = 1/4 \left(2V_3 + V_2 + V_4 + \frac{(\Delta x)^2}{\varepsilon_0 \varepsilon_r} \rho \right) \text{ for right edge} \quad (4.19)$$

To calculate the thermal conditions in the 2-D domain, the initial temperature distribution of each internal nodes is equal to the average of the four adjoining nodes and only the Laplace form of equation 4.7 needs to be used as shown in equation 4.20.

$$T_{(x,y)} = \frac{1}{4} (T_{(x+\Delta x,y)} + T_{(x-\Delta x,y)} + T_{(x,y+\Delta y)} + T_{(x,y-\Delta y)}) \quad (4.20)$$

When the voltage is applied across the sample, and when $\Delta x = \Delta y$ the 2-D FDM formula for equation 4.7 needs to include both the source term and transport term become equation 4.21. The detailed derivation of the FDM formula of equation 4.21 is explained in appendix D2:

$$T_{new(x,y)} = T_{(x,y)} + \frac{k\Delta t}{\rho_m c_p \Delta x^2} (T_{(x+\Delta x,y)} + T_{(x-\Delta x,y)} + T_{(x,y+\Delta y)} + T_{(x,y-\Delta y)} - 4T_{(x,y)}) + \frac{\Delta t S_{heat}}{\rho_m c_p} \quad (4.21)$$

Equation 4.21 notation can be simplified to

$$T_{new(0)} = T_0 + \frac{k\Delta t}{\rho_m c_p \Delta x^2} (T_1 + T_2 + T_3 + T_4 - 4T_0) + \frac{\Delta t S_{heat}}{\rho_m c_p} \quad (4.22)$$

To incorporate the Neumann boundary conditions the nodes placed on the left and right edges, equations 4.23 and 4.24 are used.

$$T_{new(0)} = T_0 + \frac{k\Delta t}{\rho_m c_p \Delta x^2} (2T_1 + T_2 + T_3 - 4T_0) + \frac{\Delta t S_{heat}}{\rho_m c_p} \quad (4.23)$$

$$T_{new(0)} = T_0 + \frac{k\Delta t}{\rho_m c_p \Delta x^2} (2T_3 + T_2 + T_4 - 4T_0) + \frac{\Delta t S_{heat}}{\rho_m c_p} \quad (4.24)$$

The details of the simulation process for the 2-D model and the results are detailed in section 4.5.

4.4 Space charge accumulation in 1-D thin film samples

4.4.1 Single layer samples

For single layer thin film samples, the space charge is simulated for three different cases. In the first case the electric conductivity is considered dependent on the electric field only, and temperature considered isothermal at some arbitrary temperature, while in the second case the effect of field and temperature dependent conductivity was applied. In the third case the homocharge and heterocharge accumulation at the interfaces will also be considered by artificially modifying the conductivity. Therefore in this case, the conductivity will be field and distance dependent and isothermal conditions assumed. In this chapter, the value of the conductivity parameter (σ_0) was chosen arbitrary to illustrate the model behaviour and therefore its value does not represent that typical of a particular material. Fitting of all the model parameters to particular materials will be undertaken in chapter 6 when the model behaviour is compared directly with experimental data. The details of all the charge transport simulation cases are explained in the following subsections:

4.4.1.1 Field dependent conductivity only ($\sigma(E)$)

In this case, the electrical conductivity was considered to be just field dependent, and temperature effects ignored. Therefore the main electrical conductivity equation (equation 4.6) was replaced with:

$$\sigma(E) = \sigma_0 \left(\frac{E}{E_0}\right)^\gamma \quad (4.25)$$

Where the exponential function of temperature is absorbed into the constant σ_0 .

Assuming the thickness of dielectric is 200 μm , and the external applied voltage is 7kV. The procedure of calculation follows the flowchart diagram shown in figure 4.5. The initial conditions were that the space charge was everywhere equal to zero and the initial electric potential at each node was determined from Laplace's equation. After initialising the parameters, Poisson's equation is solved to find the electric potential distribution at the time step t . Convergence of the solution to Poisson's equation was determined when the electric potentials at all nodes between two subsequent iterations, $V(x)$, was below a pre-specified tolerance. Once convergence was achieved in the numerical solution of Poisson's equation, the electric field, E , conductivity, $\sigma(E)$ current density, J , and the space charge ρ accumulation were then calculated using equations (4.1), (4.25), (4.2), and (4.5) respectively. This process is repeated starting by solving Poisson's equation for

the new space charge distribution for each time step, Δt , updating the space charge until the pre-defined time or a steady state is obtained.

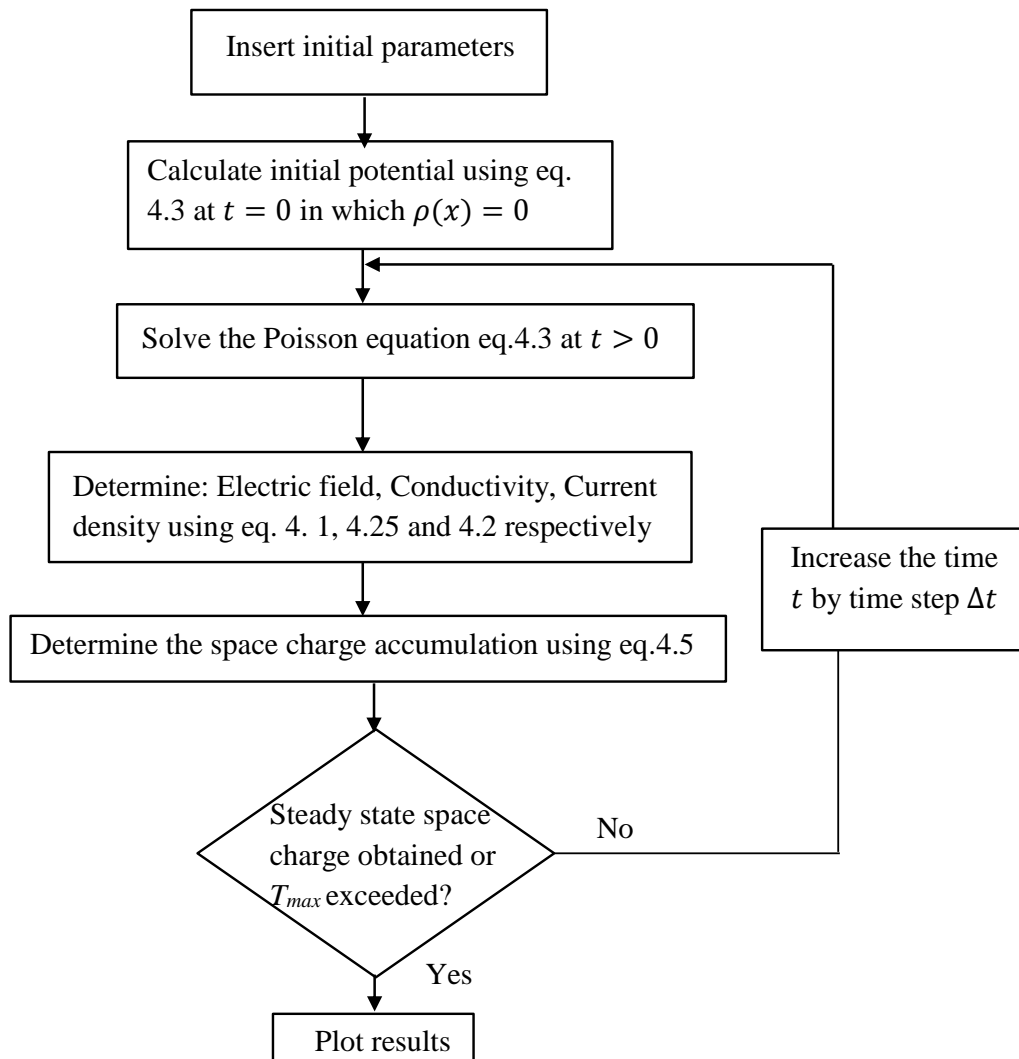


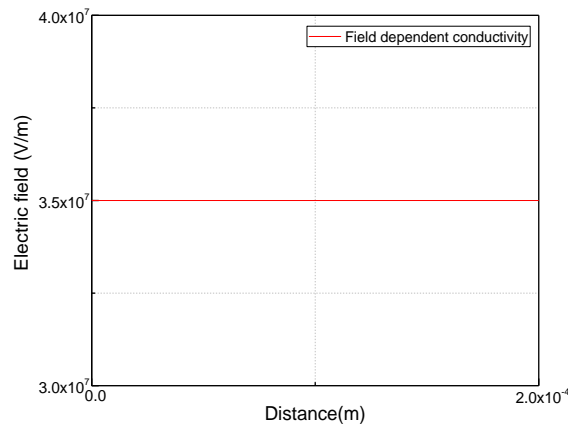
Figure 4.5: Flowchart of the numerical procedure of calculation the space charge due to the field dependent conductivity.

Figures 4.6 shows the result of calculation, for the model parameters given in table (4.1), in which the electric field and electrical conductivity are distributed uniformly across the insulation as under these conditions, zero space charge accumulation occurs in the thin film sample. Therefore, in this case the thin film sample can be considered as an ideal material, as resistive heating inside the insulation, charge injection, impurity diffusion from the electrodes, ionization of impurities inside the sample bulk and conducting defects inside the sample were not included in the simulation. Therefore the result of zero accumulated space charge is expected due to the uniform distribution of electric field that

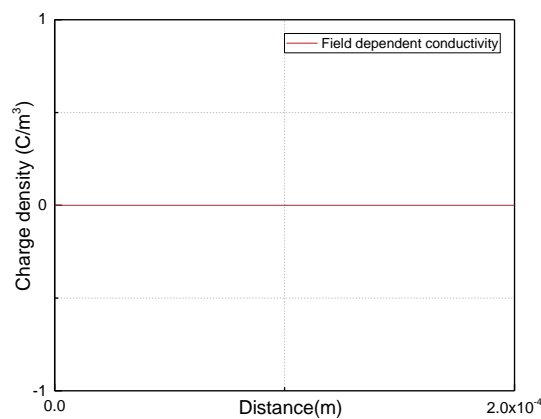
led to the uniform distribution of conductivity ($\nabla(\frac{\epsilon}{\sigma}) = 0$). In figure 4.6 (a) the resultant electric field was constant over the thickness of the insulation with a value of 3.5×10^7 V/m. This is the same as the Laplacian value equal to the applied voltage divided by the sample thickness $7\text{kV}/200\mu\text{m}$.

Table 4.1: Model parameters for field dependent conductivity.

Constants	Symbols	Values
Applied voltage	V	7kV
Conductivity constant	σ_0	2.95×10^{-14} S/m
Relative permittivity	ϵ_r	2.3
Vacuum permittivity	ϵ_0	8.854×10^{-12} F/m
Electric field reference	E_0	10kV/mm
Field power index	γ	1.8
Maximum time	T_{max}	1s



(a)



(b)

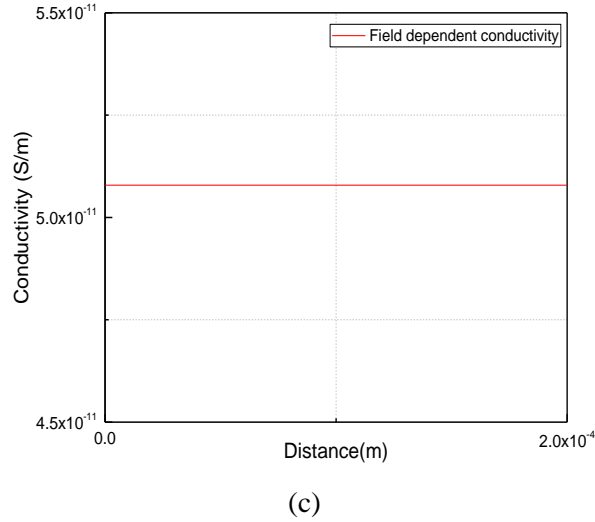


Figure 4.6: (a) Electric field, (b) Charge density, (c) conductivity profiles as a function of position in a thin film sample when the conductivity is field dependent.

As shown in figure 4.6(b), the accumulation of space charge is zero as the field dependent conductivity is also constant (as shown in figure 4.6(c)), hence $\nabla \left(\frac{\epsilon}{\sigma} \right) = 0$.

4.4.1.2 Field and Temperature dependent conductivity, $\sigma(E, T)$:

The basic electrostatic simulation was extended by including the temperature dependence as well as field dependent conductivity. Two sources of heat generation were also considered independently in these simulations. First was Joule (resistive) losses due to electrical conduction within the insulation material by including the Joule heat source term. The second heat source term was used to mimic the temperature gradient conditions inside a DC cable by using different temperature boundary conditions on each side of the sample. These two contributions will be treated separately below although in a real situation these two heat sources should be combined.

4.4.1.2.1 Temperature gradient due to heat generation losses inside the thin film sample

In this case, the resistive (Joule) heating of the insulation material is taken into account. Based on the literature, the rate of temperature rise depends on heat generation due to the current flowing in the insulation material, the specific heat capacity of the insulation material and heat dissipation due to thermal conduction to the surroundings [65]. The heat generation under DC voltage is equal to the electrical conductivity times the square of the electric field (σE^2) [65, 116]. Although, the resistive heating of insulation material is usually small, it may still have an impact on space charge accumulation and the

resultant electric field distribution as the insulator material has a poor thermal conductivity. To show this effect, the transient form of heat conduction equation and Joule heat generation inside the dielectric were considered. Hence, equation (4.7) becomes:

$$\rho_m c_p \frac{\partial T}{\partial t} = \nabla \cdot (k \nabla T) + \sigma(E, T) E^2 \quad (4.26)$$

with $\sigma(E, T)$ given by equation (4.6).

Initial simulations of the charge transport and space charge accumulation were undertaken based on field and temperature dependent conductivity and includes just the effect of Joule heating as described above in a thin film sample of thickness 0.2mm.

The temperature at the inner side ($x=0$) and at the outer side ($x=d$) of insulation were fixed at 293K (20 °C). The initial parameters, the initial conditions and procedure of calculations are the same as the case of field dependent conductivity only, section 4.4.1.1, but here equation 4.26 was used in the calculation of the temperature profile and equation 4.6 was used to calculate the field and temperature dependent conductivity as shown in figure 4.7. The model parameters used are shown in table 4.2. The parameters of heat conduction equation (4.7) were chosen based on [59], whereas the parameters of the electrical conductivity equation (4.6) were chosen based on [48, 54] except σ_0 which had been chosen arbitrary.

The results of this simulation are shown in figure 4.8. The steady state distributions of temperature, electrical conductivity, electric field and charge density, are shown across the insulation thickness. At the beginning when ($t = 0$), the temperature was isothermal, and equal to 293K. In figure 4.7(a) the steady state temperature inside the insulation had increased to a maximum value of 293.2 K at the centre of the sample. The temperatures of the two surfaces remained at 293 K due to the fixed boundary conditions. In this case, Joule heating (σE^2) only makes a small difference to the temperature profile.

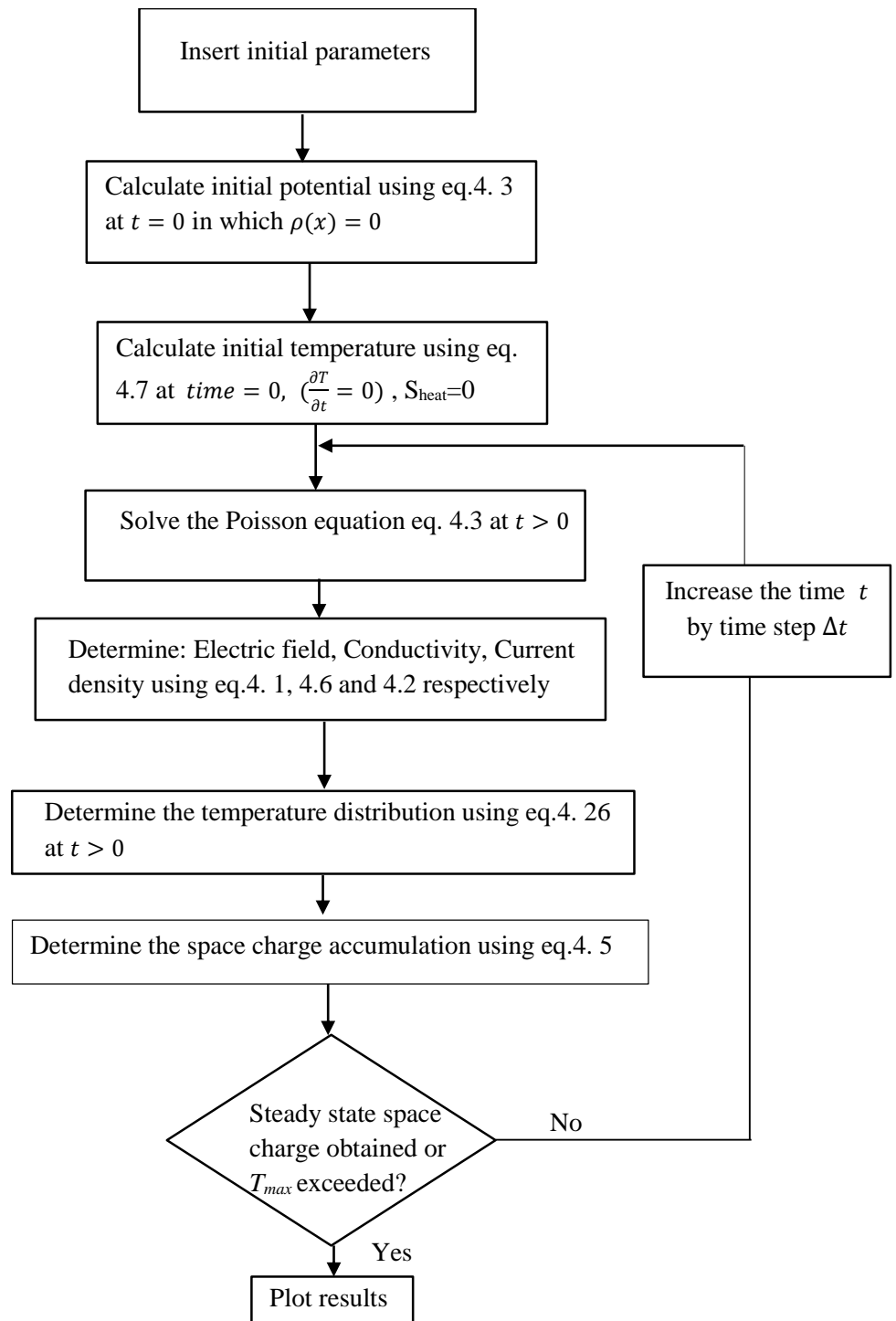


Figure 4.7: Numerical procedure of calculation the space charge due to the field dependent conductivity and temperature (Joule heating) dependent conductivity.

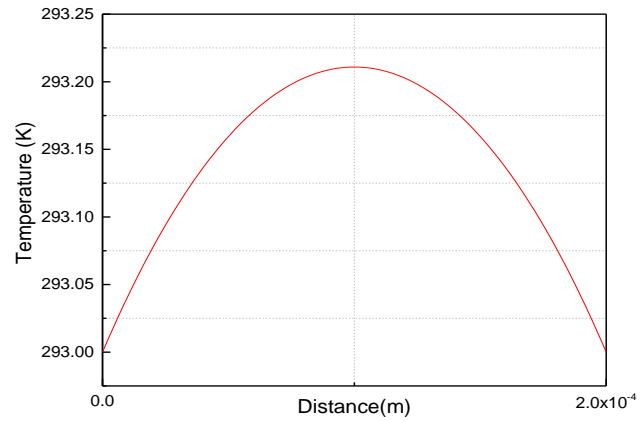
This small temperature increase in the bulk of the sample led to an increase the electrical conductivity in the bulk and which decreases towards the inner and outer interfaces as shown in figure 4.8(b). As a result, the electric field decreases in the bulk and increases

at the inner and outer interfaces compared with the Laplacian field solution (which was shown in figure 4.6(a)).

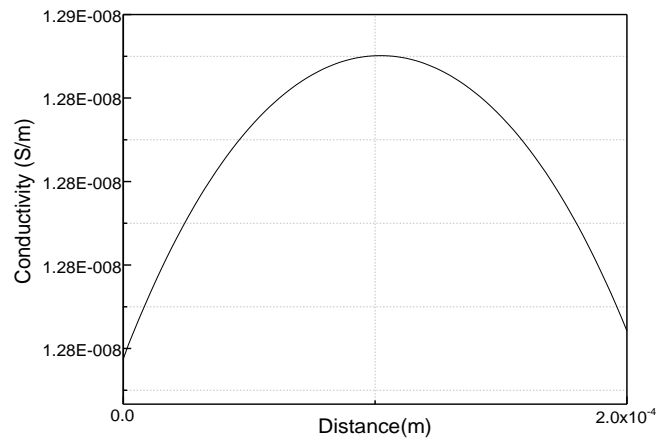
The electrical conductivity within the bulk of insulation sample is no longer uniform and results in the accumulation of space charge as shown in figure 4.8(d). The resultant steady state space charge distribution is linear across the sample thickness from -0.06 Cm^{-3} at the inner surface to $+0.06 \text{ Cm}^{-3}$ at the outer surface and zero at the centre of the sample. It should be mentioned that the amount of heat losses inside the sample is directly affected by the value of applied voltage as it is proportional to the square of the internal electric field. The greater the applied voltage, the greater the Joule heating inside the insulation and therefore the greater the consequence on space charge accumulation.

Table 4.2: Model parameters for temperature dependent conductivity.

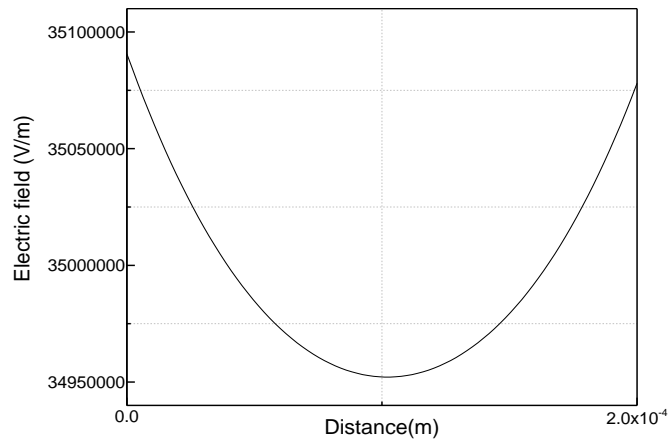
Constants	Symbols	Values
Applied voltage	V	7000V
Conductivity constant	σ_0	$2.5 \cdot 10^{-12} \text{ S/m}$
Relative permittivity	ϵ_r	2.3
Vacuum permittivity	ϵ_0	$8.854 \cdot 10^{-12} \text{ F/m}$
Electric field reference	E_0	10kV/mm
Field power index	γ	1.8
Temperature coefficient	α	0.1
Temperature reference	T_0	293K
Thermal conductivity	k	0.329 W /m K
Specific heat of material	c_p	2250 J kg/K
Density of material	ρ_m	920 kg/m ³
Maximum time	T_{max}	1s



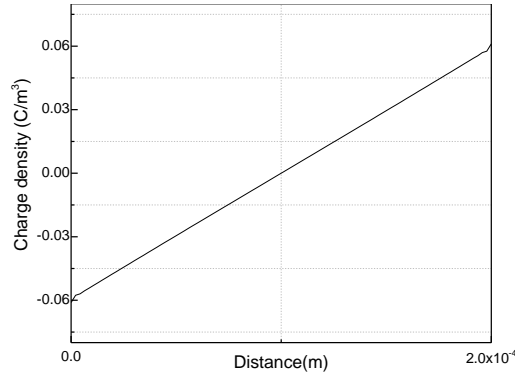
(a)



(b)



(c)



(d)

Figure 4.8:(a) Temperature,(b) conductivity,(c) electric field, (d) charge density distribution in a thin film sample when the conductivity when the DC heat generation is considered.

4.4.1.2.2 Temperature gradient due to a temperature difference between electrodes

To mimic the effects of heat dissipation of the central conductor when the HV cable is operated under load conditions, the electro-thermal charge transport model simulations can be conducted under non-identical thermal boundary conditions. In this case, a temperature gradient can be investigated if the temperature between the two sides of the dielectric is made different as would be the case for a cable carrying a load current. The temperature gradient can be obtained by setting a temperature difference between the boundary surface sides. In this simulation case, the Joule heating inside the insulation sample is neglected for simplicity and if the effect of a steady state temperature gradient is of interest, then only the Laplace form of the heat conduction equation needs to be solved ($\frac{\partial T}{\partial t} = 0$, $S_{heat} = 0$) resulting in a steady state temperature distribution inside the sample. In the simulations, the temperature of the outer surface for all cases was fixed at 293K, while the temperature of the inner surface was changed from 293K to 313K, 333K and 353K to get different temperature gradients of 0, 20, 40, and 60 °C between inner and outer surfaces respectively. The procedure of numerical calculation is shown in figure 4.9. Again, the thickness of the sample, the value of external applied voltage and the model parameters were the same as those used for the previous field and temperature dependent conductivity case, table 4.2.

The results of the simulations are shown in figure 4.10 where the steady state electric potential, electric field, conductivity and space charge distributions are shown for each thermal gradient. The results shows that, when the temperature was isothermal, i.e. there was no difference between the temperature of the inner and the outer surfaces, the conductivity and electric field were distributed uniformly and the sample was free of any

space charge accumulation as was found for the field dependent conductivity case, section 4.4.1.1. However, when the temperature difference (gradient of temperature) increases between the inner and outer of insulation surfaces, the electric potential distribution becomes non-uniform in the bulk of the insulation (see figure 4.10(a)). The corresponding electric field decreases from the isothermal case with increasing temperature and increases with decreasing temperature at the lower temperature side of the sample as shown in figure 4.10(b). For example, when the temperature at the inner interface was set to 353K and the temperature of the outer surface of the insulation was set to 293K ($\Delta T=60\text{ }^\circ\text{C}$), the electric field at the inner surface decreased from the isothermal case of $3.5 \times 10^7\text{ V/m}$ to $2.87 \times 10^7\text{ V/m}$, whereas it was increased to $4.21 \times 10^7\text{ V/m}$ at the outer surface of insulation. This effect is related to the so called ‘inversion effect’ of field strength as reported in cylindrical geometry cables [45, 117] when under load conditions. The change in the electric field profile for different field gradients is due to the change in electrical conductivity (which is both temperature and field dependent). Due to the temperature profile, the conductivity of the material at the high temperature side increases whilst that at the low temperature side decreases as shown in figure 4.10(c). As the electrical conductivity becomes non-uniform inside the sample, space charge accumulation takes place inside the sample. The steady state space charge distributions are shown in figure 4.10(d) for each temperature gradient case. Increasing the temperature gradient increases the amount of space charge accumulated from zero (in the isothermal case) to around 1.5 Cm^{-3} when the temperature gradient across the sample was $60\text{ }^\circ\text{C}$. The space charge is located approximately uniformly across the sample thickness. It is this space charge that is responsible for the changes in the electric field distributions.

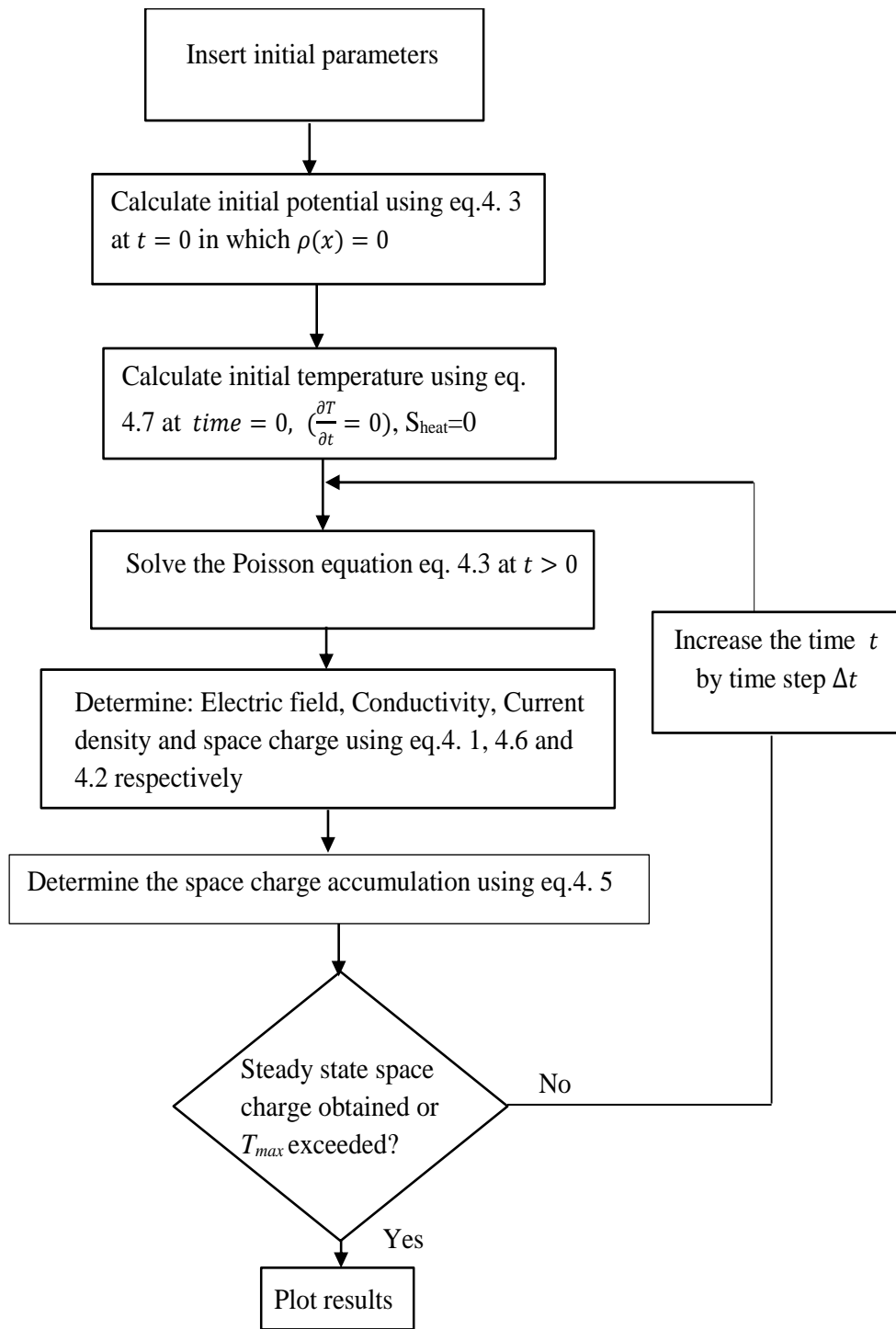
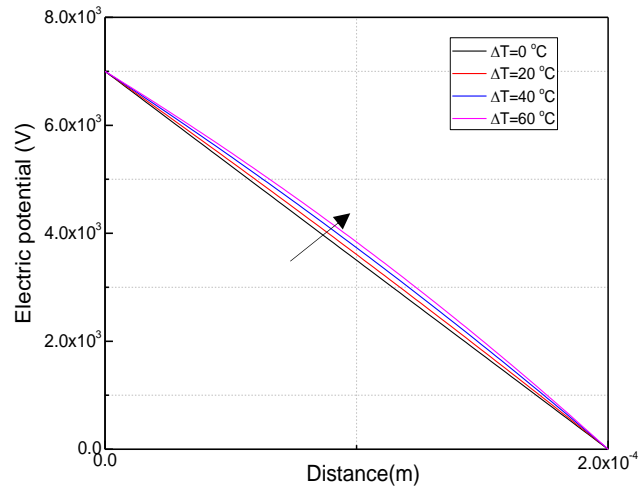
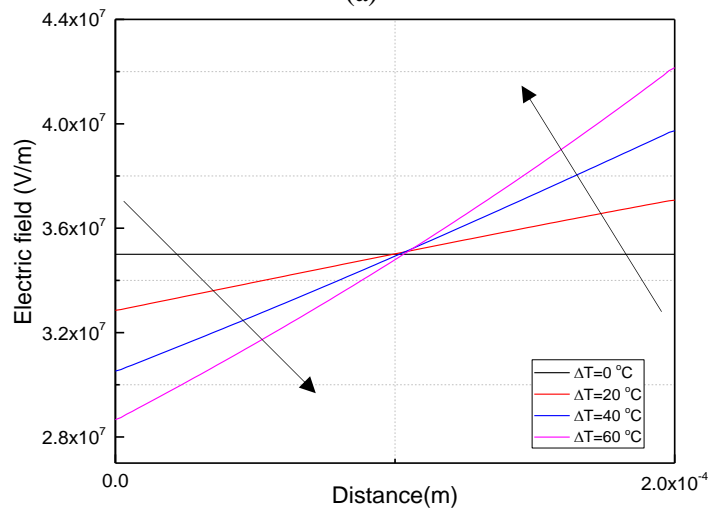


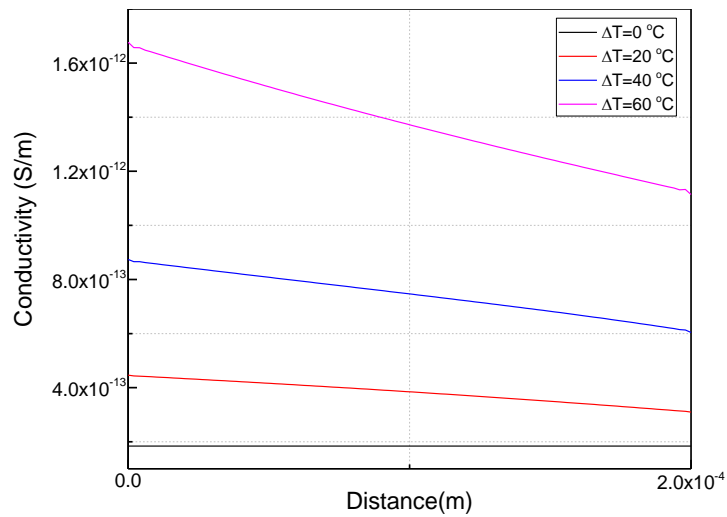
Figure 4.9: Numerical procedure of calculation the space charge due to the field dependent conductivity and temperature (conductor heating) dependent conductivity.



(a)



(b)



(c)

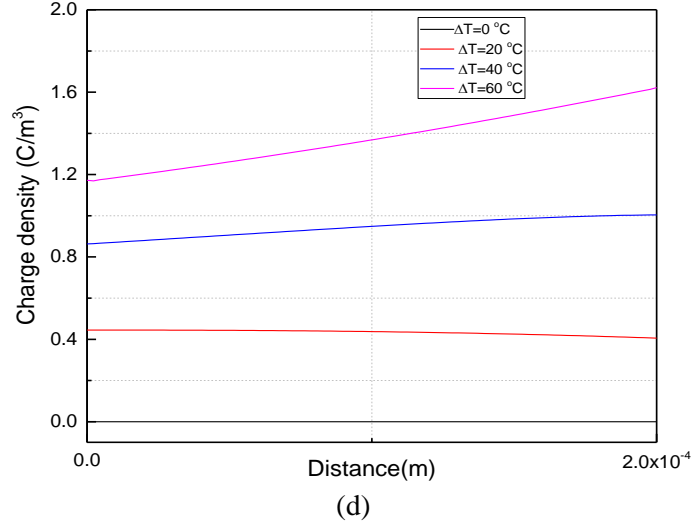


Figure 4.10: (a) electric potential, (b) electric field, (c) conductivity, (d) charge density distribution in a thin film sample when the conductivity is temperature dependent.

4.4.1.3 Field and distance dependent conductivity, $\sigma(E, X)$

The results of previous simulations for the cases of field and temperature dependent conductivity did not include the mechanisms of heterocharge or homocharge accumulation close to the electrodes. This is a common observation by researchers in the field when attempting to explain space charge observations [118]. To be able to simulate the mechanisms of homocharge and heterocharge accumulation the electrothermal charge transport model will be modified. This is achieved following [58] in modifying equation 4.6 for $\sigma(E, T)$ to include a conductivity modification factor in the expression for field and temperature dependent electrical conductivity, $\sigma(E, T, x)$ as given by equation 4.9. In this case, the electrical conductivity is both field, temperature and distance dependent. If temperature effects are excluded, and the insulation assumed to be at an isothermal temperature, the expression for electrical conductivity can be stated as:

$$\sigma(E, x) = \sigma_0 \left(\frac{E}{E_0} \right)^\gamma (1 + (n_a - 1) \cdot e^{\frac{x_{min} - x_i}{d_a}}) (1 + (1 - n_b) \cdot e^{\frac{x_i - x_{max}}{d_b}}) \quad (4.27)$$

To show the effect of conductivity modification on space charge accumulation, three different case studies were examined and compared with the case of non-modified conductivity, which are:

- Homo-charge accumulation on one side.
- Homo-charge accumulation on both sides.
- Hetero-charge accumulation on both sides.

In each case, the thickness of the sample was assumed to be $140 \mu m$, a 5kV voltage was applied at the inner electrode at position $X = x_{min} = 0$ and a voltage of 0V was applied

at the outer electrode at position $X = x_{max} = 140\mu m$. The enhancement factor $n_{a,b}$ was set equal to 10 for simulating homo-charge accumulation, while the reduction factor was set to $n_{a,b} = \frac{1}{10}$ to model hetero-charge accumulation, at inner and/or outer interfaces. The space charge depths, d_a and d_b , were assumed the same and were set equal to $20\mu m$. The model parameters are shown in table 4.3.

Table 4.3: Model parameters for field dependent conductivity.

Constants	Symbols	Values
Applied voltage	V	5000V
Conductivity constant	σ_0	$2.26*10^{-13}$ S/m
Relative permittivity	ϵ_r	2.3
Vacuum permittivity	ϵ_0	$8.854*10^{-12}$ F/m
Electric field reference	E_0	10kV/mm
Field power index	γ	1.8
Maximum time	T_{max}	10second

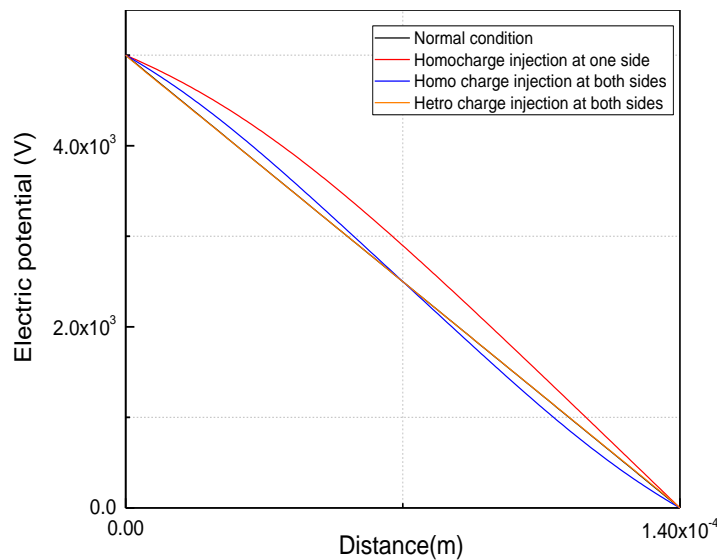
The results of simulation for the three different cases as well as the case for the unmodified electrical conductivity are shown in figure 4.11. These demonstrate the effect of conductivity modification on electric potential, electric field, space charge and conductivity distribution respectively. When the conductivity was not modified, $n_{a,b} = 1$ (the normal condition), the same results were obtained as for the field dependent conductivity (see figure 4.6). Hence, in normal condition the electric field and the conductivity was distributed uniformly and no space charge was accumulated inside the sample.

Considering the first case, enhancing the conductivity at the inner interface by setting the magnification factor $n_a = 10$ and keeping $n_b = 1$ led to an accumulation of space charge adjacent to the inner electrode having the same polarity as the adjacent electrode, which is named homocharge as shown in figure 4.11(c). The accumulation of homocharge leads to a reduction in the electric field in the place where the electrical conductivity was enhanced as shown in figure 4.11(b). The space charge accumulation at the other side of insulation where the conductivity was not enhanced was still zero.

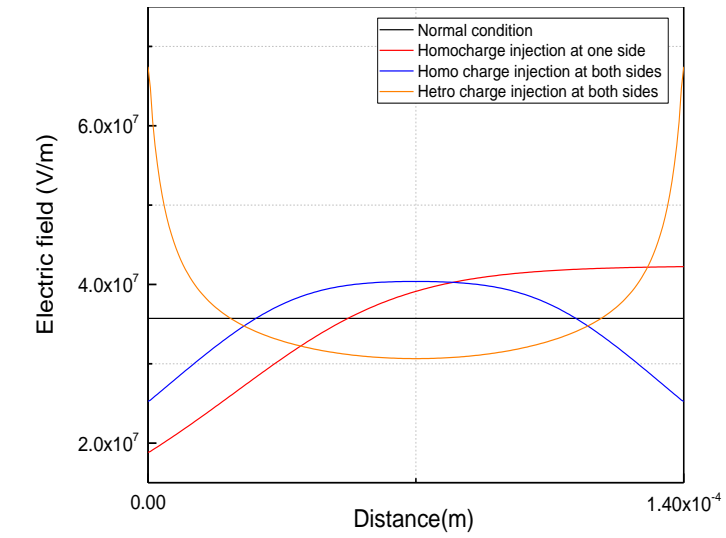
However, the electric field increased due to the presence of the homocharge at the inner electrode.

In case of homocharge accumulation at both sides of the sample, case 2, where the enhancement factors $n_{a,b} = 10$ were used, the enhanced conductivity in the insulation near to the two surfaces led to homocharge accumulation adjacent to both surfaces as shown in figure 4.11(c). The resultant homocharge accumulation led to reduced electric fields in the insulation close to the electrodes and an increase in the electric field within the center of the sample as shown in figure 4.11(b).

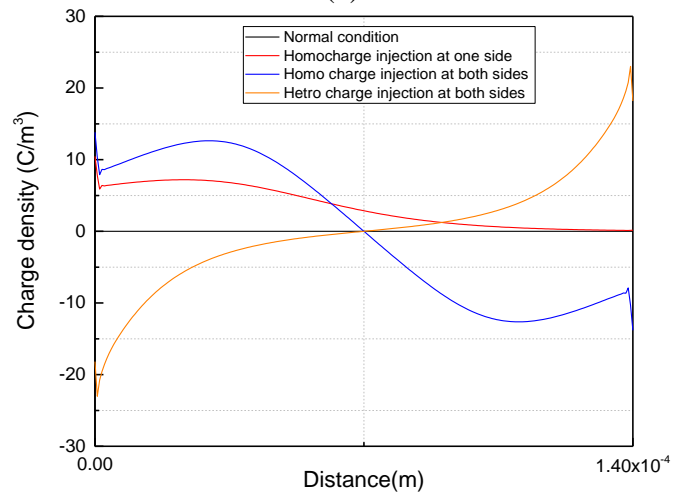
On the other hand, a reduction of conductivity at the inner and outer interfaces $n_{a,b} = 0.1$ caused the accumulation of charge having the opposite polarity as the electrodes and is called hetero-charge as shown in figure 4.11(c). The formation of heterocharge is shown to enhance the electric field in the insulation close to the interfaces and reduce it within the central region as shown in figure 4.11(b). The effect of heterocharge accumulation is in agreement with other work [119, 120]. The electrical conductivity distributions that give rise to the accumulation of homocharge and heterocharge are shown in figure 4.11(d).



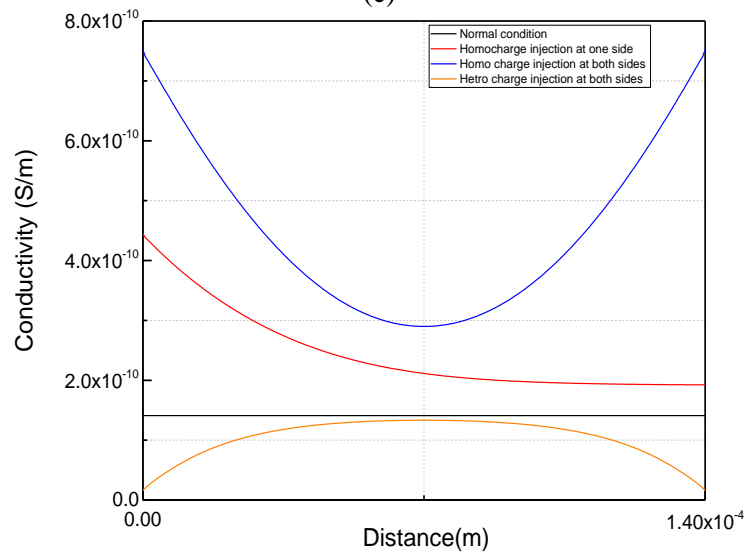
(a)



(b)



(c)



(d)

Figure 4.11: (a) electric potential, (b) electric field, (c) charge density, (d) Conductivity distribution in a thin film sample due to the homocharge and/or heterocharge injection from electrode (s).

4.4.2 Two layer thin film samples

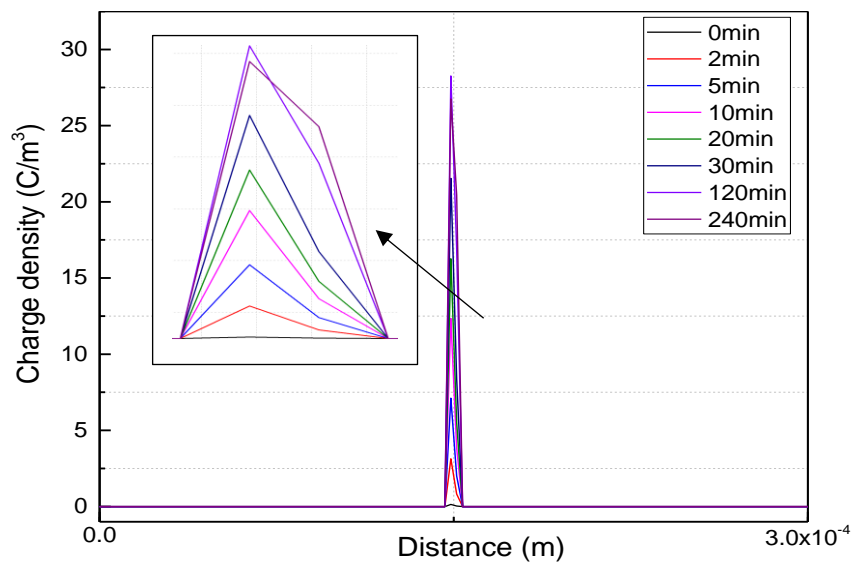
As mentioned in section 3.2.3, the combination of insulation material is often used in high voltage insulation system to control the internal electric field distribution, such as in cable joints and terminations [82]. In the case of two non-identical materials, the space charge accumulates at the interface between the two dielectrics, if the permittivity and/or conductivity gradient is present. In order to accumulate the space charge at the interface between two layers of the thin film samples the permittivity and/or conductivity of the samples should therefore be different. Experimentally, interfacial charge between two layers of LDPE samples was obtained when the conductivity of the samples were not the same (see section 3.3.3). Here, the charge transport model is extended to be able to determine the space charge accumulation at the interface between two layer thin film samples with the properties of LDPE and it is assumed each layer have different conductivity. It is also assumed that the permittivity of both dielectrics are equal, $\epsilon_1 = \epsilon_2$, and the thickness of each dielectric is $150\mu\text{m}$. The external voltage was applied on the insulation at $x=0$ and grounded at the end ($x= d$) as shown before in figure 4.3. As mentioned in section (4.3.1) the spatial intervals between the nodes of both LDPE samples were assumed equal, $\Delta x_1 = \Delta x_2$. The effect of impurity leading to the formation of hetero and homo charge regions are neglected. The model parameters are shown in table 4.4.

Table 4.4: Double layer model constants in case of field dependent conductivity.

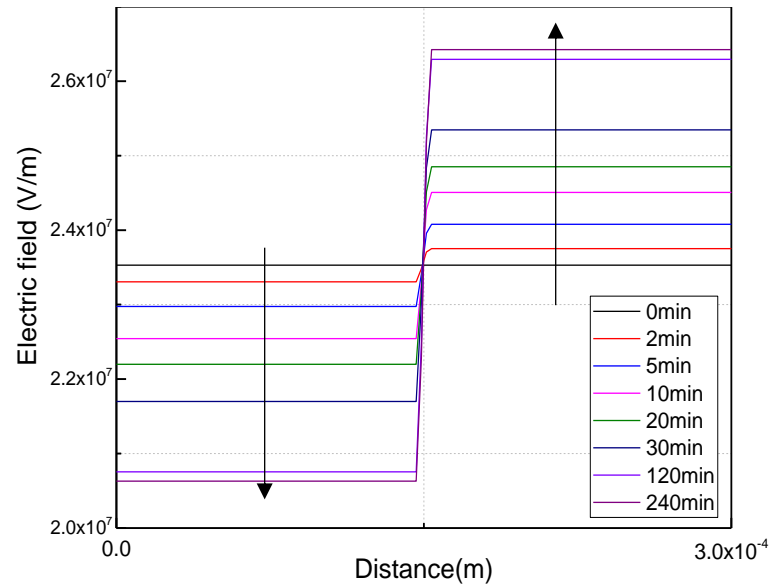
Constants	Symbols	Values
Applied voltage	V	7kV
Conductivity constant of layer 1	σ_{01}	$2 \times 10^{-17} \text{S/m}$
Conductivity constant of layer 2	σ_{02}	$1 \times 10^{-17} \text{S/m}$
Relative permittivity of layer 1 and layer 2	ϵ_r	2.3
Vacuum permittivity	ϵ_0	$8.854 \times 10^{-12} \text{F/m}$
Electric field reference of layer 1 and layer 2	E_0	10kV/mm
Field power index at layer 1 and layer 2	γ	1.8
Maximum time	T_{max}	14400s

The reference conductivity, σ_{o1} , of the first sample (the one that attached with the high voltage electrode) was set on 2×10^{-17} , whereas the reference conductivity of the second sample σ_{o2} (the one that attached with ground electrode) was set on 1×10^{-17} . A 7kV DC voltage was applied on the high voltage electrode and the electrical conductivity was considered to be just field dependent and temperature effects ignored. The procedure of calculation of the space charge and electric field distribution is the same as the case of one layer thin film sample and it follows the flowchart diagram shown in figure 4.4.

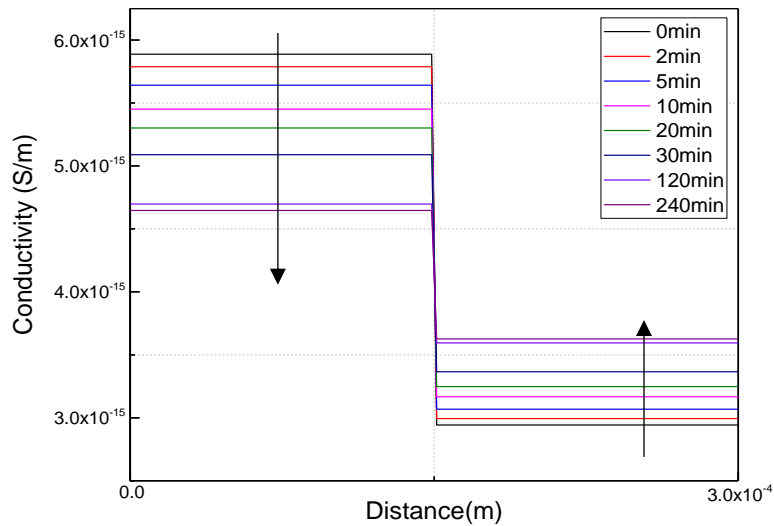
At the initial time (when the time=0), the electric field distribution was uniform across both insulation samples. However, with passing the time, due to the conductivity difference of the layers and due to the effect of field dependent conductivity, space charge was build up at the interface between the two layers and the electric field distribution changed to a non-uniform state as shown in figure 4.12. With passing the time, the electric field in the high conductivity layer decreased, whereas the electric field in lower conductivity layer increased. At the same time the difference between the conductivity of the samples decreased owing to the field dependence of electrical conductivity. Steady state was achieved when the gradient of current density at the interface became zero. Due to neglecting the mechanism of heterocharge and homocharge accumulation at the electrodes the electric field was distributed uniformly in the bulk of the two layers.



(a)



(b)



(c)

Figure 4.12: (a) Space charge, (b) Electric field, (c) conductivity distribution in two layer thin film insulation when they have different conductivity.

4.5 Extension of the charge transport model in single layer from 1-D to 2-D

The results of the 1-D charge transport model have shown that in order to accumulate the space charge within a thin film sample it is necessary to have a non-uniform electric conductivity distribution. This was shown for the cases where either a temperature distribution was introduced or the electrical conductivity was artificially modified due to the presence of diffused impurities or by using layered samples of different conductivity. Another way in which charge can accumulate even under isothermal temperature conditions is to introduce electric field non-uniformity by including conducting defects.

In order to simulate the accumulation of space charge in thin film samples containing defects, the 1-D simulation model was extended for the calculation of space charge accumulation in a two dimensional (2-D) flat plane geometry in order to define an electrically conducting defect. In case of 2-D simulations, field and temperature dependent conductivity are included as described in the following subsections:

4.5.1 Simulation of space charge accumulation in 2-D thin film sample when the conductivity is just field dependent, $\sigma(E)$

In this initial simulation case, the temperature dependence of electrical conductivity is ignored, and therefore the conductivity is assumed only field dependent. The mechanisms of homocharge and heterocharge formation at the electrodes were also ignored in this simulation. The dimensions of the 2-D finite difference domain was 1 mm along the X and Y axis to satisfy a two-dimensional square (2-D) geometry and these were divided into 30 nodes along each direction to produce a 30x30 mesh. The distance between two nodes along both X and Y axis was set equal ($\nabla x = \nabla y$).

A conducting defect was modelled by equalizing the electric potential of the nodes comprising the defect. When placed in the insulator and not in contact with the electrodes, the electric potential of the defect is floating and determined by the average of all the electric potentials at adjoining nodes. The electrical conductivity of the defect nodes was assumed equal to $1 \cdot 10^{-8}$ S/m; which was much higher than the electrical conductivity of the surrounding nodes of the dielectric sample. Moreover, as the defect is electrically conducting, the space charge on the defect nodes was assumed zero. Therefore, the space charge accumulations at the defected nodes were equal to zero. The procedure of calculation the space charge accumulation due to the field dependent conductivity in 2-D is the same as 1-D that mentioned in figure 4.4. Initially at $t = 0$, space charge (ρ) = 0, and in this case, Poisson's equation (4.16) becomes Laplace equation (4.14). In order to simplify the simulation model outputs, 2-D graphs were obtained of the electric potential, V , electric field, E , and space charge density, ρ , along the axis of the defect as defined in figure 4.13.

First, the space charge was calculated under positive polarity of applied voltage. The value of equations constants and material properties which were used in the model are shown in table 4.5.

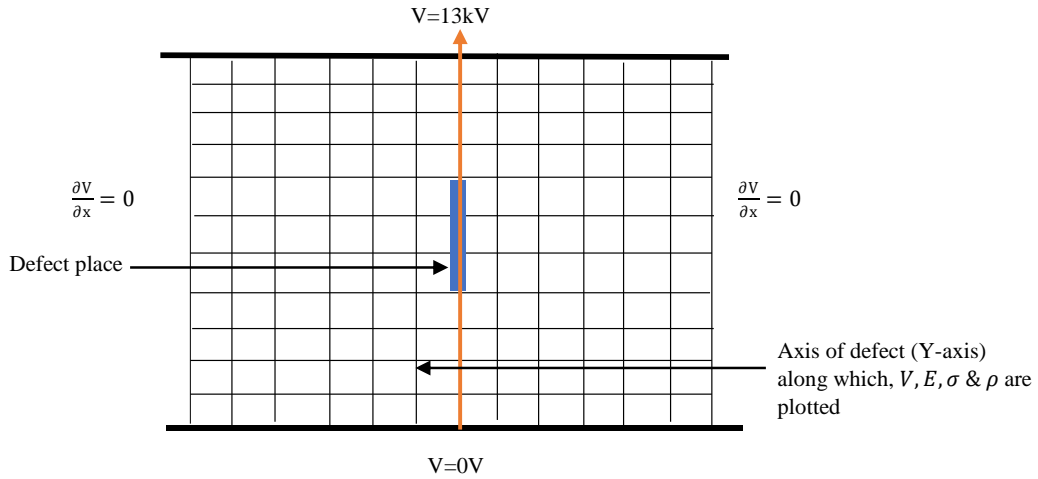


Figure 4.13: Schematic representation of 2D thin film sample used for the simulation.

Table 4.5: 2-D Model constants in case of field dependent conductivity.

Constants	Symbols	Values
Applied voltage	V	13kV
Conductivity constant	σ_0	$1 \cdot 10^{-13}$ S/m
Relative permittivity	ϵ_r	2.3
Vacuum permittivity	ϵ_0	$8.854 \cdot 10^{-12}$ F/m
Electric field reference	E_0	1kV/mm
Field power index	γ	1.8
Maximum time	T_{max}	100s

The simulation results are shown in figure 4.14 for space charge accumulation surrounding the central line conducting defect of 4 nodes after the application of the 13kV applied voltage. The results presented in figure 4.14 also showed the case when no defect was present inside the sample for comparison. In the defect free case, no space charge accumulated in the dielectric as a consequence of the uniform electric field. The defect free case matches the results obtained from the 1-D model that was described in section 4.4.1.1 (field dependent conductivity). Therefore, in case of no defects, the electric field is equal to Laplacian field and equal to the applied voltage divided by the sample thickness 1.3×10^7 V/m. However, when the line shape defect with length 0.133mm was introduced at the middle of the sample as shown in figure 4.14, the simulations demonstrated that after 0.1second, the amount of space charge accumulated adjacent to the defect was about 1C/m^3 which was the consequence of the enhanced electric field

surrounding the defect to a peak value of 1.95×10^7 V/m. The accumulation of space charge was found to increase with time until a steady state was obtained after approximately 10 seconds. The formation of a steady space charge had the effect of reducing the electric field enhancement from its peak value from 1.95×10^7 V/m to 1.77×10^7 V/m which was located adjacent to the defect. The formation of this space charge also slightly increased the electric field adjacent to the electrodes from the Laplace value 1.3×10^7 V/m to 1.34×10^7 V/m. The accumulated space charge can therefore be seen as equivalent to homocharge accumulation at the defect/dielectric boundary. This effect was much higher for the nodes along the axis of the defect.

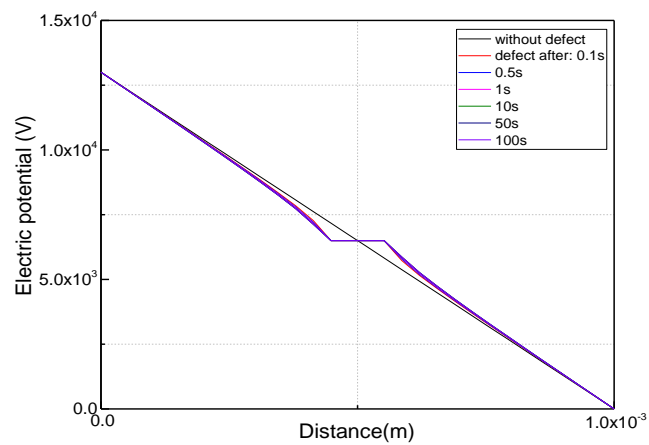
In order to show the dynamics of space charge density during polarity reversal, the boundary condition of the top electrode was first set to 13kV and simulation performed until steady state was achieved as in the case above. Directly following this, the top electrode boundary condition was set to -13kV and the simulation allowed to continue from its previous state until a new steady state was achieved.

The simulation results of polarity reversal condition are shown in figure 4.15. Immediately after the polarity of the applied voltage was reversed, the peak electric field along the axis of the defect was of opposite polarity and had a peak value located at the defect interface and having a magnitude of 2.1×10^7 V/m which was much higher than the peak steady state electric field under positive polarity (1.77×10^7 V/m), this was due to the presence of the steady state charge distributed around the defect from the previous polarity. However, the peak electric field magnitude quickly decreased as the remaining space charge was neutralised and a new steady state homocharge distribution (of opposite polarity) was established. The magnitude of the steady state peak electric field was the same as for the initial polarity (1.77×10^7 V/m).

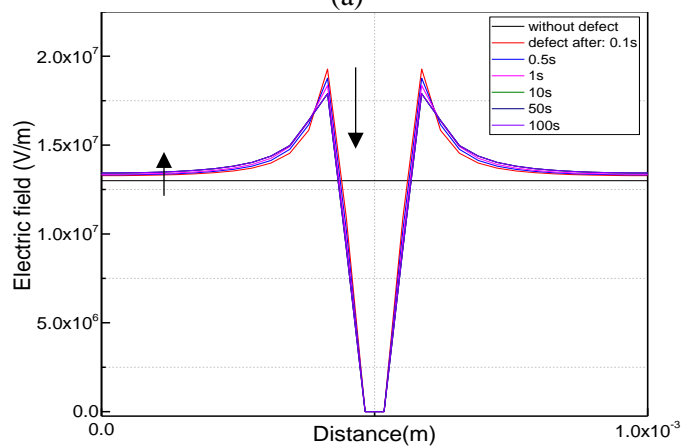
In both positive and negative applied voltage, the steady state was obtained after 10s, and the same amount and shape of space charge was accumulated but with opposite polarities. This phenomenon has been reported as a “mirror image effect” in [121, 122].

Finally, the high voltage electrode boundary condition was set to zero and the simulation allowed to run from the current state to replicate a voltage off experiment. The simulation results are shown in figure 4.16. On removal of the applied voltage, space charge decreased with time. It was found that the time required for the decay of space charge was much longer than that required for accumulating space charge under an applied

voltage. The time required for space charge accumulation to reach a steady state was just 10seconds on voltage application. However, the space charge decay was simulated for 50 seconds which is five times longer than the polarization time, but there is still a significant amount of space charge inside the sample which was about $2C/m^3$. This observation agrees with the results of space charge measurement under voltage-off condition that was discussed in chapter 3 where the time taken for charge to decay is much longer than the time for the space charge to establish a steady state owing to the field dependence of electrical conductivity. Moreover, the charge decay rate was initially fast in the first few seconds close to the defect and then became slower and slower. This is again due to the consequence that the electric field is much lower when the applied voltage was set to zero and hence the electric field dependent electrical conductivity of the dielectric was reduced in accordance with equation (4.25). An alternative explanation for this type of phenomena that is often presented in the literature is that de-trapping the shallow traps at the beginning accounts for the faster decay and that the charge trapped in deep traps take a much longer time in order to de-trap [36]. Here, this effect is explained as due only to the field dependent conductivity.



(a)



(b)

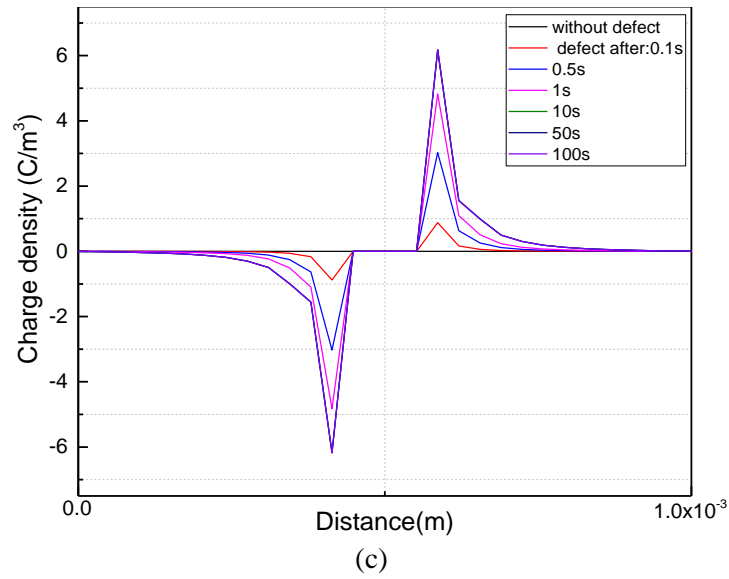


Figure 4.14: (a) Potential, (b) Charge density, (c) Electric field distribution profiles as a function of position first without defect, second with defect at the middle of the sample for different instants of time.

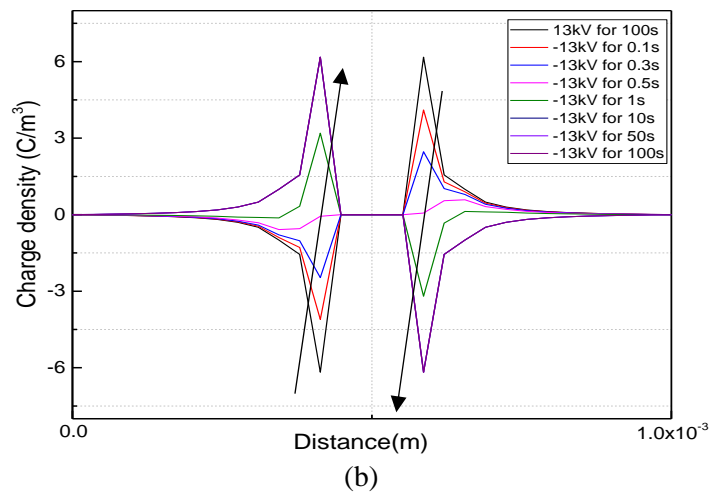
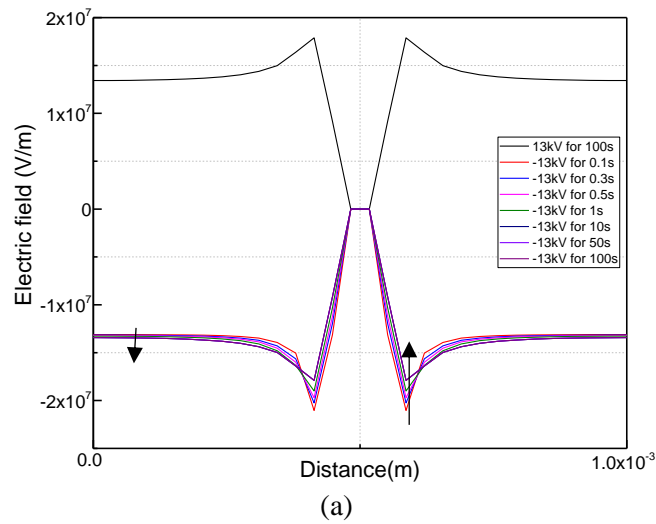
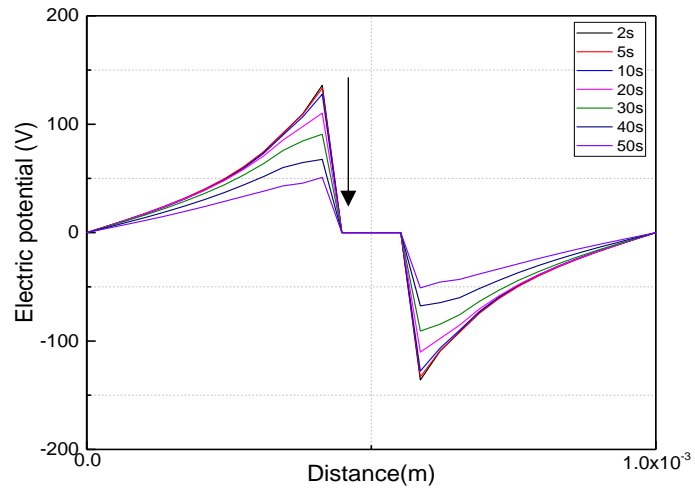
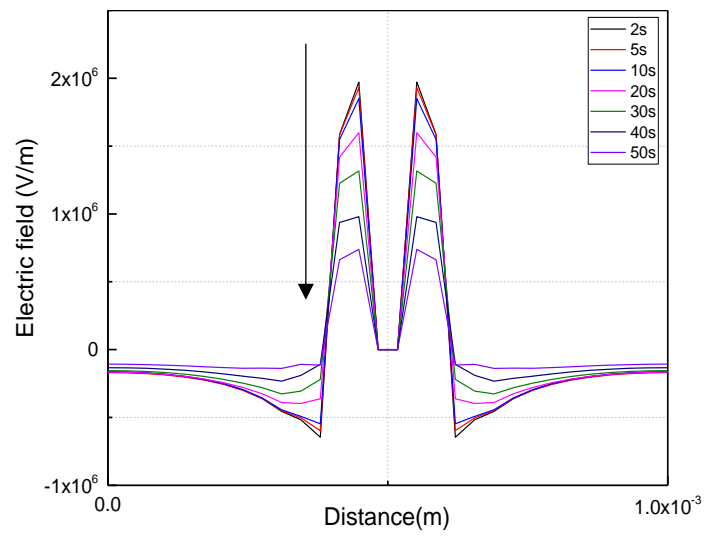


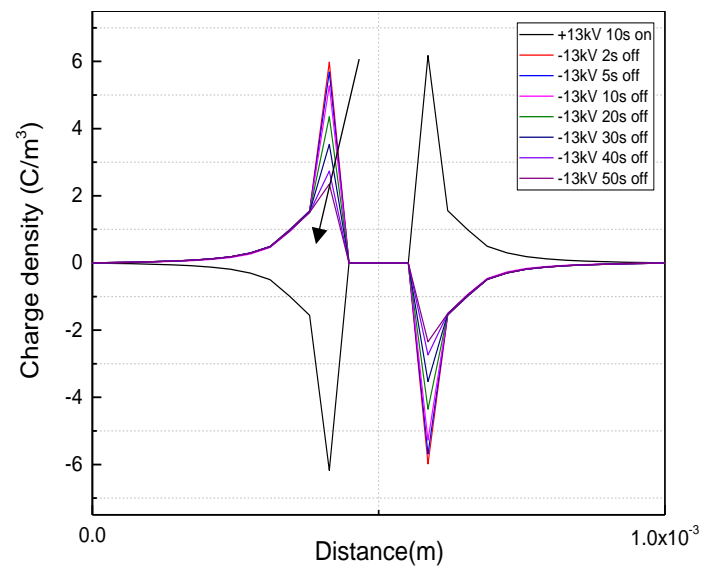
Figure 4.15: (a) Charge density, (b) Electric field distribution at different times when defect located at the middle of the sample is under polarity reversal.



(a)



(b)



(c)

Figure 4.16: (a) Electric potential, (b) Space charge, (c) Electric field distribution under polarity reversal and depolarization with defect located at the middle of the sample.

4.5.2 Simulation of space charge accumulation in 2-D thin film sample when the conductivity is field and temperature dependent

In practice, defects in the insulation will lead to electric field enhancement and inhomogeneous current density and this will give rise to local temperature gradients due to local Joule heating losses. Therefore, in this case after initializing the conducting defect, the field and temperature dependent conductivity are considered at the same time. As in the previous case, the dimensions of the 2-D domain was assumed 1 mm along the X and Y axis to satisfy a two dimensional (2D) geometry and these were divided into 35 nodes along each direction to get a 35x35 mesh. Again the distance between two nodes along both X and Y axis was equal ($\Delta x = \Delta y$).

The boundary conditions was set according to section 4.3.2. The electric potential and temperature at each internal node was then determined by solving the FDM formula of Poisson's equation, (4.16), and the heat conduction equation, (4.21). In this case the only source of heat was considered was Joule heating ($\sigma(x, y)E^2(x, y)$). Therefore, the top and bottom boundaries were set to a fixed temperature, 293 K, and equation 4.21 becomes in 2-D:

$$T_{new(x,y)} = T_{(x,y)} + \frac{k\Delta t}{\rho_m c_p \Delta x^2} (T_{(x+\Delta x,y)} + T_{(x-\Delta x,y)} + T_{(x,y+\Delta y)} + T_{(x,y-\Delta y)} - 4T_{(x,y)}) + \frac{\Delta t \sigma_{(x,y)} E^2_{(x,y)}}{\rho_m c_p} \quad (4.28)$$

The same as the case of field dependent conductivity, an electrically conducting defect was modelled by equalizing the potential of the nodes comprising the defect. When placed in the insulator and not in contact with the electrodes, the electric potential and temperature of the defect was floating and its electric potential was determined by the average value of the adjoining nodes. The electrical conductivity of the defect nodes was assumed to be equal to $1 \cdot 10^{-8}$ S/m; which was much higher than the electrical conductivity of the surrounding nodes of the dielectric sample. Again, the space charge on the defect nodes was assumed zero as the defect was assumed to be electrically conducting. The temperature of the nodes at the conducting defect were set to be equal in order to model a thermally conductive defect.

The procedure of numerical calculation is the same as shown in 1-D and followed the flow chart diagram that shown in figure 4.7. The simulation model calculates the time dependent space charge accumulation due to the electric field and the temperature

gradient originating from the Joule heating losses within the insulation material under different applied voltages. The value of the model parameters and material properties which were used in the model are shown in table 4.6.

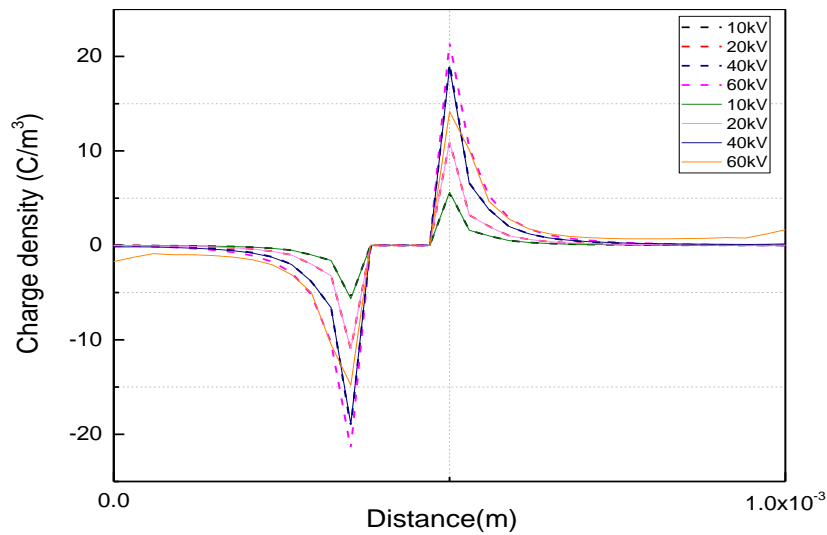
Again, in order to simplify the simulation model outputs, 2-D graphs were obtained of the electric potential, V, electric field, E, space charge density, ρ , and temperature, T, along the axis of the defect. However, in this case the defect is not exactly contained at the middle of the sample. But displaced to node 15 along the y-axis.

Table 4.6: 2-D Model constants in case of field and temperature dependent conductivity.

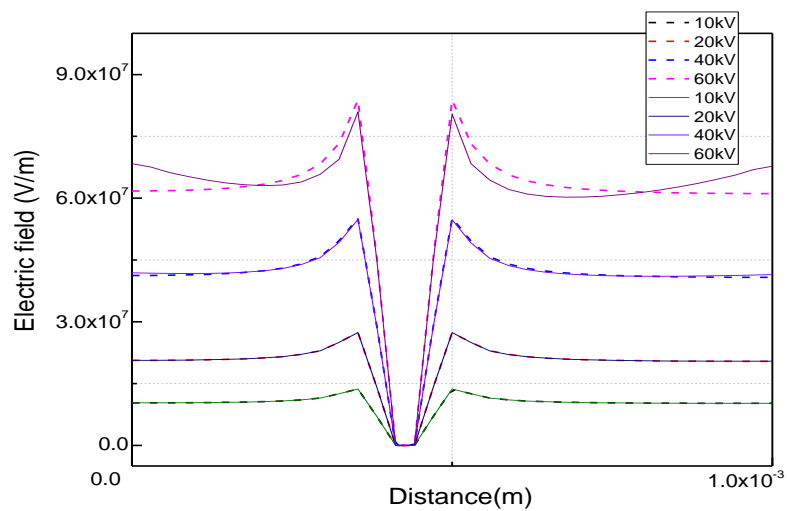
Constants	Symbols	Values
Applied voltage	V	10kV to 60kV
Conductivity constant	σ_0	$1*10^{-13}$ S/m
Relative permittivity	ϵ_r	2.3
Vacuum permittivity	ϵ_0	$8.854*10^{-12}$ F/m
Electric field reference	E_0	1kV/mm
Electric field coefficient	γ	1.8
Temperature coefficient	α	0.1
Temperature reference	T_0	293 K
Thermal conductivity	k	0.329 W /m K
Specific heat of material	c_p	1250 J kg/K
Density of material	ρ_m	920 kg/m ³

Figure 4.17, shows the results when electrical and thermal effects are considered in the simulations, *i. e.* $\frac{\partial T}{\partial t} \neq 0$. Here simulation results are shown for different applied voltages (from 10kV/mm to 60kV/mm) and with fixed temperatures of 293K at the top and bottom electrodes. The results show that when the temperature dependent conductivity was also considered in the simulations by including Joule heating of the insulation material, the temperature was no longer isothermal. The rate of temperature rise depends on heat generation due to the Joule heating, and heat dissipation due to thermal conduction to the surroundings [65]. As demonstrated in equation 4.28, the heat generation under DC voltage is equal to the conductivity times square of electric field (σE^2) [65, 116].

Therefore, as shown in figure 4.17(a) under low applied field $<40\text{kV/mm}$, dielectric heating was small and did not have a significant effect on the accumulated space charge in comparison with the case of only field dependent conductivity (see figure 4.17(b)). However, increasing the applied voltage above 40kV/mm led to a significant increase in the local Joule heating surrounding the defect and resulted in a reduction of the accumulated space charge. On the other hand, increasing the Joule heating led to reduction of the electric field around the defect and enhancement of it adjacent to both top and bottom electrodes, which might cause premature breakdown initiating from defects at the insulation-semiconducting interfaces.



(a)



(b)

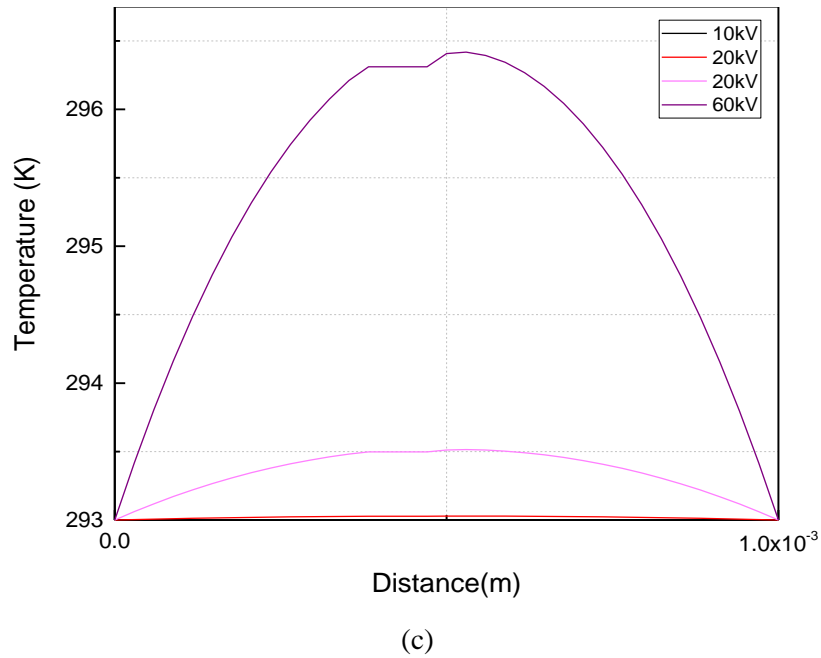


Figure 4.17: (a) Space charge, (b) Electric field, (c) Temperature distribution around the defect at different applied voltages. The dotted lines represent the results of field dependent conductivity, whereas the solid lines represent the results of field and temperature dependent conductivity.

4.6 Summary

In this chapter an electro-thermal model of charge transport inside the solid thin film sample has been developed. The model has been applied on single layer and double layer samples at different situations which can be summarized as followings:

- 1- For single layer thin film samples, the model was developed first for 1-D plane geometry. It was found that the electric field was distributed uniformly and no space charge accumulated when the conductivity was field dependent only. However, when the electrical conductivity of the material was non-uniform due to temperature dependent effects or when the electrical conductivity was modified due to the diffusion of impurities, space charge was shown to accumulate.
- 2- In 1-D double layer thin film samples, when the layers had same thickness and the same permittivity but different in conductivity, the space charge accumulated at the interface between the dielectrics even in the case of field dependent conductivity. However, due to neglecting the homocharge/heterocharge injection from the electrodes, no space charge was accumulated adjacent to the electrodes and in the bulk of the samples.

- 3- In the 2-D single layer thin film simulations, the model with field/temperature dependent electrical conductivity has been used to perform simulations for local Joule heating and of space charge accumulation in a 2-D domain. The results showed that when the conductivity was made just a field dependent, a significant amount of space charge accumulated around the defect. This had the effect of decreasing the electric field enhancement surrounding the defect that would have occurred in the absence of space charge. When the temperature dependent conductivity was also considered in the simulations, then under low applied field $<40\text{kV/mm}$, dielectric heating was small and did not have a significant effect on the accumulated space charge. However, increasing the applied voltage above 40kV/mm led to a significant increase in the local Joule heating surrounding the defect and resulted in a reduction of the accumulated space charge and defect field as well as an increase in field at the electrodes.

5 Simulation of the PEA Space Charge Measurement System

5.1 Overview

As mentioned in chapter 3, one of the current difficulties of the traditional method of space charge reconstruction from the raw PEA data is in determining the coefficients of attenuation and dispersion of the acoustic signal as the pressure waves propagate through the sample [23]. Although attenuation and dispersion coefficients can be described by a set of inverse transfer functions to reconstruct the signal, realizing the value of the inverse transfer function coefficients from the raw PEA data is problematic. To succeed, the raw PEA output measurements must be required with zero bulk space charge and this may be difficult to achieve in practise as space charge may accumulate even under low applied fields. The procedure normally used employs deconvolution techniques [96] to extract the coefficients and the application of this technique may result in oscillations and instability in the recovered signal. The mathematical instability of this technique can lead to the possibility of false detail being interpreted as space charge accumulation. In order to avoid these issues, in this study, an alternative approach is taken where the simulation model for charge transport as described previously in chapter 4 is used together with a simulation model of a PEA instrument to generate simulated raw PEA output data in thin film samples that can be directly compared to experimental raw PEA data. In this way, PEA data can be interpreted in terms of an electro-thermal model for charge accumulation as described in chapter 4, without the need to apply numerically unstable signal processing techniques in order to recover the space charge profile. This chapter therefore deals with the description of the additional simulation model techniques required for acoustic wave formation, propagation and detection within the PEA system.

In this chapter the electro-acoustic theory related to the operation of the PEA apparatus will be introduced. The basic theory will allow the development of a simulation model of 1D acoustic wave generation (based on the output from the electro-thermal transport model of chapter 4) and their propagation and detection within the PEA apparatus. The simulation model will also include factors such as the voltage pulse duration which limits spatial resolution, the propagation, acoustic reflections at interfaces of different acoustic properties, attenuation and dispersion of the acoustic waves in a lossy dispersive medium as well as propagation in a medium at a given temperature and when a temperature gradient is imposed across the sample. The detection of the acoustic waves using a thin

film of piezo-electric (PVDF) material is also included along with the effect of the HP filter response of the PVDF sensor capacitance and the 50 Ω input resistance of the buffer amplifier. The limited bandwidth 500MHz of the storage oscilloscope will also be taken into account. Initial simulations in case of charge free samples will be conducted in order to demonstrate the common imperfections of the PEA instrument including the effect of voltage pulse width, acoustic reflections at the PVDF sensor and at the sample/semicon top electrode due to acoustic impedance differences between the materials. The effect of a temperature gradient within the sample on the PEA acoustic wave propagation will also be simulated.

5.2 Forces on space charge in solid dielectrics

As described in chapter 2, the basic principle behind the PEA method is the Coulomb force, in which, an external applied electric field induces a mechanical force on electric charges in the material. The transient increment of applied field by applying a pulse voltage of short duration will lead to the production of longitudinal acoustic (pressure) waves from space charge. The pressure waves propagate through the insulation material and in to the aluminium base plate of the PEA apparatus where they are detected and transformed into an electrical signal by a piezoelectric transducer which is mounted on the opposite surface of the aluminium ground electrode.

The general equation that describes the different sources of force density (force per unit volume) in a dielectric material is given by equation 5.1 [68].

$$\vec{f} = \rho \cdot \vec{E} - \frac{\epsilon_0}{2} \cdot E^2 \cdot \nabla \epsilon_r - \frac{\epsilon_0}{2} \cdot \nabla (E^2 \cdot \alpha) \quad (5.1)$$

There are three contributions to the force density, \vec{f} . The first is due to the Coulombic interaction of charge density, ρ , with the electric field, E , as described above. The second term on the right hand side of equation 5.1 represents the force density due to a spatially varying relative permittivity. In most uniform parallel electrode PEA configurations this contribution is zero provided the sample is homogeneous. However the second term may become important and lead to the formation of acoustic waves if for example the sample is made of a sandwich of two different materials of different relative permittivity, ϵ_r , or if the material has a spatially varying permittivity owing to a temperature gradient applied across it. The third term on the right hand side of equation 5.1 contains the gradient of the product of the electric field squared and the electrostriction coefficient, α . The

electrostriction coefficient represents the degree of deformation on the material on application of the electric field.

5.3 Origin of the acoustic pressure waves

In the case of plane-plane thin film PEA system, the electrostriction term is often neglected and only the first two terms of equation 5.1 are considered to be significant in contributing to the force density [67]. The total force density vector can therefore be written as:

$$\vec{f} = \rho \cdot \vec{E} - \frac{1}{2} \cdot E^2 \cdot \nabla \epsilon \quad (5.2)$$

The calculation of force density can be simplified, if the force density is expressed as the divergence of Maxwell's tensor, M_{ij} . The main advantage of this method of calculation is that the force vector can be written in terms of the vector electric field without requiring the calculation of the interfacial surface charge densities at each of the two PEA electrodes [68]. Therefore, by using Poisson's equation to eliminate charge density (ρ), in equation 5.2, and taking into account that the electric field is determined from the gradient of a scalar potential field, the force density vector can be written as the following equation [69]:

$$\vec{f}_i = \frac{\partial M_{ij}}{\partial x_j} = \frac{\partial(\epsilon E_i E_j)}{\partial x_j} - \frac{1}{2} \frac{\partial(\epsilon E^2 \delta_{ij})}{\partial x_j} \quad (5.3)$$

Where the subscripts, i and j , refer to the individual components of the 3-D vector and δ_{ij} is the Kronecker's delta function, $\delta_{ij} = 1$ when $i = j$, zero otherwise. [23]. The detail of changing the equations of force density equation to Maxwell's tensor equation is shown in appendix E.

The Maxwell tensor can therefore be identified as:

$$M_{ij} = \epsilon E_i E_j - \frac{1}{2} \epsilon E^2 \delta_{ij} \quad (5.4)$$

The application of a pulsed field, ΔE , results in a transient term in Maxwell's tensor as:

$$M_{ij} + \Delta M_{ij} = \epsilon(E_i + \Delta E_i)(E_j + \Delta E_j) - \frac{1}{2} \epsilon(E + \Delta E)^2 \delta_{ij} \quad (5.5)$$

And after subtracting M_{ij} , the transient can be represented as:

$$\Delta M_{ij} = \epsilon(E_i \Delta E_j + E_j \Delta E_i + \Delta E_i \Delta E_j) - \frac{1}{2} \epsilon \Delta E^2 \delta_{ij} - \epsilon E_k \Delta E_k \delta_{ij} \quad (5.6)$$

Where the subscript, k , is an auxiliary index such that $E^2 = E_k E_k$. For the one dimensional case, $i = j = k = 1$, the Maxwell's tensor becomes a scalar which can be written as [23]:

$$\Delta M = \varepsilon E \Delta E + \frac{1}{2} \varepsilon \Delta E^2 \quad (5.7)$$

ΔM has units of force per metre², and can therefore be interpreted as a source of pressure in the dielectric during a transient change in the applied electric field, ΔE . This expression does not contain the space charge density distribution, $\rho(x)$, explicitly but space charge is implicit from the non-uniformity in the electric field distribution, $E(x)$, within the sample that the space charge produces.

In this study the time dependent pulsed applied voltage of unit magnitude, $V_p(t)$, that produces the field increment, ΔE , in the sample is assumed to have a Gaussian wave shape and is given by

$$V_p(t) = e^{-\frac{4 \ln(2) \cdot (t-t_p)^2}{t_w^2}} \quad (5.8)$$

Where t_p is a pulse delay time and t_w is the pulse width at the half peak height. The reason of using the Gaussian shape is because it is widely recognised in the literature that the electrode charge peaks of the PEA system have the shape of a Gaussian pulse. In most of the literature discussing the output response of the PEA measurement system, the shape of the pulse voltage has been represented by the Gaussian shape [75, 78, 97].

Figure 5.1 is an example of Gaussian pulse of width 25 nS with magnitude of one and pulse delay time of 100 nS.

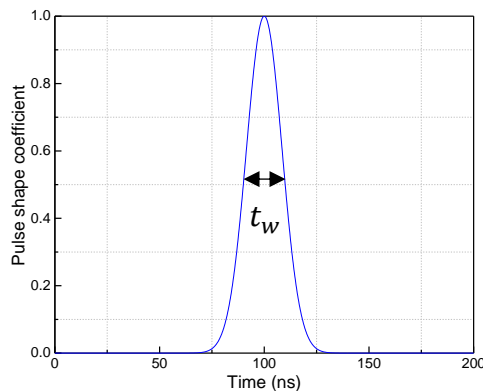


Figure 5.1: The shape of Gaussian voltage pulse with a width of 25ns and a pulse delay of 100nS.

The time dependent pulse electric field ($\Delta E(x, t)$) applied to the sample can be written as

$$\Delta E(x, t) = E_p \cdot V_p(t) \quad (5.9)$$

Where, E_p is the magnitude of the Laplacian pulsed field distribution in the sample and it assumes that the pulsed field is of sufficiently short duration so as not to modify the space charge that exists in the insulation [123]. Therefore, E_p can be calculated using Laplace equation which for a thin film of 1-D geometry, E_p is a constant independent of x and given by $\frac{V_p}{d}$ where V_p is the peak magnitude of the pulsed voltage, and d is the sample thickness. After substitution of equation 5.9 into equation 5.7, the 1D transient Maxwell scalar becomes:

$$\Delta M(x, t) = \varepsilon E(x, t) E_p V_p(t) + \frac{1}{2} \varepsilon \Delta E_p^2 V_p(t)^2 \quad (5.10)$$

$E(x, t)$ is the DC electric field distribution inside the sample as calculated from the electro-thermal charge transport model of chapter 4, at a given time step, t , or alternatively if no space charge is assumed present, the electric field is uniform and independent of time and given by $\frac{V_{DC}}{d}$, where V_{DC} is the DC voltage applied across the sample and d is the sample thickness.

5.4 Propagation of pressure wave in plane-plane geometry

Once, a source transient pressure occurs within the sample due to the application of a pulse voltage, the transient pressure will propagate as a longitudinal wave through the sample and into the aluminium base plate of the PEA system. The governing equations for longitudinal wave propagation in isotropic lossless media for 1D Cartesian geometry are:

$$\frac{\partial P}{\partial t} = -C \frac{\partial v}{\partial x} + \frac{\partial M}{\partial t} \quad (5.11)$$

$$\frac{\partial v}{\partial t} = -\frac{1}{\rho} \frac{\partial P}{\partial x} \quad (5.12)$$

Where, the coordinate, x , corresponds to the distance into the insulating layer. P is the scalar pressure field, v is the vector velocity in the direction x , C represents the effective modulus of the material and ρ the material's mass density. The effective modulus (C) of solid insulations can be represented by equation 5.13[118].

$$C = K + \frac{4}{3}G \quad (5.13)$$

Where K represents the bulk modulus and G is the shear modulus of the material.

Equation (5.11) also includes the pressure source term which is the Maxwell scalar as defined in the previous section. Equations 5.11 and 5.12 are two first order differential equations that together constitute a wave equation with a propagation velocity as given by equation 5.14.

$$c = \sqrt{\frac{\text{Effective modulus}(C)}{\text{density}(\rho)}} \quad (5.14)$$

There are different ways to obtain the speed of sound of the tested material. Experimentally, it can easily be found from the time interval between the pressure waves from the aluminium electrode and the semicon electrode of the PEA instrument and the sample thickness ($c = \text{Thickness}/\text{time}$) [54]. Alternatively, it can be obtained from the measured mechanical properties of the sample material which are density and effective modulus [124] as given by equation 5.14.

As mentioned in chapter 4, during operation and whilst under load, HVDC cable insulation is subject to a temperature gradient due to Joule heating of the cable conductor and heat loss from the outer layers of the cable to the surroundings. In order to assess the impact of a temperature gradient across an insulator on the build-up of space charge, researchers are currently active in performing PEA measurements on thin film samples in which a temperature gradient is induced in the sample by heating the electrodes of the PEA instrument to different temperatures. Chen et al in [76] obtained the temperature gradient across the thin film sample experimentally. They heated the upper Al electrode of PEA by oil circulation and cooled the lower Al electrode by water circulation. However, when interpreting PEA raw data in terms of a space charge distribution they have assumed that the only source term for the production of acoustic waves in the PEA instrument is that due to space charge [125]. Based on equation 5.2 and the above theory on the PEA measurement system suggests that there are other sources of acoustic waves as the result of the varying permittivity. When a material is heated it expands and reduces the material density. This has two effects; the first is that the permittivity of the insulation will no longer be uniform (lower in hot regions) and therefore a source of acoustic waves in accordance with equation (5.2) and secondly, that the acoustic velocity will also be non-uniform across the sample. Whilst researchers usually take into account the second effect in terms of recalibration of the distance from the time measurements [126, 127],

the first effect has not been addressed so far in the literature. Hence in the development of the PEA simulation model, the material parameters of permittivity, density and bulk modulus will need to be made temperature dependent quantities.

The longitudinal sound velocity (c) is usually a function of temperature of the material that the sound wave is traveling through. This is due to the fact that the values of C and ρ for a given material are temperature dependent. In both cases, their value will decrease when the temperature increases [128]. As mentioned in [124], the value of effective modulus of polyethylene (PE) decreases from 3Gpa at 30 °C to 1.5Gpa at 90°C. The density will also decrease as the material will be subject to thermal expansion. In the case of LDPE sample the temperature dependent acoustic velocity is found to be linearly proportional to temperature over the temperature range of 20-70°C [129]. In that range of temperature, the temperature dependence of acoustic velocity can be given by the equation below [76, 129].

$$v_{LDPE} = 2272.5 - 9.5 * T \quad (5.15)$$

Where v_{LDPE} is acoustic velocity in the LDPE material and T is the temperature in °C. Based on equation 5.15, increasing the temperature leads to decrease the acoustic velocity of the pressure waves that propagate across the sample.

To find the density of the sample at different temperature, the linear thermal expansion coefficient of the sample is required, α_L , which is defined as the fractional increase in length per unit rise in temperature. Typical values for LDPE range over values of $10 \times 10^{-5} / ^\circ\text{C}$ to $20 \times 10^{-5} / ^\circ\text{C}$ [130]. For isotropic materials such as an amorphous polymers, the volumetric expansion coefficient is defined as three times that of the linear expansion coefficient [131].

$$\alpha_V \cong 3\alpha_L \quad (5.16)$$

Based on equation (5.16), the value of density at different applied temperature can therefore be expressed by:

$$\rho(T) = \frac{\rho_{20^\circ\text{C}}}{(1 + \alpha_V(T - 20^\circ\text{C}))} \quad (5.17)$$

Where $\rho(T)$ is the density of the dielectric at temperature, T . and $\rho_{20^\circ\text{C}}$ is the mass density of the sample material as measured at 20 °C.

After calculation of the mass density and acoustic velocity at a given temperature T , the effective modulus of the sample material at temperature, T , was then obtained from equation (5.14). Therefore, the effective modulus and density under linear temperature gradient distributed across the sample based on equation (5.18) and (5.19) respectively.

$$C = C_{20^{\circ}\text{C}} + \frac{C_{upper} - C_{20^{\circ}\text{C}}}{d} \cdot x, \quad 0 < x < d \quad (5.18)$$

$$\rho = \rho_{20^{\circ}\text{C}} + \frac{\rho_{upper} - \rho_{20^{\circ}\text{C}}}{d} \cdot x, \quad 0 < x < d \quad (5.19)$$

Where C_{upper} and ρ_{upper} are effective modulus and density of upper side of the sample, d is the thickness of the sample.

The dielectric permittivity of olefinic polymers such as LDPE is close to 2.3 at 20°C and varies with mass density. This is a small temperature dependence and therefore it is usually assumed as a constant [1, 41]. In this simulation model, the temperature dependent permittivity is also accounted for as the permittivity is involved in the expression for the source of pressure waves, equation 5.2. According to [132], in a polyethylene sample the value of permittivity is proportional with the value of density. If we assume, $\varepsilon \propto \rho$:

$$\varepsilon_{20^{\circ}\text{C}} = k \rho_{20^{\circ}\text{C}} \quad (5.20)$$

The value of k was found from the permittivity and density values at 20°C and then it was used to determine the value of permittivity at different temperatures. The same as equations (5.18 and 5.19), under temperature gradient, the permittivity distributed across the dielectric sample based on equation (5.21).

$$\varepsilon = \varepsilon_{20^{\circ}\text{C}} + \frac{\varepsilon_{upper} - \varepsilon_{20^{\circ}\text{C}}}{d} \cdot x, \quad 0 < x < d \quad (5.21)$$

Where ε_{upper} the permittivity of upper side of the sample that was found is based on equation (5.21) at different temperature gradients.

5.4.1 Perfectly-matched layer (PML)

When employing numerical techniques to integrate the equations related to propagation of the pressure waves, it is usual to reduce or bound the spatial extend of the computational domain. One way to achieve this is to use absorbing boundary layers that absorb all pressure waves that propagate into them. Perfectly-Matched-Layer (PML) absorbing boundary conditions are implemented by using a notional material that has a

variable complex acoustic impedance that introduces a region of high attenuation and produces no acoustic reflections for waves traveling into it.

The acoustic wave equations in the PML regions on each boundary of the domain can be expressed as [133]:

$$\rho \frac{\partial v}{\partial t} + C\alpha \rho v = -\frac{\partial p}{\partial x} \quad (5.22)$$

$$\frac{1}{c} \frac{\partial p}{\partial t} + \alpha p = -\frac{\partial v}{\partial x} + \frac{\partial M}{\partial t} \quad (5.23)$$

The wave equation in the remaining lossless parts of the computational domain (the region of interest) have the same form as the equations above but with the attenuation coefficient, α , set to zero and in the insulating material and that the Maxwell source term will also need to be inserted.

5.5 PEA Model Implementation - FDTD equations in MATLAB

The PEA computational domain based on the FDM are divided in to 8 layers corresponding to the separate materials used in the PEA apparatus and the domain bounded by PMLs as shown in figure 5.2. Each layer is discretised to several number of nodes. The distance between the nodes are equal and defined by Δx .

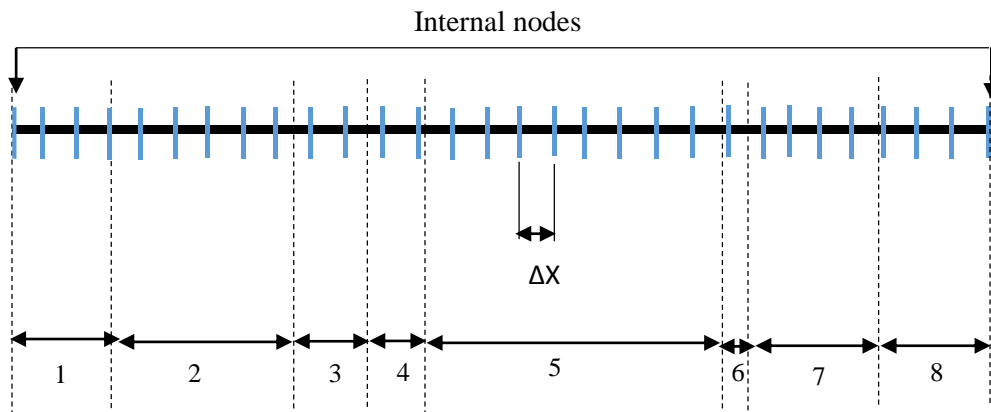


Figure 5.2: Discretised PEA layers based on FDM.

In figure 5.2, domain:

- 1 represents the top PML absorbing layer
- 2 represents the top aluminium
- 3 represents the top semicon electrode
- 4 represents the sample
- 5 represents the base aluminium electrode

6 represents the PVDF sensor material

7 represents the PMMA layer

8 represents the right hand PML absorbing layer

The model equations 5.22 and 5.23 can be expressed in terms of a set of 1D FDTD equations with the PMLs as boundary conditions as equation 5.24 – 5.31 [134]:

$$p^{n+1}(i) = A(i)p^n(i) - \frac{1}{2}B(i)(v^n(i+1) - v^n(i-1)) + (\Delta M^{n+1}(i) - \Delta M^n(i)) \quad (5.24)$$

$$A(i) = e^{-\gamma(i)\Delta t} \quad (5.25)$$

$$B(i) = C(i) \frac{\Delta t}{\Delta x} \quad (5.26)$$

$$v^{n+1}(i) = M(i)v^n(i) - \frac{1}{2}N(i)(p^n(i+1) - p^n(i-1)) \quad (5.27)$$

$$M(i) = e^{-\gamma(i)\Delta t} \quad (5.28)$$

$$N(i) = \frac{\Delta t}{\rho(i)\Delta x} \quad (5.29)$$

Where the superscript n is the iteration time index, Δx and Δt are the spatial and time steps respectively. The index i refers to the discrete sample coordinate points in the x direction. The attenuation coefficients $\alpha(i)$ and $\gamma(i)$ are non-zero only in the PML regions. In the PML, the corresponding attenuation coefficient increases from zero to a maximum in a quadratic form from the inner to the outer surfaces. For example, if the PML contains n layers (spatial steps Δx), in the right PML boundary region:

$$\alpha(i) = \alpha_{max} \left(\frac{i}{n}\right)^2, \text{ where, } i=1, \dots, n-1 \quad (5.30)$$

$$\gamma(i) = C \cdot \alpha_{max} \left(\frac{i+1/2}{n}\right)^2, \text{ where, } i=1, \dots, n-1 \quad (5.31)$$

Where $\alpha_{max} = -\log(k) c / (C dx)$, k is a constant. c is velocity and C is the effective modulus.

For the other PML layer, the same procedure is used for setting the attenuation coefficients. Based on above theory, the FDTD equations, (equations 5.24-5.31), were coded into MATLAB. The model constants such as, the spatial steps (Δx), time steps (Δt), time delay for the Gaussian pulse (t_p), width of the Gaussian pulse (t_w), maximum time to simulate (T_{max}), and attenuation constant (k), was set to the values shown in table (5.1). The pulse voltage (V_p) and the DC voltage (V_{DC}) were chosen to match that which

had been applied during a typical laboratory based experiment. The initial conditions were that the pressure and velocity were zero everywhere and that the PEA pulse voltage was zero. The MATLAB code of the process of generation, propagation and detection of the acoustic pressure wave is illustrated in the block diagram shown in figure 5.3. The PEA sensor output voltage was obtained by integrating the pressure wave across the PVDF thickness at each time step, Δt , as given in equation 5.32.

$$V_{out} = \int_{\text{Region 5}} P(x) dx \quad (5.32)$$

Table 5.1: Model constants.

Constants	Symbols	Values
Spatial steps	Δx	5×10^{-7} m
Time steps	Δt	10×10^{-11} s
Gaussian pulse time delay	t_p	5×10^{-8} s
Width of the Gaussian pulse	t_w	1.5×10^{-9} s
Maximum simulation time	T_{max}	4×10^{-7}
Attenuation constant	k	0.5

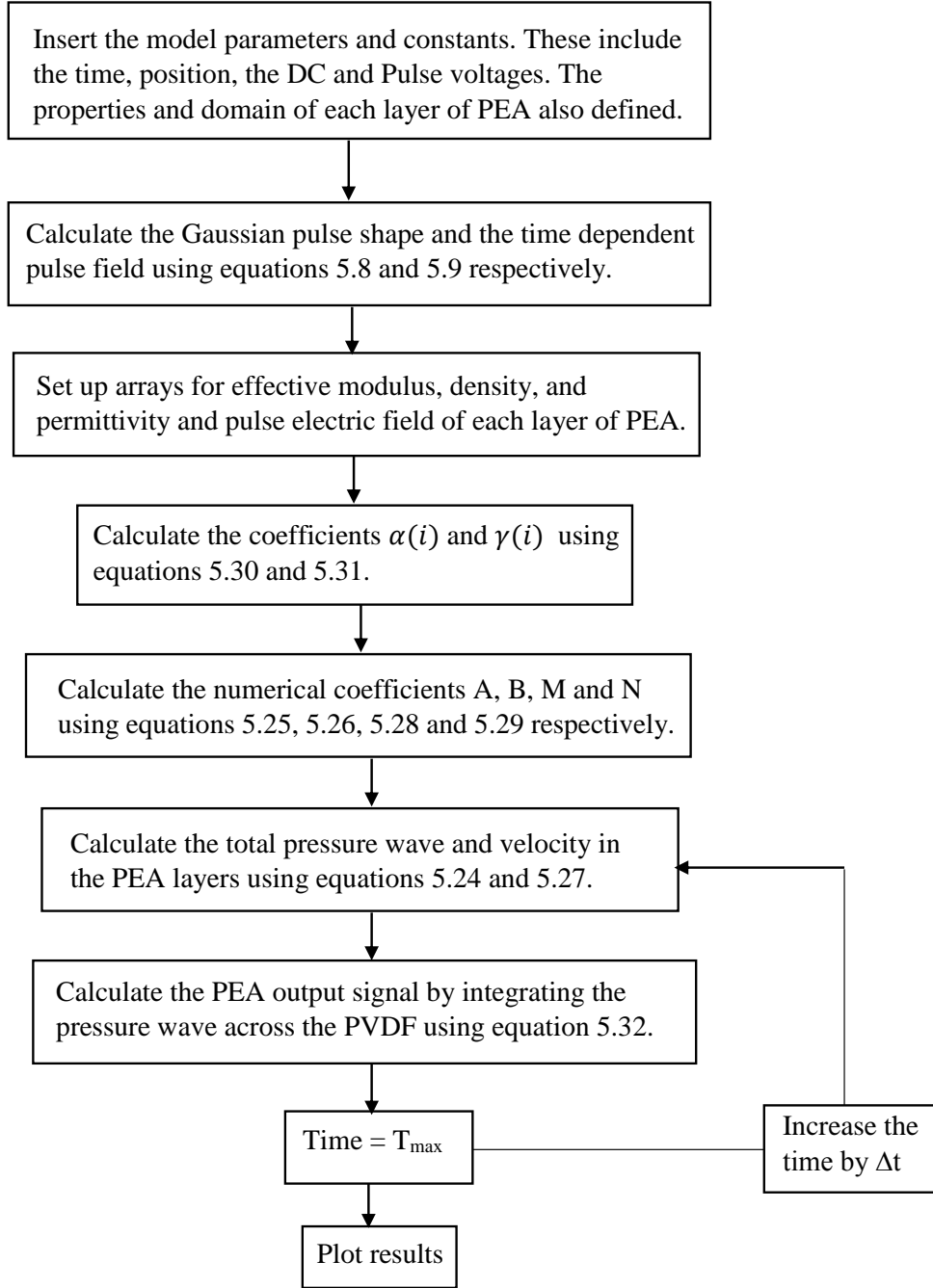


Figure 5.3: Procedure of generation, propagation of acoustic pressure wave in PEA system.

5.6 Initial simulations in the absence of space charge

In the initial simulations, the sample was assumed free of space charge, $\rho(x,t)=0$, and therefore in a thin film sample the electric field, $E(x,t)$ can be assumed to be distributed uniformly. $E(x,t)$ in the absence of space charge is given by V_{DC}/d , where V_{DC} is the applied DC voltage and d is the sample thickness. The temperature was assumed to be isothermal at 20°C and so all material parameters can be considered constants over the

thickness of the sample. The thicknesses used for each layer of PEA apparatus and their properties are summarised in table 5.2 [23, 67, 130, 135], which were chosen to match the PEA apparatus based in the laboratory.

In addition, the acoustic properties of the semicon and polymer sample, and the acoustic properties of PVDF and PMMA were initially assumed to be the same such that there was no acoustic mismatch between them, therefore removing the possibility of acoustic reflections occurring at these interfaces. The simulation therefore relates to an ideal case in which no signal distortions should occur. Figure 5.4 shows the acoustic pressure wave for time, $t=0$, across the eight subdomains of the PEA model as produced by the MATLAB code. At time $t=0$, the pulsed voltage had not yet been applied and the pressure waves had not yet been generated. After the pulse delay time, compressive (positive) pressure is generated within the sample due to the applied pulse voltage as shown in figure 5.5. Here, the sample is under uniform compression. After the voltage pulse had receded, the pressure within the sample bulk returns to zero as shown in figure 5.6(a), but pressure waves are generated at the two electrode/insulator interfaces and propagate in the direction shown by the arrows. In fact, two waves propagate from each source (interface), a compressive wave in one direction and a rarefaction wave in the opposite direction. The pressure waves that propagate towards the lower electrode and to the PVDF sensor through the aluminium base plate form the useful signal, while the other waves moved towards the upper electrode and away from the PVDF detector. The positions of the pressure waves at various times of propagation are shown in figure 5.6. Figure 5.6(b) shows the pressure waves at the time when the acoustic wave generated at the sample/Al base plate interface had propagated one third of the way through the Al base plate. In figure 5.6(c) the pressure wave generated at the sample /Al base plate approaching the PVDF detector layer. In figure 5.6(d) acoustic reflection occurs at the Al base plate /PVDF interface. Part of this acoustic pulse propagates through the PVDF sensor whilst the reflected pressure wave propagates back towards the sample. At the same time, the pressure wave from the semicon/sample interface has reached the sample /Al interface where this is partly transmitted and reflected. Figure 5.6(e) the pressure wave generated from the sample/Al interface has now propagated through the PVDF detector and into the PMMA layer whilst the pressure wave generated at the semicon/sample interface has now propagated into the Al base plate. In figure 5.6(f) the pressure wave generated at the semicon/sample interface has reached the Al base

plate/PVDF interface where it is partially transmitted and reflected. At each time step, the pressure wave across the PVDF thickness was integrated to give the PVDF output voltage, $V_{out}(t)$, which is shown in figure 5.7. This voltage is a function of time but the x-axis can be converted to distance inside the sample by multiplying the time axis by the speed of sound in the sample. In this case the simulated PEA output data consists of two equal magnitude peaks of opposite polarity representing just the electrode charges as the simulation assumes no space charge was present inside the sample. Once the space charge distribution has been obtained as shown in figure 5.7(a); this can be integrated along the sample thickness to give an uncalibrated graph of the electric field distribution inside the sample as shown in figure 5.7(b). In this case, for an ideal PEA signal response and for a space charge free sample, the calculated electric field is uniform over the thickness of the sample within the resolution limit of the PEA response.

Table 5.2: Material properties used in PEA simulation.

Material	Density (kg/m ³)	Effective modulus (GPa)	Velocity (m/s)	Thickness (mm)	Relative permittivity
Top absorber	2700	107	6295	4	1
Top Aluminium	2700	107	6295	7	\
Semicon	917	3.987	2085	1	1
Polymer	917	3.987	2085	0.15	2.3
Base Aluminium	2700	107	6295	10	\
PVDF	1200	8.7	2692	0.009	8.4
PMMA	1200	8.7	2692	5	4
Bottom absorber	1200	8.7	2692	4	1

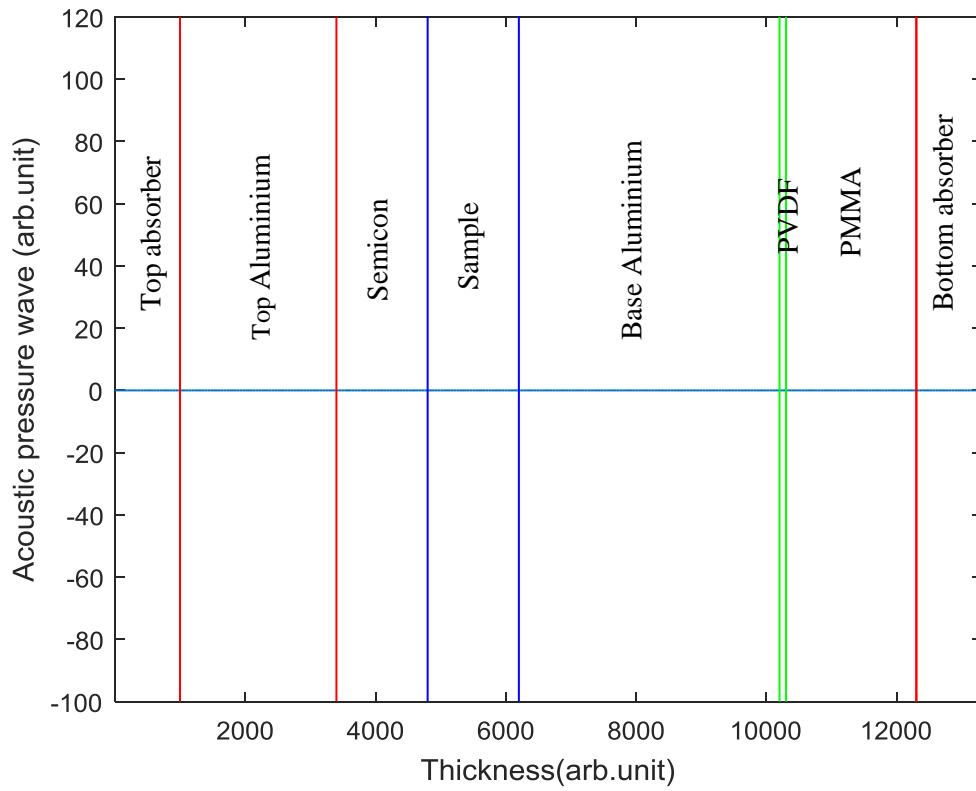


Figure 5.4: Acoustic pressure wave at time=0.

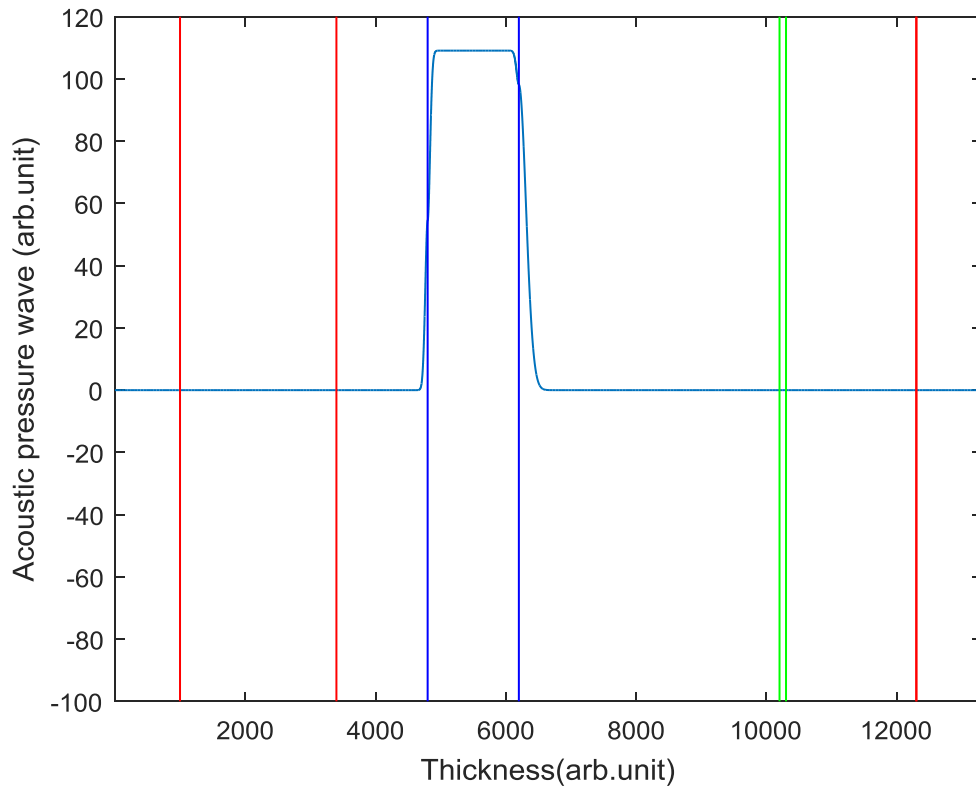
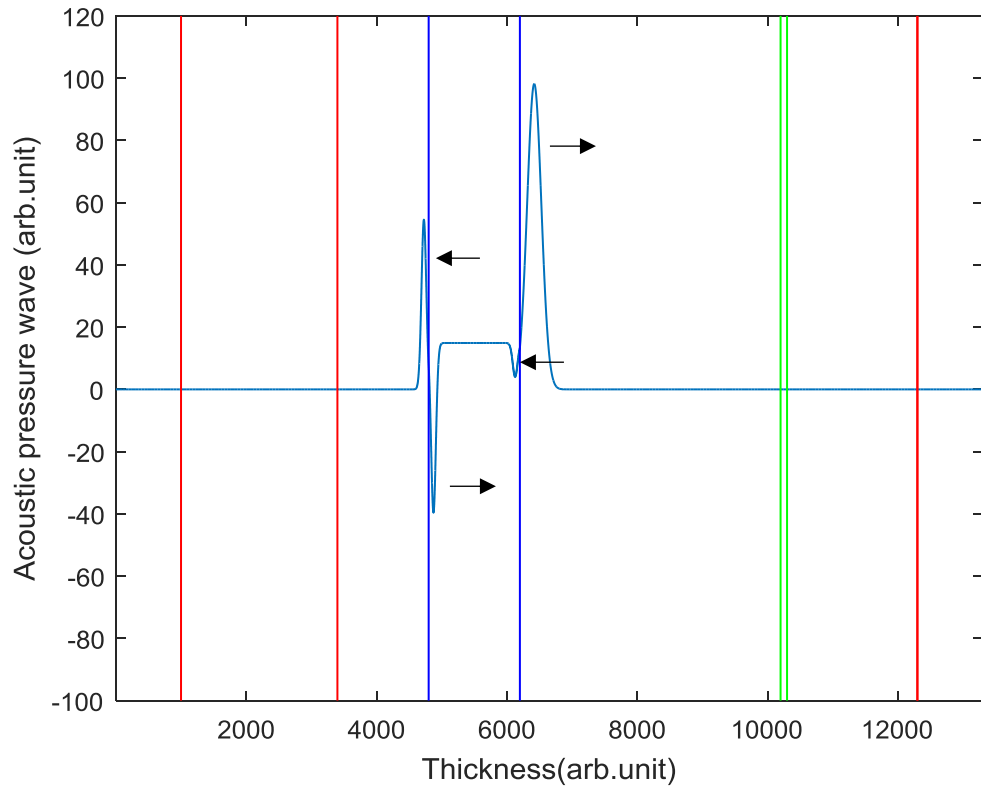
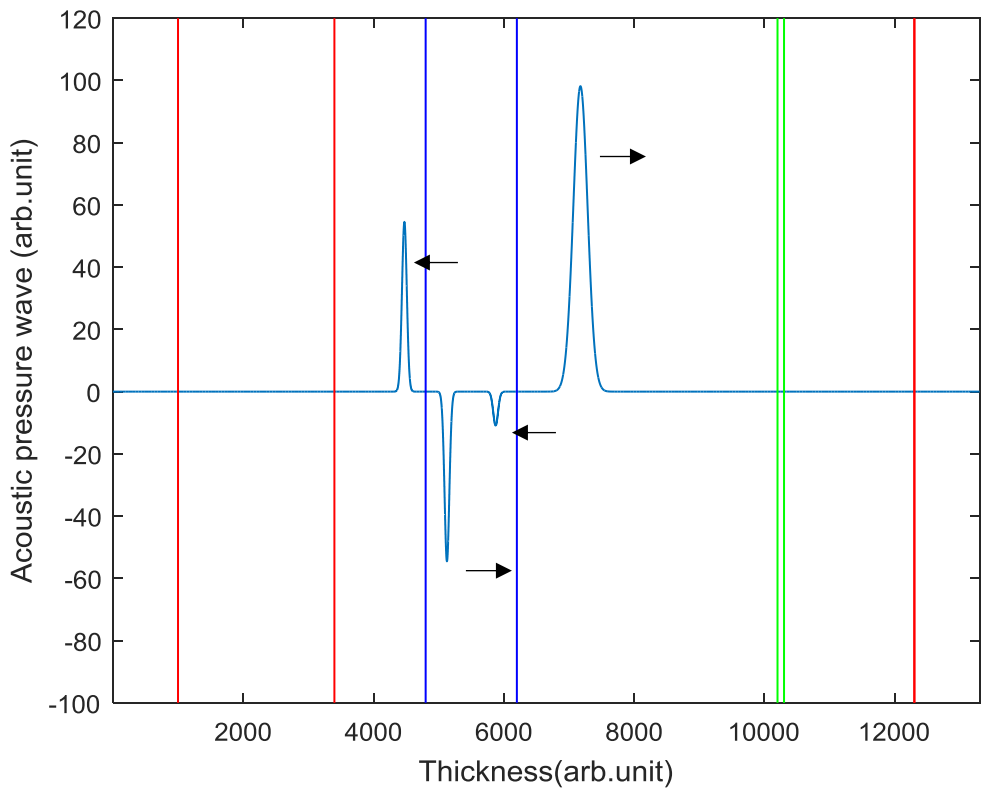


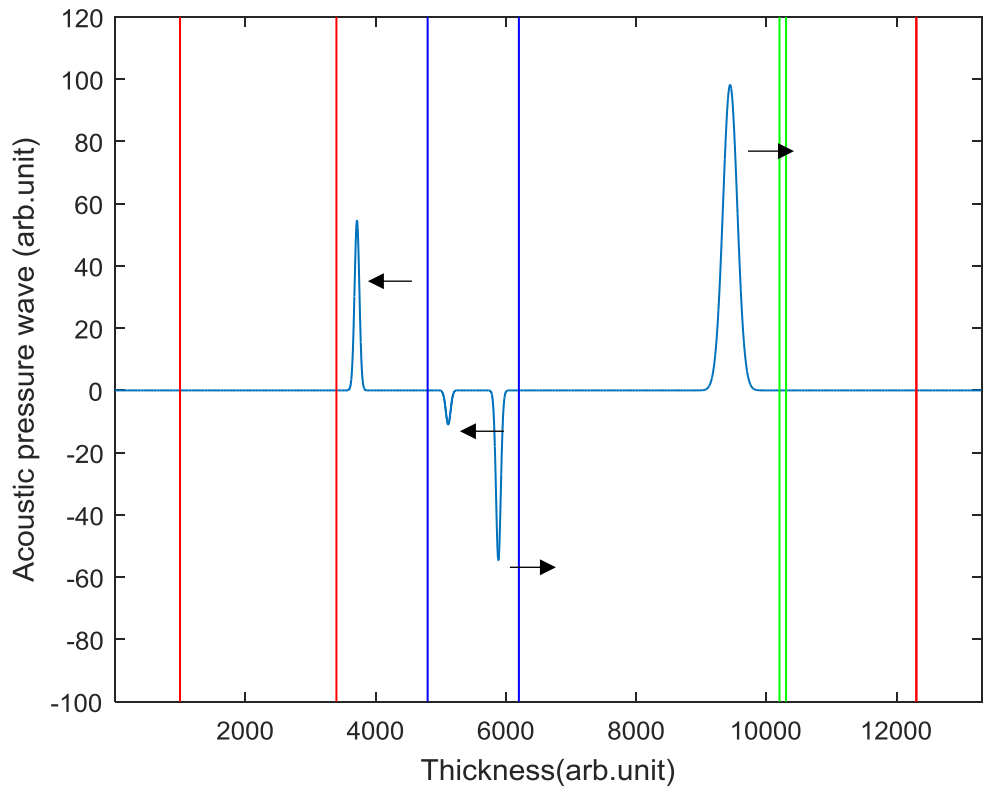
Figure 5.5: Applied pulse voltage on PEA system.



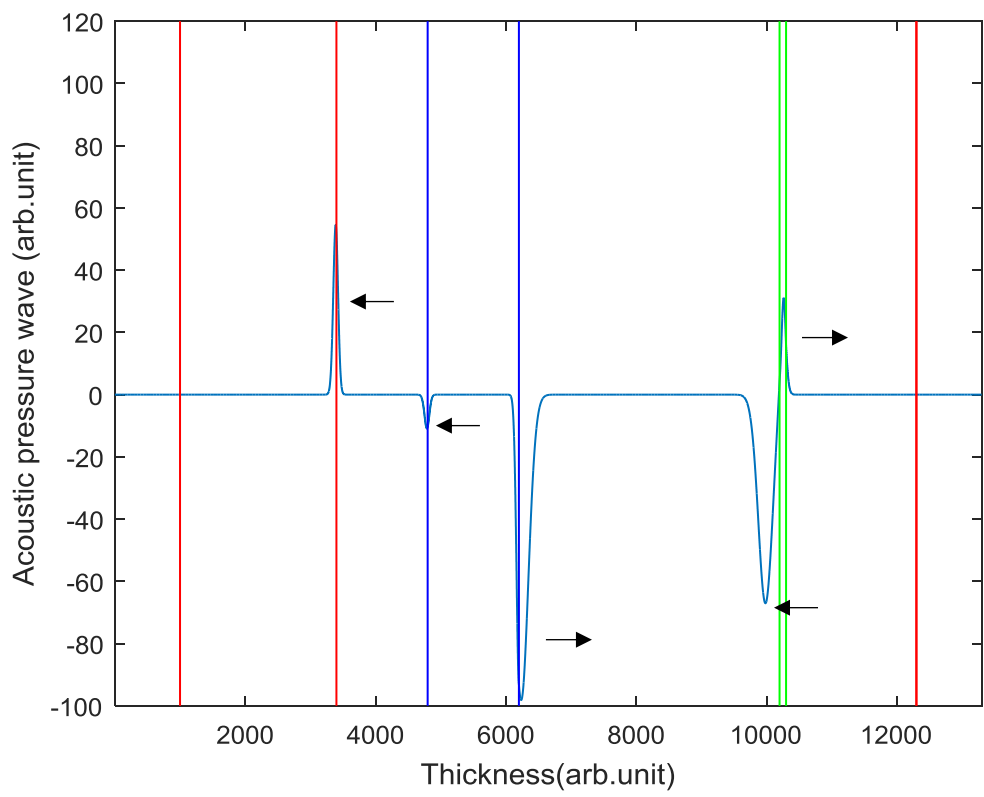
(a)



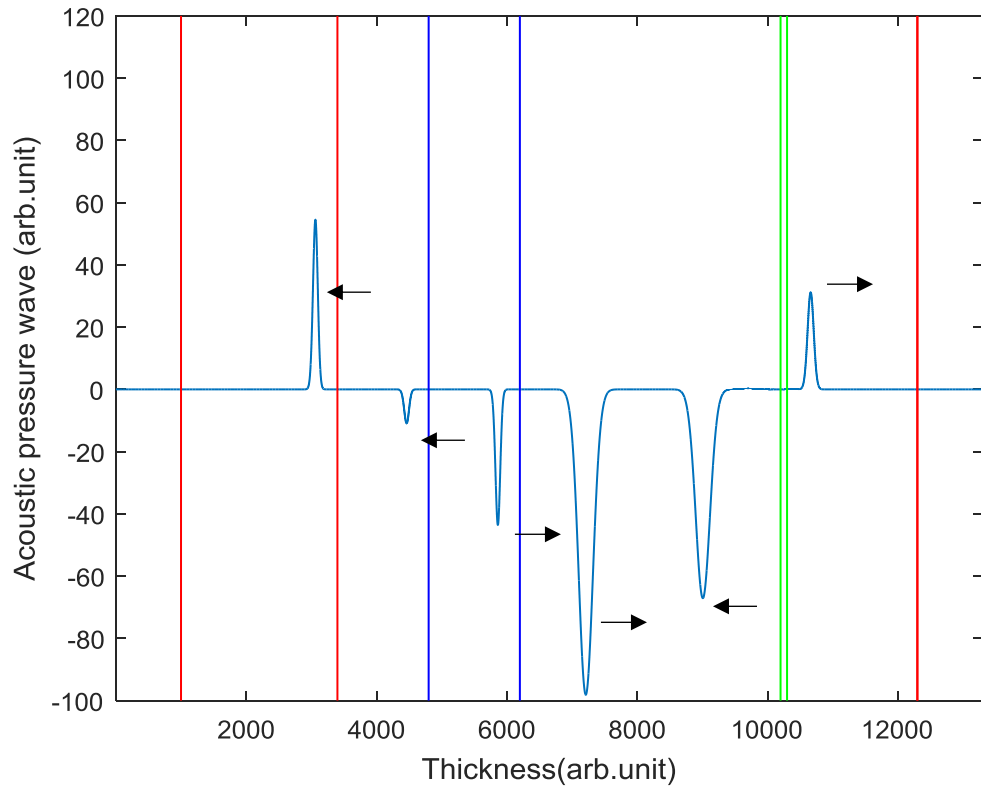
(b)



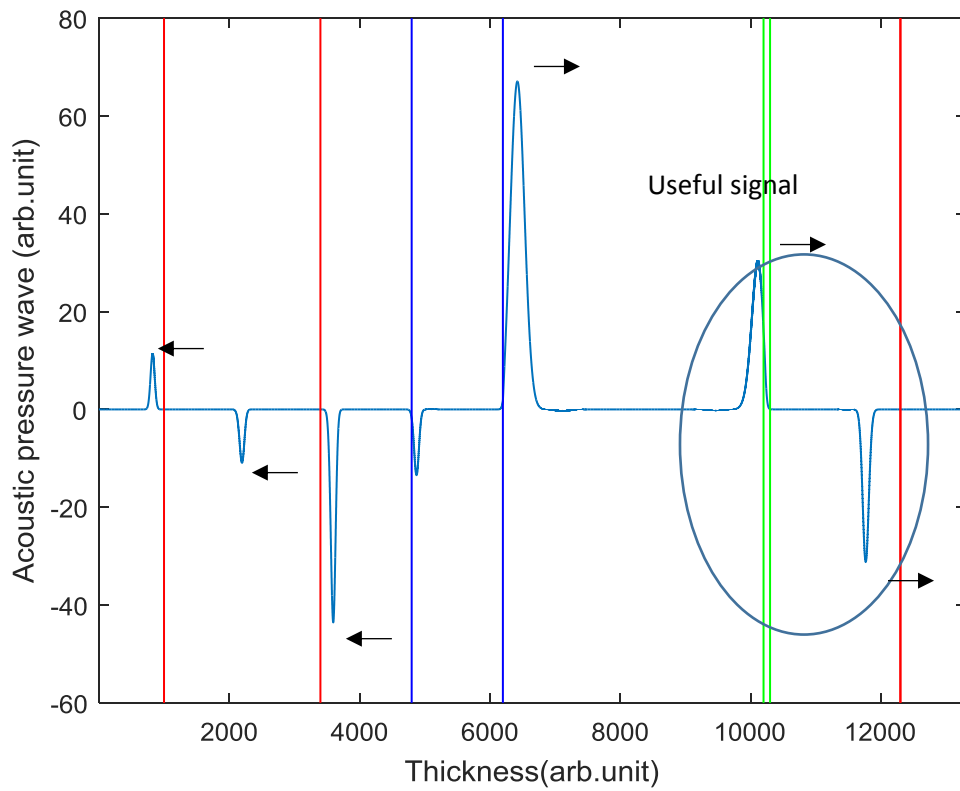
(c)



(d)



(e)



(f)

Figure 5.6: (a)-(f) Pressure wave propagating through the PEA layers at various times. The direction of propagation is shown by the arrows.

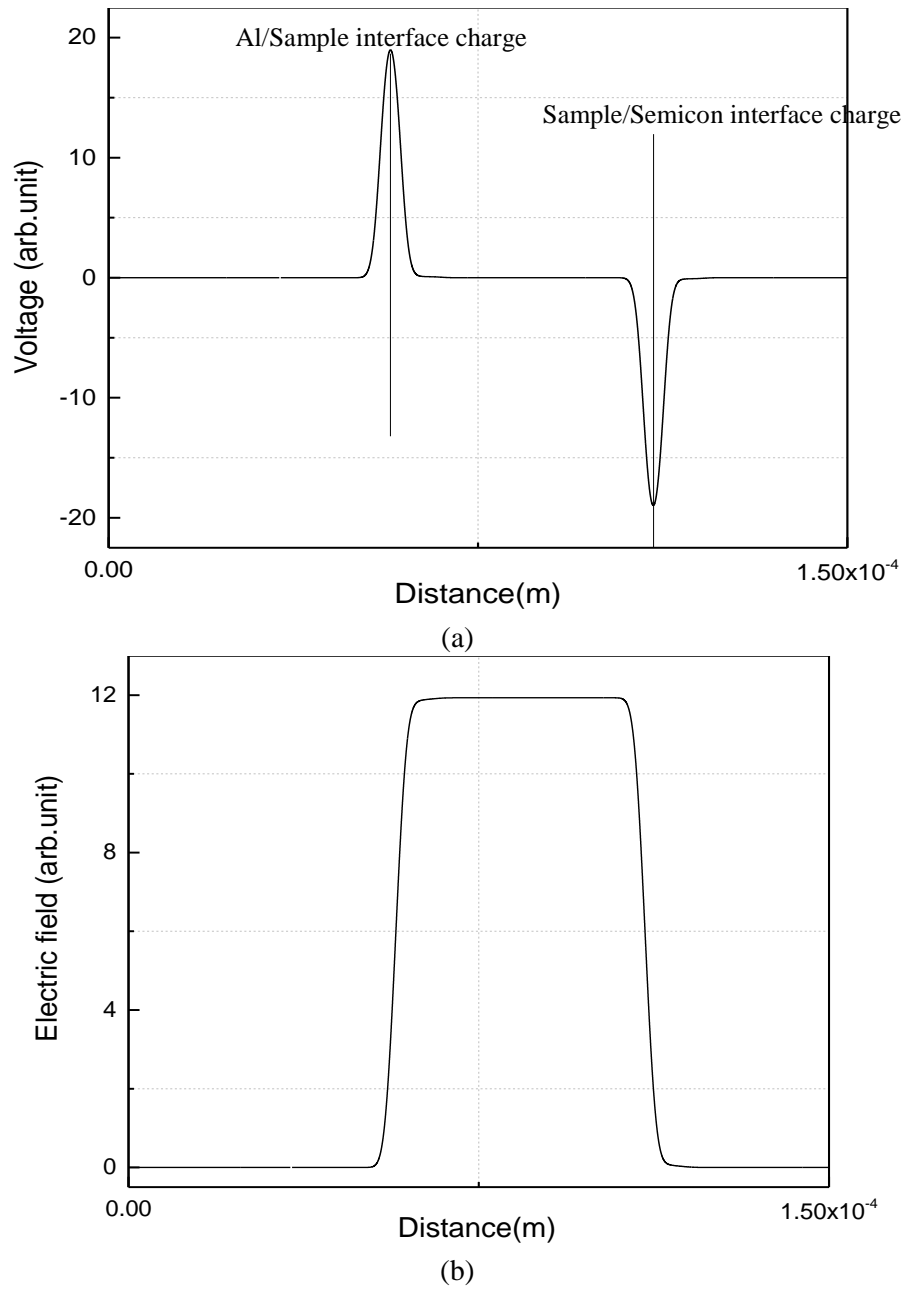


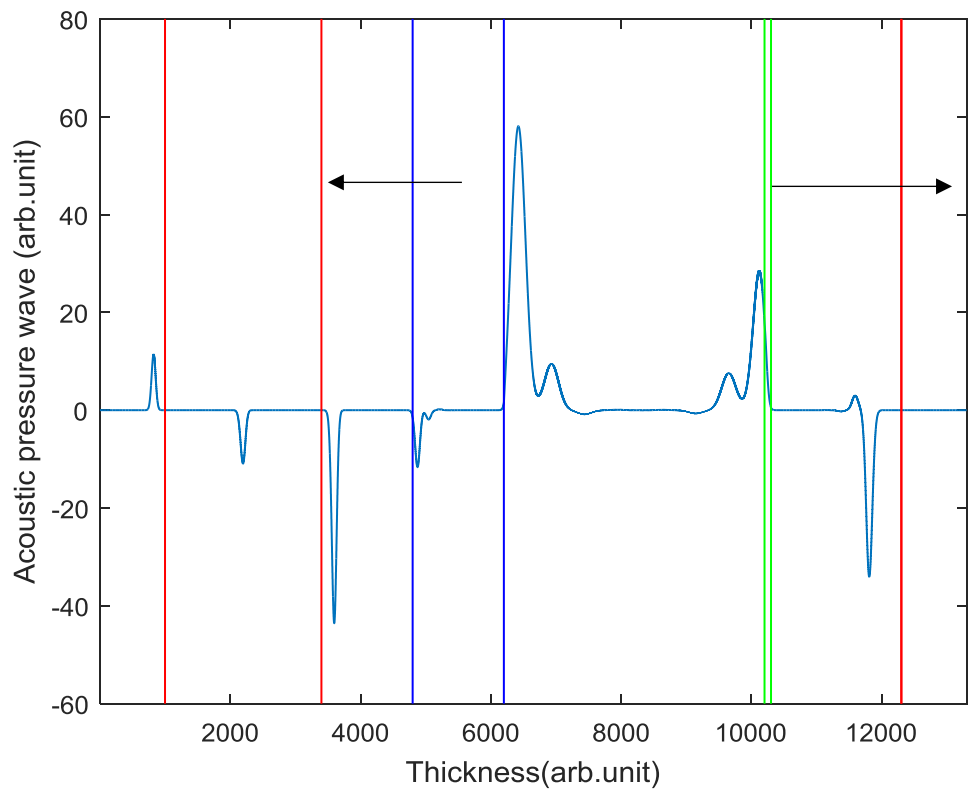
Figure 5.7: (a) Acoustic pressure wave in a total domain,(b) PVDF output voltage, (b) PVDF output electric field distribution, of ideal (lossless) sample in PEA simulation model.

However, in a practical PEA system, the choice of materials is such that perfect acoustic matches are not possible and unwanted acoustic reflections can be obtained at the interfaces between them. To illustrate this, if the values of the acoustic properties of PMMA and PVDF are changed to their literature (real) values as shown in table 5.3, and the simulation repeated, the influence of reflection due to the different acoustic properties of PVDF and PMMA on the PEA output signal can be observed. As shown in figure 5.8(a), the acoustic reflection at the PVDF-PMMA interface leads to the formation in this

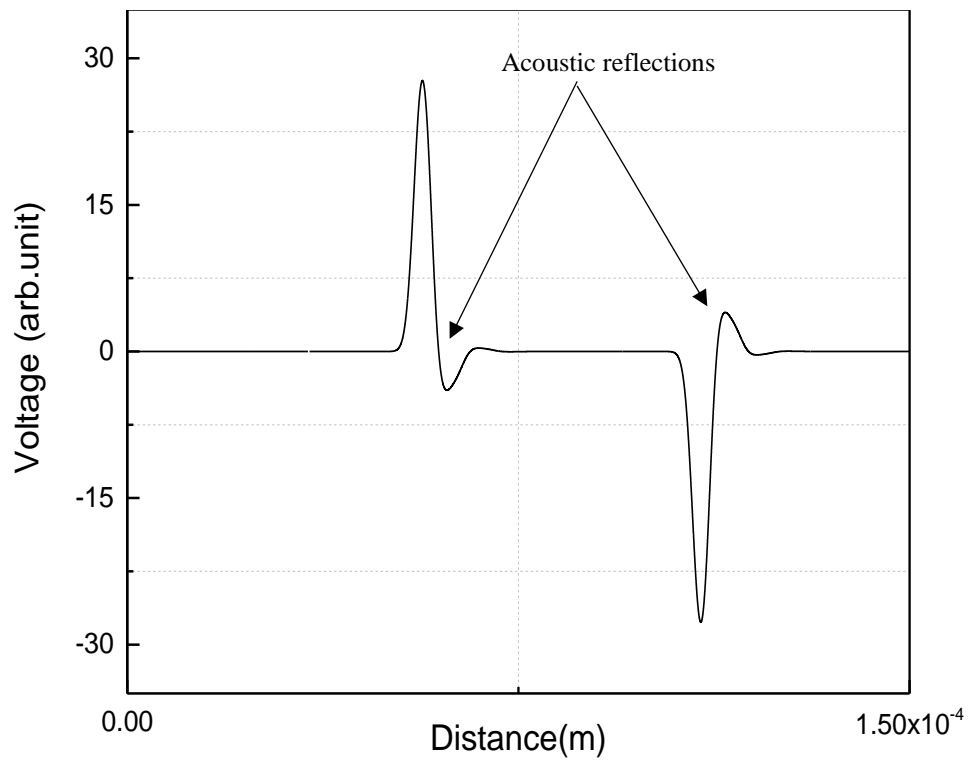
case of signal overshoots as shown in figure 5.8(b). In this case, only a part of the acoustic wave is transmitted to the bottom PMMA absorber, the other part is reflected back through the PVDF sensor at the interface and this interferes with the incident wave. These unwanted reflections can lead to misinterpretation of the PEA response in terms of space charge regions that actually do not exist. Integrating this charge profile over the thickness of the sample yields the electric field distribution (again uncalibrated). Here the unwanted acoustic reflections at the PVDF/PMMA interface cause ripples to appear in the calculated electric field errors in the electric field at the interfaces as shown in figure 5.8(c).

Table 5.3: Material properties used in PEA simulation in case of mismatch between PVDF/PMMA.

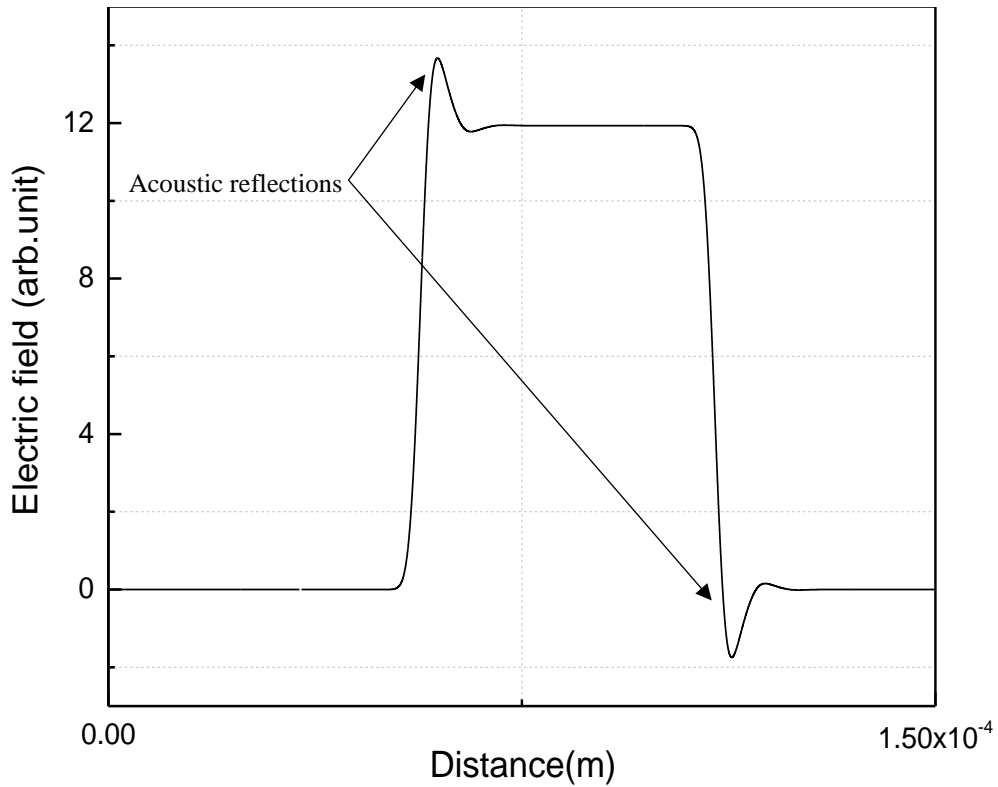
Material	Density (kg/m ³)	Effective modulus (GPa)	Velocity (m/s)	Thickness (mm)	Relative permittivity
Top absorber	2700	107	6295	4	1
Top Aluminium	2700	107	6295	7	\
Semicon	917	3.987	2085	1	1
Polymer	917	3.987	2085	0.15	2.3
Base Aluminium	2700	107	6295	10	\
PVDF	1760	10.8	2477	0.009	8.4
PMMA	1200	8.7	2692	5	4
Bottom absorber	1200	8.7	2692	4	1



(a)



(b)



(c)

Figure 5.8: (a) Acoustic pressure, (b) PVDF output voltage, (c) PVDF output electric field distribution, of ideal (lossless) sample when it is the impedance mismatch between PVDF and PMMA.

Similarly, it is often assumed in the literature that the semicon top electrode has the same acoustic properties as the sample material [76, 123]. This is particularly important with regard to the acoustic attenuation and dispersion correction of the PEA response (to be discussed later). The typical approach of attenuation/dispersion correction taken in the literature [136] is to compare the electrode responses at the two electrode interfaces. Any difference in the magnitude and pulse width of the two peaks at the two electrodes is assumed to be due to attenuation and dispersion as the pressure wave from the top electrode has to propagate through the sample and the propagation coefficients obtained are then used as the basis for correction of the PEA raw data. However, a difference in the two peaks can also occur if there is a difference in the acoustic properties of the sample and the top semicon electrode of the PEA apparatus. To illustrate this, a series of PEA simulations were performed in the case that the acoustic properties of semicon were not the same as the acoustic properties of the dielectric material. It was found that the amplitude of the peak located at the dielectric/semicon interface (the second peak) was changed in proportion to the mismatch of the acoustic properties of the semicon and insulation layers as shown in figure 5.9, whilst the width of the peak remains the same.

Figure 5.9, shows how the value of effective modulus of the semicon material impacts on the PEA response at the semicon-dielectric interface. When the value of semicon effective modulus was 4GPa both the semicon electrode and the insulator material have the same value. In this case, the magnitude of the PEA electrode response at the semicon interface has the same value as the response from the aluminium/insulator interface. However decreasing or increasing the value of effective modulus of semicon relative to that of the insulator material leads to mismatch in the acoustic signal peaks from the interface charge at the two electrodes. In the simulated response of the PEA shown in figure 5.9, when the effective modulus of the semicon material is made less than that of the sample, the acoustic mismatch leads to an increase in the peak amplitude at the semicon/insulator interface whilst the peak corresponding to the aluminium electrode remains unchanged. On the other hand, when the effective modulus of the semicon material is made greater than that of the sample, the acoustic mismatch leads to decrease in the peak amplitude at the semicon/insulator interface. From the point of view of interpreting the PEA raw data in terms of a space charge distribution, when the modulus of the semicon is greater than that of the insulator, the space charge density at the semicon/insulator interface is underestimated. In this case, the difference in the peak amplitudes could be miss-interpreted as acoustic attenuation and an incorrect correction applied to the data.

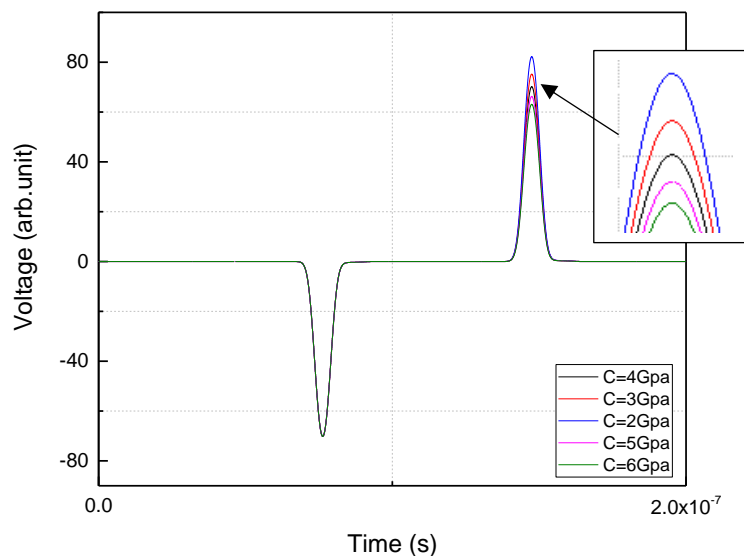


Figure 5.9: Effect of Electrode properties on PEA acoustic signal.

5.7 Corrections for acoustic attenuation and dispersion of the pressure waves

The ‘ideal’ simulations of the PEA output as shown previously in figure 5.4 demonstrate that the predicted interface charge peaks at the electrodes have equal but opposite peaks that are related to the opposite interface charges due to the applied HVDC voltage. However, real space charge measurements using the PEA, for example the calibration data shown in chapter 3, reveal that in general, the interface charge from the aluminium electrode always has a higher amplitude and shorter duration compared to the peak from the top electrode of opposite polarity. The difference may be due to the different paths taken by the two pressure waves. The pressure wave from the aluminium electrode/sample interface pass directly to the aluminium electrode and propagate to the PVDF sensor whilst the pressure wave from the top (semicon) electrode has first to propagate through the sample before transferring into the aluminium electrode.

In a non-ideal acoustic medium, the acoustic wave is distorted during its propagation due to the effect of attenuation and dispersion, such as in polymer insulation materials. The distortion of the acoustic wave will become larger, if the distance of the propagation (insulation thickness) is longer. Accordingly, the detection of the PEA output signal changes as function of the transmission length. Therefore, to study the space charge in a non-ideal material (polymers) quantitatively, the effect of acoustic attenuation and dispersion must be considered.

Since the PEA technique is a 1D measurement, the general expression for the acoustic wave that travels through the non-ideal medium in a frequency domain can be described based on equation 5.33[31].

$$P(t, x) = P(t, 0) e^{(-\alpha.x)} e^{j(\omega t - \beta.x)} \quad (5.33)$$

Where $P(t, 0)$ is the amplitude of the pressure wave at the aluminium base plate-sample interface, $z=0$, α and β are frequency dependent attenuation and dispersion coefficients respectively that determine the amount of attenuation and dispersion of the pressure waves as they propagate through the sample. The propagation of an acoustic pulse in a dispersive and lossy medium is shown in figure 5.10. In figure 5.10, the acoustic pulse is shown after different time shows how the pulse is both attenuated and dispersed as it propagates through the sample material.

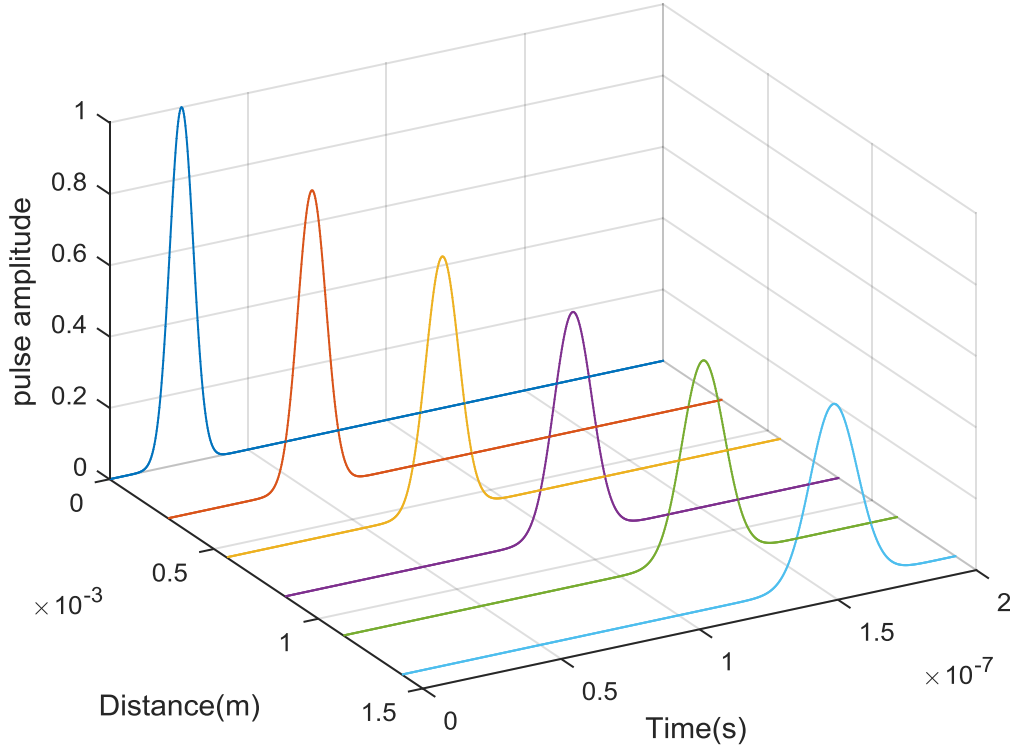


Figure 5.10: Propagation the acoustic wave in a lossy and dispersive medium.

5.8 Acoustic attenuation and dispersion to PEA simulation output data

The PEA simulation method as described above deals with the propagation of acoustic waves through a lossless medium. The following method is proposed for the inclusion of attenuation and dispersion into the PEA simulation model by post analysis of the simulated PEA signal. The aim is to carry out attenuation and dispersion correction on an idealised PEA response such that the instabilities associated with the traditional space charge recovery method (described in section 3.2.4) can be avoided. That is in this new method, the numerically unstable calculation of the inverse transfer function for the G matrix ($G(t, z)^{-1}$) will no longer be required. The process of attenuation/dispersion correction is carried out by considering two time dependent Gaussian pulses corresponding to the propagation of the pulse by one space step, Δx , based on equation 5.34 but are slightly attenuated and dispersed at each propagation of one node.

$$G(t, 0) = e^{-\frac{4 \ln(2) \cdot (t-t_p)^2}{t_w^2}}, \quad G(t, 1) = a \cdot e^{-\frac{4 \ln(2) \cdot (t-t_p)^2}{(t_w + \Delta t_w)^2}} \quad (5.34)$$

Here, t_p is delay time of Gaussian pulse, t_w is a half width of Gaussian pulse, a is an attenuation coefficient (slightly less than unity) describing the decrease in amplitude of

the pulse in propagating one node and Δt_w is the increase in half-width of the pulse in propagating one node. The transfer function related to the propagation of the pulse by one space-step is given by the ratio of the Fourier transforms of these two signals.

$$G(f) = \frac{FFT(G(t,1))}{FFT(G(t,0))} \quad (5.35)$$

This transfer function describes the propagation of the Gaussian pulse by one space step in which the Gaussian pulse has been attenuated by a factor, a , and broadened by an amount Δt_w . In order to prevent instability issues due to the division by small values close to zero, only the first 350 (out of 402) frequency components were calculated. The remaining terms were set to zero. The transfer function for the pulse to propagate 2 time steps is therefore $G(f)^2$ and for n space steps, the transfer function will be $G(f)^n$.

To obtain a matrix of transfer functions, $G(f, x)$, that describe the propagation of the pulse from one node to another, across the sample thickness, the procedure is defined below:

The first column of $G(f, x)$, $G(f, 0)$ represent the transfer function of the pulse onto itself and all frequency components will have a complex value of $(1+j0)$. The second column $G(f, 1)$ will have the frequency components of $G(f)$. The frequency components in subsequent columns can be obtained by multiplying the previous column by $G(f)$. The completed transfer function matrix will therefore be:

$$G(f, x) = \begin{bmatrix} 1 + j0 & G(1) & G(1)^2 & \cdots & G(1)^n \\ 1 + j0 & G(2) & G(2)^2 & \cdots & G(2)^n \\ 1 + j0 & G(3) & G(3)^2 & \cdots & G(3)^n \\ \vdots & \vdots & \vdots & \vdots & \vdots \\ 1 + j0 & G(f) & G(f)^2 & \cdots & G(f)^n \end{bmatrix} \quad (5.36)$$

Where here, f represents the number of frequency components of each transfer function and n represents the number of space steps, Δx , across the sample thickness.

To get the attenuation and dispersion corrected PEA output waveform in the frequency domain the transfer function matrix, $G(f, x)$, was post multiplied with the row matrix of the simulated PEA output voltage, $V_{PVDF}(x)$. Here the time variable is replaced by the distance, $x = ct$, where c is the propagation velocity of acoustic waves in the sample.

$$V(f) = G(f, x) \cdot V_{PVDF}(x) \quad (5.37)$$

Before transforming back to the time domain, the correction factors due to PVDF/ amplifier response and the oscilloscope response are first applied to $V(f)$ as explained in the next sub section.

5.9 Correction for the PVDF/Buffer amplifier and oscilloscope frequency response

So far only attenuation and dispersion correction of the ideal simulated PEA output signal has been discussed. As mentioned in chapter 2, the PVDF/ buffer amplifier and oscilloscope frequency response work as a high pass filter and low pass filter respectively which lead to further distortion and imperfection in the PEA output signal. Therefore, in order to simulate the raw experimental PEA measurement data, these two factors should be incorporated. The details of transfer function of high pass filter, *HPF*, and transfer function of the low pass filter, *LPF*, were already explained in section 2.6.3.1 and 2.6.3.2 respectively.

Here, the attenuation/dispersion corrected simulated PEA output signal requires further manipulation by multiplying the frequency domain representation of the attenuation/dispersion corrected output, $V(f)$, as calculated from equation 5.37, by the transfer function of these two filters, equations 2.22 and 2.23.

$$V_{corr}(f) = V(f).(LPF).(HPF) \quad (5.38)$$

The final corrected PEA output signal in the time domain, $V_{corr}(t)$, is then given by real value of the inverse Fourier transform of $V_{corr}(f)$ that obtained from equation 5.38.

$$V_{corr}(t) = Real(IFFT(V_{corr}(f))) \quad (5.39)$$

$V_{corr}(t)$ is the final numerical result of the new PEA simulation model which represents the PEA signal after being corrected for attenuation, dispersion and corrected for the buffer amplifier and oscilloscope responses. Hence this simulated voltage can be compared directly with raw PEA experimental data. The details of this comparison will be described in the following subsection (5.10).

5.10 Comparing the simulation result with experimental PEA raw data when there is no space charge

In a thin film sample when there is no space charge, the electric field is distributed uniformly which is called the Laplacian field. As the space charge is equal to zero within the sample material there is no need to use the charge transport model. Instead the electric

field distribution used in the PEA model can be calculated from the applied DC voltage divided by the sample thickness. A comparison can therefore be conducted between the acoustic PEA simulations (assuming constant electric field) with experimental raw PEA data obtained under a sufficiently low applied DC field to insure that the sample contains no space charge. Figure 5.11 shows typical PEA raw data that obtained from a 200 μm flat plane XLPE sample under a low DC voltage (1kV) and after a short time of about 10s after voltage application to avoid accumulation any internal space charge. As shown in figure 5.11, the PEA experimental result has a number of features introduced by the non-ideal characteristics of the laboratory based instrument. Here the PEA output signal has different amplitudes and width for the electrode charges due to absorption and dispersion of the acoustic waves as they transverse the sample. Signal overshoots following the electrode charge peaks can also be observed due to the reflection of the acoustic waves at the PVDF/PMMA interface. In addition, there is a slow baseline response observed during the time between the two electrode peaks which is due to the PVDF/buffer amplifier frequency response.

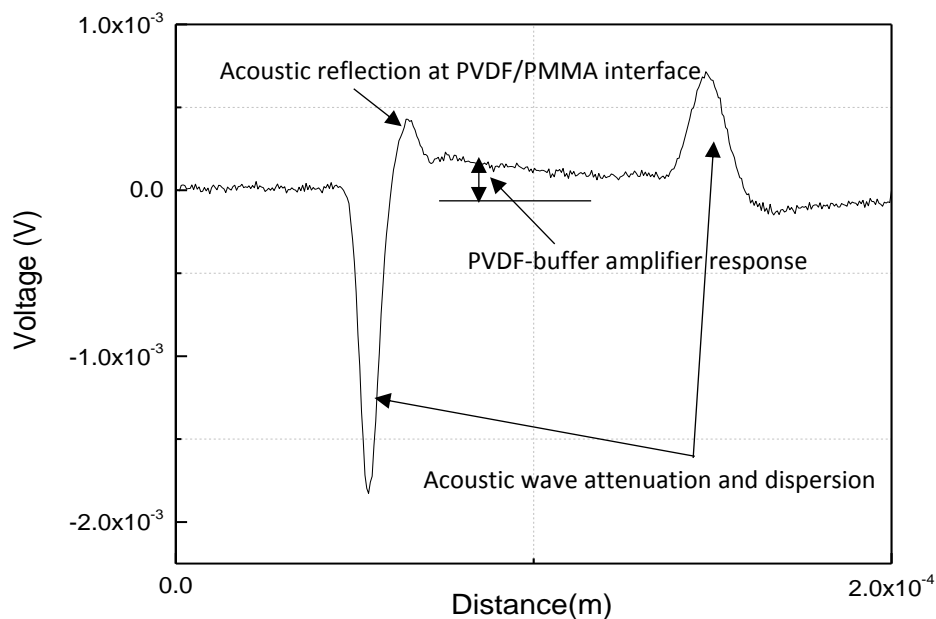


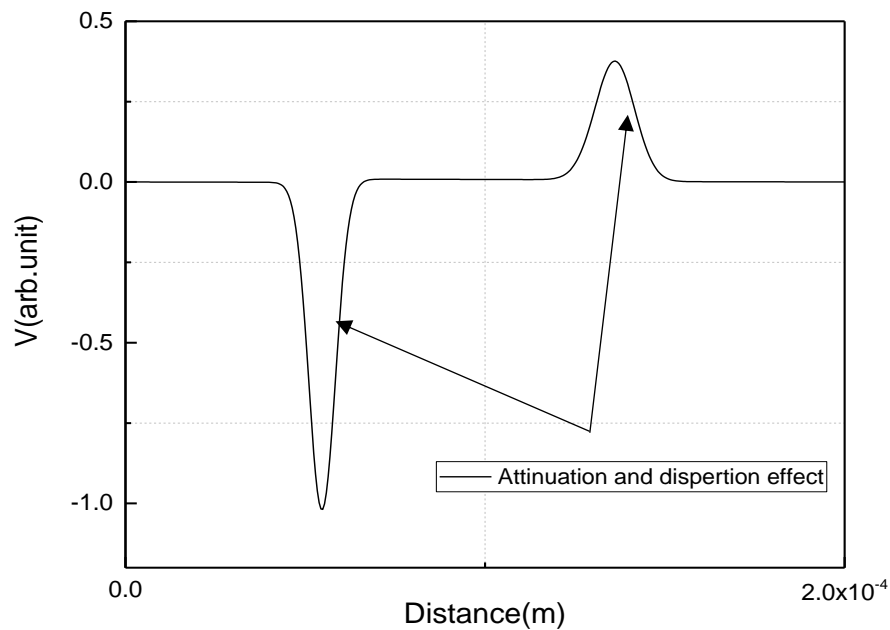
Figure 5.11: Typical experimental PEA output signal.

Therefore, to get a good match with the experimental result, the ‘ideal’ response of the simulated PEA data, shown in figure 5.7, requires the corrections for acoustic wave propagation (both attenuation and dispersion), acoustic wave reflection at the PVDF/PMMA interface, attenuation and dispersion and PVDF-buffer amplifier high pass

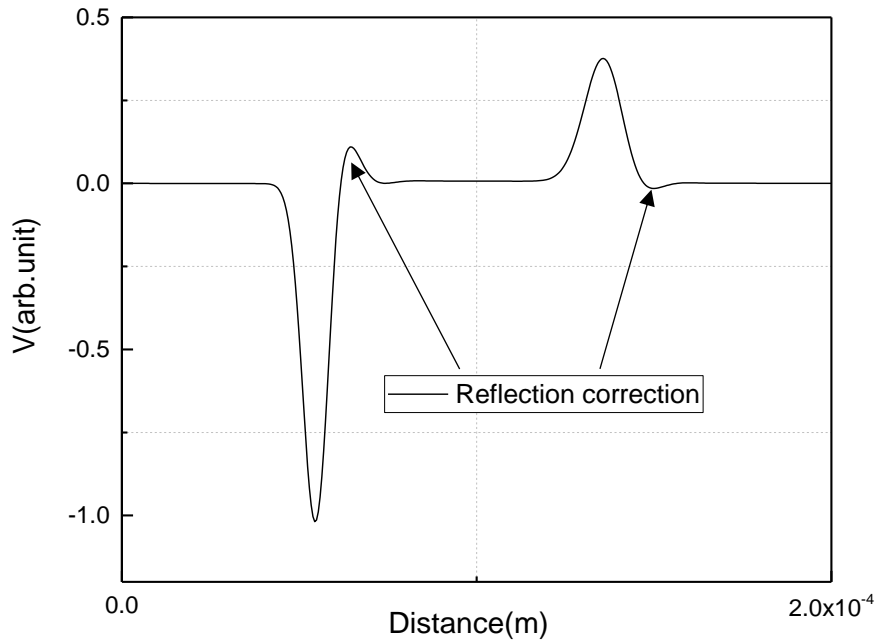
filter responses as described in the previous sections. Figure 5.12(a), shows the simulated PEA response corrected for attenuation and dispersion, 5.12(b) after correction for the acoustic miss-match between the PVDF/PMMA and 5.12(c) after correction for the HPF and LPF responses of the PVDF buffer/amplifier and the bandwidth of the oscilloscope. The parameters used for the PEA simulation to get the results shown in figure 5.12 are given in table 5.4.

Table 5.4: Material properties used in PEA simulation.

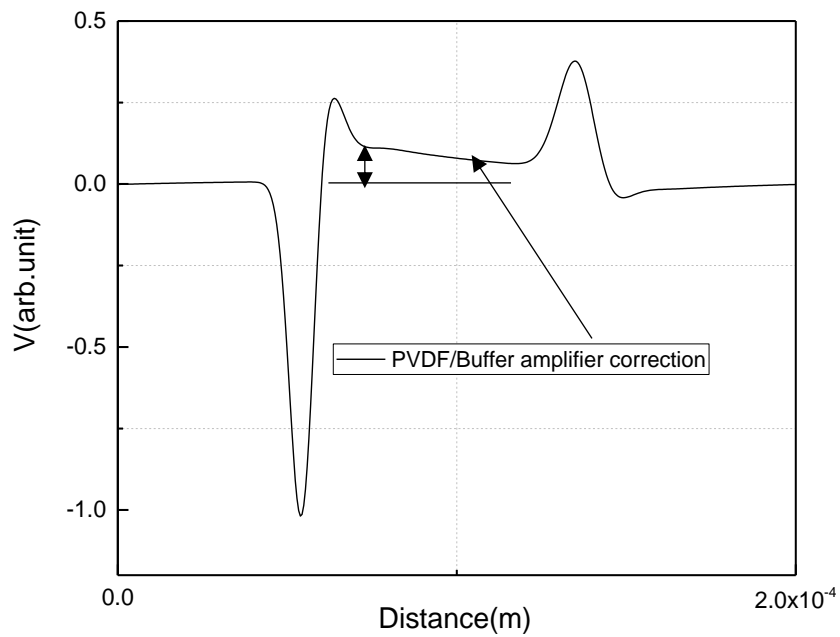
Material	Density (kg/m ³)	Effective modulus (GPa)	Velocity (m/s)	Relative permittivity
Top absorber	2700	107	6295	\
Upper Al	2700	107	6295	\
Semicon	917	3.987	2085	1
Polymer	917	3.987	2085	2.3
Aluminium	2700	107	6295	\
PVDF	1760	10.8	2477	8.4
PMMA	1200	8.7	2692	4
Bottom absorber	1200	8.7	2692	1



(a)



(b)



(c)

Figure 5.12: (a) attenuation-dispersion correction, (b) attenuation-dispersion and reflection corrections, (c) attenuation-dispersion, reflection and PVDF-buffer amplifier corrections.

After these correction processes, the results of the simulation and experiment were directly compared as shown in figure 5.13 after rescaling the simulated data to have the same amplitude as the experimental data. Although the simulated data is not exactly the same, a good agreement can be seen between them.

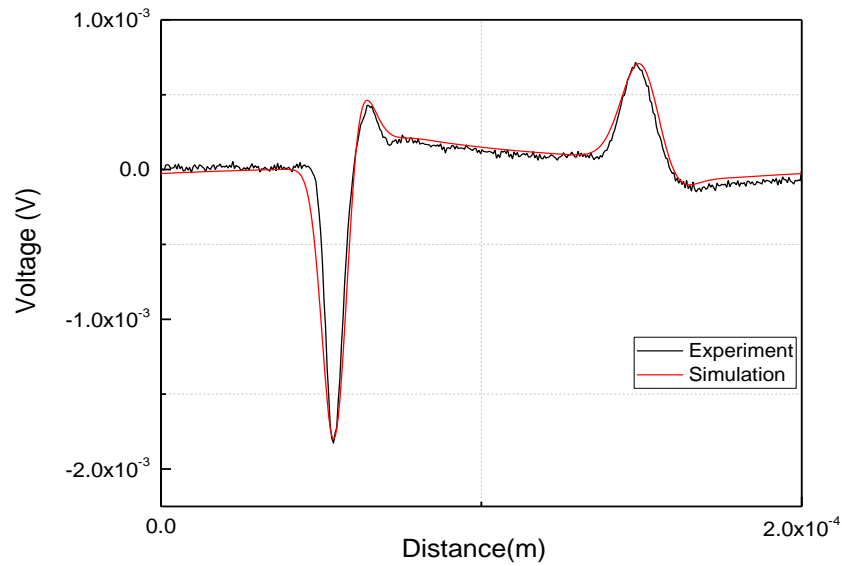


Figure 5.13: The result of PEA simulation compared with the PEA output data in XLPE sample.

5.11 Simulation and experiment to show the effect of the top electrode material on the PEA response in free charge sample

As was pointed out in section 5.6, the acoustic match between the sample and the top electrode will have an effect on the amplitude of the second PEA pulse relating to the electrode charge at the semicon/sample interface. To further test the validity of the PEA simulation model and to examine the effect of the top electrode material, experiments and corresponding simulations were performed for two different cases. In the first case the top electrode was semicon forming a good acoustic match with the insulator as used in a conventional PEA apparatus while in the second case, aluminium (Al) electrode was substituted for the semicon electrode that had a significantly different set of acoustic properties to that of the sample. For both cases a 160 μ m thick XLPE sample was used and the bottom electrode was aluminium in both cases. For the experiments, a DC voltage of 1kV was applied across the sample and PEA measurements were recorded at times less than 10s to keep the formation of any space charge to a minimum. For the simulations, the properties of table 5.4 were used in the case of the semicon top electrode but the material properties of the top electrode were changed from those of semicon to those of aluminium for the aluminium top electrode simulations.

The PEA measurements in both cases of semicon-Al and Al-Al electrodes have been conducted. In addition, the result of PEA simulation model was obtained first with semicon-Al electrode and then the model was modified by changing the mechanical

properties (Effective modulus and Density) of the semicon electrode to Al to obtain the simulation result of Al-Al electrodes. After correcting and normalising the simulated PEA acoustic waves (as the same as process as conducted in figure 5.12), the experimental and simulation results were plotted for comparison on the same graph shown in figure 5.14. The experimental results for the two cases show that when the top electrode of PEA was semicon, the amplitude of top electrode was much higher and similar to that of the first peak than was the case when Al was used for the top electrode [137]. This is because when the top electrode is semicon there is a good acoustic match between the sample and the top electrode and the pressure wave formed at the top electrode interface would not suffer reflections and the acoustic pressure waves propagating into the sample and into the top electrode will have the same magnitude. In the case of an Al top electrode, the peak at the top electrode interface is significantly reduced owing the reflection of acoustic pressure waves at the interface between the sample and the top Al electrode interfering with the directly propagating acoustic wave. As shown in figure 5.14 good agreement is found between the simulations and experiments for the two cases.

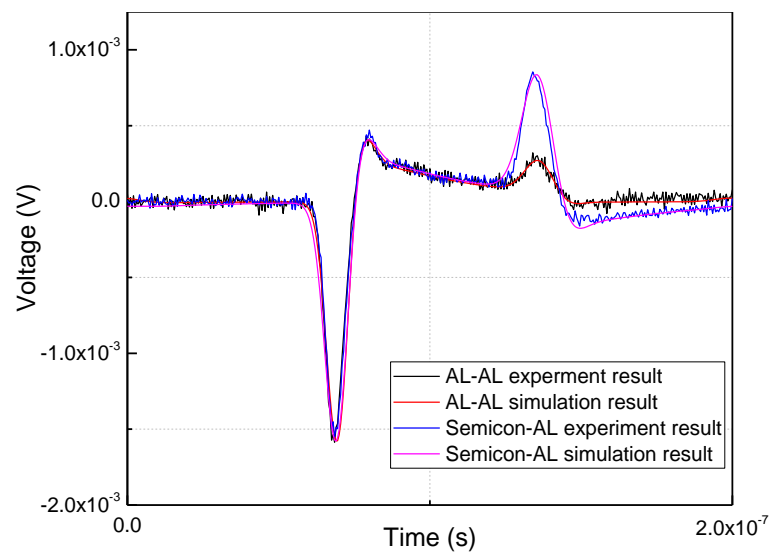


Figure 5.14: Influence of top electrode on PEA acoustic wave.

5.12 Effect of temperature gradient on PEA acoustic wave

In situations where there is a temperature difference applied across a sample, the simulation model parameters must take on temperature dependent quantities as described in section 5.4. If there are no sources of heat within the insulation due to Joule heating, then the resultant steady state temperature profile will be the solution to Laplace's

equation subject to the temperatures of the two sides of the sample as boundary conditions. For plane-plane geometry in 1-D the solution to Laplace's equation is a linear function of temperature (uniform temperature gradient). As the semicon material is just carbon loaded polyethylene, the thermal conductivity of the semicon layer was made the same as the sample material[76]. There will therefore be a uniform gradient of temperature between the temperatures applied to each side of the semicon and sample sandwich as illustrated in figure 5.2. The temperature drop across the upper aluminium (Al) electrode that forms the electrical contact with the semicon has been neglected due to its relatively high thermal conductivity which is about 208W/mK [138]. The temperature drop across the lower Al electrode and the other layers below the bottom Al electrode (PVDF, PMMA) have also been discounted and their temperature assumed to be the same as ambient temperature (20 °C). Therefore, only the temperature drop across the semicon and insulation sample have been accounted for in the simulation model. Figure 5.15, shows the temperature profile in a PEA layers in case of 40 °C temperature gradient.

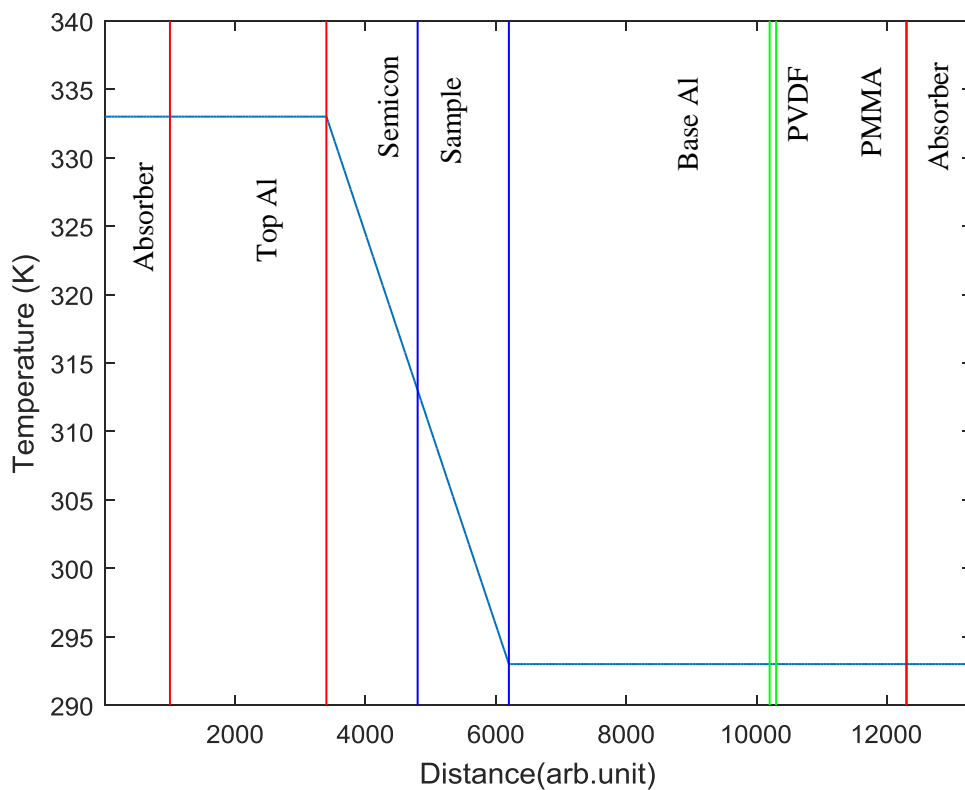


Figure 5.15: Temperature profile across the PEA layers in case of 40 °C temperature gradient across the semicon and the sample.

In order to calculate the effect of this temperature gradient on the PEA acoustic response, the acoustic properties of the semicon electrode material were assumed to have the same temperature dependence as the sample material. The temperature dependent values of the material parameters of effective modulus, density and permittivity were calculated using equations 5.18, 5.19 and 5.21 respectively. For the following simulations the sample and semicon layers were assumed to have a thickness of 150 μm . The temperature of the Al bottom electrode was kept constant at an ambient temperature of 20°C and the temperature of the Al top electrode was varied from 20°C to 60°C. Table 5.5 shows the material properties (effective modulus, density and permittivity) of LDPE sample under different value of temperature, T. At intermediate temperatures, the actual properties can be found from linear interpolation.

Table 5.5: Material properties of LDPE sample at different temperature gradient.

Material Property	$\Delta T=20\text{ }^{\circ}\text{C}$	$\Delta T=30\text{ }^{\circ}\text{C}$	$\Delta T=40\text{ }^{\circ}\text{C}$	$\Delta T=50\text{ }^{\circ}\text{C}$	$\Delta T=60\text{ }^{\circ}\text{C}$
Effective modulus (Gpa)	3.987	3.628	3.3286	2.961	2.653
Density (kg/m^3)	917	915	914	913	911
Permittivity	2.3	2.287	2.285	2.282	2.277

The PEA simulation parameters are given in table 5.6 and the simulation procedure is shown in figure 5.16.

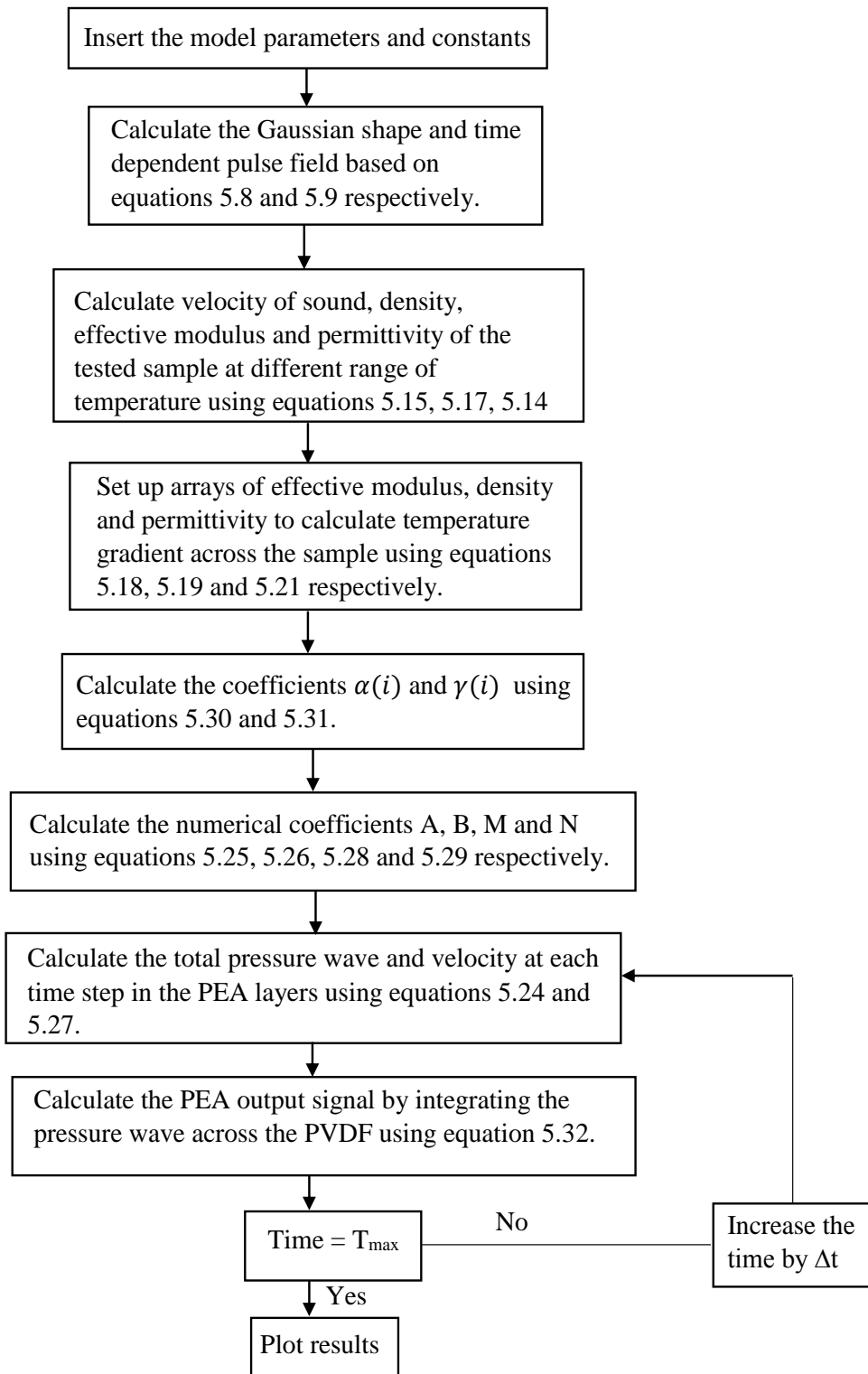


Figure 5.16: Simulation procedure of temperature gradient in a PEA system.

Table 5.6: Material properties used in PEA simulation in case of temperature gradient $\Delta T=0$ °C.

Material	Density (kg/m ³)	Effective modulus (GPa)	Velocity (m/s)	Thickness (mm)	Relative permittivity
Top absorber	1200	8.7	2692	4	1
Top Aluminium	2700	107	6295	7	\
Semicon	917	3.987	2085	0.15	2.3
Polymer	917	3.987	2085	0.15	2.3
Bottom Aluminium	2700	107	6295	10	\
PVDF	1760	10.8	2477	0.009	8.4
PMMA	1200	8.7	2692	5	4
Bottom absorber	1200	8.7	2692	4	1

The PEA simulation results assuming no space charge in the material (and therefore uniform applied electric field) are shown in figure 5.17 for different temperature gradient, ΔT , of 0, 10, 20, 30 and 40 °C.

As can be seen from figure 5.17, the establishment of a temperature gradient between the upper Al and lower Al electrodes leads to three consequences regarding the obtained PEA simulated response. Firstly, increasing temperature decreases effective modulus and density and hence the velocity of the acoustic wave propagation. The result is that the position of the upper semicon electrode charge peak is displaced to longer times when the temperature gradient is increased. In addition, the semicon charge peak has a reduced amplitude relative to the near constant amplitude bottom electrode charge peak when increasing the temperature gradient. As a constant electric field was applied in each case, the reduction of the signal amplitude at the semicon interface cannot be explained as due to a real change in the electric field profile or due to attenuation and dispersion. Instead this effect is due to the propagation of the acoustic pressure waves in a medium of continuously changing acoustic impedance. As the acoustic wave propagates at each small step in the insulator material, a fraction of the pressure wave is reflected back in the opposite direction due to the changing acoustic impedance. The transmitted wave therefore decreases slightly in amplitude as it propagates through the sample. Increasing

the temperature gradient increases the amplitudes of the incremental reflected waves and therefore the decreases the amplitude of the semicon electrode peak. The third effect is due to the incremental reflection as the acoustic wave generated at the aluminium electrode that is propagating towards the top electrode which also gives incremental reflections that propagate through the aluminium base electrode to the detector. These reflected waves produce a small PEA response in the bulk of the material that changes slightly the baseline of the PEA response between the interface charges due to the electrodes. The temperature gradient simulations described above are somewhat artificial in that it is assumed that the applied electric field is uniform and that the temperature dependence on electrical conduction has no consequence. This will be addressed in the next chapter when the electro-thermal conduction model is used to predict space charge accumulation and electric field distributions that can then be applied to the PEA simulation model.

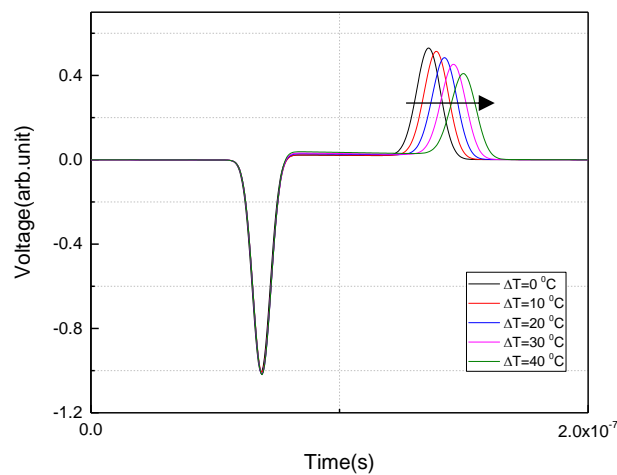


Figure 5.17: PEA acoustic wave at different temperature gradients.

5.13 Summary

In this chapter a simulation model was developed for a complete 1D PEA measurement system including the generation, propagation, attenuation, dispersion and detection of the acoustic waves from space charge. The chapter also included the effect of the HP filter response of the PVDF capacitance and the input resistance of the buffer amplifier as well as the LP filter response of the limited frequency response of the storage oscilloscope.

From the simulation results it was found that there is a mismatch between the PVDF and PMMA layer of the experimental PEA system which produces an overshoot in the signal following each electrode charge peak and this distortion could potentially lead to a misinterpretation of the actual space charge density. Acoustic mismatch between the semicon and the insulation material can also lead to non-ideal responses. The amplitude of the second peak corresponding to the position of the semicon/insulator interface is influenced whilst the peak corresponding to the aluminium electrode is unchanged. From the point of view of interpreting the PEA raw data in terms of a space charge distribution, when the effective modulus of the semicon is less than that of the insulator, the space charge density at the semicon/insulator interface is overestimated. This effect may lead to errors if the difference in the peak amplitudes is considered to be due just to attenuation and dispersion. In all simulations of this chapter, the samples were assumed free of space charge. Comparison with experimental raw PEA data is possible when the raw PEA data was obtained at low voltage and immediately after voltage application to avoid the accumulation of space charge. Comparison between the measured raw PEA data with the simulated data show good agreement and where system artefacts such as acoustic reflection at the PVDF/PMMA interface, attenuation/dispersion, and the PVDF/buffer amplifier response are successfully reproduced. Good agreement was also found between the simulation and experimental results in case of semicon-Al, Al-Al electrodes on PEA output data which show the validation of simulation models.

Finally, the results of PEA simulation in case of a temperature gradient within the sample were discussed. It was found that a temperature difference between the electrodes has three effects on the PEA output signal. The position of the sample-semicon peak moves to longer times, the amplitude of the sample semicon peak decreases due to back reflection of the pressure wave as it propagates through the sample and lastly, there is a small base line change between the electrode peaks due to back reflection of the backwards propagating acoustic pressure wave from the sample aluminium electrode.

The next step is to couple this simulation model with the charge transport model of chapter 4 to form a complete model of space charge accumulation in which the processes of space charge accumulation in dielectric material can be combined with simulation of the measurement of space charge. This will enable charge accumulation models to be developed that can be compared directly with experimental raw PEA space charge measurement data without the need to employ the traditional approach of using unstable deconvolution techniques to recover the space charge data from the raw PEA output data. The combined simulation approach will be developed in the next chapter.

6 Combining the Simulation Models and Comparing Their Results with the PEA Measuring Result

6.1 Overview

In this chapter, the electro-thermal charge transport simulation model introduced in chapter 4 and the PEA simulation model introduced in chapter 5 will be merged to be able to reproduce space charge accumulation and generate raw PEA space charge data that can be compared with experimental raw PEA data. The aim is to use the combined model as an alternative approach or framework for the robust interpretation of space charge accumulation data without the need to apply mathematically unstable algorithms to reconstruct the space charge profiles using the traditional methods as described in chapter 3. The methodology of combining the two simulation models is described in section 6.2. In section 6.3, the combined model will be applied to the case of single layer samples under isothermal conditions and for the cases of voltage application (polarisation) and voltage removal (depolarisation). In the cases of the polarisation and depolarisation simulations were conducted using different polarities. In section 6.4, the combined model will be extended to the case of an imposed temperature gradient. In section 6.5, the model will be extended to the case of two layer samples under isothermal conditions when subject to polarisation and depolarisation. In all simulations cases, the simulated results will be compared to experimental raw PEA data.

6.2 Combining the two simulation models

The electro-thermal charge transport model of a thin film sample (chapter 4) enables the space charge and electric field distribution to be predicted in 1-D thin film samples as a function of time. The charge transport model encompasses the field and temperature dependent electrical conductivity and modification to the electrical conductivity due to the diffusion of impurities. The electro thermal charge transport model predicts the space charge electric field and temperature distributions inside the sample material as a function of time. However, in order for the simulation model to be useful, the simulated charge distributions have to be compared with experimental PEA data. The 1-D simulation of a PEA acoustic signal as described in the previous chapter can be used to achieve this. The electric field distribution that is predicted from the charge transport model can be used as the input to the 1-D PEA simulation model to predict the measured raw data. Therefore, instead of employing the traditional but mathematically unstable approach of working backwards using signal processing from the PEA raw output data to reconstruct the space charge profile, a model of the charge transport and electrical conduction processes in the

insulating material is used as the input to PEA simulation model, and hence providing an output that can be compared directly with the experimental data. The procedure of combining these models and comparing with experimental data is illustrated by the flowchart diagram shown in figure 6.1. The electric field, $E(x)$, that is obtained from the modified charge transport model is used as an input for the 1-D PEA acoustic model. The result of the PEA simulation model is then corrected for attenuation, dispersion and for the PVDF/amplifier response to generate the simulated raw PEA data. A MATLAB set of programmes has been written to perform the calculations shown in figure 6.1. These were then applied to simulate experimental raw PEA data.

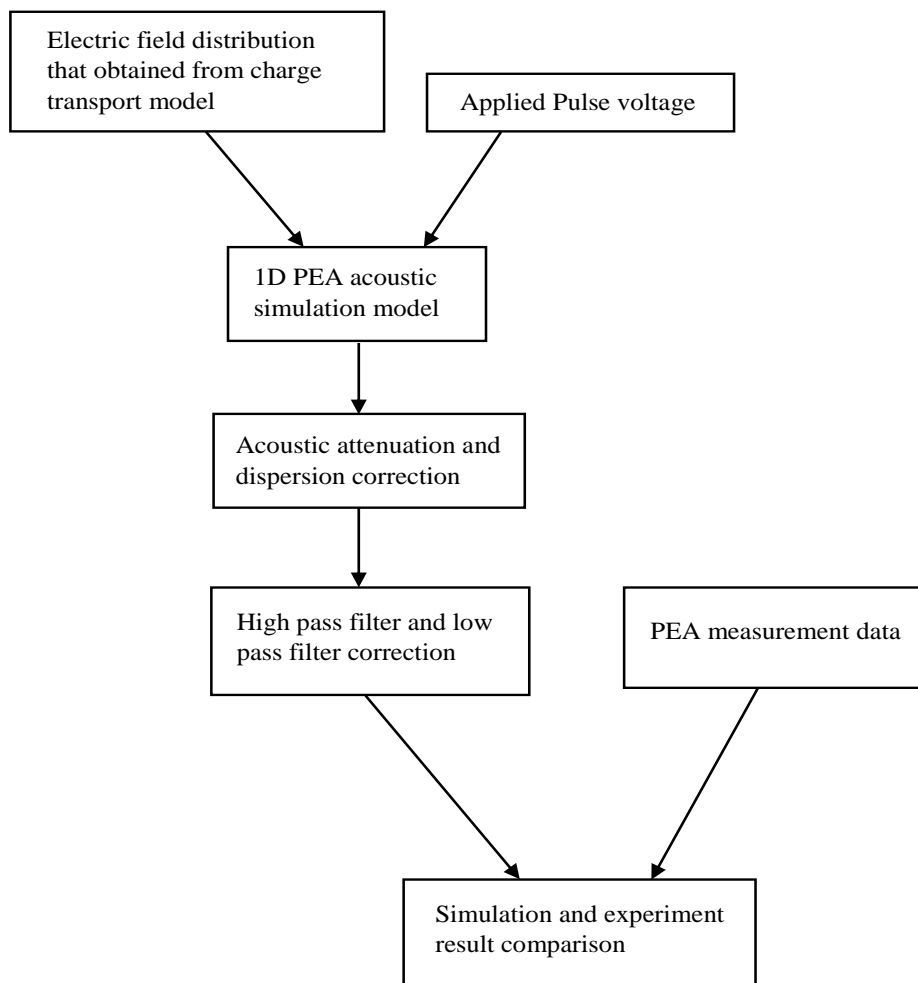


Figure 6.1: Procedure of combining the simulation models and comparing with the PEA raw data.

6.3 Simulation of charge accumulation and PEA raw data in single layer LDPE sample under isothermal conditions.

The simulation models of figure 6.1 have been applied and compared with experimental raw PEA space charge data during polarisation (voltage application) and depolarisation (voltage set to zero). In this case the conductivity is considered to be just field dependent, which means the measurements were conducted under isothermal temperature (20 °C) and there was no temperature difference between the PEA electrodes. In this case the effect of temperature was neglected in the simulations.

The charge transport model parameters especially those of the empirical conductivity equation were identified by trial and error to produce a close fit with the experimental results. The fitted values of the parameters will therefore have some variance and will be influenced by differences in the physical and environmental conditions under which each of the experiments had been conducted. For example, thin film thickness varies from one sample to another and temperature of the laboratory varies during each day. It should be mentioned that, in the case of field dependent conductivity, having identified the parameters for best-fit for the polarisation measurements, they were kept fixed throughout all subsequent simulations when depolarisation conditions were also considered.

6.3.1 Space charge accumulation under positive voltage application

6.3.1.1 Experimental PEA data

Here, typical raw experimental PEA space charge measurements were obtained under different polarities and different applied voltages. Figure 6.2 shows typical PEA raw output data of the case which was obtained from a 150 μm flat plane LDPE fresh (non-degassed) sample under 5kV DC applied voltage at different time instants. The Al electrode was at earth potential and the semicon electrode was at positive 5kV. It can be seen that the dominant change in the raw space charge profile with time was that the negative charge at the Al electrode decreased in magnitude with time and at the same time negative charge spreads into the bulk of the sample (as indicated by the arrows). This homo-charge accumulation in the bulk adjacent to the Al electrode causes positive charge to be induced at the Al electrode and this is the reason for the decrease in negative electrode charge. At the semicon (Sc) electrode, positive charge is observed to spread slightly into the sample (again indicated by the arrow in figure 6.2). This means that during poling time, homo-charge was injected from both electrodes.

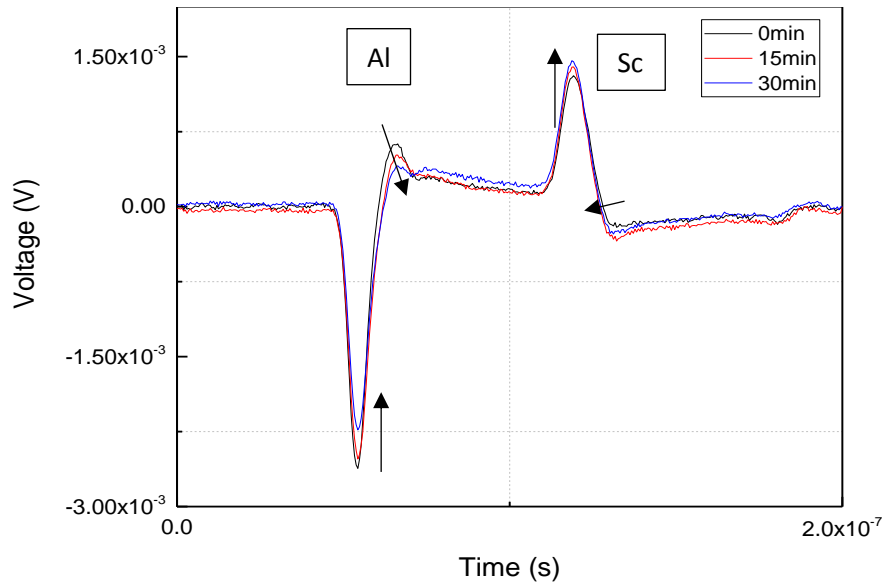


Figure 6.2: The PEA output data of LDPE sample at different voltage stressing time.

6.3.1.2 Simulation of experimental PEA data

To be able to obtain simulation results that are a good match to the experimental raw PEA results shown in figure 6.2, the parameters of the charge transport model of 1-D thin film sample were identified by trial and error and are given in table 6.1. In table 6.1, the parameters of homo-charge accumulation from both electrodes an exponential conductivity enhancement factor (as described in section 4.4) and previously used by Boggs [58] was necessary to model the charge accumulation behaviour found in the experiment. As temperature was assumed isothermal, the distribution of electric conductivity, $\sigma(x)$, was determined from the electric field dependent conductivity, $\sigma(E)$, and distance dependent conductivity. The procedure of calculation is the same as shown in chapter 4, figure 4.5, but here field and distance dependent conductivity $\sigma(E, x)$ is used instead of field dependent conductivity, $\sigma(E)$, and therefore the formula of equation (4.27) is used instead of equation (4.25). Figure 6.3, shows the result of the electrical conductivity enhancement due to impurity diffusion from the semicon electrodes, following Boggs et al. [58], as obtained from the simulations after 30 minutes.

Table 6.1: Charge transport model constants.

Constants	Symbols	Values
Applied voltage	V	5kV
Conductivity Constant	σ_0	$5.85 \cdot 10^{-18}$ S/m
Relative permittivity	ϵ_r	2.3
Vacuum permittivity	ϵ_0	$8.854 \cdot 10^{-12}$ F/m
Electric field reference	E_0	10kV/mm
Field Power Index	γ	1.8
Conductivity enhancement factor (Al)	n_a	3.3
Conductivity enhancement factor (semicon)	n_b	1.37
Depth of Conductivity Enhancement (Al)	d_a	$25 \mu\text{m}$
Depth of Conductivity Enhancement (semicon)	d_b	$15 \mu\text{m}$

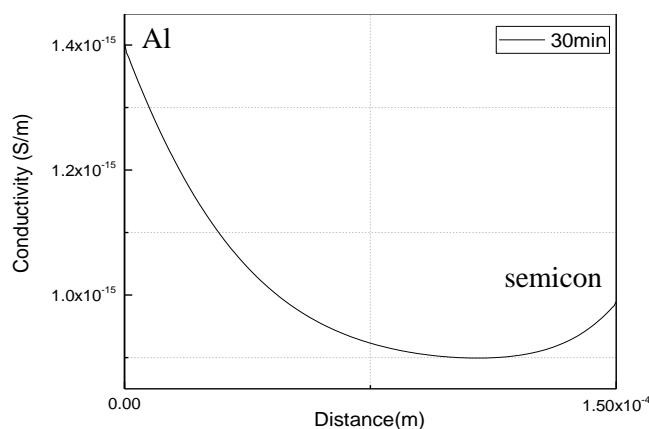


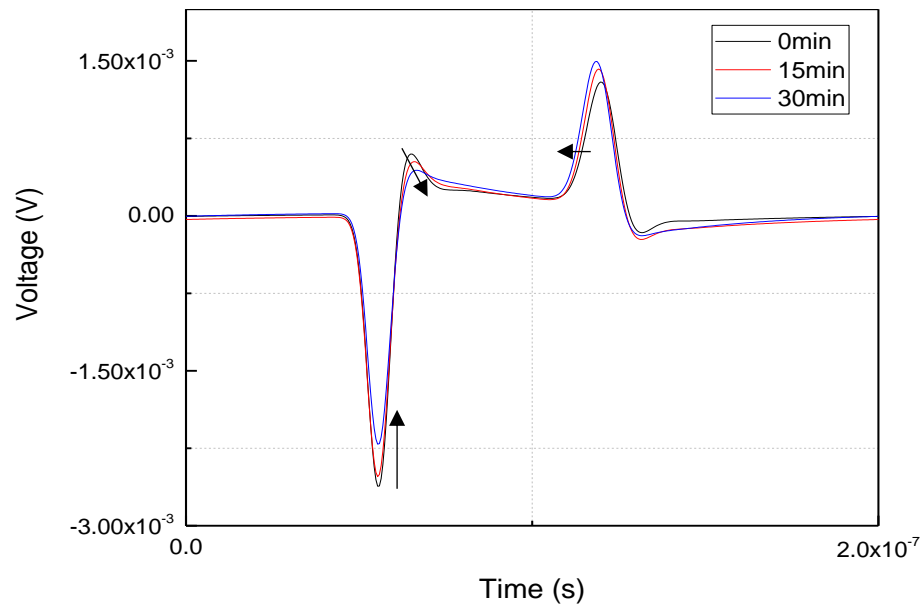
Figure 6.3: Conductivity enhancement due to impurity diffusion from the electrodes after 30minutes.

At pre-defined time steps, the simulated electric field distribution, $E(x)$, of the charge transport model was used as the input to the PEA simulation model. The parameters of the PEA simulation model were the same as those shown in table 5.3. These parameters were obtained from matching the PEA simulation to the experimental calibration data for the PEA instrument obtained at room temperature.

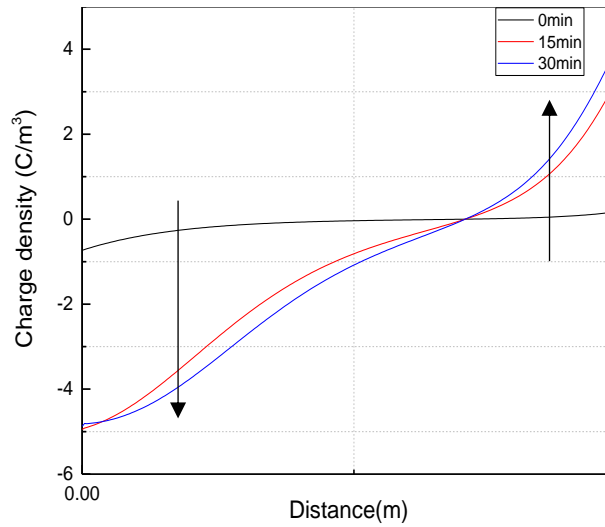
The simulation results of raw PEA data obtained over the same time intervals as the experimental measurements are shown in figure 6.4(a). The corresponding space charge

profile at each time interval which was obtained from the charge transport model is shown in figure 6.4(b). It can be seen that the electrical conductivity near to the sample interfaces is enhanced due to impurity diffusion, and this caused accumulation of homocharge inside the sample with time. However, the amount of negative homocharge accumulation near the Al was much larger than that accumulated adjacent to the semicon electrode. Therefore, the negative homocharge moves further into the bulk of the sample than the positive homocharge from the semicon electrodes. This has the effect of reducing the electric field at the Al electrode and within the region of the dielectric adjacent to the Al electrode and increases the electric field within the bulk of the sample as shown in figure 6.4(c). The electric field at the semicon electrode remains unchanged throughout this period.

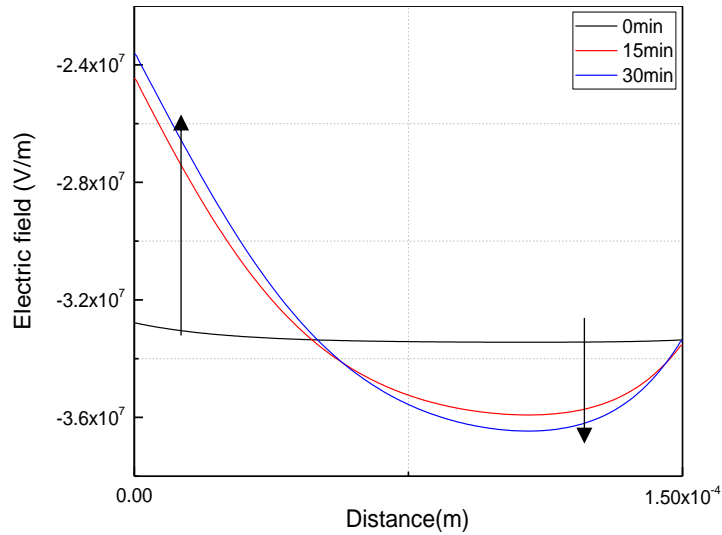
The simulation of the PEA raw data, figure 6.4(a) are therefore in good agreement with the experimental data, figure 6.2, in terms of both the space charge profiles and the time intervals for the accumulation of space charge. The space charge distribution and electric field distributions obtained directly from the charge transport simulation are therefore representative of this sample yielding PEA responses similar to the experimental raw data. In addition, using this technique it is not necessary to process the raw PEA data to recover the space charge distribution.



(a)



(b)



(c)

Figure 6.4: (a) voltage, (b) charge density, (c) Electric field distribution that obtained from the simulation models of LDPE sample to be able to compare with the experimental result (Figure 6.2) at different ageing time.

6.3.2 Space charge decay following positive voltage application

6.3.2.1 Experimental PEA data

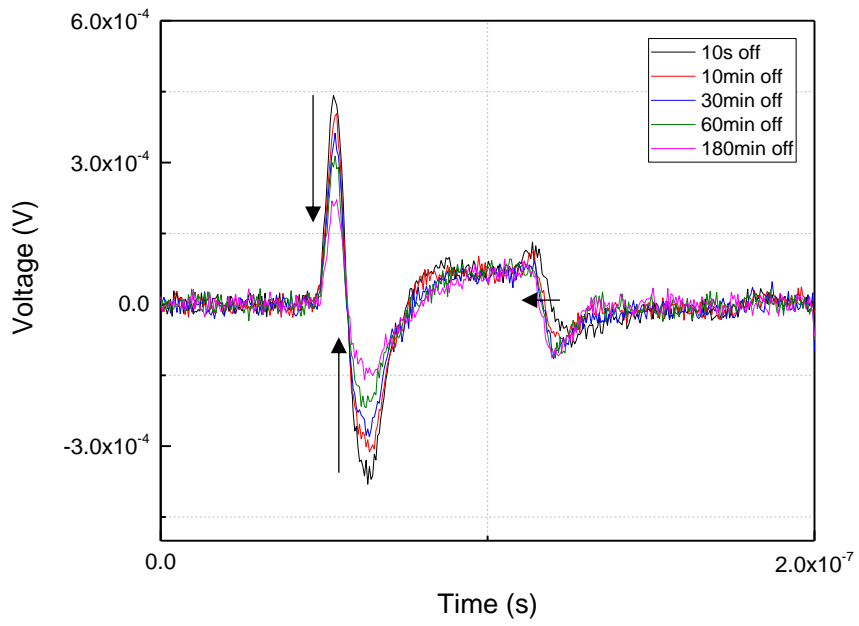
Following the experimental PEA polarisation measurements at an applied voltage of 5kV for 30 minutes, the applied voltage was then set to zero to allow the accumulated space charge to decay. The PEA raw data, which records the remaining charge within the sample was acquired periodically after removing the applied voltage. This data is presented in figure 6.5(a) and shows the raw PEA measurements that were taken at various time intervals during the decay period of 3 hours total.

6.3.2.2 Simulated raw PEA data

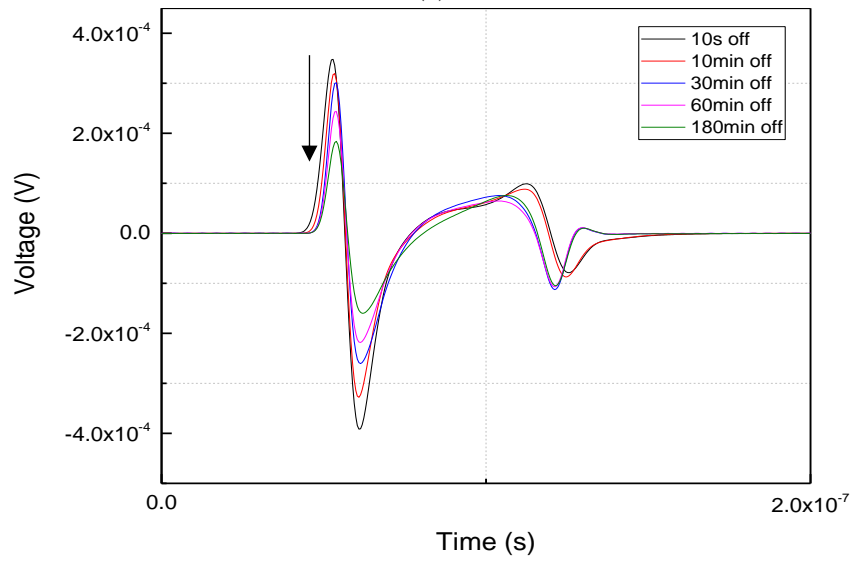
Numerical simulations of the charge decay behaviour using the charge transport and PEA simulation models with the same parameters as used previously except that the applied voltage was set to zero and the initial space charge distribution was that simulated at the end of the 30 minutes of polarisation was used as the initial condition. The simulated PEA raw data and the corresponding charge distribution from the transport model are shown in figures 6.5(b) and 6.5(c) respectively.

Comparing figure 6.5(a) (experimental raw PEA data) and figure 6.5(b) (the simulated raw data), demonstrates good agreement in terms of the shape of the PEA response and the dynamics of the charge decay. The results show that the homocharge that was accumulated during the polarisation phase causes opposite sign charges to be induced on the semicon and aluminium electrodes of the PEA. The amount of homocharge and its induced charges decay with time. The way in which the space charge decays is clearly seen in the space charge and electric field profiles obtained from the charge transport model, figure 6.5(c). The charge close to the Al electrode decays faster compared with charge decay at the semicon after the applied voltage had been removed. Therefore, in the first 30 minutes of the decay process, only the negative charge close to the aluminium electrode decays as in this region the internal electric field and the field dependent electrical conductivity is highest. However, there appears some decay of positive space charge adjacent to the semicon electrode after 30 minutes of depolarization, but still much smaller than those decays from the Al electrode. This is because the field dependent conductivity and the electric field at the semicon electrode remains small compared with that close to the Al electrode, as shown in figure 6.5(d), therefore the space charge in this region needs longer time to decay away.

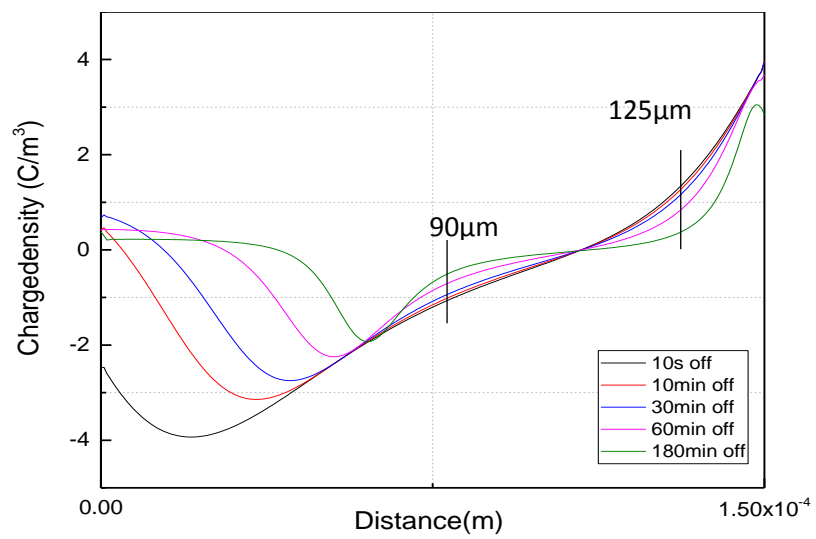
The result of the depolarization in both PEA raw data and charge transport model show that the insulation polymer holds up the decay of space charge for longer period of time compared with the time of accumulation charge during the initial polarization. Moreover, in figure 6.5(c) it is observed that the space charge first decays in the regions close to Al electrode and that some charge remains at depths of 90 μm and 125 μm in the insulation bulk even after 180 minutes. The combined simulation model is again shown to be successful this time in modelling the charge decay during depolarisation.



(a)



(b)



(c)

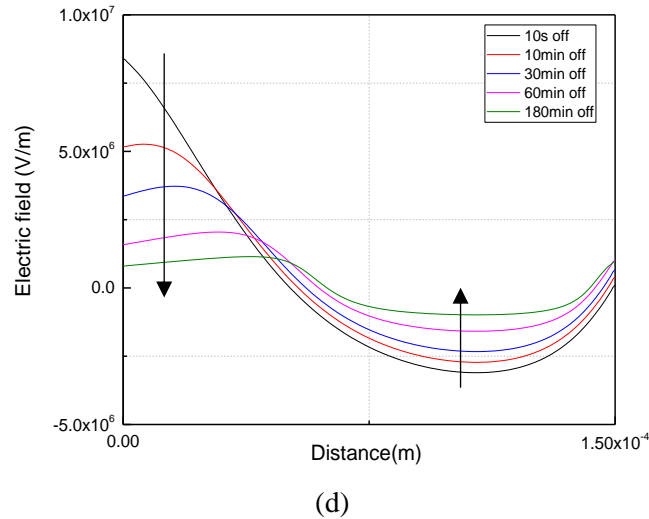


Figure 6.5: (a) PEA measurement data, (b) PEA simulation data, (c) Charge density profile, (d) Electric field distribution, in LDPE sample after removing the applied voltage.

6.3.3 Space charge accumulation under negative voltage application

Given the success in reproducing raw PEA data through simulation as described in the previous section, a repeat set of experimental PEA space charge measurements were undertaken on another fresh (non-degassed) LDPE sample during the polarisation (space charge accumulation during initial voltage application) and depolarisation (discharge of space charge when applied voltage was set to zero). The aim of this set of experiments and simulations was to determine if the simulation model is able to reproduce the space charge behaviour under the different voltage stressing regimes of polarisation, depolarisation and under opposite polarity of applied voltage. For this set of experiments, space charge was initially measured in a 150 μ m thick LDPE material under a negative applied DC voltage of -6kV applied to the top electrode and which corresponds to an applied DC electric field of 40kV/mm, 15kV/mm greater than used in the previous experiment and of opposite polarity.

6.3.3.1 Polarisation

The PEA raw experimental data taken during the polarisation phase of 30 minutes is shown in figure 6.6(a). The raw space charge profiles from the PEA instrument show similar characteristics and dynamics to those found in the original experiment at 5kV except that the polarity of the profile is inverted owing to the different polarity of applied voltage. There is an accumulation of homocharge adjacent to the Al electrode which causes induced charges on the Al electrode and the total charge on the Al electrode to decrease.

Simulations of these experimental results were obtained using the charge transport simulation model and the PEA simulation model. In this case, the same parameters of table 6.1 were used as the starting point except that the applied voltage, -6kV was used instead of 5kV. The parameters for the charge transport model were then adjusted and combined with the PEA simulation model to get match with the measured PEA raw data. In order to achieve a good match, it was found that the homocharge accumulation near the two electrodes are different in character to that found with the previous simulations. It is obvious from the experimental PEA raw data that again most of the accumulated homocharge is adjacent to the Al electrode when compared with homocharge accumulation at the semicon (top) electrode. Therefore, to reflect this, the model parameters related to the conductivity enhancement were the main parameters that required significant changes from those shown in table 6.1 to those shown in table 6.2 in order to achieve a good fit to the experimental data.

Table 6.2: Charge transport model constants.

Constants	Symbols	Values
Applied voltage	V	-6kV
Conductivity Constant	σ_0	$5.7 \cdot 10^{-18}$ S/m
Relative permittivity	ϵ_r	2.3
Vacuum permittivity	ϵ_0	$8.854 \cdot 10^{-12}$ F/m
Electric field reference	E_0	10kV/mm
Field Power Index	γ	1.8
Conductivity enhancement factor (Al)	n_a	4.5
Conductivity enhancement factor (semicon)	n_b	1.4
Depth of Conductivity Enhancement (Al)	d_a	$40 \mu\text{m}$
Depth of Conductivity Enhancement (semicon)	d_b	$10 \mu\text{m}$

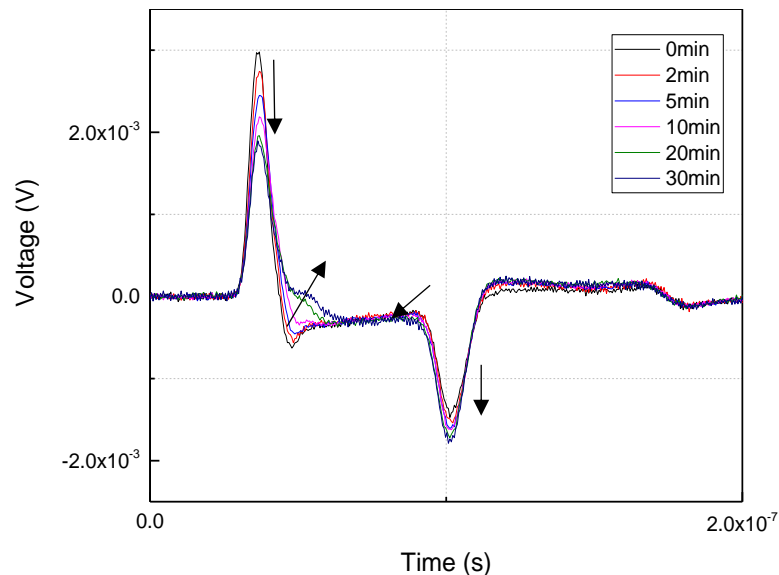
As shown in the parameters of table 6.2, the positive homocharge enhancement factor at the Al electrode is 4.5, whereas the negative homocharge enhancement factor at the semicon electrode is just 1.4. In addition, the thickness of positive homocharge accumulation region from the interface of anode electrode was $40 \mu\text{m}$, while the thickness of negative homocharge accumulation was just $10 \mu\text{m}$. According to the interpretation

given by Boggs et al [58], in the case of the sample used here, it would appear that the impurity diffusion is greater at the Al electrode and less at the semicon electrode.

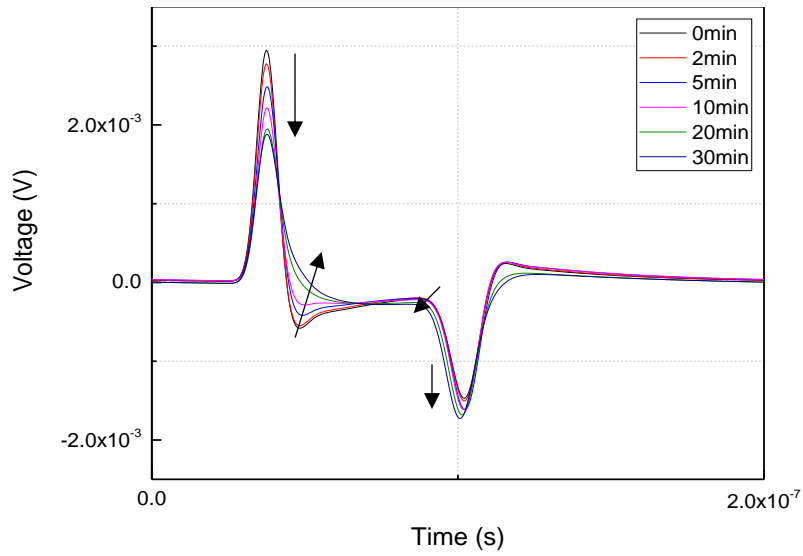
The results of the simulation of the first 30 minutes of polarisation are shown in figure 6.6(b) to 6.6(d). In figure 6.6(b) the simulated PEA data is in good agreement with the experimental raw PEA data as shown in figure 6.6(a).

Figure 6.6(c), shows the corresponding space charge profiles obtained from the charge transport simulations. Space charge is seen to be accumulated within the aluminium electrode side and into the material to a greater extent compared with the semicon homocharge accumulation. This led to a decrease in the electric field at the aluminium electrode and a smaller increase in electric field at the semicon electrode as demonstrated in the electric field profiles shown in figure 6.6(d). The data of electric field distribution (figure 6.6(d)) at different time intervals was used as an input of the PEA simulation in order to simulate the raw data shown in figure 6.6(a).

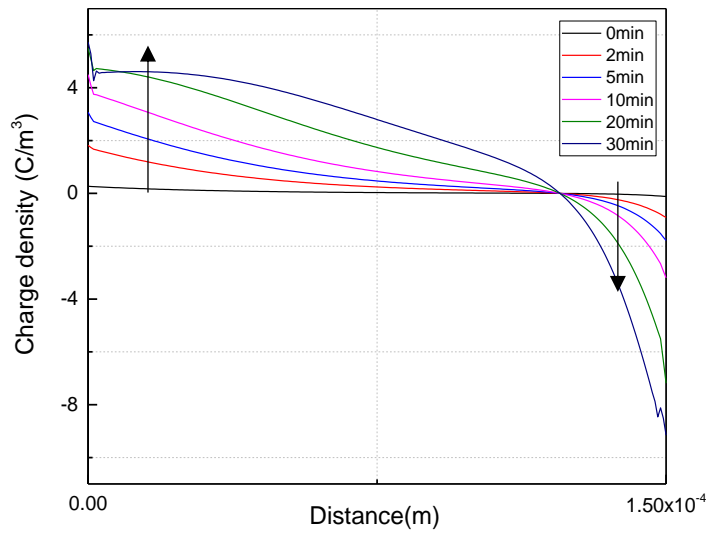
In both cases of polarization, the results of both positive and negative polarities of applied voltage showed that a good agreement can be obtained between the PEA measurements and PEA simulations as demonstrated in figure 6.2, 6.4(a) and 6.6(a), 6.6(b) respectively.



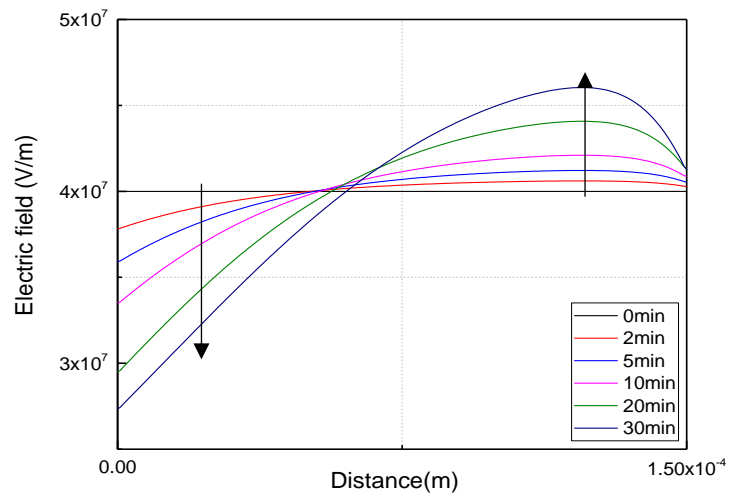
(a)



(b)



(c)



(d)

Figure 6.6: (a) Measurement PEA raw data, (b) simulation PEA data, (c) charge density profile, (d) electric field distribution, under 40kV/mm of DC applied voltage.

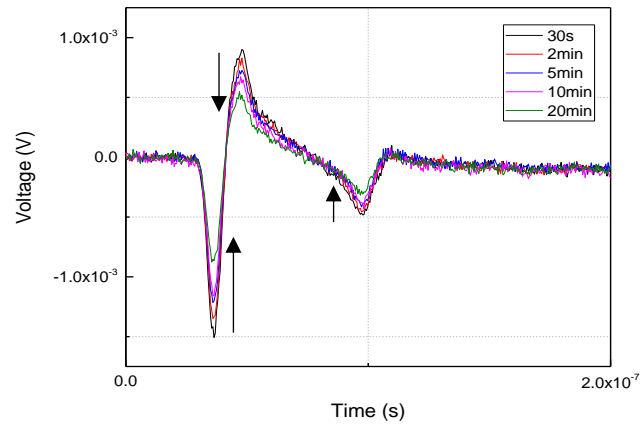
6.3.3.2 Depolarization

After applying -6kV to the PEA top electrode for 30min for the initial polarisation experiment as detailed above, the applied voltage was then set to zero and PEA space charge measurements were taken at regular intervals over the next 20 minutes. The raw experimental PEA data obtained during the depolarisation (voltage off measurement) are shown in figure 6.7(a). When the applied voltage was initially set to zero, the positive charge that was accumulated during polarization at the aluminium electrode side induces negative charge on the aluminium electrode. Similarly the smaller amount of negative homocharge that had accumulated at the semicon side of the sample induces a small positive charge on the semicon electrode. The accumulated homocharge then decays with time and this is also reflected in the reduction of the induced charges at the aluminium and semicon electrodes. However, even after 20 minutes, significant space charge remains.

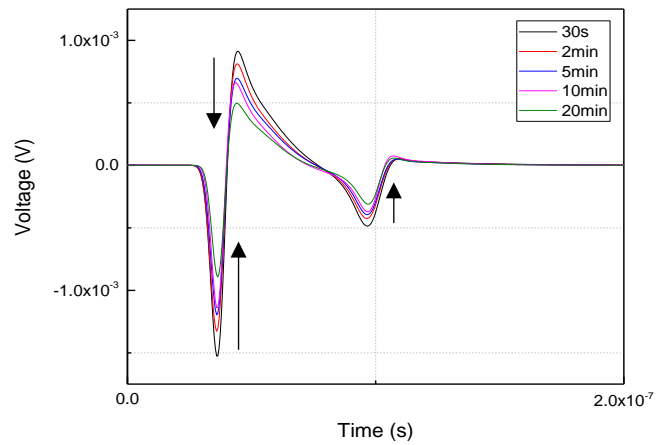
Depolarisation simulations were performed using the charge transport simulation model and PEA simulation model to replicate the raw PEA experimental data. The initial condition for the charge transport simulation was that the space charge distribution, $\rho(x)$ was kept the same as that obtained from the final time step of the polarisation simulation. The charge transport model also used the same parameters as found for the polarisation simulation, table 6.2, but here, the applied DC voltage was set to zero. The charge density profile and electric field distribution that obtained from charge transport model was saved in MATLAB at different time intervals (as the same time intervals as the PEA measurement data) as shown in figure 6.7(c) and figure 6.7(d) respectively. Again, the values of electric field distribution that are shown in figure 6.7(d) were used as an input of the PEA simulation model. The results of PEA simulation model is shown in figure 6.7(b). Comparing figures 6.7(a), the experimental raw PEA data with figure 6.7(b), the corresponding simulated raw PEA data, show good agreement and again seems to validate the simulation model.

The space charge distributions during the depolarisation obtained from the charge transport simulation, figure 6.7(c) as well as the corresponding electric field profiles, figure 6.7(d), provides further details regarding the decay process. Again, in the first 20 minutes of the decay process, only charge close to the aluminium electrode decays as in this region the internal electric field and the field dependent electrical conductivity is highest. Hence, after that time there is still positive space charge can be seen especially

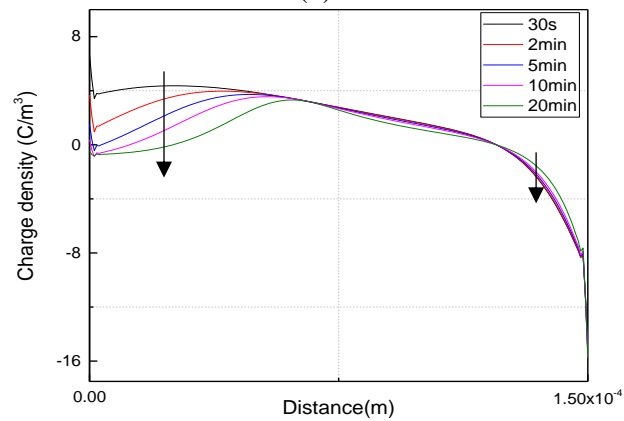
within the bulk of the sample. Moreover, there appears only to be a small amount of decay of negative space charge adjacent to the semicon electrode. This is because the field dependent conductivity and the electric field at the semicon electrode remains small compared with that close to the aluminium electrode, therefore the space charge in this region needs longer time to decay away.



(a)



(b)



(c)

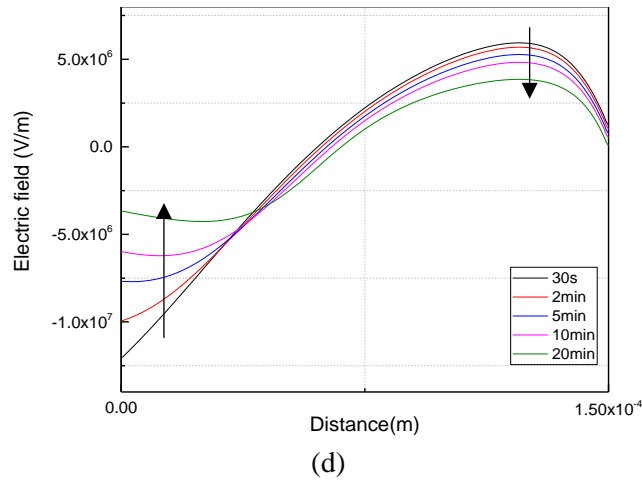


Figure 6.7: (a) PEA measurement result, (b) PEA simulation result, (c) charge density profile, (d) Electric field distribution during depolarization.

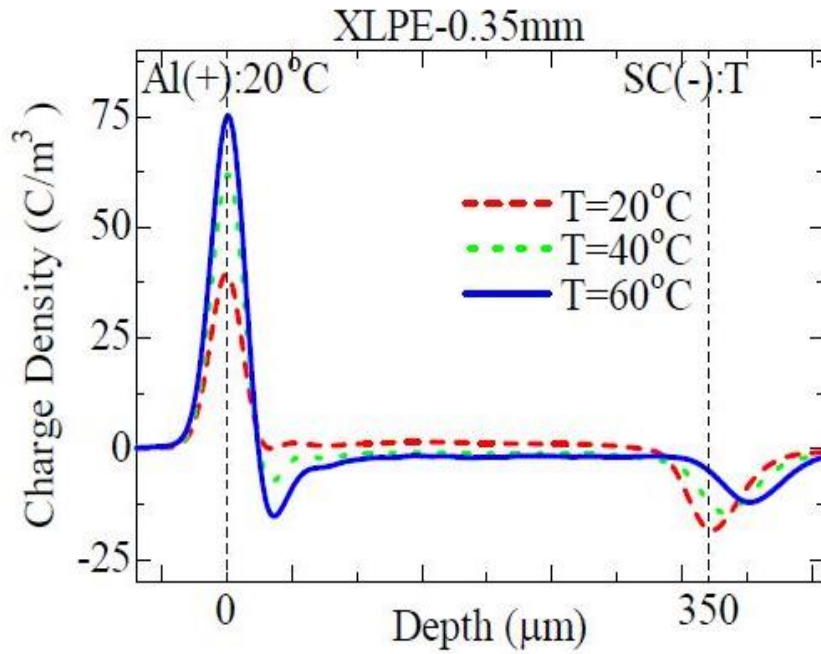
6.4 Simulation of charge accumulation and PEA raw data in single layer LDPE sample under temperature gradient.

The effect of temperature gradient on PEA acoustic properties and PEA output responses were described in chapter 5. However, in that case the sample was assumed free of charge and therefore only the Laplace form of electric field distribution was used as the input for the PEA simulation model and the charge transport model was not used. However, when a temperature gradient exists in an insulating material, the temperature dependent electrical conductivity of the material will cause space charge to build-up inside the sample modifying the internal electric field distribution. In this section, modelling of charge accumulation in thin film polyethylene samples using the electro-thermal charge transport model with an imposed temperature gradient and its subsequent detection is simulated using the PEA simulation model that was modified for acoustic pressure wave propagation in a material exhibiting a temperature gradient are described. For validation, the results of these simulations will be compared to raw PEA measurements obtained on samples containing a temperature gradient recently published in the literature [75] and where a bipolar charge transport simulation model was used in the interpretation. The experimental PEA data was obtained from a 350 μ m thick degassed thin film sample of cross linked polyethylene (XLPE) under three different temperature gradients, which were 0 $^{\circ}$ C, 20 $^{\circ}$ C and 40 $^{\circ}$ C.

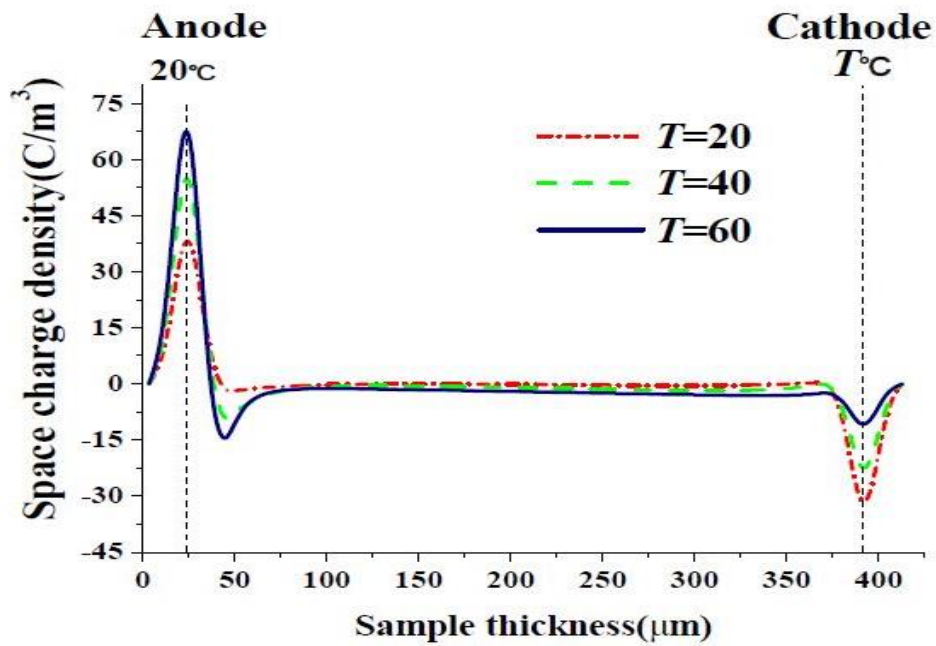
6.4.1 Experimental data

The experimental raw PEA data obtained from the XLPE sample under different temperature gradients is shown in Figure 6.8(a). In all three cases, the temperature of the aluminium electrode was kept constant at 20°C whilst the semicon electrode temperature (T) was set at 20°C, 40°C and 60°C giving temperature differences, $\Delta T = 0^\circ\text{C}$, 20°C or 40°C across the sample for each measurement. In all cases, the voltage applied to the semicon electrode was -17.5kV and the aluminium electrode of the PEA grounded. Under isothermal conditions, $T=20^\circ\text{C}$, the PEA output appears as a typical zero space charge measurement. The peak at the semicon interface has a smaller amplitude owing to attenuation of the acoustic pressure waves as they traverse the sample. When a temperature gradient is imposed, the amplitude of the peak at the the aluminium electrode increases whilst at the semicon electrode the peak amplitude decreases and moves to longer times. In addition there appears to be a build-up of negative space charge within the bulk of the sample with the greatest space charge density near the aluminium electrode. The observed changes to the PEA data appear to be in proportion to the magnitude of temperature gradient imposed. Referring back to chapter 5, many of these changes are expected for a PEA measurement in which a temperature gradient occurs within the sample. For example it is expected that the amplitude of the peak at the semicon electrode should decrease with increasing temperature gradient and that the position of the semicon peak shifts to longer times as the velocity of the pressure waves decreases at higher temperature. Similarly, a negative offset in the PEA response between the two electrode peaks should also be expected when a temperature gradient exists in the sample. The authors of [75] have attempted to explain the data using a bipolar charge transport model. Such models have been described briefly in section 4.1 and rely on the transport of positive and negative charge carriers. Consequently, such models require a significant number of parameters to characterise the transport of the charge carriers. Their simulation results are shown in figure 6.8(b) and (c). As can be seen, the simulated results based on the bipolar transport model reproduces most of the observed features of the experimental data except that the bulk charge within the material is underestimated and appears to be a maximum at the semicon electrode. Moreover, from the simulations, increasing the temperature gradient led to a significant increase in the amount of heterocharge present adjacent to the aluminium electrode. However the origin of this hetero-charge in case of temperature gradient, the authors suggested two possibilities [75]; the first possibility is due to ionization of impurities and by products in the bulk of

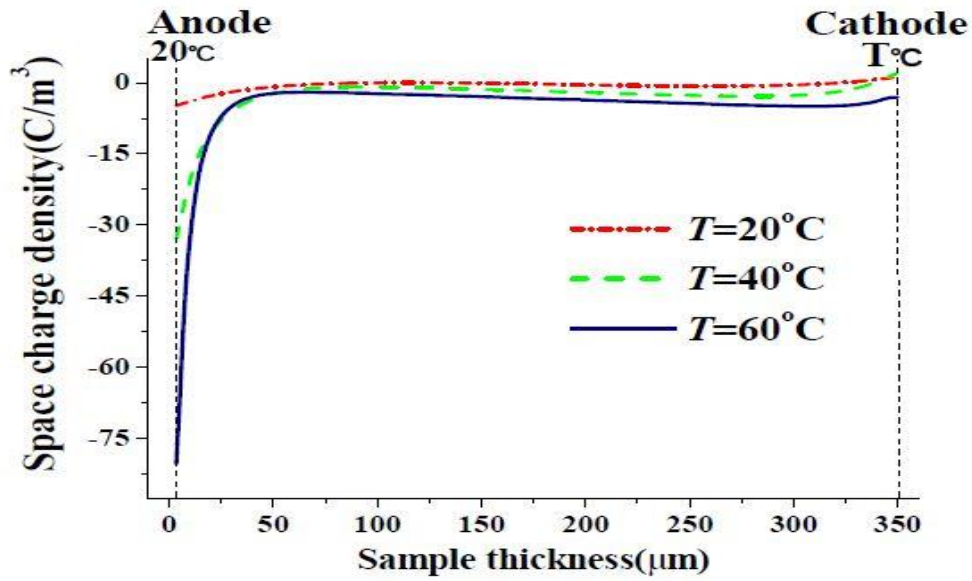
the material migrating towards the electrodes, while the second one is due to the blocked extraction of the negative carriers at the positive polarity aluminium electrode. However, they were not quite sure which one is the real source of heterocharge in case of temperature gradient.



(a)



(b)



(c)

Figure 6.8: (a) PEA measurement result, (b) and (c) simulation result of space charge distribution in case of temperature gradient [75].

6.4.2 Simulation of experimental data using the combined model

To validate the proposed combined simulation model approach and understanding the results of PEA measurements in which a temperature gradient exists in the sample as shown in figure 6.8(a), the electro-thermal charge transport model was modified to include field and temperature dependent electrical conductivity and an imposed temperature profile. The simulations were carried out without the electrical conductivity modification based on the diffusion impurities [58] as in [75] the XLPE material used was freshly made and therefore unlikely to have diffused impurities. The simulation procedure followed was described in figure 4.9 of chapter 4 where the temperature and field dependent electrical conductivity of the insulation was determined from the temperature and electric field profiles. Because the sample has homogeneous thermal properties, the temperature profile will be linear with distance inside the sample between the boundary conditions of temperature on each side of the sample. The simulations were conducted over a time interval of 20 minutes of voltage application (following ref [75]) from an initial condition of a space charge free sample at each case of temperature. The parameters of the charge transport model used are shown in table 6.3 and the parameters of the PEA simulation model in case of 20 °C temperature are shown in table 6.4. Figure 6.9(a) and (b) show the charge transport simulation results.

Table 6.3: Charge transport model constants in case of temperature gradient between the electrodes.

Constants	Symbols	Values
Applied voltage	V	17.5kV
Conductivity Constant	σ_0	$7.8 \cdot 10^{-18}$ S/m
Relative permittivity	ϵ_r	2.3
Vacuum permittivity	ϵ_0	$8.854 \cdot 10^{-12}$ F/m
Electric field reference	E_0	10kV/mm
Field Power Index	γ	2.1
Temperature reference	T_0	293K
Temperature coefficient	α	0.11K^{-1}

Table 6.4: Material properties of PEA layers in case of temperature T= 20 °C .

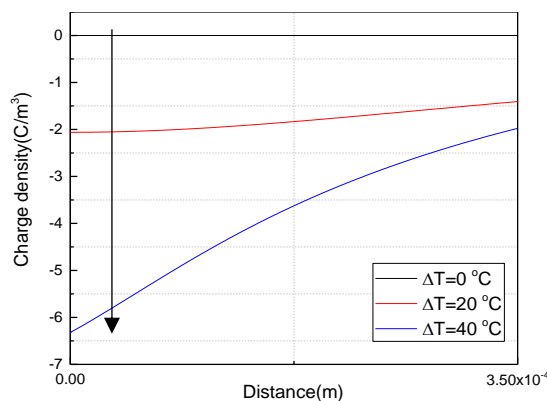
Material	Density (kg/m ³)	Effective modulus (Gpa)	Velocity (m/s)	Thickness (mm)
Top absorber	2700	107	6295	5
Top Al	2700	107	6295	10
Semicon	917	3.987	2085	0.3
Polymer	917	3.987	2085	0.35
Base Al	2700	107	6295	10
PVDF	1760	10.8	2477	0.009
PMMA	1200	8.7	2692	5
Bottom absorber	1200	8.7	2692	5

The charge density profiles obtained from the charge transport model are shown in figure 6.9(a). Under isothermal conditions (zero temperature gradient) no space charge forms within the sample. Introducing a temperature gradient has the effect of accumulating negative charge within the bulk of the sample. The density of this negative bulk charge tends to be highest where the temperature is lowest (in this case close to the aluminium

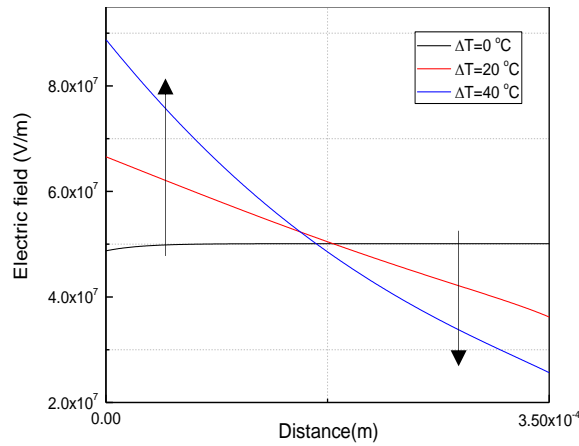
electrode). Increasing the temperature gradient causes more negative charge to accumulate within the bulk of the sample. The corresponding electric field profiles obtained from the charge transport model are shown in figure 6.9(b). These show that when a temperature gradient exists the internal electric field changes. The electric field is enhanced in the cooler region of the sample (close to the aluminium electrode) and decreases relative to the isothermal case within the hottest region of the sample (close to the semicon electrode).

In each case of temperature gradient the electric field distribution that obtained from the charge transport model (figure 6.9(b)) were used as an input for the PEA simulation model. The effective modulus, density and permittivity parameters are affected by temperature, their values at 20 , 40 and 60 °C for LDPE were already given in chapter 5 (table 5.5). These values were used to obtain their values across the thickness of the sample for each temperature gradient case, $\Delta T = 0, 20$ and 40 °C using the equations 5.17, 5.18 and 5.20 respectively. The computational procedure follows that shown in figure 5.16.

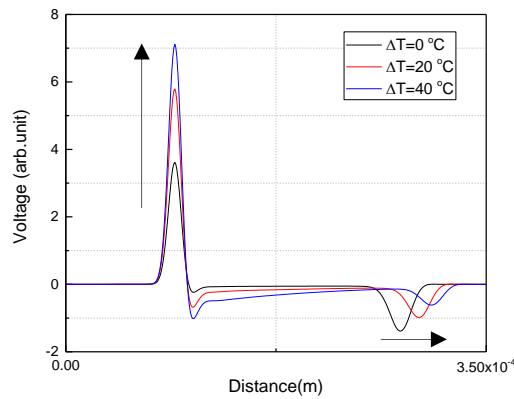
The final result of PEA simulation model is shown in figure 6.9(c), which was obtained from the combination of charge transport model and PEA simulation model. A good agreement can be seen between figure 6.8 (raw PEA data from the literature) and figure 6.9(c). All the observed features of the raw PEA data are reproduced in the combined simulation model and validates the proposed combined simulation model in case of a temperature gradient within the sample.



(a)



(b)



(c)

Figure 6.9: (a), Space charge distributions from the charge transport model under different temperature gradients (b) Electric field profiles and (c) Final PEA simulation results.

The very large amount of heterocharge predicted from the author's analysis using a bipolar recombination model, figure 6.8(c), for the case of $T = 60\text{C}$ (representing $\Delta T=40\text{C}$) is not predicted from the combined model as shown in figure 6.9(a). As the combined model gives a better representation of the raw experimental data than from the analysis using the bipolar recombination model, the existence of this large heterocharge region is not necessarily a requirement for explaining the raw PEA data.

6.5 Simulation of charge accumulation and PEA raw data in double layer LDPE samples

In chapter 3 the traditional approach to process PEA raw data was used to obtain calibrated space charge profiles in two layer samples. In this section the charge transport model and PEA model software will be developed to simulate raw PEA data and compared to experimental raw PEA data. In order to generate the experimental raw PEA

output data, samples comprising of two layers of LDPE material with the same thickness and the same permittivity experiment as the original measurements of chapter 3 were repeated. This time, to make a difference in the electrical conductivity between the two LDPE sample layers, the sample layer in contact with the Al electrode of the PEA system was heat treated at 80 °C for 48 hours. This is different to that applied previously (50 °C for 24 Hours in chapter 3). An ‘as received’ (fresh) sample layer of LDPE was used for the sample in contact with the semicon electrode of the PEA apparatus. No lubricants or specific chemical treatment were applied to the interface between the two dielectric samples. PEA measurements were undertaken during polarisation using a -7kV pure DC voltage applied to the semicon electrode for a duration of 60 minutes and following this depolarization measurements were obtained after set the voltage application to zero for a further 60 minutes.

6.5.1 Polarisation experiments and simulation

The experimental PEA raw data obtained from the polarisation experiment is shown in figure 6.10. At the beginning (0min) of measurement, the space charge consisted of two peaks of opposite polarity at the electrode interfaces typical of a single layer specimen. After 5 minutes a positive peak appears at the position of the interface between the two layers of LDPE. This is due to positive charge being accumulated at the interface between the two layers. In this case positive charge from the aluminium electrode migrates across the lower sample layer until it reaches the interface between the two layers reducing the electric field in the layer adjacent to the aluminium electrode (reduced charge peak) and boosting the electric field in the layer adjacent to the semicon layer (increased charge peak at the semicon interface). A steady state is achieved after 60 minutes when charge migrating to the interface from the aluminium layer side balances the migration of charge from the interface towards the semicon interface in the semicon layer side. This behaviour is therefore similar to that observed in the previous experiments that were mentioned in chapter 3 but this time, instead of observing negative charge at the interface, this time positive charge accumulates at the interface between the dielectrics.

Because the applied voltage to the semicon electrode was negative, and based on the theory of interfacial charge, negative interface charge is obtained if the conductivity of the sample attached to the semicon electrode has greater conductivity than the sample layer attached to the Al electrode ($\sigma_2 > \sigma_1$), based on equation below [139]:

$$\rho_{\text{interface}} = \varepsilon \cdot \left(\frac{\sigma_2 - \sigma_1}{\sigma_2 + \sigma_1} \right) \cdot \left(\frac{-V}{d} \right) < 0 \quad (6.3)$$

However, the positive interfacial charge is obtained if the conductivity of the first sample is greater than the conductivity of the second one ($\sigma_1 > \sigma_2$):

$$\rho_{\text{interface}} = \varepsilon \cdot \left(\frac{\sigma_2 - \sigma_1}{\sigma_2 + \sigma_1} \right) \cdot \left(\frac{-V}{d} \right) > 0 \quad (6.4)$$

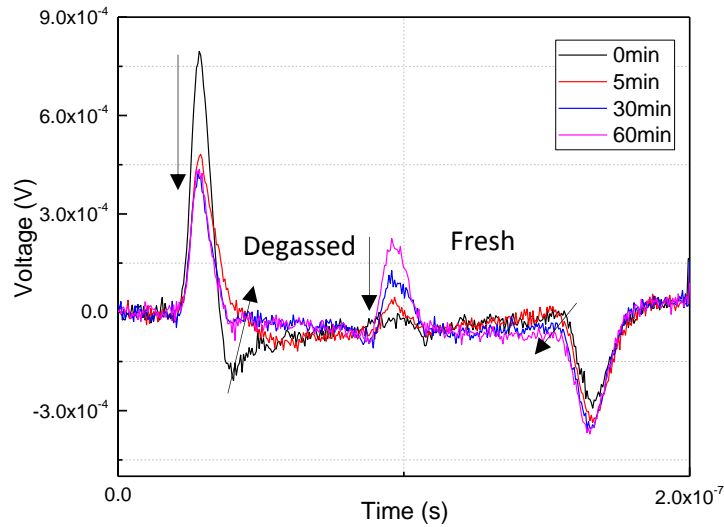


Figure 6.10: Experimental PEA raw data under polarisation.

This experimental result shows that the electrical conductivity of the ‘degassed’ sample must be greater than the conductivity of the ‘as received’ (fresh) sample. This was unexpected as the degassing procedure at 80°C was expected to reduce the level of impurity in the sample and therefore its electrical conductivity as was found in the original experiment of chapter 3. However in this repeat experiment the degassing was performed at a much higher temperature (80°C instead of 50°C) and for a longer duration. However, it may be that the thermal treatment at 80 °C for 48 hours is sufficient to cause thermal degradation [16] of the LDPE and or the impurities and this has led to an increase in the electrical conductivity.

The charge transport model was extended as described in section 4.4.2 to be able to calculate the space charge accumulation in two layer samples. The thickness of the LDPE layers was set the same as the LDPE samples that were used in the laboratory experiment (d_1 and $d_2 \cong 150\mu\text{m}$), and the permittivity (ε_r) of both sample was set on 2.3. However in the transport simulation, the electrical conductivity of the layer in contact with the Al electrode was made higher than that of the layer adjacent to the semicon electrode. The

charge transport model parameters that were used in the charge transport model simulation are shown in table 6.5. The actual values of these parameters were adjusted for a good fit with the experimental results. In addition, electrical conductivity modification due to impurity diffusion was undertaken close to the surfaces of each layer to mimic the formation of homocharge in the same way as that undertaken in the case of single layer sample simulations. As the laboratory measurements were undertaken under isothermal conditions, 20°C, just the field and distance dependent expression for electrical conductivity was used (Equation 4.27).

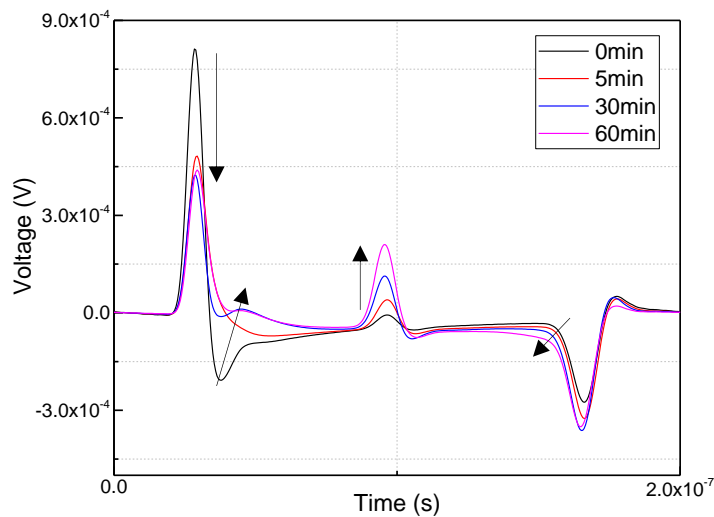
Table 6.5: Charge transport model constants in case of double layer LDPE sample.

Constants	Symbol	Values
Applied voltage	V	-7kV
Conductivity constant of layer 1 and layer 2	$\sigma_{01,2}$	6.79×10^{-18} S/m
Relative permittivity of layer 1 and layer 2	ϵ_r	2.3
Vacuum permittivity	ϵ_0	8.854×10^{-12} F/m
Electric field reference of layer 1 and layer 2	E_0	10kV/mm
Material constant at layer 1 and layer 2	γ	1.8
Conductivity enhancement factor (Al)	n_a	5.5
Conductivity enhancement factor (semicon)	n_b	1.35
Depth of Conductivity Enhancement (Al)	d_a	32 μ m
Depth of Conductivity Enhancement (semicon)	d_b	10 μ m
Maximum time	T_{max}	3600s

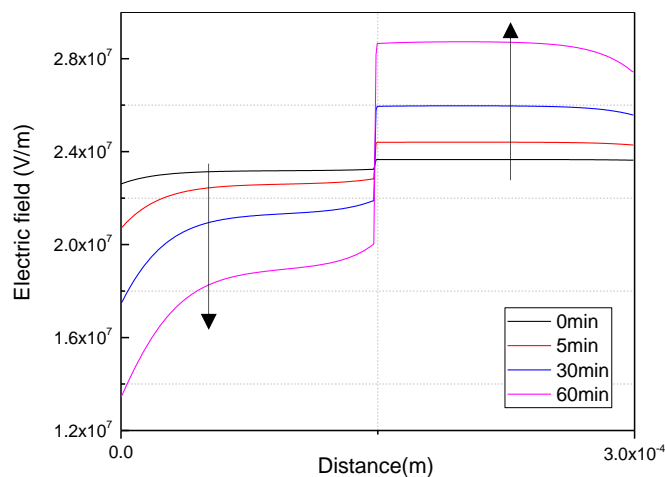
The PEA simulation program was also extended to include a second sample layer. The parameter used for the PEA simulation model are given in table 5.3. The electric field distributions from the charge transport model were then used to simulate the raw PEA data for comparison with experiment. Figure 6.11(a) shows the combined charge transport and PEA simulation results of two layer LDPE thin film insulation samples.

Comparing the experimental raw PEA data, figure 6.10 with the simulated raw PEA data, figure 6.11(a) demonstrates good agreement between the simulated PEA raw data and that observed experimentally. The electric fields used as input to the PEA simulations are

shown in figure 6.11(b) and the corresponding space charge distributions are shown in figure 6.11(c). These results show the positive interfacial charge built up between the two layers causes the electric field to decrease in the layer adjacent to the aluminum electrode and increase in the layer adjacent to the semicon electrode due to the imbalance of electrical conduction between the two dielectric layers. The greater electrical conductivity of the layer adjacent to the Al electrode was responsible for the build-up of positive charge at the interface. In addition, positive homocharge accumulated in the layer adjacent to the Al electrode. These two charge contributions induced negative charge on the Al electrode causing the original space charge peak at the Al electrode to decrease significantly. During the charging of the interface, the electric field within the ‘as received’ layer adjacent to the semicon electrode increases and this is responsible for the increase in the charge density peak at the semicon electrode. The space charge distribution is shown in figure 6.11(c) shows the formation of charge at the interface as well as the formation of homocharge in the material close to the two electrodes.



(a)



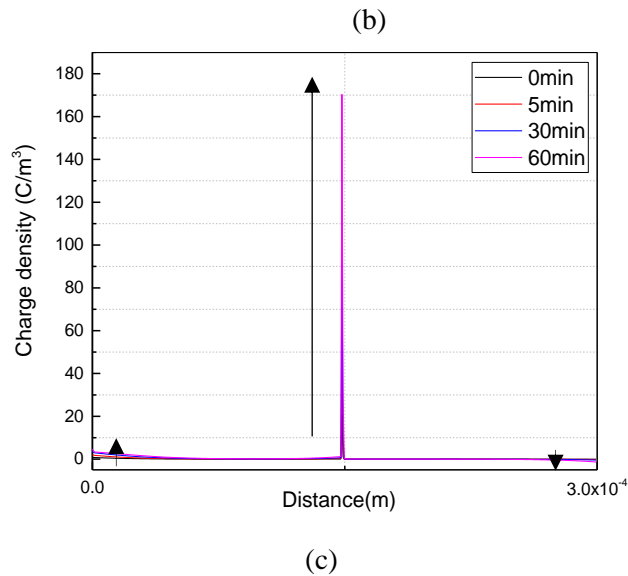


Figure 6.11: (a) PEA simulation voltage, (b) Electric field, (c) Space charge distribution in double layer LDPE under -7kV.

6.5.2 Depolarisation experiments and simulation

After the polarisation experiment for 60 minutes under -7kV DC voltage, the applied voltage was removed (set to zero). The experimental PEA raw data, which records the remaining charge, was obtained immediately after removing the applied voltage and its decay were measured. The PEA measurements were taken at time intervals during the 60 minutes total of the depolarisation test. The experimental PEA raw data obtained at three times during the depolarisation experiment are shown in figure 6.12. Charge at the interface decayed slowly and homocharge that had accumulated near to the Al electrode decreased with time. As this charge decays, the induced negative charge at the Al electrode is also observed to decay slowly.

Simulations of the charge decay were also conducted using the combined charge transport and PEA model using the same simulation parameters as for the polarisation simulations which are shown in table 6.5 and table 5.3 except that the applied voltage was set to zero and the starting charge distribution was the same as that which had formed at the end of the polarisation simulation. The simulation results are shown in figure 6.13(a) for the same times as that shown for the experimental PEA measurements that were shown in figure 6.12. The corresponding electric field distributions are shown in figure 6.13(b) and the space charge distribution in figure 6.13(c). The main contribution to the space charge profile is the charge at the interface which decreases gradually with depolarisation time. The electric field produced by this interface charge causes the electric field to be negative in the ‘degassed’ layer and positive in the ‘as received layer’. The magnitudes of these

fields are $\sim 4\text{MV/m}$ and are much lower than the field applied during the polarisation experiment. Because the LDPE has a field dependent conductivity, the effective conductivities of the layer sandwich are much lower during depolarisation than during the original polarisation, the insulation material holds up the decay of space charge for longer period of time compared with the time of accumulation charge during polarization. The presence of homocharge that had accumulated during the polarisation experiment also modifies the electric field distribution especially near to the AL electrode.

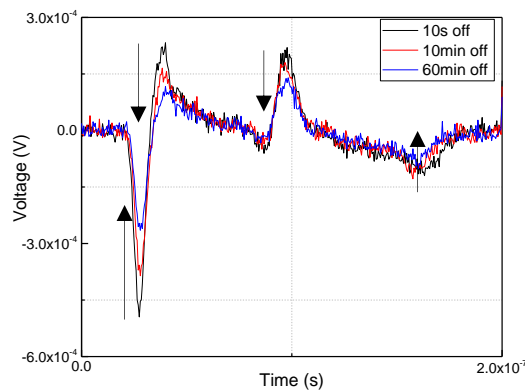
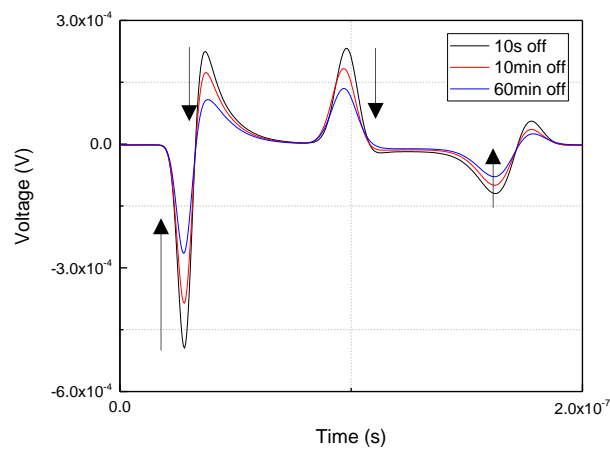
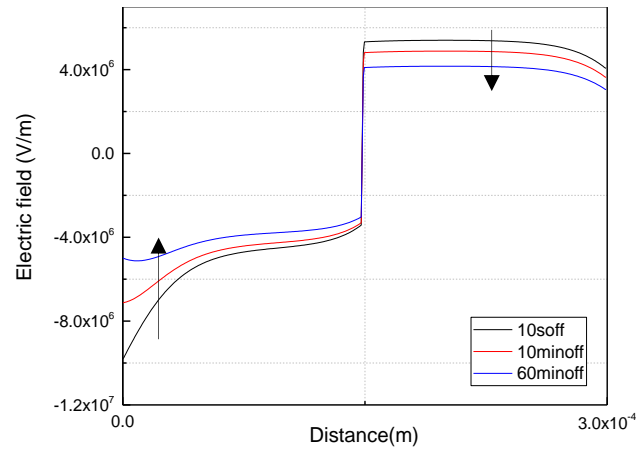


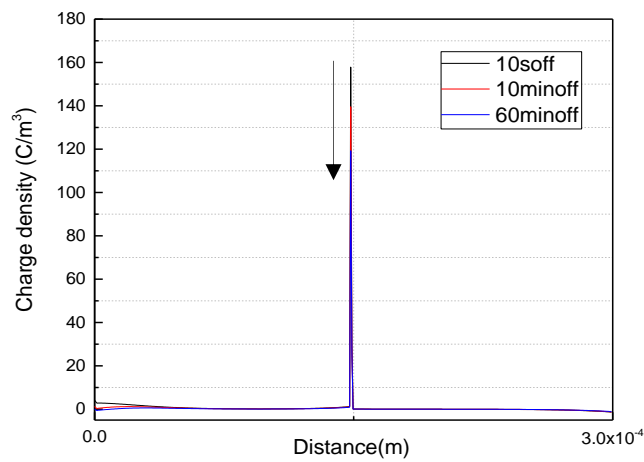
Figure 6.12: Experimental PEA raw data during depolarization period.



(a)



(b)



(c)

Figure 6.13: (a) PEA raw output simulation, (b) electric field distribution, (c) space charge distribution under depolarisation.

The results on two layer samples demonstrate the ability of the proposed combined charge transport and PEA simulation model with field dependent electrical conductivity and conductivity modification due to impurity diffusion can successfully replicate the experimental observations of space charge accumulation and decay for the case of layered samples. The results also demonstrate that the thermal conditioning of the samples has a significant effect on the electrical conductivity of the material. Conditioning at 80°C for 48 hours led to an increase in electrical conductivity while conditioning at 50°C for 24 hours (results described in chapter 3) led to a decrease in the electrical conductivity compared to the ‘as received’ (fresh) material. These temperatures are within range of the operational conditions for full size commercial HVDC cables based on XLPE. Further work is therefore required to examine if service temperatures can affect the electrical conductivity, for example, by the ionisation of impurities, that can lead to abnormal electric field distributions to arise that could influence lifetime.

6.6 Summary

In this chapter the procedure of combining the 1-D simulation model of charge transport with the 1-D of PEA acoustic wave model has been described. The electrical field distribution output of the charge transport model, $E(x)$, was used as the input of the 1D PEA acoustic model that also included corrections for acoustic wave absorption and dispersion as well as the corrections for PVDF-Buffer amplifier response and oscilloscope bandwidth. A good agreement was found between the simulation model results and experimental results in case of field dependent conductivity in both one layer and double layer samples and in case of temperature dependent conductivity in one layer thin film sample. It was shown how the result of these two models can be used to simulate successfully raw PEA experimental data and to provide a basis for the interpretation the PEA measurement data. The new combined simulation model was applied to the case of thin film insulation samples under polarization and depolarization operating conditions in one layer, and in two layer LDPE samples. In a single layer LDPE sample, the result showed when the temperature was isothermal across the sample, the space charge accumulated near to the electrodes was in the form of homocharge. However, the space charge that was accumulated close to the sample surfaces was asymmetric suggesting that the impurity diffusion was different at each surface of the specimen. The isothermal simulation results demonstrated that the time required for the decay of space charge is generally significantly longer than for the time to accumulate the charge under polarisation.

On the other hand, when there was a temperature difference between the two surfaces of the sample, the space charge was dominated by the temperature gradient and accumulated to a greater degree at the lower temperature side. The fitted results were found to be superior to that obtained by the authors using a bipolar charge transport model. This to some extent was probably due to the authors not using a PEA model that adequately corrects for the PEA system imperfections.

In double layer LDPE samples when the temperature was isothermal, the build-up of space charge at the interface was determined by the difference in electrical conductivity between the layers. Interestingly, the results demonstrate that degassing at 50°C for 24 hours decreased the electric conductivity of fresh LDPE whilst degassing at 80°C for 48 hours had the opposite effect. This is compatible with the interpretation of Boggs et al. [58] who suggest that the conductivity enhancement at surfaces or interfaces is due to the

diffusion of impurities either during the manufacture of the thin films or during storage of the films. However at 80°C the temperature may be high enough to initiate thermal ageing of LDPE or the impurities contained within it leading to an increase in the bulk electrical conductivity.

7 Assessment of the Impact of AC Ripple Voltage on the Space Charge Accumulation Inside Solid Thin Film Samples

7.1 Overview

The aim of this chapter is to assess the effect of applying an AC ripple voltage to the steady DC voltage on space charge accumulation in a thin film insulation materials. Section 7.2 describes the nature of the AC ripple voltage in HVDC system. Modification of experiment apparatus and the measurement of space charge accumulation under different ratio of ripple voltage which is superimposed on the DC voltage in both one layer and two layer thin film samples are described in section 7.3. In section 7.4 the combined simulation models of charge transport model and PEA acoustic wave model are used to analyse the results of space charge measurement for both one layer and two layer samples under the same voltage applications as the experiments. The effect of Joule heating (that obtained from the DC applied voltage) and dielectric heating (that obtained from AC ripple voltage) on space charge accumulation inside the single layer sample is examined in section 7.5. The summary and key findings of this chapter will be described in section 7.6.

7.2 AC ripple voltage in DC system

The AC ripple voltage is an undesirable phenomenon in DC transmission system which originated from convertor stations. In convertor stations, due to the switching of power electronic valves the voltage and current in HVDC side carry a ripple voltage rather than just being pure DC [140]. The ripple voltage on a transmission line is subject to attenuation along the line and therefore, the insulation closest to the convertor stations are subjected to the most severe magnitude of AC ripple voltage [141]. Figure 7.1 shows the addition of a sine wave shape AC ripple voltage that superimposed on the DC voltage. The ratio of AC ripple to DC voltage can be defined based on below equation:

$$AC\ ripple\ \% = \frac{V_{AC}}{V_{DC}} \times 100\% \quad (7.1)$$

Where V_{AC} is the peak value of AC voltage and V_{DC} is the value of DC voltage.

Based on the literature, the typical amount of ripple voltage is about 10% or more of the DC applied voltage [8]. The existence of an AC ripple voltage is expected to have an effect on aging and degradation of cable insulations [142]. Fabiani and Montanari in [143] have found that the ripple voltage has a great influence on aging and degradation of the insulation material. In addition, it has been reported in [28, 144] that, the ripple

voltage has the effect of increasing the repetition rate of partial discharges in a gas filled voids within the insulation sample. On the other hand, it has been found that the high frequency AC ripple enhances the degradation in HDPE insulation polymer [142]. All the literature examples described above had concentrated on showing the effect of AC ripple voltage on partial discharge inception and the resultant electrical degradation. However, there exists a gap of knowledge with regard to the effect of HVDC superimposed ripple voltage effect on space charge accumulation and material ageing (the precursor to degradation via partial discharges). Therefore, this chapter will focus on the effect of ripple voltage on space charge accumulation in one layer and two layer insulation material by setting up a proper experimental apparatus. At the same time the simulation models are modified in order to interpret the measurement results more accurately in cases of pure DC voltage and at different AC ripple voltages.

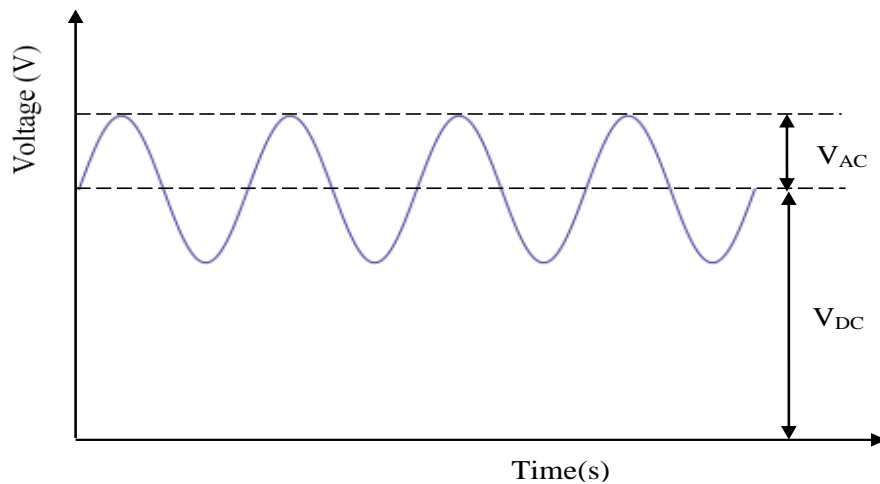


Figure 7.1: AC ripple voltage that superimposed on DC voltage wave form.

7.3 Space charge measurements

7.3.1 Experimental setup for raw PEA space charge measurement under pure DC voltage with superimposed AC ripple voltage

The PEA space charge measurements were performed in one layer and two layer low density polyethylene (LDPE) thin film samples. The measurement apparatus is shown in figure 7.2 for measuring the space charge under pure DC and DC superimposed with AC ripple voltage. The pulsed electro-acoustic (PEA) method was used to measure the space charge accumulation. Again in order to have a good match of acoustic impedance between the HV electrode and the insulation sample, semicon (carbon black loaded polyethylene) polymer was selected as a top electrode material and attached to the top Al material, while Al material was used as the ground electrode. The thickness of each layer

of LDPE sample was approximately $150 \mu\text{m}$. Therefore for double layer LDPE samples the overall thickness was $300 \mu\text{m}$.

The combined pure DC voltage and AC ripple voltage were generated by using a function generator which was subsequently amplified using a high voltage DC amplifier (Trek model 20/20 B). The gain of this model of amplifier was $2000\text{V}/1\text{V}$ with $\pm 20\text{kV}$ maximum output voltage. An oscilloscope was used to monitor the combined DC and AC ripple voltage. The amplified DC + AC ripple voltage was fed to the top PEA electrode via a protection resistor. In order to choose the suitable value for the protection resistor and the ripple voltage frequency, it was necessary to take into account the low pass filter that was formed by the resistor and the capacitance of the PEA instrument. A simulation was conducted using PSpice software by which a suitable value for the protection resistor could be chosen that would not cause attenuation of the ripple voltage applied across the sample. Figure 7.3 shows the electric circuit and the PSpice simulation result that was used to find a suitable input resistor of the PEA system. As can be seen from the figure 7.3(a), V1 is HVDC voltage, V2 is an AC ripple voltage, C1 is the coupling capacitor used to inject the PEA pulse voltage which was equal to 200pF , R2 is a resistive output impedance of the pulse generator and it is equal to 50Ω . C2 is the capacitance of the sample that is given by, $C2 = \frac{\epsilon_0 \epsilon_r A}{d}$, where, ϵ_0 is vacuum permittivity which is equal to 8.854×10^{-12} , ϵ_r is the relative permittivity of the LDPE sample and equal to 2.3; A is the area of the sample and it is equal to 1cm^2 , d is the sample thickness and it is equal to $150 \mu\text{m}$ in case of single layer. Therefore the overall value of C2 is $\sim 13\text{pF}$.

The simulation result of figure 7.3(a) is shown in 7.3(b), in which a suitable value for R1 was chosen of $1\text{k}\Omega$. The cut-off frequency is greater than 100kHz . Based on that, the frequency of AC ripple voltage can be applied without attenuation is therefore in the range of 1Hz to 100kHz . In this study the frequency was fixed on 300Hz which is suitably high to be representative of an actual high voltage DC converter ripple but low enough not to be attenuated by the PEA capacitance.

To validate the PSpice simulation result regarding the value of the input resistor of the PEA system, the DC + AC voltage (that generated by function generator and amplified by the high voltage amplifier) was measured at the top Al electrode of PEA using a high voltage probe. It was found that, the output voltage from the resistor was the same as the HV amplifier waveform and therefore validated the choice of ripple frequency and value

of protection resistance. The remaining apparatus, the PEA instrument, amplifier, oscilloscope and computer were unmodified. Raw PEA space charge measurements were taken for samples of single and double layer subjected to pure DC (0% ripple voltage), DC + 10% AC ripple voltage and DC +20% AC ripple voltage.

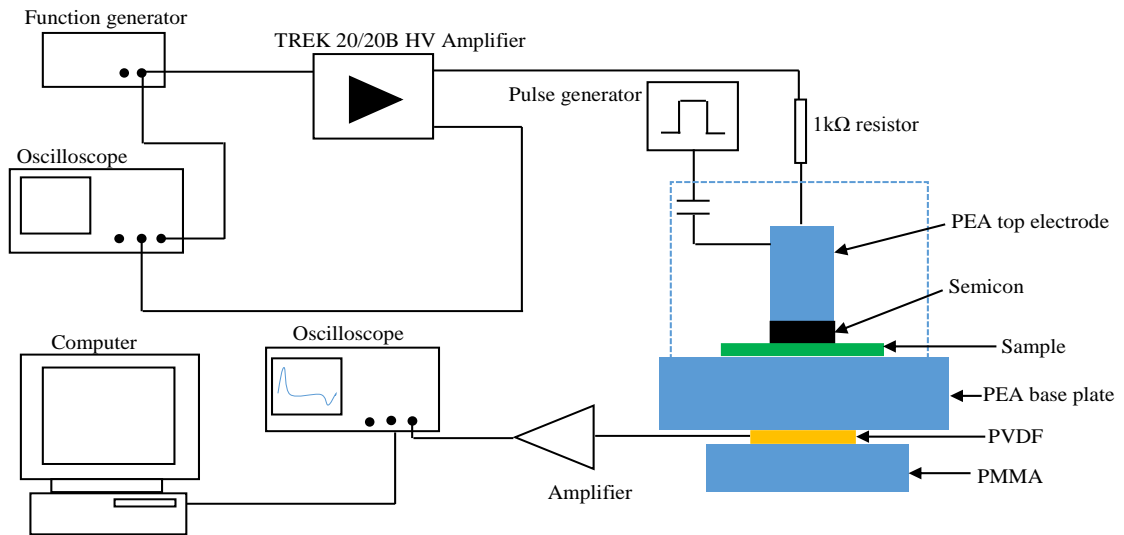
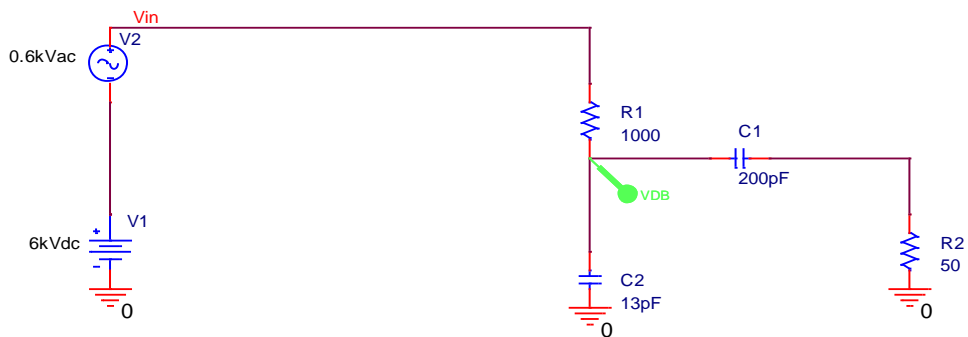
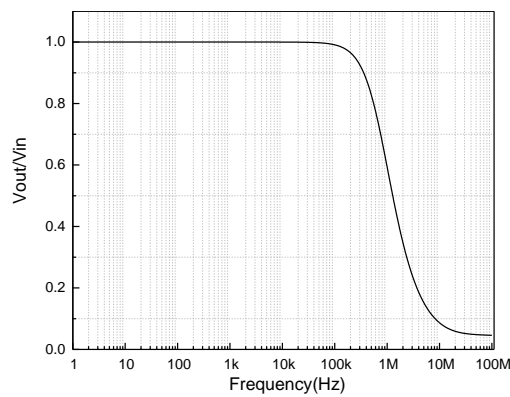


Figure 7.2: Experimental setup for measuring space charge accumulation under HVDC superimposed with AC ripple voltage.



(a)



(b)

Figure 7.3: PSpice simulation model for choosing the input resistance of the PEA system.

7.3.2 Experimental PEA measurement results – single layer LDPE

In case of pure DC voltage, 0% ripple voltage, a -6kV (40kV/mm) was applied to the PEA HV electrode for 30 minutes at ambient temperature (18°C) and the space charge was measured at different time intervals from 0 minute to 30 minutes. The raw PEA space charge measurement profiles during that time are shown in figure 7.4.

Although the raw PEA output voltage $V(t)$ is not representative of a real space charge distribution as it requires corrections of the system imperfections, it is partly related to the accumulated space charge. Therefore, by looking at the $V(t)$ results, it provides some information regarding the dynamics of the space charge inside the insulation sample. The results of figure 7.4 clearly show that the distribution of charge is dominated by positive charge accumulation adjacent to the positive Al electrode and a smaller amount of negative space charge accumulation in the sample adjacent to the negative Semicon electrode which indicates homocharge build up at the vicinities of both electrodes. The origin of these homocharge regions is the same as previously found and due to electrical conductivity modification due to the diffusion of impurities.

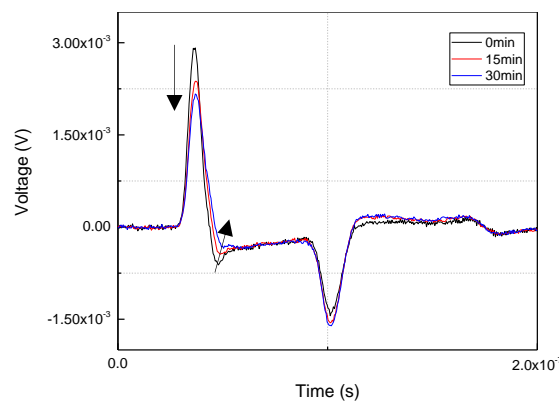
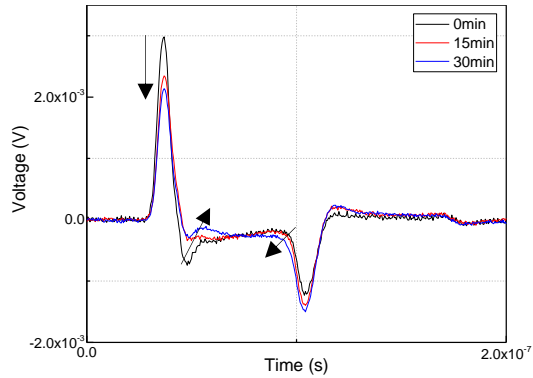


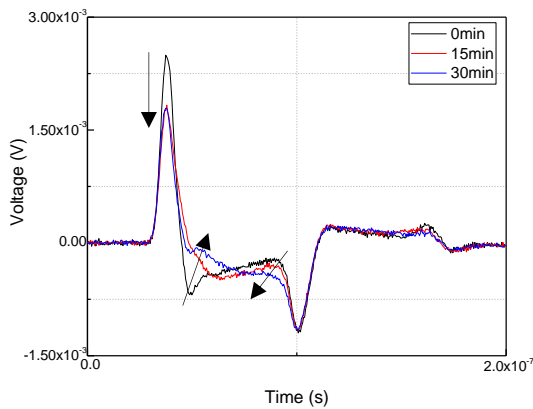
Figure 7.4: PEA raw data in case of pure DC voltage.

Measurement of space charge accumulation when a 10% AC ripple voltage and 20% AC ripple voltage was superimposed on the DC voltage was then conducted. In this case, the DC voltage was -6kV (40kV/mm) with 10% and 20% AC ripple voltage was applied for 30 minutes. The result of both cases are shown in figure 7.5 (a) and figure 7.5(b) respectively. As was found in the case of pure DC voltage, the space charge that accumulated was homocharge in the sample near both electrodes. However, on comparison with the results of pure DC voltage for the same time of space charge measurements, the amount of charge that accumulated near the electrodes was found to

be greater with the addition of the ripple voltage. Further, the amount of charge accumulated increased with increasing ripple voltage.



(a)



(b)

Figure 7.5: PEA raw data when, (a) % 10, (b) % 20, AC ripple superimposed on DC applied voltage.

7.3.3 Experimental PEA measurement results – double layer LDPE

The effect of AC ripple on space charge accumulation was also assessed in two layer insulation samples. The LDPE layer which was attached with the Al electrode was degassed under 50 °C for 24 hours, whereas the LDPE layer which was attached with semicon electrode was non-degassed. Therefore, based on the measurements that conducted in chapter 3, the two layers were expected to have different conductivity (with the aluminium side LDPE layer having the lower conductivity due to removal of impurities and in this case interfacial charge should accumulate at the interface between the layers. In case of pure DC voltage, a -6kV (20kV/mm) was applied to the sample for

30min at ambient temperature (18°C) and the space charge was measured at different times between 0 to 30minutes.

Figure 7.6 shows the experimental PEA raw output data in case of pure DC voltage, in which clearly shown the dynamics of space charge accumulation. As can be seen from figure 7.6, at the very beginning time ($t=0$), a little interfacial charge was obtained between the dielectrics, this is because the permittivity of both samples are the same and space charge had not yet accumulated at the interface between the layers. Over time, due to the difference in conductivity between the two layers, negative space charge accumulated at the interface. Due also to the diffused impurities, homocharge formed adjacent to the electrode interfaces. The diffused impurities, especially in the semicon side (non-degassed) layer caused positive charge to form close to the interface between the two layers.

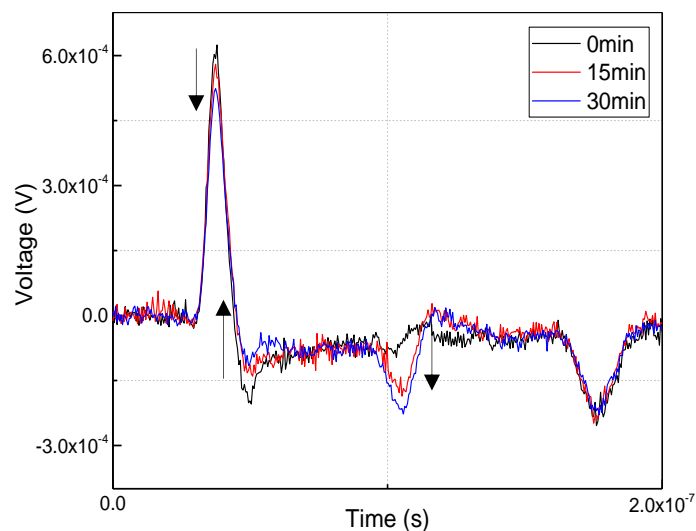


Figure 7.6: PEA raw data under -6kV DC voltage in two layer LDPE samples.

In order to measure the effect of ripple voltage on space charge in two layer samples, the experiment was repeated using two LDPE samples with the same specifications, one was degassed under the same conditions as in the case of pure DC and the other was non degassed. However, in this case an AC ripple voltage with a ratio of 10% was superimposed on the -6kV DC voltage for 30 minutes. The experimental raw PEA output data were recorded at 0, 15 and 30 minutes.

The result of these measurements are shown in figure 7.7. The addition of the ripple voltage had led to more homocharge to be accumulated near the electrodes and more space charge was accumulated at the interface between the two dielectrics.

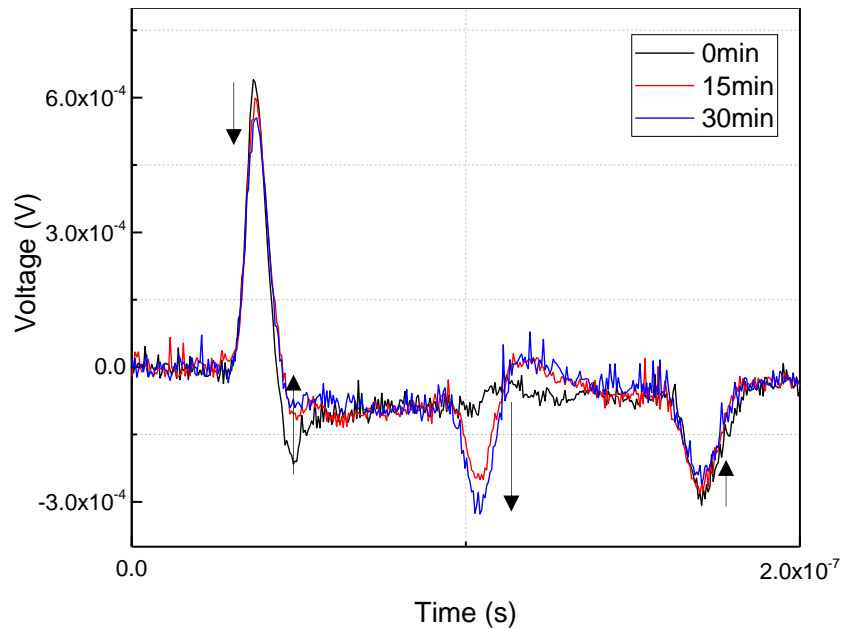


Figure 7.7: PEA measurement result, under -6kV and %10 ripple voltage in two layer LDPE samples.

7.4 Combined charge transport and PEA simulations

7.4.1 Simulation of raw PEA space charge measurement under pure DC voltage with superimposed AC ripple voltage

To be able to analyse the experimental results correctly, the simulation models of charge transport and PEA acoustic wave which were defined in chapter 4 and chapter 5 were used. The process of combining simulation models and comparing with the experimental results for both cases of pure DC and rippled DC voltage in both one layer and two layer sample was described in chapter 6. It was necessary to modify the simulation procedure for the charge transport model to incorporate time dependent boundary conditions for the applied electric potential across the sample. The AC ripple voltage is given by equation 7.2.

$$V_{ripple}(t) = V_{max} \sin(\omega t) \quad (7.2)$$

Where, V_{max} is the peak voltage and $\omega = 2\pi f$; where f is the ripple frequency which depend on the topology of the convertor. In the following simulations, the frequency was fixed on 300 Hz in all cases of simulation so that this was the same as the experimental measurements. The electric potential boundary condition was therefore changed from a pure DC voltage, V_{DC} to a time varying voltage, V_{total} given by equation 7.3.

$$V_{total} = V_{DC} + V_{max} \sin(\omega t) \quad (7.3)$$

In the charge transport simulation model the applied voltage is updated at each time step $t + \Delta t$ the total voltage that applied across the sample or samples is given by equation 7.3. The time step, Δt , used for the time increment of the charge transport model was made sufficiently small and significantly less than the period of the AC ripple voltage in order to resolve the ripple component in the simulations.

The thickness of the sample was set to $150\mu m$ for single layer and $300\mu m$ for the double layer samples, the same as those used in the experiments. The properties of LDPE were used for the insulation sample in all cases of simulations. Conductivity modification due to the presence of diffused impurities was also incorporated to simulate for formation of the homocharge regions inside the sample or sample layers. The electric conductivity was therefore modified based on equation (4.9).

In order to compare the cases of pure DC and DC with ripple voltage, the electric field profiles calculated by the charge transport model were obtained at times corresponding to the zero crossing of the AC ripple voltage. The electric field distributions used as input to the PEA simulations were therefore obtained at instances of time when the applied voltage was equal to the DC voltage applied.

For the PEA simulations the same parameters were used as previously determined from the initial calibration, table 5.3.

7.4.2 Simulation results of single layer LDPE sample

The combined charge transport and PEA simulation models were first performed on single layer samples under pure DC voltage. In this case a -6kV voltage was used in the charge transport model to match the experiments and space charge along with the corresponding electric field distributions were calculated at different times (over the same time intervals as experimental data). At each predefined time, the electric field distribution that was obtained from the charge transport model was used as the input for the PEA simulation model in order to simulate raw PEA data to be compared directly

with the experimental results. Figure 7.8 shows the simulation results in case of pure DC voltage. The model parameters in case of pure DC voltage used for the charge transport simulations are shown table 7.1.

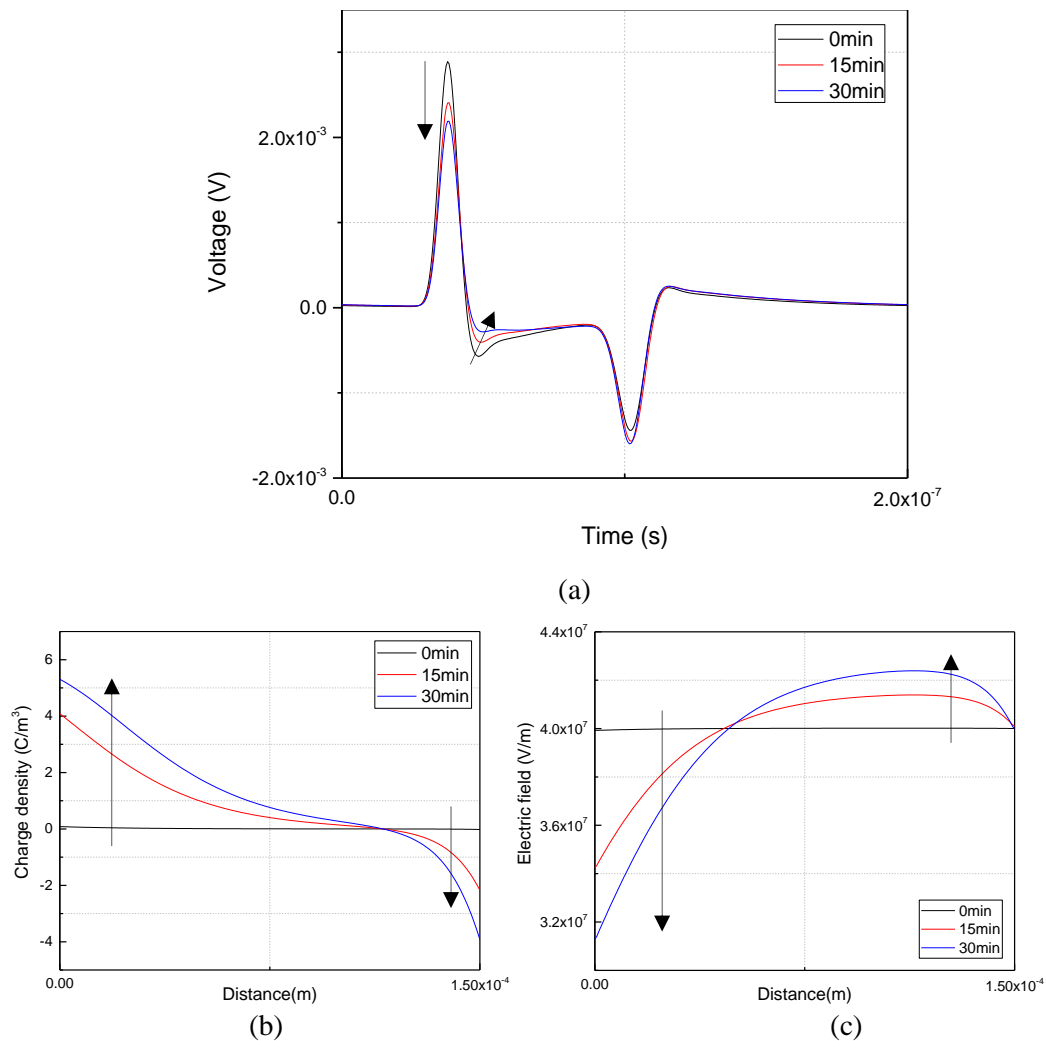


Figure 7.8: (a) PEA simulation, (b) Space charge, (c) Electric field distribution under -6kV voltage in 150 μ m LDPE sample.

As shown in Figure 7.8(a), at the initial time the space charge is about zero and electric field is distributed uniformly (see figure 7.8(b)). After the passing of time (15min and then 30min) homocharge accumulated adjacent to the electrodes. This is due to the modification of the insulation conductivity due to the presence of diffused impurities. The accumulation of homocharge and the corresponding electric field distribution are shown in figure 7.8(b) and 7.8(c) respectively. These results demonstrate that the homocharge is distributed further into the insulation at the aluminium electrode side than

at the semicon side. Figure 7.8(a) is the result of PEA simulation after correcting the signal which agrees well with the corresponding experimental result shown in figure 7.4.

Table 7.1: Charge transport model parameters of single layer LDPE sample under pure DC voltage.

Constants	Symbols	Values
Applied voltage	V	-6kV
Initial conductivity	σ_0	$4.63 \cdot 10^{-18}$ S/m
Relative permittivity	ϵ_r	2.3
Vacuum permittivity	ϵ_0	$8.854 \cdot 10^{-12}$ F/m
Electric field reference	E_0	10kV/mm
Field Power Index	γ	1.8
Positive magnification factor	n_a	2
Negative magnification factor	n_b	1.3
Distance constant of positive homocharge regions	d_a	$20\mu\text{m}$
Distance constant of negative homocharge regions	d_b	$10\mu\text{m}$
Maximum time	T_{max}	1800s

The calculation of space charge accumulation and corresponding electric field profiles were then performed under 10% and 20% (equivalent to 600V and 1200V AC peak voltage) of AC ripple superimposed on to the -6kV DC voltage. The results of these simulations are shown in figure 7.9 and 7.10 respectively. The model parameters that were used to obtain good match with experimental data in both cases of 10% and 20 % of AC ripple were the same as the values shown in table 7.1 except for the parameters that were used for conductivity modification due to diffused impurities which are shown in table 7.2 and 7.3 respectively. The simulation results of figures 7.9 and 7.10 show that superimposing the AC ripple on DC voltage led to more charge to be accumulated adjacent to the electrodes and in the bulk of the sample in the form of homocharge. The greater ratio of ripple voltage, the more charge were observed to accumulate. As with the pure DC case, the simulations show that the homocharge accumulation distribution

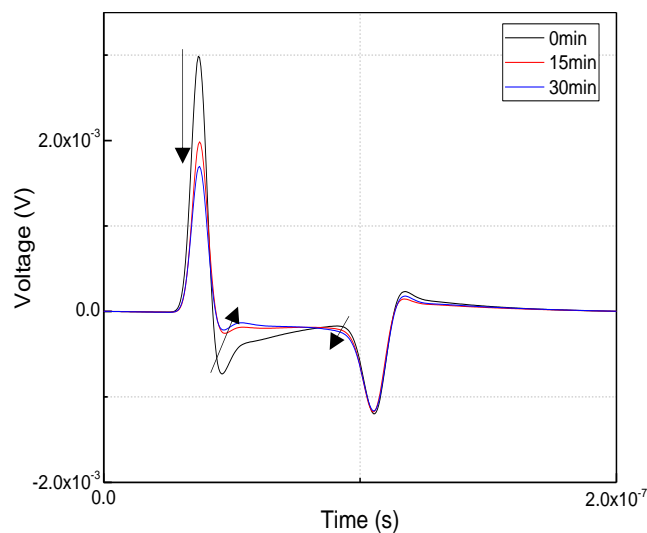
spreads further into the sample compared with the homocharge distributed near the semicon electrode. The simulation of PEA output data agrees with the experimental raw PEA data in all cases (under pure DC, 10% ripple and 20% ripple). In the case of the electric field profiles, the maximum electric field inside the sample increased from 42.3MV/m under pure DC to 43MV/m when 20% AC ripple voltage was also superimposed. The increase in electric field will have implications for insulator lifetimes.

Table 7.2: Electrical conductivity parameters in case of 10% AC ripple that superimposed on DC voltage.

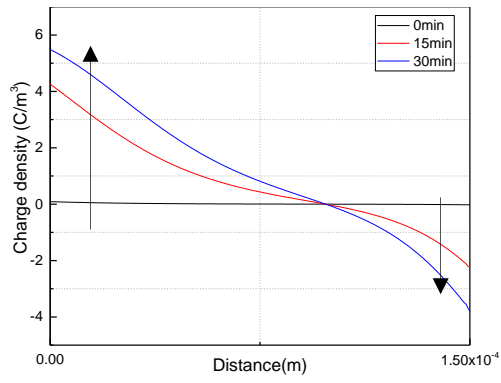
Positive magnification factor	n_a	2.8
Negative magnification factor	n_b	1.5
Distance constant of positive homocharge regions	d_a	23 μm
Distance constant of negative homocharge regions	d_b	13 μm

Table 7.3: Electrical conductivity parameters in case of 20% AC ripple that superimposed on DC voltage.

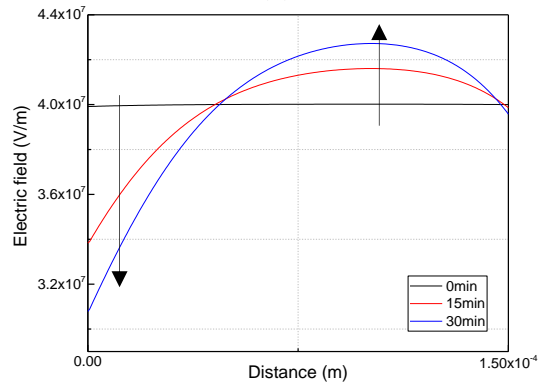
Positive magnification factor	n_a	4
Negative magnification factor	n_b	1.9
Distance constant of positive homocharge regions	d_a	40 μm
Distance constant of negative homocharge regions	d_b	20 μm



(a)

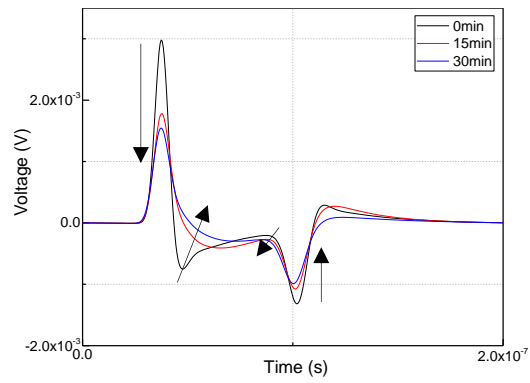


(b)

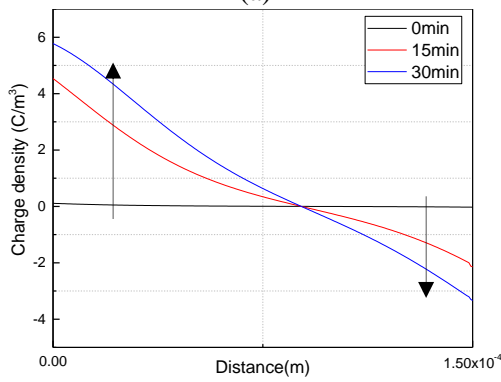


(c)

Figure 7.9: (a) PEA simulation, (b) Space charge, (c) Electric field distribution under -6kV and % 10 ripple voltage in 150 μ m LDPE sample.



(a)



(b)

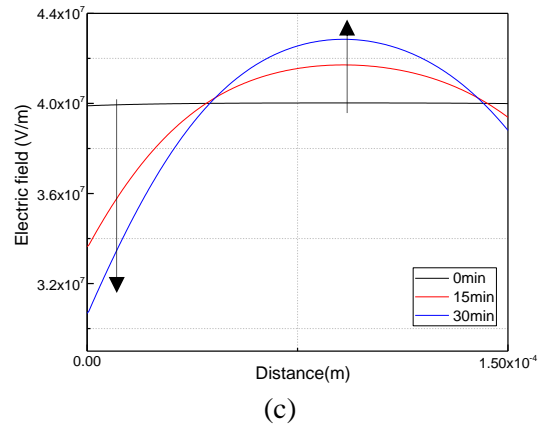


Figure 7.10: (a) PEA simulation, (b) Space charge, (c) Electric field distribution under -6kV and %20 ripple voltage in 150 μ m LDPE sample.

7.4.3 Simulation results of double layer LDPE samples

Simulations were also conducted on double layer samples in order to analyze the space charge accumulation under pure DC and with the addition of 10% AC ripple voltage. The computational procedure followed section 6.5 related to the double layer specimens except that the voltage boundary conditions for the charge transport model were made time dependent as explained in section 7.4.1. As one of the layers was degassed to reduce the concentration of impurities, the conductivity of the two layers had to be different. It was assumed that the conductivity of the LDPE adjacent to the high voltage electrode (semicon) is higher than the conductivity of the LDPE layer that was adjacent to the ground electrode. In addition, the electrical conductivity equation was modified based on equation 4.9 (by this the homocharge accumulated adjacent to the electrodes and at the interface between the samples) to incorporate electrical conductivity modification due to diffused impurities. To mirror the experiments, the maximum simulation time was set on 30 minutes. The parameters used for the charge transport model for both cases of pure DC and rippled DC in order to get a good match with the experimental raw PEA data are shown in table 7.4. However the parameters of conductivity enhancement are changed in case of 10% AC ripple as shown in table 7.5. The electric field and space charge profiles which were obtained from the charge transport model were saved at the predetermined times. The electric field profiles during the zero crossing of the AC voltage waveforms at different times of 0, 15 and 30 minutes were used as the input for the PEA simulation model. The parameters used for the PEA model simulations were the same as those previously given (table 5.3).

Figures 7.11 and 7.12 show the simulation results under 0% ripple (pure DC applied voltage), and 10% ripple voltage respectively. In both cases of pure DC and rippled DC

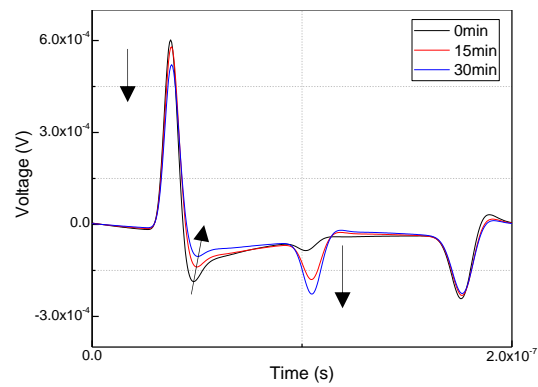
voltages, homocharge was accumulated adjacent to the two electrodes. Charge also accumulated either side of the interface between the two layers. These are due to the conductivity modification due to impurity diffusion. However, superimposing the 10% of AC ripple on DC voltage, led to more homocharge to be accumulated adjacent to the electrodes and more interfacial charge was obtained either side of the interface between the layers. In addition to the bulk charging of the layers, space charge accumulated at the interface between the two layers. The amount of interface charge was higher when AC ripple voltage was applied to the sample. In both cases a good agreement can be seen between the experimental raw PEA data and the simulated PEA data both in terms of the homocharge accumulation and the charge at the interface between the two sample layers. The results of both simulation and experiment show that the effect of ripple on two layer samples was more severe compared with the one layer insulation sample especially at the interface between the layers. In the case of the electric field profiles, the maximum electric field inside the sample increased from 22.3MV/m under pure DC to 23.0MV/m when 10% AC ripple voltage was also superimposed. The increase in electric field under voltage ripple conditions will have implications for insulator lifetimes.

Table 7.4: Charge transport model parameters of double layer LDPE samples under pure DC voltage.

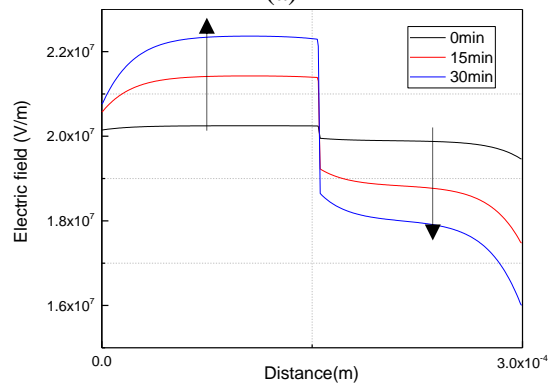
Constants	Symbols	Values
Applied voltage	V	-7kV
Conductivity constant of layer 1 and layer 2	$\sigma_{01,2}$	5.44×10^{-18} S/m
Relative permittivity of layer 1 and layer 2	ϵ_r	2.3
Vacuum permittivity	ϵ_0	8.854×10^{-12} F/m
Electric field reference of layer 1 and layer 2	E_0	10kV/mm
Material constant at layer 1 and layer 2	γ	1.8
Conductivity enhancement factor (Al)	n_a	2.5
Conductivity enhancement factor (semicon)	n_b	2.3
Depth of Conductivity Enhancement (Al)	d_a	15 μ m
Depth of Conductivity Enhancement (semicon)	d_b	30 μ m
Maximum time	T_{max}	1800s

Table 7.5: Electrical conductivity enhancement parameters of double layer LDPE samples in case of 10% AC ripple that superimposed on DC voltage.

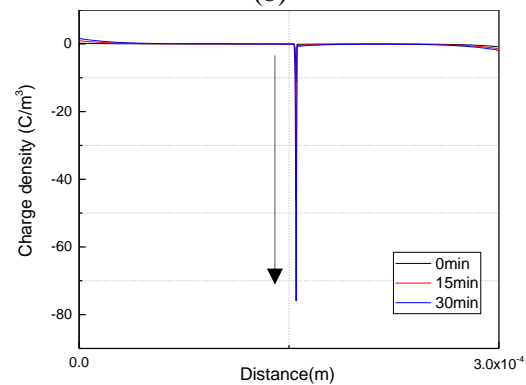
Positive magnification factor	n_a	2.65
Negative magnification factor	n_b	2.48
Distance constant of positive homocharge regions	d_a	22 μm
Distance constant of negative homocharge regions	d_b	38 μm



(a)



(b)



(c)

Figure 7.11: (a) PEA measurement, (b) PEA simulation, (c) Electric field, (d) space charge distribution under -6kV voltage in two layer LDPE.

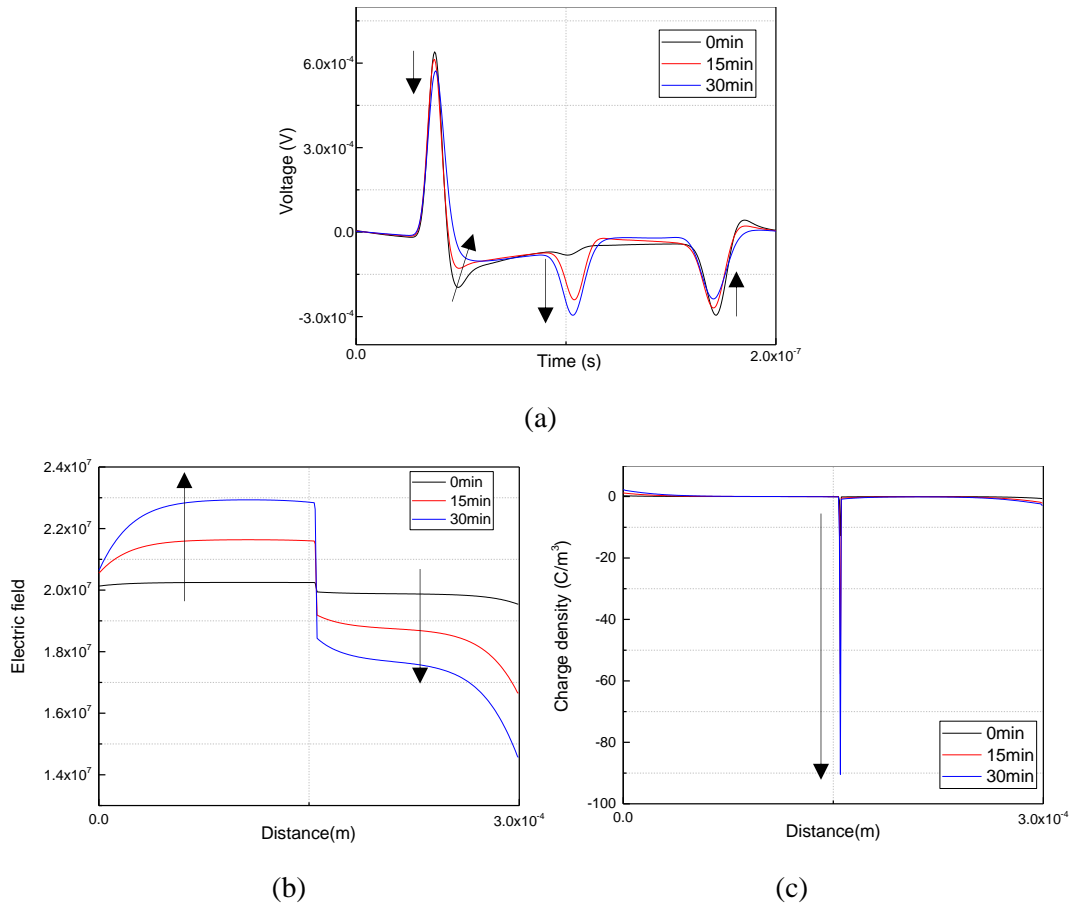


Figure 7.12: (a) PEA measurement, (b) PEA simulation, (c) Electric field, (d) space charge distribution under -6kV and %10 ripple voltage in two layer LDPE.

7.5 Effect of dielectric heating+ Joule heating (result in the rippled DC voltage) on space charge accumulation inside single layer insulation sample.

All materials exhibit a DC conductivity that is dependent on temperature. A DC conduction current will lead to Joule heating within the material. This source of heating will give rise to an increase in the DC current and a further increment in the amount of Joule heating. Under normal operating conditions, the Joule heating will be balanced by thermal conduction to the centre conductor of the cable and the cables outer armour. A small steady state temperature increase is therefore to be expected. However, if the rate of Joule heating increases to a greater extent than this heat can be transported away by thermal conduction then a steady state is no longer achievable and the insulator temperature can increase without limit leading to thermal runaway and breakdown of the insulator material. When an AC voltage is also applied (ripple voltage) dielectric heating due to polarisation of the insulating material can lead to an additional source of heat called dielectric heating that could potentially lead to even less margin to thermal runaway. In

order to examine the effect of Joule and dielectric heating on space charge accumulation in insulator samples, the electro-thermal charge transport model was modified to be able to calculate: The space charge accumulation when the conductivity was just field dependent and the applied voltage was pure DC. Secondly, the space charge accumulation when the conductivity was both field and temperature dependent and the applied voltage was pure DC. In this case the temperature gradient was obtained due to Joule heating originating inside the dielectric material. The final case was the calculation of the space charge when the conductivity was both field and temperature dependent and the applied voltage was DC superimposed with %10 and %20 AC ripple voltage. The Joule heating and dielectric heating were determined based on the equation 7.4.

$$\rho_m c_p \frac{\partial T}{\partial t} = \nabla \cdot (k \nabla T) + \underbrace{\sigma(E, T) E^2}_{\text{Joule heating}} + \underbrace{\omega \varepsilon_0 \varepsilon' E_m}_{\text{Dielectric heating}} \quad (7.4)$$

Where, ε' is an imaginary permittivity of the insulation material and E_m is the Laplacian electric field.

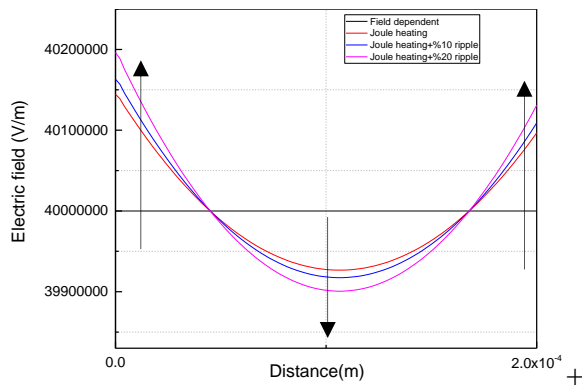
In this case the temperature gradient was obtained due to the Joule heating result of DC voltage application and dielectric heating as a result of the applied AC ripple voltage. In all cases a DC voltage of 8kV was applied across the sample material corresponding to an electric field of 40kV/mm within a 200 μ m thick sample. For the combined DC + AC ripple, the applied AC ripple peak voltage of 800V and 1.6kV was superimposed on the value of DC voltage. The model parameters are shown in table 7.6. In table 7.6 the values for the models parameters were chosen based on literature values [10, 48, 54, 59] except for the reference conductivity parameter which was chosen arbitrary. The frequency of the AC ripple voltage was 300Hz.

Table 7.6: Charge transport model parameters for calculating the joule heating and dielectric heating inside the insulation sample.

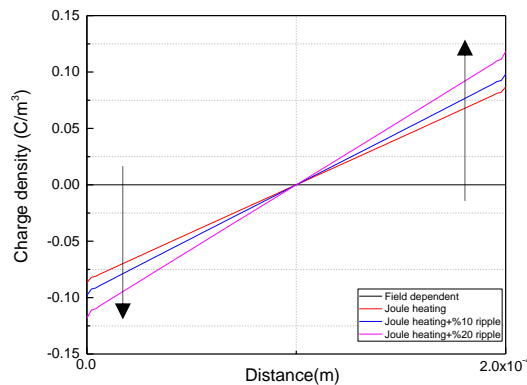
Constants	Symbols	Values
Applied voltage	V	8kV
Reference conductivity	σ_0	$2 * 10^{-14}$ S/m
Relative permittivity	ε_r	2.3
Vacuum permittivity	ε_0	$8.854 * 10^{-12}$ F/m
Imaginary permittivity	ε'	0.0003

Laplace field (VDC/d)	E_m	40kV/mm
Electric field reference	E_0	10kV/mm
Material constant	γ	1.8
Temperature coefficient	α	0.1
Reference temperature	T_0	293K
Thermal conductivity	k	0.329 W /m K
Specific heat of material	c_p	2250 J kg/K
Density of material	ρ_m	920 kg/m ³
Maximum time	T_{max}	20s

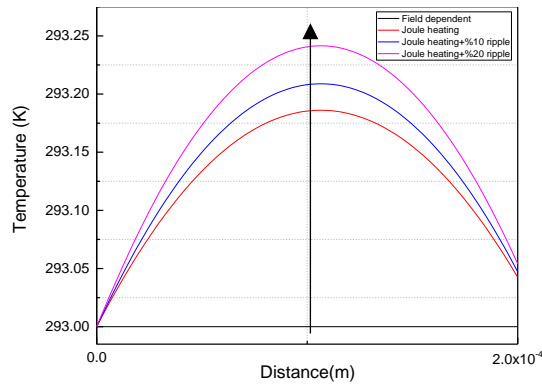
The results of the charge transport model simulations of the four cases are shown in figure 7.13. Here the electric field distribution (a), space charge distribution (b) and temperature distribution (c) are shown.



(a)



(b)



(c)

Figure 7.13: (a) Electric field, (b) space charge, (c) temperature distribution in 1-D insulation sample under 40kV/mm DC with different ration of ripple voltage.

The result of first case and second case were already shown in chapter 4. Here, they repeated to compare with the cases of combined DC + AC ripple voltage. In the first case, when the conductivity was only field dependent no space charge was accumulated and as expected from theory, the electric field was distributed uniformly. In the second case, when the conductivity was field and temperature dependent under pure DC applied voltage the effect of Joule heating was to increase the temperature slightly within the bulk of the sample. This results in space charge accumulation within the sample and a reduction of electric field in the bulk and enhancement at the part of dielectric adjacent to the both surfaces. In the final case, when the applied voltage contained an AC ripple voltage, and when the Joule heating and dielectric heating were considered, the dielectric heating caused a higher temperature to be produced. As a result, more space charge was accumulated which led to increasing the non-uniformity of electric field distribution across the insulation sample. Dielectric and Joule heating can therefore both contribute to a non-uniform electric field inside the insulation, with an electric field enhancement that is greatest at the sample surfaces. It is possible that this effect could cause the initiation of breakdown from defects situated at the interfaces of the insulation particularly at higher applied voltages.

7.6 Summary

In this chapter the effect of ripple voltage (that originated from the convertor stations and superimposed on DC voltage at the DC side of transmission power system) on space charge accumulation was examined in both one layer and two layer LDPE samples. Experimentally, the assessment was conducted by modifying the electrical power supply

that was applied on PEA system. While the boundary condition of electrical power supply of the charge transport model was modified in order to assess the effect of ripple voltage numerically.

In a single layer LDPE sample, the experiments and the simulations were performed under 0%, 10% and 20% AC ripple voltage which were superimposed on -6kV DC voltage for 30 minutes. In all cases, the charge were accumulated in the form of homocharge. However it was found that increasing the ratio of AC ripple led to accumulate more homocharge adjacent to the electrodes. This also had the impact of increasing the maximum electric field in the insulation.

The effect of ripple voltage on space charge accumulation in double layer LDPE material was also examined experimentally and interpreted using simulation models. Experimentally, the conductivity difference between the layers were obtained by degassing one of the samples and using it combination with a non-degassing sample. From both simulation and experiments, a homocharge was found to accumulate adjacent to the electrodes and interfacial charge was observed between the layers. However, when the ratio of AC ripple was 10%, the homocharge accumulation near the electrodes and the peak of interfacial charge were found to be larger compared with the case of 0% AC ripple (only DC voltage).

Comparing between the results that were obtained from one layer and two layer samples show that, the effect of ripple voltage is to cause more homocharge to form in the insulation and at interfaces and results in an increase in the maximum electric field. These findings show that the ripple voltage that originated from the DC convertor stations influences the accumulation of space charge and interface charge. The effect is small but significant and could potentially lead to a consequential decrease in lifetime of the insulation.

Finally, the charge transport model was modified to be able to calculate the effect of joule heating (due to DC applied voltage) and dielectric heating (due to AC ripple voltage) on space charge accumulation. It was found the ripple voltage can build the dielectric heating and by which can effect on space charge and electric field distribution, although the value of dielectric heating and it is effect on space charge was found to be very small.

8 Discussion

8.1 Overview

HVDC equipment is subject to ageing and degradation of the primary insulating materials and this limits the service lifetime and reliability of modern HV power transmission. Of particular concern are the failure modes related to polyethylene based HVDC cable insulation as used in current and future HVDC transmission systems. These polymeric insulation materials are subject to both electrical and thermal stresses during service.

The electrical stress arises due to the applied HVDC voltage and can cause space charge to accumulate within the insulation that can modify the internal electric field. However, the main thermal stresses applied to the cable is due to joule heating of the central conductor when the cable is in operation and carrying full load current. In XLPE based polymer based cables the temperature of the insulation adjacent to the central conductor is limited to 90°C to prevent the onset of thermal degradation through oxidation whereas the temperature of the outer region of the cable insulation is dependent on the conditions in which the cable is situated. In submarine cables, the temperature will be limited by the temperature of the sea bed and the sea water can act as a sink of heat energy. Consequently during service the cable insulation will be subject to a thermal gradient set up by the temperature of the central conductor and the sea temperature. Besides the thermal stress, the temperature gradient within the cable insulation will also lead to space charge accumulation and further modification of the internal electric field if the insulating material exhibits a field dependent electrical conductivity.

The impact of thermal and electrical stresses are therefore interrelated processes that cannot be uncoupled in a simple manner and studied separately. Measurement of the internal electric field is usually obtained through space charge measurements. Equipment such as the pulsed electroacoustic (PEA) method has been used extensively to measure space charge and from the space charge distribution obtain the electric field profile. However, PEA apparatus is subject to significant limitations when applied to materials that are subject to a temperature gradient and the signal processing required to reconstruct the space charge profiles involves unstable mathematical transformations that can render the technique unreliable. The traditional approach for using the PEA technique and its limitations are described in chapter 3. As the output signal of the PEA system is not real space charge due to many distractions and imperfections of the PEA layers, researchers try to find the original space charge before getting any distortion which is termed the

traditional approach of space charge recovery. Deconvolution, attenuation/dispersion and calibration are the main three steps that have been taken to recover the space charge. However, most of the researchers avoid calculating the attenuation and dispersion coefficients, because any fault in finding these coefficients lead to instability and fault interpreting in space charge recovery data. Besides that the assumption of perfect acoustic match between the PEA layers can potentially lead to incorrect calibration of space charge profile. In addition the temperature gradient which mostly originated from the cable conductor has direct effect on the acoustic properties of the sample and the PEA layers. In a traditional method of space charge recovery it is also difficult to account the effect of temperature gradient on the acoustic properties and permittivity of the sample. Non-considering of these factors or the inaccuracy introduced in not considering these factors correctly during space charge recovery from raw PEA data are the two weak points that limit the progress of understanding space charge phenomena in insulation systems.

For the reasons given above, in this work, an alternative approach was taken to study the impact of electro-thermal stresses (including the presence of ripple voltage) on cable insulation systems on space charge accumulation and subsequent internal electric field modification. The starting point was the formulation of a one-dimensional time-domain finite difference based simulation model (chapter 4) for electrical transport that encompasses the non-linear electric field and temperature dependent electrical conductivity. This model extends and modifies the work of Bodega [54] and Jeroense [46] who applied the model for calculating the space charge in a cylindrical geometry of XLPE and paper insulation material respectively under field and temperature dependent conductivity. Electric conductivity modification due to the presence of diffused impurities that can lead to homocharge accumulation at the sample interfaces. This modification was based on papers [58, 80, 81], where it was used to calculate the homocharge and heterocharge accumulation due to the diffusion of impurities from the electrodes. This model was applied to single layer and double layer samples under isothermal and temperature gradient conditions. The model output gives the time evolution of space charge and the electric field distribution inside the insulator material. The developed model therefore has the capability to calculate the effect of many factors on space charge accumulation such as, electric field, temperature (temperature gradient due to temperature difference between the electrodes, Joule heating inside the sample due

to the applied DC voltage and dielectric heating due to the AC ripple voltage) and effect of AC ripple which superimposed on DC voltage. For the first time the effect of Joule heating, dielectric heating and AC ripple voltage on space charge accumulation are counted. The details of the charge transport model in cases of pure DC and DC superimposed with AC ripple are described in chapter 4 and chapter 7 respectively. This model was then extended in chapter 4 to two-dimensions in order to assess the impact of space charge accumulation around electrically conducting defects in order to reflect inhomogeneity of the insulation material.

To be useful and to compare the electrical transport simulation model predictions with PEA based experimental data it was necessary to develop a simulation model of the PEA instrument again based on the finite difference method for the generation, transport and detection of the acoustic waves. The PEA simulation takes into account all the instrument imperfections of resolution, acoustic reflections, attenuation and dispersion, influence of temperature on acoustic wave propagation and the response of the piezo sensor and amplifier as described in chapter 5. The development of the PEA simulation model follows the theory provided by Hole [145] coupled with the theory of acoustic wave propagation in elastic media. In this model, the effect of the PEA top electrode properties, type of electrodes and effect of temperature gradient on the acoustic properties (effective modules and density) and permittivity of the sample can be established for the first time. The simulation model also included attenuation/dispersion correction as well as the instrumental effects of having a capacitive piezoelectric sensor driving a 50 Ohm input impedance amplifier (which works as a high pass filter) and oscilloscope frequency response which works as a low pass filter. The details of these corrections are also explained in chapter 5. Comparison of PEA simulations with experimental raw PEA data under the conditions of zero space charge accumulation show good agreement and validate the developed PEA simulation model. The PEA simulation parameters once tuned to the experimental apparatus under zero space charge conditions remained fixed for all subsequent simulations.

In order to develop the above simulation models, the finite difference method was used and implemented in MATLAB. Based on the models, instead of employing the traditional approach of working backwards from the PEA raw output data to recover the space charge profile through signal processing, simulation models of the charge transport and electrical conduction processes in insulating materials can be used as the input to the PEA

simulation model and this provides simulated PEA raw output signal that can be compared directly with experimental data.

Combining the charge transport and PEA simulation models provides a framework for understanding the dynamics of space charge accumulation based on comparison with experimental PEA space charge data without the need to employ the mathematically unstable techniques of space charge recovery as outlined in chapter 3. The simulation results were compared with the experimental results in cases of polarisation and depolarization in both single layer and double layer LDPE samples. In each of the case studies, the parameters of the charge simulation model were changed until the output of the combined charge transport and PEA simulation became the same as the PEA measurement raw data (the PEA simulation parameters were kept at their tuned values). Therefore, the only difficulty was finding the appropriate parameters for the charge transport model that would enable a match in terms of the amount of space charge, its spatial extent and the dynamics of charge accumulation/decay during initial polarisation and depolarisation stages. After that the simulation results were saved for the same time intervals as that from the PEA measurements.

8.2 Space charge accumulation in single layer samples

Initial 1-D simulations for the case of uniform internal electric field in the thin film sample, it was found that no space charge accumulated when the electrical conductivity was field dependent only. Only when the electrical conductivity of the material was made non-uniform due to temperature dependent effects or when the electrical conductivity was modified due to the diffusion of impurities, space charge was found to accumulate. Applying the combined simulation model to the case of thin film insulation samples under polarization and depolarization operating conditions in single layer LDPE samples the result showed when the temperature was isothermal across the sample, the space charge accumulated near to the electrodes was in the form of homocharge. As mentioned above, the experimental results showed the homocharge was accumulated near the electrodes in case of isothermal temperature in the LDPE samples. In chapter 6, to be able to match the simulation results with the experimental results the electrical conductivity of the insulation samples were modified according to Boggs model [58]. Based on that, the nonlinear electric field distribution and space charge accumulation is obtained not just due to the electrical applied voltage, but also due to the impurity diffusion within the insulation sample. However, the space charge that was accumulated close to the sample

surfaces was asymmetric suggesting that the impurity diffusion was different at each surface of the specimen. The asymmetry in the diffused impurities can be traced back to the method in which the material was supplied. The LDPE was formed of a flattened tube and the tube was wound as a roll as shown in figure 8.1. This roll, was then stored in the laboratory for 10 years. The asymmetry in impurities can therefore be explained in terms of the manufacturing of the LDPE tube in which the inner surface is enclosed and protected from the environment whilst the outer surface remains exposed to the atmosphere.

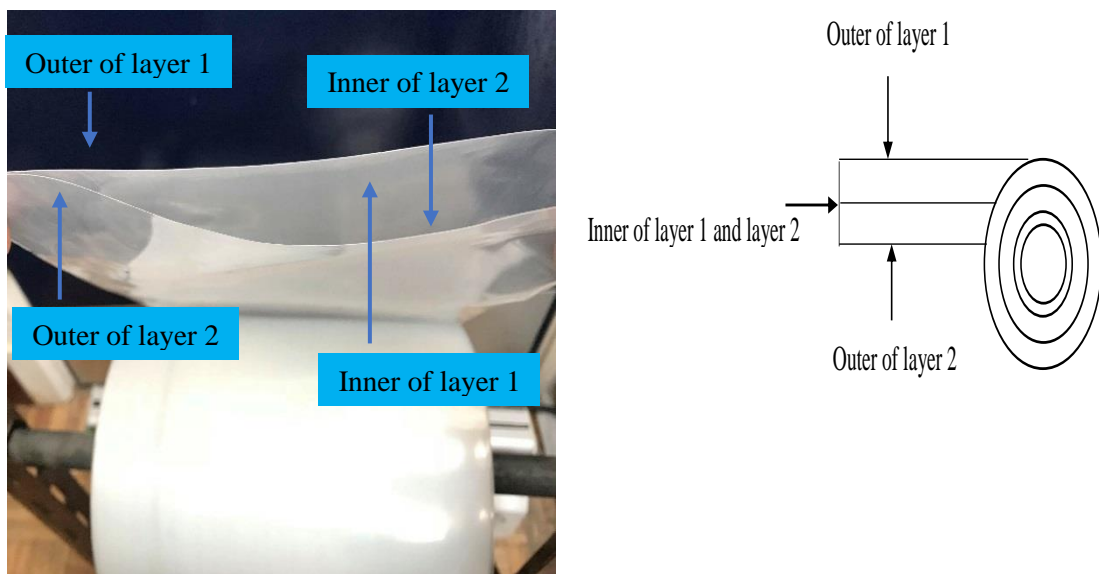


Figure 8.1: As supplied LDPE material.

The depolarisation results also demonstrated that the time required for the decay of space charge is generally significantly longer than for the time to accumulate the charge under polarisation. This is consistent with the field dependent electrical conductivity expression used in the charge transport model. Following voltage removal, the main source of electric field is removed and only the field due to accumulated space charge remains. The electrical conductivity therefore reduces which slows down the process of charge decay.

In case of degassed LDPE sample the conductivity was smaller in comparison with the 'as received' LDPE sample, which means homocharge had formed due to diffused impurities and not just due to charge injection from electrodes. This again is in agreement with Hjerrild and et al in [58], in which they state that the impurity diffusion from semiconductor into polymer can take place and leads to an enhanced electrical conductivity and by which will cause the formation of homocharge regions within the insulation.

A comparison was also made between LDPE and XLPE single layer samples. The amount of homocharge that accumulated in LDPE was higher than that accumulated in XLPE by more than a factor of two. This difference is likely to be due to their differences in impurity level, morphology, chemical structure and thermal treatment after cross-linking.

8.3 Effect of thermal gradient on charge accumulation

As the PEA measurement system in the laboratory was not capable of space charge measurements under temperature gradients conditions the results of the developed simulation models in case of temperature gradient were therefore compared with PEA measurement and simulation results of the published work which were carried out at Xian University[75]. In that paper, the PEA measurement and the bipolar charge transport model were used to measure and interpret the accumulation of space charge inside 350 μm thick XLPE sample under an applied field strength of 50kV/mm. Space charge measurements were conducted with temperature gradients of 0°C, 20°C and 40 °C applied across the sample. To be able to simulate the PEA results as the published work, the two simulation models were modified to reflect the configuration of the PEA. In this case the modification of the electrical conductivity due to diffused in impurities was not undertaken as it was assumed that the XLPE material was free of impurities. However from the results of charge transport model, the temperature gradient caused the accumulation of heterocharge to occur in the sample near the lower temperature electrode and accumulation homocharge near the high temperature electrode. The heterocharge and homocharge was obtained just due to the effect of temperature gradient even without the conductivity modification. The heterocharge was accumulated near the lower temperature side electrode. This is because the electric conductivity of the XLPE is higher at the high temperature side compared to that at the lower temperature side. The authors of the experimental PEA measurement work used a bipolar charge transport model including injection and extraction of charge carriers at the interfaces and the PEA electrodes. The authors concluded that the temperature gradient acts to reduce extraction of charge carriers from the lower temperature side compared with injection charge carrier from the high temperature side. However given that the combined model was found to give a better fit to the PEA output data compared to the author's result of using the bipolar charge transport model supports the conclusion that the non-polar charge transport

without charge injection/extraction is sufficient to describe the results obtained. This to some extent may be due to the authors not using a PEA model that adequately corrects for the PEA system imperfections particularly in the case of applied temperature gradient.

8.4 Space charge accumulation in double layer samples

The dominant space charge accumulation feature was the build-up of space charge at the interface between the two layers when the electrical conductivity of the two layers was made different. In these experiments the electric conductivity of the layers were modified by conditioning the material under vacuum at 50°C for 24 hours. In the case of two layer LDPE samples, when a degassed layer was attached to the Al electrode and used with an ‘as received’ layer attached to the negative HV electrode, negative space charge accumulated at the interface between the two layers. This is due to the ‘as received’ layer having a higher electrical conductivity and hence initial current density. The build-up of charge at the interface decreases the electric field in the ‘as received’ layer and enhances the electric field in the degassed layer. A steady state is achieved then the process of field modification leads to the same current density flowing through both layers. In addition to the accumulation of charge at the interface, smaller amounts of homocharge were observed to accumulate in the sample close to the electrodes. The origin of these homo charges was due to electrical conductivity modification due to the presence of the diffused impurities that had formed either during manufacture of the thin films or occurred during storage of the films in the laboratory.

When the applied voltage was removed, the only source of electric field is the charge accumulated at the interface. This interface charge slowly decreased with time causing the magnitudes of the electric field in both layers to decrease. However, even after 60 minutes of depolarisation, a significant amount of space charge remained in the sample at the interface between the dielectrics which is about 4.5 C/m³. The significantly longer time for the interface charge to decay was due to the field dependent electrical conductivity.

On the other hand, when sample layers were degassed under vacuum 80 °C for 48 hours, the sample layers acquired an electrical conductivity that was greater than that of the ‘as received’ layer. This unexpected result is probably due to thermal decomposition during the degassing stage of the host polymer. This conclusion is supported in the literature [16], which it is mentioned that LDPE cannot be used above 70 °C. Increasing the temperature above that degree might cause aging and degradation.

8.5 Effect of ripple voltage on space charge accumulation

In chapter 7 for the first time combined simulation and experiments were conducted in order to find out the effect of AC ripple superimposed on the DC voltage on space charge accumulation. In practise this ripple voltage originates from the convertor stations of HVDC transmission system. The space charge were measured and simulated in one layer and two layer LDPE samples with different ratio of ripple voltages (0%, 10% and 20%). The results of both simulation and experiment showed that the greater the ratio of ripple voltage led to greater amount of space charge to be accumulated adjacent to the electrodes. However, it was found that the effect of ripple on two layer was more severe compare with the one layer insulation sample especially at the interface between the samples. The increment in the space charge density near the electrodes or at the interface between the electrodes can be explained by the time-dependent charging and discharging of the sample due to the applied AC ripple voltage. On the positive half cycle of the ripple voltage, the electric field increases at the electrodes and conversely, on the negative half cycle, the electric field decreases. The consequence of this is that the field dependent conductivity of the dielectric near the electrodes will be higher during the positive half cycle compared to the negative half cycle of the ripple voltage. Also, the local time constant associated with charging and discharging determined by the local permittivity and electrical conductivity ($\tau_{loc} = \frac{\epsilon_0 \epsilon_r}{\sigma_{loc}}$) will therefore be smaller during the positive half cycle of the ripple voltage and consequently during the positive half cycle, charge will penetrate deeper and allow more charge to accumulate. With increasing magnitude of ripple voltage, more homo-charge must accumulate to reduce the electric fields at the injecting electrodes and bring the current in the dielectric at the electrodes into equilibrium with the current in the body of the sample. Although the results showed that the effect of ripple is small, it is significant and could potentially lead to a consequential decrease in lifetime of the insulation. Again from all the cases of measuring space charge in case of ripple voltage a good agreement were found between the simulation and experimental results.

In case where the applied voltage was not pure DC (AC ripple voltage superimposed) and when the conductivity was field and temperature dependent, besides the Joule heating that generated due to the DC voltage, the dielectric heating was also generated due to the effect of AC ripple voltage. In order to determine the effect of dielectric heating on space charge accumulation the electro-thermal charge transport model was modified and the

external applied voltage first was pure DC and then DC superimposed with 10% and 20% AC ripple voltage. It was found that the dielectric heating caused higher temperature to be produced in the bulk of the sample compared with the case of Joule heating that obtained under pure DC voltage. As a result, more space charge was accumulated which led to increasing the non-uniformity of electric field distribution across the insulation sample. Dielectric and Joule heating can therefore contribute to a non-uniform electric field inside the insulation, with an enhancement that is greatest at the sample surfaces. However, experimentally it is difficult to measure the dielectric heating and its effect on space charge accumulation especially under low applied voltage and under low frequency of AC ripple.

8.6 Samples containing conducting defects

In chapter 4 the proposed charge transport simulation model was extended to two dimensions in order to assess the influence of electrical conducting defects on space charge accumulation. In the case of charge transport simulations in a homogeneous single layer sample (without the conducting defects) the electric field was found to be distributed uniformly and no space charge were accumulated. This is the same as was found in the 1-dimensional model. However, in the case of a non-homogeneous sample, where the sample contained conducting defects, a significant amount of space charge was found to accumulate in the dielectric surrounding the defects and this amount increased with time until a steady state was obtained. The accumulation of space charge around the defect had the effect of decreasing the electric field enhancement surrounding the defect that would have occurred in the absence of space charge and increasing it near the electrodes. This effect was found to be highest for the nodes along the axis of the defect. On the other hand, when the conductivity was temperature dependent and Joule heating in the dielectric was considered, the effect on space charge accumulation was very small as the local heating of the material surrounding the defects was also small. This justifies why Joule heating of the dielectric is often neglected in the literature and assumed to be significantly smaller than that due to heating by the central conductor under typical service fields of up to 20 kV/mm. In case of a homogeneous single layer sample the Joule heating that was produced at the middle of the sample under 37.5kV/mm was found to be about 0.17 °C, while when the sample contained conducting defects the Joule heating around the defect was found to be 0.5 °C under 40kV/mm. However, for the parameters that were used in the simulation, increasing the voltage to above 40kV/mm led to

significant increase in the Joule heating surrounding the defect and resulted in a reduction of the accumulated space charge and defect field, and increased the electric field at the electrodes. When the applied voltage was 60kV/mm the Joule heating losses around the defect increased in temperature by 3.5 °C.

8.7 Charge transport in LDPE

The success in employing the combined charge transport models to simulating raw PEA output data and hence space charge accumulation in LDPE samples over a wide range of conditions as detailed in chapters 4-7 provides justification for the use of the empirical expression for electrical conductivity, equation 2.16. This equation relates the intrinsic electrical conductivity of polyethylene to a power law dependence on electrical field and exponential dependence on temperature. As an empirical function, it does not relate to a particular charge carrier. However, function wise, the formula share similar characteristics as the equation derived from the electron hopping model, equation 2.14, where the power law field dependence is replaced by a hyperbolic function of the field. The shared features are the increasing conductivity with increasing electric field magnitude and increasing temperature. However, from the double layer experiments, it was found that the conductivity decreased when the sample was degassed at 50°C suggesting that charge transport in the ‘as received’ LDPE is dominated or mediated by the presence of impurities either introduced during the manufacturing of the thin films or acquired by the diffusion of impurities from the environment during storage (the thin film LDPE is approximately 10 years old). This observation supports the view that diffused impurities enhances the electric conductivity at the interfaces of the samples and leads to homocharge accumulation as was deduced from the single layer experiments. The equation used for the enhancement of conductivity was given by equation 4.9. This equation for the modified electrical conductivity is the product of the field and temperature dependent conductivity and a spatial function dependent on an assumed exponential function of distance that reflects the distribution of impurities. The use of the product of these two quantities for the effective conductivity implies that the presence of impurities enhances the conduction mechanism rather than adding a second but separate conduction mechanism based on the impurities present. In terms of the hopping transport model this can be explained in terms of the impurities donating additional charge carriers rather than altering the potential barrier depths as this would also reflect in a different temperature dependence. On the other hand, degassing for an extended time at 80 °C had

the reverse effect of increasing the electrical conductivity. This temperature may therefore mark the onset temperature for thermal degradation of the LDPE material used and the degradation products formed enhancing the electrical conductivity.

In the electro-thermal charge transport model, Schottky charge injection at the electrodes is not considered and therefore no charge is explicitly injected or extracted from the sample. Given the success of the combined model in replicating experimental data, this point suggests that the charge injection mechanism is not an important factor in governing charge accumulation dynamics. In addition, the use of a more complex bipolar charge transport model often proposed in the literature is not a requirement in understanding the dynamics of charge accumulation in the materials used in this work. This is partly because the internal electric field that governs charge transport is determined by the net charge density distribution as is the response of the PEA instrument.

8.8 Impact on electro-thermal ageing

The capability of insulation material to withstand high electrical and high thermal stress is reduced over time. The reduction of the performance of the insulation material over time is called ageing. In the literature two different approaches for the understanding of material aging and the role of space charge have been introduced. Both ageing models are summarized by Mazzanti et al. in [146]. In the DMM (Dissado-Mazzanti –Montanari) model [147, 148], space charge was considered as both cause and effect of polymer ageing, while the other proposition which is supported by the Crine model and the Lewis model [146], associate space charge just as a marker of aging. The DMM model is based on thermodynamic approach to the degradation rate of insulation material subjected to electrical and thermal stress. Based on this model the local electric field is modified due to the presence of space charge and by which enhances the aging reaction [146]. The expression to describe the rate of electro-thermal aging is shown in equation 1 [149, 150].

$$\frac{dX}{dt} = k_f - (k_f + k_b)X \quad (8.1)$$

Here, X defines the progress of the reaction, between zero and one with time and k_f and k_b are the forward and backwards reaction rate constants respectively. The concept of a back reaction implies that it is possible for the ageing reaction to be reversed from the aged state back to an unaged state.

The forward and reverse reactions requires a field-assisted crossing of a free energy barrier, G, from the ground state of the reactant to that of the product, which lies an energy Δ higher. Thus:-

$$k_f = \frac{kT}{h} \exp\left(-\frac{G-C'E^{2b}}{kT}\right) \quad (8.2)$$

$$k_b = \frac{kT}{h} \exp\left(-\frac{G-\Delta}{kT}\right) \quad (8.3)$$

Where, k and h are Boltzmann and Plank constant respectively. T is absolute temperature. The available field energy concentration in the specific location to drive the reaction is described by $C'E^{2b}$ where E is the electric field. The ageing reaction will approach a field and temperature dependent equilibrium value for the reaction progress, X . It is assumed that failure will occur if the reaction progress, X , reaches or exceeds a critical fraction A^* . An expression for the lifetime can be deduced [146] as

$$L(E, T) = \frac{h}{2kT} \exp\left[\frac{\frac{\Delta H}{k} - \frac{C'E^{2b}}{2}}{T} - \frac{\Delta S}{k}\right] \ln\left[\frac{A_{eq}(E)}{A_{eq}(E-A^*)}\right] \left[\cosh\left(\frac{\frac{\Delta}{k} - C'E^{2b}}{2T}\right)\right]^{-1} \quad (8.4)$$

Where, $A_{eq}(E)$ is the value of A at the equilibrium between forward and backward reactions. ΔH and ΔS are the activation enthalpy and entropy per moiety respectively. The parameters, Δ , C' , b , A^* can be considered as generic parameters whose values can be found from experimental lifetime data [151].

Based on the above equations, increasing electric field and temperature act to enhance forward reaction (k_f) to become greater than the backward reaction (k_b) causing aging and degradation to occur. Therefore enhancement in electric field distribution inside the insulation material has effect on life time of insulation polymers.

Defects and particularly the macroscopic conducting defect can give rise the electric field immediately to above the average applied field. In DC fields the conducting regions of degradation will form space charge regions that will lower their field-enhancing capability and hence tend to prolong the lifetime. However in a thermal gradient the space charge around the degraded region will be reduced and the field enhancement will move back towards that calculated in the simulation. This clearly shown in Chapter 4.

On the other hand, the results of chapter 7 shows that the AC ripple which superimposed on DC voltage can enhance the electric field in the bulk of the sample. The greater the amount of AC ripple, the greater enhancement of electric field will occur due to the accumulation of homocharge inside the sample. If the degree of field enhancement is sufficiently high this will ultimately cause enhanced aging and reduced lifetime.

9 Conclusions and Future Work

9.1 Conclusions

The work describes the successful development of an electro-thermal charge transport model and PEA apparatus simulation model based on finite the difference techniques for the understanding of space charge accumulation in insulating materials and as a non-subjective framework for the interpretation of PEA space charge detection techniques. A non-polar empirical based electro-thermal charge transport model based on an empirical equation for electrical conductivity was used to determine the accumulation of space charge in single layer or double layer thin film samples subject to applied voltage regimes of polarisation and depolarisation. The applied voltage was pure DC and DC superimposed ripple voltage under conditions of isothermal and/or temperature gradient conditions. The charge transport model developed here also had provision for Joule heating and dielectric heating of the insulation in order to examine effects due to the DC and AC components of current flow through the insulation. This model is based on an empirical function for the electric field and temperature dependent electrical conductivity. The model is shown to possess many of the known features that influence the accumulation of space charge in thin film samples. In order to compare the output of space charge accumulation as predicted by the charge transport model it was necessary to also simulate the PEA space charge measurement technique. In this work a finite difference based simulation model was developed to take the output data from the space charge accumulation model (the electric field distribution) as an input and to determine the generation of the longitudinal acoustic pressure waves from the space charge distribution. The model simulates the propagation of the acoustic waves through the PEA instrument to the piezo-electric detector and conversion into an electrical signal. The PEA simulation model includes the generation of artefacts in a real system by modelling the reflection of acoustic waves at material boundaries of different acoustic impedance, attenuation and dispersion of the propagating acoustic waves and the frequency response of the detector/amplifier response. The electro-acoustic simulation model can therefore simulate and predict PEA raw data that can be directly compared with the experiment. This methodology overcomes the potential problems and pit-falls associated with the traditional method of reconstructing the space charge profiles directly from the raw PEA output data using unstable deconvolution and matrix inversion techniques [23].

The two simulation models have been applied to the case of single layer specimens under isothermal conditions. The results of the simulations were successful in replicating experimental derived raw PEA data including replicating the effects of acoustic reflections at the PVDF piezo sensor/absorber interface, the distortion of the signal due to the high pass frequency response and attenuation and dispersion of the acoustic waves as they traverse across the sample material. It was also demonstrated that the simulation models can overcome the limited spatial resolution of the PEA instrument (~5% of the sample thickness) as the charge transport model can simulate space charge profiles and electric field profiles at the precision of the finite difference grid. Thus the simulations allow the electric fields at the sample electrodes to be estimated with much greater certainty than is the case from the PEA instrument alone. Further simulations have demonstrated the potential for error in the traditional method of space charge profile recovery when different materials are used for the top electrode and the sample.

The case where the temperature was isothermal, single and double layer simulations and experiments have also demonstrated that significant build-up of homocharge at the interface regions of the samples. In the simulations this effect could be reproduced by incorporating the effects of impurity diffusion into the surfaces of the sample and supports the idea first described by Boggs [58] that impurity diffusion from the surfaces (or from the semicon materials if present) lead to a modification of the electrical conductivity close to the surfaces. For homocharge injection, the material conductivity must be increased close to the sample surfaces. Repeat experiments on samples of different thermal conditioning at 50 °C and at 80 °C partly confirm this hypothesis. At low temperature, conditioning at 50 °C results in the removal of impurities, lower electric conductivity enhancement and reduced homocharge formation. However prolonged conditioning at 80 °C had the reverse effect. These results demonstrate the criticality of the environmental temperature when conditioning the samples to remove impurities. A temperature of 80 °C is sufficient to initiate thermal ageing of the LDPE samples used for the experiments.

Results from polarisation and depolarisation experiments and simulations have shown that the rate of formation of the heterocharge regions is higher than for the subsequent discharge of the homocharge when the applied voltage was decreased to zero. This is the consequence of the material's field dependent conductivity. During polarisation, the material has a high conductivity leading to the fast accumulation of homocharge at the

electrodes. However on depolarisation, the electric field within the sample is due only to the charge contained within it and will be much less than that during the initial polarisation. Consequently, due to the lower field dependent electrical conductivity, the homocharge takes much longer to decay. The field dependent electrical conductivity therefore offers an alternative explanation to charge trapping at deep trapping centres to explain the retention of charge in insulators following voltage removal.

The combined simulation model was also successful in replicating the thermal gradient experiments and simulation results that were conducted at Xi'an Jiaotong University [75], where the effect of temperature gradient on space charge accumulation in XLPE thin film samples was investigated. In the work carried out at Xi'an, the space charge accumulation was explained in terms of a bipolar charge transport model with the provision for charge trapping and recombination and the injection and extraction of charge at the electrodes. The fact that the proposed interpretation framework as proposed in this thesis gave superior fits to the experimental data than the bipolar charge transport model gives credence that the empirical field and temperature dependent charge transport model with significantly fewer free parameters provides a better representation than the significantly more complex bipolar transport model. An additional reason for the superior fit using the combined model approach used here was that in the original work did not take into account all the artefacts of longitudinal acoustic wave propagation in a medium in which the material characteristics are continuously changing through the thickness of the sample due to the imposed temperature gradient.

The combined simulation framework and experimental verification has been applied to the case of applied ripple voltage superimposed on the steady DC voltage. The effect of ripple voltage on space charge accumulation has therefore been investigated for the first time. The simulation and in parallel, verification experiments were carried out in both one layer and double layer samples. It was found that the addition of an AC ripple voltage led to increased homocharge accumulation at the electrode interfaces in comparison to the pure DC case. Increasing the ratio of the AC ripple to the DC voltage led to an increase in the amount of space charge accumulated. The effect of ripple on space charge accumulation in two layer sample was found more severe especially for charge accumulation at the interface between the samples. These findings show how the AC ripple voltage occurring in DC convertor stations causes space charge to modify the internal electric field which potentially affects the progress of electro-thermal ageing

which determines the life time of the cable insulation. The convertor manufacturing companies already try to limit the ratio of ripple voltage to about 10% by installing DC smoothing capacitors in parallel with the DC circuit at both sides of convertor stations. However, the disadvantage of this method for ripple control is the high economic cost.

In the case of superimposed ripple voltage it was shown that dielectric heating (due to AC ripple voltage) contributed to the Joule heating due to the DC voltage component. The effect of dielectric and Joule heating on space charge accumulation were to heat the interior of the sample. This heating caused a marginal increase in temperature under normal operating conditions. This led to an increase in the conductivity within the bulk of the sample that led to more space charge accumulation. Dielectric and Joule heating which is usually neglected in the literature, can therefore contribute to non-uniform heating by the electric field inside the insulation and therefore potentially to reduced lifetime.

The charge transport model was extended to the case of space charge accumulation around electrically conducting defects. In this case it is not possible to probe space charge accumulation experimentally using the PEA approach. To do this defects were defined on a 2-D grid to represent spatial non-homogeneity. The accumulation of space charge was found to occur in the dielectric surrounding the defect due to electric field enhancement and electric field dependent electrical conductivity. When including the effect of Joule heating due to the transport of charge under DC applied voltage, local heating occurred around defects which had the further effect of increasing the electrical conductivity of the dielectric causing the amount of space charge to become less. For the parameters that were used in the simulation, under applied fields $<40\text{kV/mm}$, dielectric heating was small and did not have a significant effect on the accumulated space charge. However, increasing the applied voltage above 40kV/mm led to a significant increase in the local Joule heating surrounding the defect and resulted in a significant reduction of the accumulated space charge and an increase in field at the electrodes.

9.2 Main contribution of this work to the research field

This research has proposed a novel framework, through the proposed combined simulation models, to enhance the understanding of space charge characteristics in thin film insulation polymers as well as a robust interpretation methodology for experimental space charge measurements based on the pulsed electroacoustic (PEA) technique. The knowledge gained from this fundamental research enables researchers and technicians to

develop models to characterise the electrical properties of electrical insulation materials through comparison between the simulation predictions and raw PEA space charge measurements. This work lays the foundations for the power industry to adopt robust methodologies for the selection of insulation materials for improved reliability of the HV cable transmission system. The main novel contributions of this research work can be summarized by the following points:

- 1- A package of simulation programs has been developed, encompassing an electro-thermal model for electrical conduction to predict space charge accumulation and a PEA simulation program to predict PEA raw output data. This was shown to be successful in reproducing experimental raw PEA data without the need to employ signal processing techniques that degrade the PEA data in determining the space charge distribution [152]. The proposed combined simulation technique offers a number of advantages over the traditional signal processing techniques usually employed by researchers in the field [30, 31, 97]. The proposed novel combined simulation technique can be used to calculate electric field and space charge distributions in insulating materials to a spatial resolution determined by the number of nodes used in the numerical simulation of charge transport. This means that the electric field and space charge distributions can be calculated at all points within the insulation thickness making it possible to determine the electric fields at the sample surfaces. This is not possible using the traditional approach as the electric field is determined from the recovered space charge distribution which has limited spatial resolution [97]. The space charge distributions predicted using the novel framework are consistent electrostatically and are not affected by instrumental imperfections such as acoustic reflections, acoustic attenuation and dispersion, and the characteristics of the high pass filter network formed due to the capacitance of the PEA acoustic sensor and the resistive input impedance of the amplifier [46]. The predicted space charge and electric field distributions are also unaffected by choice of the deconvolution parameters used correcting for the PEA system response and for the corrections for acoustic pressure wave attenuation and dispersion [31]. The proposed novel combined simulation approach can be applied to model and analyse the space charge accumulation behaviour in single layer and double layer thin film LDPE and XLPE samples under isothermal conditions or when a temperature difference is applied across the sample [75].

- 2- The electrical characteristics of LDPE thin film insulation were explored using the novel approach under different electrical and temperature conditions. The LDPE thin film samples that were used in this research, it was found that under DC applied voltage the space charge was accumulated in the form of homocharge due to the diffusion of impurities either during the manufacture or during storage of the thin film material. This supports the work of Boggs [58, 80] that homocharge distributions are caused by enhanced electrical conductivity at the sample surfaces due to the presence of diffused impurities and not due to alternative explanations given in the literature based on the imbalance between charge injection from the electrodes and bulk transport in the insulator material [1]. Degassing the LDPE sample under 50 °C for 24 hours led to a decrease in the electrical conductivity giving credence that charge transport in the LDPE material was extrinsic in nature i.e. dominated by the presence of impurities. This casts doubt on using the bipolar charge transport models[107, 108], in which charge carriers of both polarities (electrons and holes) are assumed to contribute to the electrical conductivity. In these models the conductivity is assumed to be intrinsic to the material in terms of the polymer chemistry and morphology forming charge trapping centres. Degassing the LDPE sample under 80 °C for 48 hours led to enhancement the conductivity and the onset of thermal degradation and the formation of additional impurity from the products of chemical reactions.
- 3- The combined simulation model was used to analyse the experimental results during the imposition of a thermal gradient. In this case the authors of the experimental work [75] employed a bipolar charge transport model to interpret the space charge distributions that had formed. However it was found that the combined novel simulation model based on a non-polar charge transport model combined with electric field and temperature dependent electrical conductivity gave superior fits to the experimental data. This demonstrates that it is not necessary to invoke a complex bipolar model with significant numbers of model parameters to describe charge injection and transport of both electrons and holes when attempting to explain the experimental data [75].
- 4- The combined simulation approach was used to assess the effect of AC ripple voltage superimposed on the steady DC component of space charge accumulation. The ripple voltage has its origins from the switching of the power electronic devices within the convertor stations. Space charge was measured experimentally and simulated using the proposed combined simulation model for the first time. The tests and simulations

were conducted on one layer and two layer LDPE thin film samples. It was found that the presence of AC ripple voltage increases space charge accumulation compared to the accumulation observed when just the DC voltage was applied to the samples. The larger the ripple voltage the more space charge was accumulated and resulted in greater electric fields within the bulk of the sample. The greater field will impact on reducing the lifetime of the insulation.

- 5- The proposed non-polar electro-thermal charge transport model was adapted to 2-D in order to consider space charge accumulation when electrically conducting defects were present for the first time. It was found that under isothermal temperature conditions and when the conductivity was field dependent a significant amount of space charge was accumulated around the defect. When Joule heating that originated due to the electric current flow inside the insulation was considered the space charge accumulation around the defect decreased leading to higher field enhancement at the defect. The effect of Joule heating has the potential to reduce insulator lifetime.

9.3 Suggestion for future work

In this study the development of a package of software simulation models has been shown to be successful in providing an alternative methodology for the understanding of the behaviour of space charge accumulation inside single layer and double layer thin film samples under a number of different situations. However, there are many other situations in which this methodology could be applied and adapted. Future work could include:

- 1- Testing the predictions of the electro-thermal model on space charge measurements at other isothermal temperatures. At present, the work has tested the predictions at room temperature 20°C and under temperature gradient conditions 20° to 60°C. This will require adaption of the existing PEA apparatus for use at elevated temperatures with PVDF copolymer for higher temperature stability.
- 2- The dynamics of space charge accumulation during polarisation measurements and space charge decay during voltage off measurements demonstrate the existence of an electric field dependent electrical conductivity. The origin of the field dependence is not known. The relationship between the empirical model for electrical conductivity and the semi-physical model based on charge hopping transport should therefore be explored further.

- 3- The combined simulation model framework has been applied successfully to the case of materials having similar material properties. The technique was successful at explaining the differences in electric conductivity between the 'as received' and degassed LDPE. However it is worthwhile to extend the proposed models for two different materials such as XLPE and EPR which are usually used for field grading in cable joints.
- 4- In this work the program codes of the proposed simulation models have been applied to thin film geometry samples. However to be more relevant to the practical application of insulating materials for HV cables, the existing code could be extended from the plane geometry case to the cylindrical geometry case. Traditional methods for space charge recovery based on signal processing are not possible in the case of cylindrical geometry as the source terms for acoustic wave generation also include other factors as well as the space charge. However the proposed framework in this thesis will not suffer this limitation as it will include all acoustic wave source terms in the PEA simulation.
- 5- The preliminary results of this study demonstrate that the presence of an AC ripple voltage superimposed on the DC voltage had a significant effect on space charge accumulation in both single layer and double layer thin film samples. Further work related to this is required to understand the effect of ripple voltage in practical engineering situations. For example, the effect of thyristor firing angle in the case of LCC systems on AC ripple or the effect of high frequency ripple voltage in the case of VSC systems on space charge accumulation is still an open question to be answered. In the case of polarization and polarity reversal it would be interesting to know in both thin film and cable geometry samples.
- 6- The effect of AC ripple voltage on life time of the cable insulation is another interesting research gap that can be considered in the future.

Appendix A: Publications

- 1- A. Mulla, S. Dodd, N. Chalashkanov, and L. Dissado, "Development of simulation models for calculating space charge accumulation around defects in a thin film sample under HVDC," in *Electrical Materials and Power Equipment (ICEMPE), 1st International Conference on*, 2017, pp. 1-4.
- 2- A. Mulla, S. Dodd, N. Chalashkanov, and L. Dissado, "Electro-thermal model for calculating the space charge around Defects in a 2-D thin film sample," in *Electrical Insulation and Dielectric Phenomenon (CEIDP), IEEE Conference on*, 2017, pp. 824-827.
- 3- A. Mulla, S. Dodd, N. Chalashkanov, and L. Dissado, "Numerical model for calculating the space charge around defects inside polymer films", *Proc. 16th Int.Symp.Electrets (ISE)*, Leuven, 2017, p152.
- 4- A. Mulla, S. Dodd, N. Chalashkanov, and L. Dissado, "Numerical model for assessing the impact of AC ripple voltage on the space charge accumulation inside solid thin film samples," *2nd IEEE International Conference on Solid Dielectrics (ICD)*, Budapest,,2018, pp1-4.
- 5- A. Mulla, S. Dodd, N. Chalashkanov, and L. Dissado, "Measurement the effect of AC ripple voltage on space charge accumulation in double layer polymer samples,". Accepted at 37th Electrical Insulation Conference (EIC), Calgary, 2019.

Appendix B: High pass and low pass filter circuits

1- High pass filter

$$Z_{output} = R$$

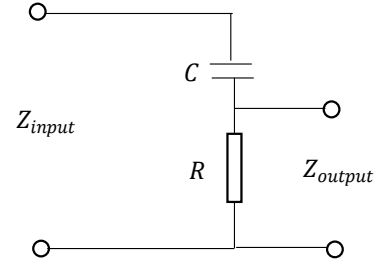
$$Z_{input} = R + \frac{1}{j\omega C}$$

$$H_{pf} = \frac{Z_{output}}{Z_{input}} = \frac{R}{R + \frac{1}{j\omega C}}$$

$$= \frac{j\omega CR}{j\omega CR + 1}$$

$$\text{But, } \tau = RC$$

$$H_{pf} = \frac{j\omega\tau}{1 + j\omega\tau}$$



2- Low pass filter

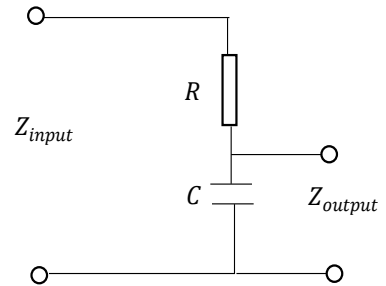
$$Z_{output} = \frac{1}{j\omega C}$$

$$Z_{input} = R + \frac{1}{j\omega C}$$

$$L_{pf} = \frac{Z_{output}}{Z_{input}} = \frac{\frac{1}{j\omega C}}{R + \frac{1}{j\omega C}}$$

$$= \frac{1}{j\omega CR + 1}$$

$$L_{pf} = \frac{1}{1 + j\omega\tau}$$



Appendix C: FDM Formula to Derive Poisson's Equation and Heat conduction Equation in 1-D thin film sample:

1- Poisson's equation

$$\frac{\partial^2 V}{\partial x^2} = -\frac{\rho}{\epsilon_0 \epsilon_r} \quad (C1-1)$$

$$\frac{V(x+\Delta x) - 2V(x) + V(x-\Delta x))}{\Delta x^2} = -\frac{\rho}{\epsilon_0 \epsilon_r} \quad (C1-2)$$

$$V(x+\Delta x) - 2V(x) + V(x-\Delta x) = -\frac{\Delta x^2 \rho}{\epsilon_0 \epsilon_r} \quad (C1-3)$$

$$2V(x) = V_{(x+\Delta x)} + V_{(x-\Delta x)} + \frac{\Delta x^2 \rho}{\epsilon_0 \epsilon_r} \quad (C1-4)$$

$$V(x) = \frac{1}{2} (V_{(x+\Delta x)} + V_{(x-\Delta x)} + \frac{\Delta x^2 \rho}{\epsilon_0 \epsilon_r}) \quad (C1-5)$$

2 -Heat Conduction Equation

$$\rho_m c_p \frac{\partial T}{\partial t} = \nabla \cdot (k \nabla T) + S_{heat} \quad (C2-1)$$

$$\rho_m c_p \frac{T_{new(x)} - T(x)}{\Delta t} = k \frac{\partial^2 T}{\partial x^2} + S_{heat} \quad (C2-2)$$

$$\rho_m c_p \frac{T_{new(x)} - T(x)}{\Delta t} = k \frac{T_{(x+\Delta x)} - 2T(x) + T_{(x-\Delta x)}}{\Delta x^2} + S_{heat} \quad (C2-3)$$

$$T_{new(x)} - T(x) = \frac{k \Delta t}{\rho_m c_p} \frac{T_{(x+\Delta x)} - 2T(x) + T_{(x-\Delta x)}}{\Delta x^2} + \frac{\Delta t S_{heat}}{\rho_m c_p} \quad (C2-4)$$

$$T_{new(x)} = T(x) + \frac{k \Delta t}{\rho_m c_p \Delta x^2} (T_{(x+\Delta x)} - 2T(x) + T_{(x-\Delta x)}) + \frac{\Delta t S_{heat}}{\rho_m c_p} \quad (C2-5)$$

$$T_{new(x)} = (1 - 2 \frac{k \Delta t}{\rho_m c_p \Delta x^2}) T(x) + \frac{k \Delta t}{\rho_m c_p \Delta x^2} (T_{(x+\Delta x)} + T_{(x-\Delta x)}) + \frac{\Delta t S_{heat}}{\rho_m c_p} \quad (C2-6)$$

Appendix D: FDM Formula to Derive Poisson's and Heat Conduction Equation in 2-D thin film sample:

1- Poisson's equation

$$\frac{\partial^2 V}{\partial x^2} + \frac{\partial^2 V}{\partial y^2} = - \frac{\rho}{\epsilon_0 \epsilon_r} \quad (D1-1)$$

$$\frac{V_{(x+\Delta x, y)} - 2V_{(x, y)} + V_{(x-\Delta x, y)}}{\Delta x^2} + \frac{V_{(x, y+\Delta y)} - 2V_{(x, y)} + V_{(x, y-\Delta y)}}{\Delta y^2} = - \frac{\rho}{\epsilon_0 \epsilon_r} \quad (D1-2)$$

But, $\Delta x^2 = \Delta y^2$

$$V_{(x+\Delta x, y)} - 2V_{(x, y)} + V_{(x-\Delta x, y)} + V_{(x, y+\Delta y)} - 2V_{(x, y)} + V_{(x, y-\Delta y)} = - \frac{\Delta x^2 \rho}{\epsilon_0 \epsilon_r} \quad (D1-3)$$

$$4V_{(x, y)} = V_{(x+\Delta x, y)} + V_{(x-\Delta x, y)} + V_{(x, y+\Delta y)} + V_{(x, y-\Delta y)} + \frac{\Delta x^2 \rho}{\epsilon_0 \epsilon_r} \quad (D1-4)$$

$$V_{(x, y)} = \frac{1}{4} (V_{(x+\Delta x, y)} + V_{(x-\Delta x, y)} + V_{(x, y+\Delta y)} + V_{(x, y-\Delta y)} + \frac{\Delta x^2 \rho}{\epsilon_0 \epsilon_r}) \quad (D1-5)$$

2- Heat conduction equation

$$\rho_m c_p \frac{\partial T}{\partial t} = k \left(\frac{\partial^2 T}{\partial x^2} + \frac{\partial^2 T}{\partial y^2} \right) + S_{heat} \quad (D2-1)$$

$$\rho_m c_p \frac{T_{new(x,y)} - T(x,y)}{\Delta t} = k \left(\frac{T_{(x+\Delta x,y)} - 2T_{(x,y)} + T_{(x-\Delta x,y)}}{\Delta x^2} + \frac{T_{(x,y+\Delta y)} - 2T_{(x,y)} + T_{(x,y-\Delta y)}}{\Delta y^2} \right) + S_{heat} \quad (D2-2)$$

But, $\Delta x^2 = \Delta y^2$

$$T_{new(x,y)} = T_{(x,y)} + \frac{k\Delta t}{\Delta x^2 \rho_m c_p} \left(T_{(x+\Delta x,y)} - 2T_{(x,y)} + T_{(x-\Delta x,y)} + T_{(x,y+\Delta y)} - 2T_{(x,y)} + T_{(x,y-\Delta y)} \right) + \frac{\Delta t S_{heat}}{\rho_m c_p} \quad (D2-3)$$

$$T_{new(x,y)} = \left(1 - 4 \frac{k\Delta t}{\Delta x^2 \rho_m c_p} \right) T_{(x,y)} + \frac{k\Delta t}{\Delta x^2 \rho_m c_p} \left(T_{(x+\Delta x,y)} + T_{(x-\Delta x,y)} + T_{(x,y+\Delta y)} + T_{(x,y-\Delta y)} \right) + \frac{\Delta t S_{heat}}{\rho_m c_p} \quad (D2-4)$$

Appendix E: Maxwell's Tensor for PEA

From Gauss's law: $\nabla \cdot (\varepsilon \vec{E}) = \rho$ (E1)

Assume ε isotropic, $\varepsilon_x = \varepsilon_y = \varepsilon_z = \varepsilon$ and in the equations that follow, subscripts i, j are the individual components of three dimensional (3-D) vectors, $i = j = 1, 2, 3$ etc.

Repeated subscripts refer to summation over all values of that subscript.

$$\nabla \cdot (\varepsilon \vec{E}) = \frac{\partial \varepsilon E_j}{\partial x_j} = \sum_{j=1}^3 \frac{\partial \varepsilon E_j}{\partial x_j} = \frac{\partial \varepsilon E_1}{\partial x_1} + \frac{\partial \varepsilon E_2}{\partial x_2} + \frac{\partial \varepsilon E_3}{\partial x_3} = \rho \quad (E2)$$

On the other hand, based on reference [68], the total force density that acts on an insulation body can be described by equation 3.

$$F_i = \rho \vec{E} - \frac{1}{2} E^2 \nabla \varepsilon - \frac{1}{2} \nabla (a E^2) \quad (E3)$$

Assume that $a = 0$, ie, the electrostriction term is neglected. In this case equation 3 becomes:

$$F_i = \rho \vec{E} - \frac{1}{2} E^2 \nabla \varepsilon \quad (E4)$$

However, the force density can be described by the divergence of Maxwell tensor, M_{ij} . On eliminating ρ using equation (2) the force density becomes:

$$F_i = \frac{\partial M_{ij}}{\partial x_j} = E_i \frac{\partial (\varepsilon E_j)}{\partial x_j} - \frac{1}{2} E^2 \frac{\partial \varepsilon}{\partial x_i} \quad (E5)$$

But,

$$\frac{\partial((\varepsilon E_j)E_i)}{\partial x_j} = E_i \frac{\partial(\varepsilon E_j)}{\partial x_j} + \varepsilon E_j \frac{\partial E_i}{\partial x_j}$$

Therefore,

$$E_i \frac{\partial(\varepsilon E_j)}{\partial x_j} = \frac{\partial((\varepsilon E_j)E_i)}{\partial x_j} - \varepsilon E_j \frac{\partial E_i}{\partial x_j} \quad (\text{E6})$$

Substitution of equation (6) into equation (5), the expression for force density becomes

$$F_i = \frac{\partial M_{ij}}{\partial x_j} = \frac{\partial(\varepsilon E_i E_j)}{\partial x_j} - \varepsilon E_j \frac{\partial E_i}{\partial x_j} - \frac{1}{2} E^2 \frac{\partial \varepsilon}{\partial x_i} \quad (\text{E7})$$

Also,

$$\frac{\partial(\varepsilon E^2)}{\partial x_i} = E^2 \frac{\partial \varepsilon}{\partial x_i} + \frac{\varepsilon \partial E^2}{\partial x_i} \quad (\text{E8})$$

but,

$$\frac{\varepsilon \partial E^2}{\partial x_i} = \frac{\varepsilon \partial(E_j E_j)}{\partial x_i} = \varepsilon E_j \frac{\partial E_j}{\partial x_i} + \varepsilon E_j \frac{\partial E_j}{\partial x_i} = 2\varepsilon E_j \frac{\partial E_j}{\partial x_i} \quad (\text{E9})$$

Substituting (9) in (8) and the result of (8) into (7), the expression for force density becomes

$$F_i = \frac{\partial M_{ij}}{\partial x_j} = \frac{\partial(\varepsilon E_i E_j)}{\partial x_j} - \varepsilon E_j \frac{\partial E_i}{\partial x_j} - \frac{1}{2} \frac{\partial(\varepsilon E^2)}{\partial x_i} + \varepsilon E_j \frac{\partial E_j}{\partial x_i} \quad (\text{E10})$$

Provided that E is derived from the gradient of a scalar potential, the two crossed terms cancel*, and equation (10) becomes:

$$F_i = \frac{\partial M_{ij}}{\partial x_j} = \frac{\partial(\varepsilon E_i E_j)}{\partial x_j} - \frac{1}{2} \frac{\partial(\varepsilon E^2)}{\partial x_i} \quad (\text{E11})$$

Equation 11 can be expressed as**:

$$F_i = \frac{\partial M_{ij}}{\partial x_j} = \frac{\partial(\varepsilon E_i E_j)}{\partial x_j} - \frac{1}{2} \frac{\partial(\varepsilon E^2 \cdot \delta_{ij})}{\partial x_j} \quad (\text{E12})$$

Where δ_{ij} is the Kronecker delta function having matrix elements of value, 1 when $i = j$ and zero otherwise. Factorising we have:

$$F_i = \frac{\partial M_{ij}}{\partial x_j} = \frac{\partial[\varepsilon E_i E_j - \frac{1}{2} \varepsilon E^2 \delta_{ij}]}{\partial x_j} \quad (\text{E13})$$

The Maxwell tensor can therefore be identified as:

$$M_{ij} = \varepsilon E_i E_j - \frac{1}{2} \varepsilon E^2 \delta_{ij} \quad (\text{E14})$$

*Proof that the two crossed terms cancel (adapted from Böttcher [153])

If the field vector is derived from the gradient of a scalar potential, V, i.e.

$$\frac{\partial V}{\partial x_i} = E_i$$

Taking the second differential:

$$\frac{\partial^2 V}{\partial x_j \partial x_i} = \frac{\partial E_i}{\partial x_j}$$

When V has continuous second derivatives, the order of differentiation may be interchanged.

Interchanging the indices, i, j gives:

$$\frac{\partial^2 V}{\partial x_i \partial x_j} = \frac{\partial E_j}{\partial x_i}$$

Therefore:

$$\frac{\partial E_j}{\partial x_i} = \frac{\partial E_i}{\partial x_j}$$

** Show that

$$\begin{aligned} \frac{\partial(\epsilon E^2)}{\partial x_i} &= \frac{\partial(\epsilon E^2 \partial_{ij})}{\partial x_j} \\ \frac{\partial(\epsilon E^2)}{\partial x_i} &= \left(\frac{\partial(\epsilon E^2)}{\partial x_1}, \frac{\partial(\epsilon E^2)}{\partial x_2}, \frac{\partial(\epsilon E^2)}{\partial x_3} \right) \\ \frac{\partial(\epsilon E^2 \partial_{ij})}{\partial x_j} &= \sum_{j=1}^3 \frac{\partial(\epsilon E^2 \partial_{ij})}{\partial x_j} = \frac{\partial}{\partial x_j} \begin{bmatrix} \epsilon E^2 & 0 & 0 \\ 0 & \epsilon E^2 & 0 \\ 0 & 0 & \epsilon E^2 \end{bmatrix} = \left(\frac{\partial(\epsilon E^2)}{\partial x_1}, \frac{\partial(\epsilon E^2)}{\partial x_2}, \frac{\partial(\epsilon E^2)}{\partial x_3} \right) \end{aligned}$$

References

- [1] G. Mazzanti and M. Marzinotto, *Extruded Cables for High-Voltage Direct-Current Transmission: Advances in Research and Development* vol. 93: John Wiley & Sons, 2013.
- [2] F. Mauseth, S. Hvidsten, H. H. Sæternes, and J. Aakervik, "Influence of DC Stress Superimposed with High Frequency AC on Water Tree Growth in XLPE Insulation," in *Nordic Insulation Symposium*, 2013.
- [3] G. F. Reed, H. Al Hassan, M. J. Korytowski, P. T. Lewis, and B. M. Grainger, "Comparison of HVAC and HVDC solutions for offshore wind farms with a procedure for system economic evaluation," in *Energytech, 2013 IEEE*, 2013, pp. 1-7.
- [4] Z. Huang, "Rating methodology of high voltage mass impregnated DC cable circuits," University of Southampton, 2014.
- [5] G. Asplund, K. Eriksson, and K. Svensson, "DC transmission based on voltage source converters," in *CIGRE SC14 Colloquium, South Africa*, 1997, pp. 1-7.
- [6] M. Bahrman and B. Johnson, "The ABCs of HVDC transmission technologies," *IEEE Power and Energy Magazine*, vol. 2, pp. 32-44, 2007.
- [7] C. H. Chien and R. W. Bucknall, "Analysis of harmonics in subsea power transmission cables used in VSC–HVDC transmission systems operating under steady-state conditions," *Power Delivery, IEEE Transactions on*, vol. 22, pp. 2489-2497, 2007.
- [8] P. Olsen, F. Mauseth, and E. Ildstad, "The effect of DC superimposed AC voltage on partial discharges in dielectric bounded cavities," in *High Voltage Engineering and Application (ICHVE), 2014 International Conference on*, 2014, pp. 1-4.
- [9] P. K. Olsen, F. Mauseth, and E. Ildstad, "Modelling of Partial Discharges in Polymeric Insulation Exposed to Combined DC and AC Voltage," in *Nordic Insulation Symposium*, 2013.
- [10] T. Liu, "Dielectric Spectroscopy of Very Low Loss Model Power Cables," University of Leicester, 2010.
- [11] G. Moore, "Electric Cables Handbook 1997," ed: Wiley-Blackwell.
- [12] T. L. Hanley, R. P. Burford, R. J. Fleming, and K. W. Barber, "A general review of polymeric insulation for use in HVDC cables," *IEEE Electrical Insulation Magazine*, vol. 1, pp. 13-24, 2003.
- [13] M. Jeroense and P. Morshuis, "Electric fields in HVDC paper-insulated cables," *Dielectrics and Electrical Insulation, IEEE Transactions on*, vol. 5, pp. 225-236, 1998.
- [14] L. A. Dissado and J. C. Fothergill, *Electrical degradation and breakdown in polymers*: IET, 1992.
- [15] T. Worzyk, *Submarine power cables: design, installation, repair, environmental aspects*: Springer Science & Business Media, 2009.
- [16] R. Arrighi, "From impregnated paper to polymeric insulating materials in power cables," *IEEE transactions on electrical insulation*, pp. 7-18, 1986.
- [17] F. Precopio, "The invention of chemically crosslinked polyethylene," *IEEE Electrical Insulation Magazine*, vol. 15, pp. 23-25, 1999.
- [18] C. T. Choo, "Space charge determination in HVDC power cable and its influence on electric field," University of Southampton, 2010.
- [19] X. Chen, L. Hu, Y. Xu, X. Cao, and S. Gubanski, "Investigation of temperature effect on electrical trees in xlpe cable insulation," in *Electrical Insulation and Dielectric Phenomena (CEIDP), 2012 Annual Report Conference on*, 2012, pp. 612-615.
- [20] I. A. Tsekmes, "Electrical characterization of polymeric DC mini-cables by means of space charge and conduction current measurements," TU Delft, Delft University of Technology, 2012.
- [21] G. Chen, M. Hao, Z. Xu, A. Vaughan, J. Cao, and H. Wang, "Review of high voltage direct current cables," *Power and Energy Systems, CSEE Journal of*, vol. 1, pp. 9-21, 2015.

- [22] R. Bodega, P. Morshuis, and G. Perego, "Measurement and Modeling of Space Charge Accumulation in Polymeric HVDC Cable Systems," in *JICABLE'07 International Conference on Power Insulated Cables 2007*, pp. 1-6.
- [23] H. Zheng, "Application of PEA technique to space charge measurement in cylindrical geometry HV cable systems," Department of Engineering, 2015.
- [24] P. Morshuis and M. Jeroense, "Space charge measurements on impregnated paper: a review of the PEA method and a discussion of results," *IEEE Electrical Insulation Magazine*, vol. 13, pp. 26-35, 1997.
- [25] T. Tohmine, T. Fujitomi, H. Miyake, Y. Tanaka, Y. Ida, and Y. Inoue, "Measurement of space charge accumulated in multi-layered samples composed of different insulators used in the joints of DC transmission cables," in *Electrical Insulating Materials (ISEIM), 2017 International Symposium on*, 2017, pp. 299-302.
- [26] H. Meng, Z. Yuanxiang, S. Qinghua, S. Yanchao, and Z. Ling, "Effect of interface on space charge behavior in multi-layer oil-paper insulation," in *Electrical Insulation and Dielectric Phenomena (CEIDP), 2012 Annual Report Conference on*, 2012, pp. 654-657.
- [27] K. Wu, R. Su, and X. Wang, "Space charge behavior under temperature gradient and its effects on material aging," in *Electrical Materials and Power Equipment (ICEMPE), 2017 1st International Conference on*, 2017, pp. 1-9.
- [28] M. A. Fard, A. Reid, and D. Hepburn, "Analysis of HVDC superimposed harmonic voltage effects on partial discharge behavior in solid dielectric media," *IEEE Transactions on Dielectrics and Electrical Insulation*, vol. 24, pp. 7-16, 2017.
- [29] M. Birlle and C. Leu, "Dielectric heating in insulating materials at high dc and ac voltages superimposed by high frequency high voltages," in *Proc. 18th International Symposium on High Voltage Engineering (ISH)*, 2013, pp. 1025-1030.
- [30] A. Vazquez, G. Chen, A. Davies, and R. Bosch, "Space charge measurement using pulsed electroacoustic technique and signal recovery," *Journal of the European Ceramic Society*, vol. 19, pp. 1219-1222, 1999.
- [31] Y. Li, M. Aihara, K. Murata, Y. Tanaka, and T. Takada, "Space charge measurement in thick dielectric materials by pulsed electroacoustic method," *Review of scientific instruments*, vol. 66, pp. 3909-3916, 1995.
- [32] F. J. Keller, W. E. Gettys, and M. J. Skove, *Physics, classical and modern*: McGraw-Hill College, 1993.
- [33] W. H. Hayt Jr, "Engineering Electromagnetics 1989," ed: McGraw-Hill, Inc.
- [34] C.-O. Olsson, B. Källstrand, and H. Ghorbani, "Conductivity of crosslinked polyethylene influenced by water," in *Electrical Insulation and Dielectric Phenomena (CEIDP), 2014 IEEE Conference on*, 2014, pp. 832-835.
- [35] D. Van der Born, "Investigation of space charge injection, conduction and trapping mechanisms in polymeric HVDC mini-cables," TU Delft, Delft University of Technology, 2011.
- [36] T.-c. Zhou, G. Chen, R.-j. Liao, and Z. Xu, "Charge trapping and detrapping in polymeric materials: Trapping parameters," *Journal of Applied Physics*, vol. 110, p. 043724, 2011.
- [37] S. Le Roy, P. Segur, G. Teyssedre, and C. Laurent, "Description of bipolar charge transport in polyethylene using a fluid model with a constant mobility: model prediction," *Journal of physics D: Applied physics*, vol. 37, p. 298, 2004.
- [38] J. Brunson, "Hopping conductivity and charge transport in low density polyethylene," 2010.
- [39] Z. Xu, W. Choo, and G. Chen, "DC electric field distribution in planar dielectric in the presence of space charge," presented at the 2007 IEEE International Conference on Solid Dielectrics, 2007.
- [40] H. Ghorbani, M. Jeroense, C.-O. Olsson, and M. Saltzer, "HVDC Cable Systems—Highlighting Extruded Technology," *Power Delivery, IEEE Transactions on*, vol. 29, pp. 414-421, 2014.

- [41] S. Boggs, D. H. Damon, J. Hjerrild, J. T. Holboll, and M. Henriksen, "Effect of insulation properties on the field grading of solid dielectric DC cable," *Power Delivery, IEEE Transactions on*, vol. 16, pp. 456-461, 2001.
- [42] E. Ildstad, J. Sletbak, B. Nyberg, and J. Larsen, "Factors affecting the choice of insulation system for extruded HVDC Power Cables," *paper D1-203, CIGRE Session*, 2004.
- [43] I. W. McAllister, G. C. Crichton, and A. Pedersen, "Charge accumulation in DC cables: a macroscopic approach," in *1994 IEEE International Symposium on Electrical Insulation*, 1994, pp. 212-216.
- [44] J. Holbøll, K. Bambery, and R. Fleming, "Space charge and steady state current in LDPE samples containing a permittivity/conductivity gradient," in *Electrical Insulation and Dielectric Phenomena, 2000 Annual Report Conference on*, 2000, pp. 381-384.
- [45] S. Qin and S. Boggs, "Design considerations for High Voltage DC components," *Electrical Insulation Magazine, IEEE*, vol. 28, pp. 36-44, 2012.
- [46] M. J. P. Jeroense, *Charges and Discharges in HVDC Cables-in particular in mass-impregnated HVDC cables*: TU Delft, Delft University of Technology, 1997.
- [47] J. Gu, X. Li, and Y. Yin, "Calculation of electric field and temperature field distribution in MVDC polymeric power cable," in *Properties and Applications of Dielectric Materials, 2009. ICPADM 2009. IEEE 9th International Conference on the*, 2009, pp. 105-108.
- [48] I. W. McAllister, G. C. Crichton, and A. Pedersen, "Space charge fields in DC cables," in *1996 IEEE International Symposium on Electrical Insulation*, 1996, pp. 661-665.
- [49] S. Palit, D. Varghese, H. Guo, S. Krishnan, and M. A. Alam, "The Role of Dielectric Heating and Effects of Ambient Humidity in the Electrical Breakdown of Polymer Dielectrics," *IEEE Transactions on Device and Materials Reliability*, vol. 15, pp. 308-318, 2015.
- [50] C. Olsson, "Numerical investigation of temperature and electric field dynamics in polymer insulation at HVDC," in *Electrical Insulation Conference, 2009. EIC 2009. IEEE*, 2009, pp. 504-508.
- [51] J. Hjerrild, S. Boggs, J. Holboll, and M. Henriksen, "DC-field in solid dielectric cables under transient thermal conditions," in *Solid Dielectrics, 2001. ICSD'01. Proceedings of the 2001 IEEE 7th International Conference on*, 2001, pp. 58-61.
- [52] W. Choo and G. Chen, "Electric field determination in DC polymeric power cable in the presence of space charge and temperature gradient under dc conditions," in *Condition Monitoring and Diagnosis, 2008. CMD 2008. International Conference on*, 2008, pp. 321-324.
- [53] W. Choo, G. Chen, and S. Swingler, "Space charge accumulation under effects of temperature gradient and applied voltage reversal on solid dielectric dc cable," in *Properties and Applications of Dielectric Materials, 2009. ICPADM 2009. IEEE 9th International Conference on the*, 2009, pp. 946-949.
- [54] R. Bodega, *Space charge accumulation in polymeric high voltage DC cable systems*: TU Delft, Delft University of Technology, 2006.
- [55] R. Coelho, "Charges in non homogeneous dielectrics," in *Electrical Insulation and Dielectric Phenomena, 1997. IEEE 1997 Annual Report., Conference on*, 1997, pp. 1-10.
- [56] W. Choo and G. Chen, "Electric field determination in DC polymeric power cable in the presence of space charge," in *Electrical Insulation and Dielectric Phenomena, 2007. CEIDP 2007. Annual Report-Conference on*, 2007, pp. 489-492.
- [57] A. R. Blythe and D. Bloor, *Electrical properties of polymers*: Cambridge University Press, 2005.
- [58] J. Hjerrild, J. Holboll, M. Henriksen, and S. Boggs, "Effect of semicon-dielectric interface on conductivity and electric field distribution," *Dielectrics and Electrical Insulation, IEEE Transactions on*, vol. 9, pp. 596-603, 2002.
- [59] C. Olsson, "Diffusion in polymers with temperature dependent properties," in *International Heat Transfer Conference 13*, 2006.

- [60] T. Takada, T. Maeno, and H. Kushibe, "An electric stress-pulse technique for the measurement of charges in a plastic plate irradiated by an electron beam," *IEEE transactions on electrical insulation*, pp. 497-501, 1987.
- [61] T. Maeno, H. Kushibe, T. Takada, and C. Cooke, "Pulsed electro-acoustic method for the measurement of volume charges in E-beam irradiated PMMA," in *Electrical Insulation & Dielectric Phenomena, 1985. Annual Report 1985. Conference on*, 1985, pp. 389-397.
- [62] Y. Li and T. Takada, "Progress in space charge measurement of solid insulating materials in Japan," *IEEE Electrical Insulation Magazine*, vol. 5, pp. 16-28, 1994.
- [63] T. Takada and T. Sakai, "Measurement of electric fields at a dielectric/electrode interface using an acoustic transducer technique," *Electrical Insulation, IEEE Transactions on*, pp. 619-628, 1983.
- [64] K. Fukunaga, "Industrial applications of space charge measurement in Japan," *Electrical Insulation Magazine, IEEE*, vol. 15, pp. 6-18, 1999.
- [65] N. Kasayapanand, "Numerical modeling of natural convection in partially open square cavities under electric field," *International communications in heat and mass transfer*, vol. 34, pp. 630-643, 2007.
- [66] J. Zhang, C. Zhao, H. Li, and W. Tao, "3D Numerical Simulation of Heat Transfer of a Heated Plate under the Electric Field Generated by a Needle Electrode," *Mathematical Problems in Engineering*, vol. 2014, 2014.
- [67] R. Bodega, P. Morshuis, and J. Smit, "Space charge measurements on multi-dielectrics by means of the pulsed electroacoustic method," *IEEE transactions on dielectrics and electrical insulation*, vol. 13, pp. 272-281, 2006.
- [68] S. Hole, T. Ditchi, and A. Lewiner, "Non-destructive methods for space charge distribution measurements: what are the differences?," *IEEE transactions on dielectrics and electrical insulation*, vol. 10, pp. 670-677, 2003.
- [69] V. Griseri, L. A. Dissado, and J. C. Fothergill, "Improvement of PEA signal analysis using simulations for complex geometry samples," *Journal of Physics D: Applied Physics*, vol. 35, p. 19, 2001.
- [70] Z. Xu, "Space charge measurement and analysis in low density polyethylene films," University of Southampton, 2009.
- [71] M. Taleb, G. Teyssedre, S. Roy, and C. Laurent, "Modeling of charge injection and extraction in a metal/polymer interface through an exponential distribution of surface states," *Dielectrics and Electrical Insulation, IEEE Transactions on*, vol. 20, pp. 311-320, 2013.
- [72] J. Fothergill, "The coming of Age of HVDC extruded power cables," in *Electrical Insulation Conference (EIC), 2014*, 2014, pp. 124-137.
- [73] M. Fu, G. Chen, and J. C. Fothergill, "The influence of residue on space charge accumulation in purposely modified thick plaque XLPE sample for DC application," 2005.
- [74] S. Le Roy and G. Teyssedre, "Ion generation and transport in low density polyethylene under electric stress," in *Electrical Insulation and Dielectric Phenomena (CEIDP), 2015 IEEE Conference on*, 2015, pp. 63-66.
- [75] Z. Lv, J. Cao, X. Wang, H. Wang, K. Wu, and L. Dissado, "Mechanism of space charge formation in cross linked polyethylene (XLPE) under temperature gradient," *IEEE Transactions on Dielectrics and Electrical Insulation*, vol. 22, pp. 3186-3196, 2015.
- [76] X. Chen, X. Wang, K. Wu, Z. Peng, Y. Cheng, and D. Tu, "Space charge measurement in LPDE films under temperature gradient and DC stress," *IEEE Transactions on Dielectrics and Electrical Insulation*, vol. 17, 2010.
- [77] K. Wu and C. Cheng, "Interface charges between insulating materials," *IEEE Transactions on Dielectrics and Electrical Insulation*, vol. 24, pp. 2633-2642, 2017.
- [78] S. Le Roy, F. Boufayed, G. Teyssedre, C. Laurent, P. Segur, R. Bodega, *et al.*, "Computer simulation of space charge distribution in an XLPE-EPR sandwich," in *Electrical Insulation and Dielectric Phenomena, 2005. CEIDP'05. 2005 Annual Report Conference on*, 2005, pp. 661-664.

- [79] G. Chen, Y. Tanaka, T. Takada, and L. Zhong, "Effect of polyethylene interface on space charge formation," *IEEE Transactions on Dielectrics and Electrical Insulation*, vol. 11, pp. 113-121, 2004.
- [80] S. Boggs, "A rational consideration of space charge," *IEEE Electrical Insulation Magazine*, vol. 20, pp. 22-27, 2004.
- [81] H. Herman, J. Thomas, and G. Stevens, "Spectroscopic and chemometrics analysis of cable condition in the Artemis program," in *Solid Dielectrics, 2004. ICSD 2004. Proceedings of the 2004 IEEE International Conference on*, 2004, pp. 623-627.
- [82] P. Morshuis, A. Cavallini, D. Fabiani, G. C. Montanari, and C. Azcarraga, "Stress conditions in HVDC equipment and routes to in service failure," *Dielectrics and Electrical Insulation, IEEE Transactions on*, vol. 22, pp. 81-91, 2015.
- [83] R. Bodega, P. Morshuis, U. Nilsson, G. Perego, and J. Smit, "Polarization mechanisms of flat XLPE-EPR interfaces," in *Proc. Nord. Ins. Symp*, 2005, pp. 224-227.
- [84] P. Morshuis and A. Tsekmes, "Polymeric HVDC Cable Systems—Dealing with Interfaces," *高电压技术*, vol. 41, pp. 1104-1113, 2015.
- [85] F. Rogti and M. Ferhat, "Maxwell–Wagner polarization and interfacial charge at the multi-layers of thermoplastic polymers," *Journal of Electrostatics*, vol. 72, pp. 91-97, 2014.
- [86] P. H. Morshuis, R. Bodega, D. Fabiani, G. C. Montanari, L. A. Dissado, and J. J. Smit, "Dielectric interfaces in DC constructions: space charge and polarization phenomena," in *Solid Dielectrics, 2007. ICSD'07. IEEE International Conference on*, 2007, pp. 450-453.
- [87] T. Vu, G. Teyssedre, B. Vissouvanadin, S. Roy, and C. Laurent, "Correlating conductivity and space charge measurements in multi-dielectrics under various electrical and thermal stresses," *Dielectrics and Electrical Insulation, IEEE Transactions on*, vol. 22, pp. 117-127, 2015.
- [88] T. N Vu, G. Teyssedre, B. Vissouvanadin, S. Roy, C. Laurent, M. Mammeri, *et al.*, "Electric field profile measurement and modeling in multi-dielectrics for HVDC application," in *Solid Dielectrics (ICSD), 2013 IEEE International Conference on*, 2013, pp. 413-416.
- [89] J. Hu, J. Wu, and Y. Yin, "Space charge on the contact interface between two insulations of the same materials," in *Condition Monitoring and Diagnosis (CMD), 2016 International Conference on*, 2016, pp. 761-764.
- [90] J. Li, B. Du, X. Kong, and Z. Li, "Nonlinear conductivity and interface charge behaviors between LDPE and EPDM/SiC composite for HVDC cable accessory," *IEEE Transactions on Dielectrics and Electrical Insulation*, vol. 24, pp. 1566-1573, 2017.
- [91] A. K. Mitra. *Finite Difference Method for the Solution of Laplace Equation*. Available: http://akmitra.public.iastate.edu/aero361/design_web/index.html accessed on (15/03/2015).
- [92] J.-M. Jin, *Theory and computation of electromagnetic fields*: John Wiley & Sons, 2011.
- [93] S. Gane, "Solution of the advection equation using finite difference schemes and the method of characteristics," University of Glasgow, 2000.
- [94] G. W. Recktenwald, "Finite-difference approximations to the heat equation," *Class Notes*, 2004.
- [95] N. Meftali and S. Bouazabia, "Modelling of the transient transport of electrons in dielectrics for one-carrier pulsed injection," in *Electrical Insulation Conference (EIC), 2013 IEEE*, 2013, pp. 16-19.
- [96] G. Chen, Y. Chong, and M. Fu, "Calibration of the pulsed electroacoustic technique in the presence of trapped charge," *Measurement Science and Technology*, vol. 17, p. 1974, 2006.
- [97] Y. Tanaka, K. Hanawa, K. Suzuki, and T. Takada, "Attenuation recovery technique for acoustic wave propagation in PEA method," in *Electrical Insulating Materials, 2001.(ISEIM 2001). Proceedings of 2001 International Symposium on*, 2001, pp. 407-410.

- [98] G. Chen and Z. Xu, "Space charge dynamics in low density polyethylene under dc electric fields," in *Journal of Physics: Conference Series*, 2008, p. 012008.
- [99] G. Chen, Y. Chong, and M. Fu, "A Novel Calibration Method in the Presence of Space Charge in Dielectric Materials Using the Pulsed Electroacoustic Technique," in *2006 IEEE 8th International Conference on Properties & applications of Dielectric Materials*, 2006, pp. 289-292.
- [100] M. Fu, G. Chen, and X. Liu, "Space charge behaviour in LDPE after AC electrical ageing," in *Solid Dielectrics, 2004. ICSD 2004. Proceedings of the 2004 IEEE International Conference on*, 2004, pp. 217-220.
- [101] W. Lei, K. Wu, Y. Wang, Y. Cheng, X. Zheng, L. Dissado, *et al.*, "Are nano-composites really better DC insulators? A study using silica nanoparticles in XLPE," *IEEE Transactions on Dielectrics and Electrical Insulation*, vol. 24, pp. 2268-2270, 2017.
- [102] Y. Li and T. Takada, "Experimental observation of charge transport and injection in XLPE at polarity reversal," *Journal of Physics D: Applied Physics*, vol. 25, p. 704, 1992.
- [103] G. Montanari, C. Laurent, G. Teysse, A. Campus, and U. Nilsson, "From LDPE to XLPE: investigating the change of electrical properties. Part I. space charge, conduction and lifetime," *IEEE transactions on dielectrics and electrical insulation*, vol. 12, pp. 438-446, 2005.
- [104] F. Rogti and M. Ferhat, "Temperature effect on space charge dynamics in multi-layer insulation Fluorinated Ethylene Propylene (FEP) Low Density Polyethylene (LDPE)," in *Electrical Insulation and Dielectric Phenomena (CEIDP), 2013 IEEE Conference on*, 2013, pp. 283-286.
- [105] S. Delpino, D. Fabiani, G. Montanari, C. Laurent, G. Teysse, P. Morshuis, *et al.*, "Polymeric HVDC cable design and space charge accumulation. Part 2: insulation interfaces," *IEEE Electrical Insulation Magazine*, vol. 24, pp. 14-24, 2008.
- [106] Y. Tanaka, G. Chen, T. Tay, and T. Takada, "Effect of interface on space charge in polyethylene," in *Electrical Insulating Materials, 2001.(ISEIM 2001). Proceedings of 2001 International Symposium on*, 2001, pp. 505-508.
- [107] J. Alison and R. Hill, "A model for bipolar charge transport, trapping and recombination in degassed crosslinked polyethene," *Journal of Physics D: Applied Physics*, vol. 27, p. 1291, 1994.
- [108] F. Boufayed, G. Teysse, C. Laurent, S. Le Roy, L. A. Dissado, P. Segur, *et al.*, "Models of bipolar charge transport in polyethylene," *Journal of applied physics*, vol. 100, p. 104105, 2006.
- [109] J. Tian, J. Zou, Y. Wang, J. Liu, J. Yuan, and Y. Zhou, "Simulation of bipolar charge transport with trapping and recombination in polymeric insulators using Runge–Kutta discontinuous Galerkin method," *Journal of Physics D: Applied Physics*, vol. 41, p. 195416, 2008.
- [110] E. Belgaroui, I. Boukhris, A. Kallel, G. Teysse, and C. Laurent, "A new numerical model applied to bipolar charge transport, trapping and recombination under low and high dc voltages," *Journal of Physics D: Applied Physics*, vol. 40, p. 6760, 2007.
- [111] F. Boufayed, S. Leroy, G. Teysse, C. Laurent, P. Segur, L. Dissado, *et al.*, "Simulation of bipolar charge transport in polyethylene featuring trapping and hopping conduction through an exponential distribution of traps," in *Electrical Insulating Materials, 2005.(ISEIM 2005). Proceedings of 2005 International Symposium on*, 2005, pp. 340-343.
- [112] K. S. Suh, S. J. Hwang, J. S. Noh, and T. Takada, "Effects of Constituents of XLPE on the Formation of Space Charge," *IEEE Transactions on Dielectrics and Electrical Insulation*, vol. 1, pp. 1077-1083, 1994.
- [113] M. Fu, G. Chen, L. A. Dissado, and J. C. Fothergill, "Influence of thermal treatment and residues on space charge accumulation in XLPE for DC power cable application," *IEEE Transactions on Dielectrics and Electrical Insulation*, vol. 14, 2007.

- [114] P. H. Morshuis, R. Bodega, D. Fabiani, G. C. Montanari, L. A. Dissado, and J. J. Smit, "Calculation and Measurement of Space Charge in MV-size Extruded Cables Systems under Load Conditions," in *2007 IEEE International Conference on Solid Dielectrics*, 2007, pp. 502-505.
- [115] M. N. Sadiku, *Numerical techniques in electromagnetics*: CRC press, 2000.
- [116] C. Olsson, "Modelling of thermal behaviour of polymer insulation at high electric DC fields," in *CON-6, 5th European Thermal-Sciences Conference, Eindhoven, The Netherlands*, 2008.
- [117] D. Fabiani, G. Montanari, C. Laurent, G. Teyssedre, P. Morshuis, R. Bodega, *et al.*, "HVDC cable design and space charge accumulation. part 3: effect of temperature gradient," *IEEE Electrical Insulation Magazine*, vol. 24, pp. 5-14, 2008.
- [118] L. E. Kinsler, A. R. Frey, A. B. Coppens, and J. V. Sanders, "Fundamentals of Acoustics, John Wiley & Sons," *Inc, New York*, 2000.
- [119] E. Belgaroui and A. Kallel, "Transient and steady-state currents in disordered polyethylene film under charge packet effects," in *Electrical Insulation and Dielectric Phenomena, 2009. CEIDP'09. IEEE Conference on*, 2009, pp. 133-137.
- [120] Z. Lv, X. Wang, K. Wu, X. Chen, Y. Cheng, and L. Dissado, "Dependence of charge accumulation on sample thickness in Nano-SiO₂ doped IDPE," *IEEE Transactions on Dielectrics and Electrical Insulation*, vol. 20, pp. 337-345, 2013.
- [121] K. Bambery and R. Fleming, "Space charge accumulation in two power cable grades of XLPE," *Dielectrics and Electrical Insulation, IEEE Transactions on*, vol. 5, pp. 103-109, 1998.
- [122] M. Fu, L. A. Dissado, G. Chen, and J. C. Fothergill, "Space charge formation and its modified electric field under applied voltage reversal and temperature gradient in XLPE cable," *Dielectrics and Electrical Insulation, IEEE Transactions on*, vol. 15, pp. 851-860, 2008.
- [123] S. Hole, "Behind space charge distribution measurements," *IEEE Transactions on Dielectrics and Electrical Insulation*, vol. 4, pp. 1208-1214, 2012.
- [124] K. Bambery and R. Fleming, "The temperature dependence of space charge accumulation in cross-linked polyethylene," *Journal of Thermal Analysis and Calorimetry*, vol. 50, pp. 19-31, 1997.
- [125] K. Wu, Z. Lv, Q. Zhu, X. Wang, Y. Cheng, and L. Dissado, "Space charge formation and conductivity characteristics of PE and oil impregnated paper under a temperature gradient," in *Electrical Insulating Materials (ISEIM), Proceedings of 2014 International Symposium on*, 2014, pp. 93-96.
- [126] Q. Zhu, K. Wu, H. Wang, W. Xia, and S. Lv, "The study of PEA space charge waveform recovery under temperature gradient," in *Solid Dielectrics (ICSD), 2013 IEEE International Conference on*, 2013, pp. 464-467.
- [127] X. Wang, Z. Lv, K. Wu, X. Chen, D. Tu, and L. A. Dissado, "Study of the factors that suppress space charge accumulation in LDPE nanocomposites," *IEEE Transactions on Dielectrics and Electrical Insulation*, vol. 21, pp. 1670-1679, 2014.
- [128] H. Nishimura, F. Inoue, A. Nakashiba, and T. Ishikawa, "Design of electrofusion joints and evaluation of fusion strength using fusion simulation technology," *Polymer Engineering & Science*, vol. 34, pp. 1529-1534, 1994.
- [129] C. Zhang, K. Kaneko, and T. Mizutani, "Temperature increase and charging current in polyethylene film during application of high voltage," *Applied Physics Letters*, vol. 79, pp. 3839-3841, 2001.
- [130] G. Kaye, "Kaye & Laby-Tables of Physical and Chemical Constants," ed: Longman, 1995.
- [131] D. W. Van Krevelen and K. Te Nijenhuis, *Properties of polymers: their correlation with chemical structure; their numerical estimation and prediction from additive group contributions*: Elsevier, 2009.
- [132] V. Lanza and D. Herrmann, "The density dependence of the dielectric constant of polyethylene," *Journal of Polymer Science*, vol. 28, pp. 622-625, 1958.
- [133] P. M. Morse and K. U. Ingard, *Theoretical acoustics*: Princeton university press, 1968.

- [134] K. S. Yee, "Numerical solution of initial boundary value problems involving Maxwell's equations in isotropic media," *IEEE Trans. Antennas Propag*, vol. 14, pp. 302-307, 1966.
- [135] M. Wadamori, M. Fukuma, T. Maeno, K. Fukunaga, and M. Nagao, "Proposal of numerical analysis model of acoustic wave propagation and generation on PEA method," in *Properties and Applications of Dielectric Materials, 2003. Proceedings of the 7th International Conference on*, 2003, pp. 863-866.
- [136] M. Fu and G. Chen, "Space charge measurement in polymer insulated power cables using flat ground electrode PEA system," *IEE Proceedings-Science, Measurement and Technology*, vol. 150, pp. 89-96, 2003.
- [137] K. Fukunaga, "Progress and prospects in pea space charge measurement techniques-[feature article]," *IEEE Electrical Insulation Magazine*, vol. 24, pp. 26-37, 2008.
- [138] M. Kaviani, *Principles of heat transfer*: John Wiley & Sons, 2002.
- [139] F. Rogti, "Space charge behavior and its modified electric field in the cross-linked polyethylene under applied voltage DC and different temperatures," *Journal of Electrostatics*, vol. 71, pp. 1046-1054, 2013.
- [140] M. A. Fard, A. Reid, and D. Hepburn, "Influence of HVDC converter operation on partial discharge characteristics," in *Power Modulator and High Voltage Conference (IPMHVC), 2016 IEEE International*, 2016, pp. 680-683.
- [141] F. Mauseth, M. Amundsen, A. Lind, and H. Faremo, "Water tree growth of wet XLPE insulation stressed with DC and high frequency AC," in *Electrical Insulation and Dielectric Phenomena (CEIDP), 2012 Annual Report Conference on*, 2012, pp. 692-695.
- [142] W. Zhao, W. H. Siew, M. J. Given, E. Corr, Q. Li, and J. He, "Assessment of HDPE aged under DC voltage combined with AC harmonic stresses of various frequencies," *IEEE Transactions on Dielectrics and Electrical Insulation*, vol. 24, pp. 1189-1196, 2017.
- [143] D. Fabiani and G. Montanari, "The effect of voltage distortion on ageing acceleration of insulation systems under partial discharge activity," *IEEE Electrical Insulation Magazine*, vol. 17, pp. 24-33, 2001.
- [144] M. A. Fard, M. E. Farrag, S. McMeekin, and A. Reid, "Partial discharge behavior under operational and anomalous conditions in HVDC systems," *IEEE Transactions on Dielectrics and Electrical Insulation*, vol. 24, pp. 1494-1502, 2017.
- [145] S. Hole, "PEA Signal Simulation in the case of Plane-Wire-Plan Geometry samples", University of Leicester 2013.
- [146] G. Mazzanti and G. Montanari, "Electrical aging and life models: the role of space charge," *Dielectrics and Electrical Insulation, IEEE Transactions on*, vol. 12, pp. 876-890, 2005.
- [147] L. Dissado, G. Mazzanti, and G. Montanari, "The incorporation of space charge degradation in the life model for electrical insulating materials," *Dielectrics and Electrical Insulation, IEEE Transactions on*, vol. 2, pp. 1147-1158, 1995.
- [148] L. Dissado, G. Mazzanti, and G. Montanari, "A new thermo-electrical life model based on space-charge trapping," in *Electrical Insulation, 1996., Conference Record of the 1996 IEEE International Symposium on*, 1996, pp. 642-645.
- [149] L. Dissado, G. Mazzanti, and G. Montanari, "The role of trapped space charges in the electrical aging of insulating materials," *IEEE Transactions on Dielectrics and Electrical Insulation*, vol. 4, pp. 496-506, 1997.
- [150] Z. Zuo, C. Yao, L. Dissado, N. Chalashkanov, and S. Dodd, "Simulation of electro-thermal ageing and breakdown in polymeric insulation under high frequency trapezoidal-wave pulses," *IEEE Transactions on Dielectrics and Electrical Insulation*, vol. 24, pp. 3766-3775, 2017.
- [151] L. Dissado, A. Thabet, and S. Dodd, "Simulation of DC electrical ageing in insulating polymer films," *Dielectrics and Electrical Insulation, IEEE Transactions on*, vol. 17, pp. 890-897, 2010.

- [152] B. Vissouvanadin, T. Vu, L. Berquez, S. Le Roy, G. Teyssedre, and C. Laurent, "Deconvolution techniques for space charge recovery using pulsed electroacoustic method in coaxial geometry," *IEEE Transactions on Dielectrics and Electrical Insulation*, vol. 21, pp. 821-828, 2014.
- [153] C. J. F. Böttcher, "Theory of Electric Polarization," vol. 1, D. i. S. Fields, Ed., Second Edition ed. Elsevier, 1973.